UNIVERSITÀ DEGLI STUDI DI PADOVA

DIPARTIMENTO DI SCIENZE CHIMICHE
CORSO DI LAUREA MAGISTRALE IN CHIMICA

TESI DI LAUREA MAGISTRALE

Synthesis of photoactive conjugated D-π-A organic dyes for the sensitization of inorganic semiconducting nanomaterials

Relatore: Prof. Enzo Menna
Controrelatore: Prof. Antonio Barbon

LAUREANDO: Bertoluzzo William

Anno accademico 2021/2022

Nothing in life is to be feared,

it is only to be understood.

Now is the time to understand more,

so that we may fear less.

-Marie Curie

Table of Contents

Abstract

Nowadays, the world is in the middle of an energy transition. The exploitation of fossil fuels accompanied the development of humanity since the mid-18th century, but now the whole planet is paying the price. Any research effort aimed at founding a society free from carbon emissions is a road worth taking. In the last decades, the use of hydrogen as energy vector has been theorized and has encouraged a lively amount of research, in particular on technologies designed to its production and storage. The idea of a device able to produce hydrogen without any energy input from the outside is particularly compelling. Photoelectrochemical cells (PECs) have been investigated to exploit the sunlight to achieve a self-sustained reduction of water to yield hydrogen gas. Often, however, the conversion efficiency of these devices is too low to make it cost-effective, or they use rare and precious metals as palladium or platinum. The use of much less scarce and expensive materials would be appreciable. Inexpensive and widely available compounds, such as transition metal dichalcogenides (TMDs) like molybdenum disulfide (MoS_2), can catalyze the hydrogen evolution reactions (HER) from water quite efficiently, once they're nanostructured in monolayers. The energetic requirements to catalyze the reaction for this material are similar to the one of platinum, making it an extraordinary and cheap subsititute. To further improve its properties, it could be interesting to sensitize the molybdenum disulfide with an organic dye able to absorb and exploit the sunlight. Once photoexcited, this organic molecule should be able to access to a intramolecular charge transfer state (ICT) in which it donates an electron to the semiconductor, facilitating and pushing the catalysis of the HER.

In this thesis work, two organic sensitizers of the D-π-A type will be synthesized, and the grafting onto the nanostructured semiconductor will be attempted. Evidences and proofs of the occurred functionalization of MoS_2 will be sought, together with a possible electronic communication between the two parts of the hybrid material obtained.

Riassunto

Al giorno d'oggi, il mondo è nel mezzo di una transizione energetica. Lo sfruttamento dei combustibili fossili ha accompagnato lo sviluppo dell'umanità sin dalla metà del XVIII secolo, ma ora l'intero pianeta ne sta pagando il prezzo. Qualsiasi sforzo di ricerca volto a fondare una società senza emissioni di carbonio è una strada che vale la pena essere percorsa. Negli ultimi decenni, l’utilizzo dell'idrogeno come vettore energetico è stato teorizzato e ha incoraggiato una vivace attività di ricerca, in particolare sulle tecnologie volte alla sua produzione e stoccaggio. L'idea di un dispositivo in grado di produrre idrogeno senza alcun apporto di energia dall'esterno è particolarmente interessante. Le cellule fotoelettrochimiche (PECs) sono state studiate per sfruttare la luce solare per ottenere una riduzione autosufficiente dell'acqua per produrre idrogeno gassoso. Spesso, tuttavia, l'efficienza di conversione di questi dispositivi è troppo bassa per renderli convenienti, o usano metalli rari e preziosi come palladio o platino. L'uso di materiali più comuni e meno costosi sarebbe sicuramente apprezzabile. Composti economici e ampiamente disponibili, come i dicalcogenuri dei metalli di transizione (TMDs) di cui il bisolfuro di molibdeno (MoS_2) è un esempio, possono catalizzare la reazione di evoluzione di idrogeno (HER) dall'acqua in modo abbastanza efficiente, una volta che sono nanostrutturati in monostrati. Le caratteristiche energetiche di questo materiale necessarie per catalizzare la reazione sono simili a quelle del platino, rendendolo un sostituto straordinario ed economico. Per migliorare ulteriormente le sue proprietà, potrebbe essere interessante sensibilizzare il bisolfuro di molibdeno con un colorante organico in grado di assorbire e sfruttare la luce solare. Una volta fotoeccitata, questa molecola organica dovrebbe essere in grado di accedere a uno stato di trasferimento di carica intramolecolare (ICT) in cui dona un elettrone al semiconduttore, facilitando e spingendo la catalisi dell'HER.

In questo lavoro di tesi, verranno sintetizzati due sensibilizzatori organici del tipo D-π-A e verrà tentato il grafting sul semiconduttore nanostrutturato. Si cercheranno le evidenze e le prove dell'avvenuta funzionalizzazione del bisolfuro di molibdeno, unitamente alla presenza di un’eventuale interazione elettronica tra i due componenti del materiale ibrido ottenuto.

1. Introduction

1.1. Energy and hydrogen as energetic vector

Today's world is at the center of an energy transition. The development of human society over the last century has been linked to the exploitation of fossil fuels, and this led to our dependence from them. The use of fossil fuels is also what allowed humanity to reach a consistent technological advance in an extremely short period of time. One of the greatest negative effects of this exploitation is undoubtedly the increase in pollution levels, on a scale such that the Earth is no longer able to bear any more without going against irreversible consequences. One of the many negative effects that the planet is experiencing because of pollution, and perhaps the most obvious, is climate change. Often, in the eyes of society, the issue of climate change is the main topic when discussing energy transition, which is seen as economically heavy and not convenient, but necessary for the well-being of humanity. Even in times when climate change had not yet shown its effects and was only a possible scenario, early warnings by scientists about human dependence on fossil fuels have encouraged the study and development of systems based on renewable energy sources. The role of hydrogen in this transition was recognized from the beginning by the scientific community. The most important support for the idea that hydrogen could play a major role in the energy transition appeared at the beginning of the 21st century [1]. With the hope of an energy storage method free of greenhouse gas and CO_2 emissions, hydrogen has continuously stimulated curiosity and hope for future development. Despite the long and expensive path that has opened to obtain a stable and usable technology, hydrogen has proved to be a road that is worth to be traveled [2]. For this reason, it has now become one of the most researched technologies in energy storage. Very often, hydrogen technology is compared to lithium-ion batteries; from this comes the comparison between battery-powered vehicles and fuel-cell vehicles. To achieve a zero-emission society, it will be necessary one day to convert, or replace, all internal combustion vehicles with one of these two technologies. Both batteries and fuel cells are potentially more environmentally friendly than fossil fuels. In some respects, batteries are superior to fuel cells, while in other circumstances it is the opposite. Hydrogen, along with the implementation of renewable energy sources, has the potential to fund a zero-emission society. The integration of hydrogen in smart grids, although it is still in its infancy, will become a fundamental requirement in the future [3]. The development of 100% emission-free cities is unthinkable without intelligent energy systems where hydrogen plays a key role in mitigating the production fluctuations of renewable sources, implementing long-term electricity storage solutions [4]. A great advantage of the implementation of fuel cells is the cogeneration capacity, where thermal energy, sometimes perceived as a loss of efficiency, can be used for residential and industrial heating [5].

Despite its disadvantages, hydrogen is an integral part of long-term energy storage solutions to enable the full exploitation of renewable energy sources.

Any effort in the direction of researching and manufacturing devices able to economically produce or store hydrogen could be a step forward to the foundation of a society free from emissions and that’s a debt we have towards the planet.

The mimicry of natural photosynthesis, in which oxygen and carbon-based compounds are obtained from inexpensive and plentiful sources (water, carbon dioxide, and solar radiation), has attracted a lot of interest in the pursuit of sustainable ways to energy [6]. A procedure known as artificial photosynthesis is being researched to replicate the initial stage of natural photosynthesis, which is the production of oxygen and protons from water and sunlight. This apparatus consists of two electrodes submerged in an aqueous solution. Here, water is oxidized to produce protons and electrons that are used to generate molecular hydrogen, the most significant solar fuel [7]. At any pH, the standard potential (E°) for water electrolysis into H_2 and O_2 [Equation 1] is 1.23 V.

$$H_2O \rightarrow H_2 + {}^{1}/_{2}\, O_2 \qquad (1)$$

The volume of hydrogen produced is equal to double that of oxygen, according to the reaction stoichiometry. Water splitting is a multi-electronic (two electrons are evolved for each hydrogen molecule and four electrons are generated for each oxygen molecule), multi-atomic, energy-demanding, kinetically difficult process, with high activation barrier. The voltage needed for water splitting is increased to 1.8-2.0 V, which is the voltage commonly used in industrial electrolyzers, due to thermodynamic losses and overpotentials linked to kinetics [8]. To force the reaction towards the products, catalysts are hence required. This process can be artificially achieved by using three different methods: photovoltaics together with an electrolyzer, photocatalysis, and photoelectrochemical cells (PEC) [9].

1.2. Dye-sensitized photoelectrochemical cells (DS-PECs)

A PEC is a device that can use electrochemical processes to transform solar radiation into energy carriers without using an external power source. PECs for water splitting consist of a cathode, where protons are reduced to H_2, and an anode, where water oxidation occurs. A PEC can have a photoanode with a passive cathode, a photocathode with a passive anode, or both a photoanode and a photocathode, depending on the photoactive electrode(s). An n-type or p-type semiconductor (SC) makes up the photoanode and photocathode, respectively. The electrodes are connected by an external circuit after being soaked into two different half-cells that are each filled with a water (buffer) solution [10]. The water splitting reaction has initially been demonstrated by Fujishima and Honda in 1972 employing TiO_2 as a SC at the photoanode and a Pt wire as the cathode [11]. TiO_2 has been frequently utilized for PEC water splitting even though it has little capability to exploit the visible light. WO_3, Fe_2O_3, and $BiVO_4$ as a photoanode and Si and Cu_2O as a photocathode, among other effective visible light active SC, have all been described. Unfortunately, most of these SCs for PEC water splitting have inadequate light harvesting and charge transport capabilities. Utilizing a visible light inactive SC that has been properly sensitized by a molecular antenna, or dye, designed to effectively absorb the visible portion of the solar spectrum and initiate the charge transfer processes, is one effective way to extend the light absorption of TiO_2-based devices to the visible range and resolve issues presented by visible light active SC. In this scenario, a dye-sensitized photo-electrochemical cell (DS-PEC) is produced. Since dye-sensitization is a critical element of the most crucial process, light harvesting, it plays a significant role. The sensitizer should ensure a quick charge transfer to the SC while avoiding charge recombination pathways, be stable under long-term irradiation, and absorb a significant portion of the visible spectrum [12]. The hydrogen evolution catalyst (HEC) at the cathode and the water oxidation catalyst (WOC) at the anode, respectively, properly catalyze the oxidation and reduction of water in the half-cells. These catalysts can either be adsorbed onto the surface of the SC or dispersed in the aqueous medium [13]. The dye is promoted to the excited state upon light absorption, creating an electron/hole pair. Once in the SC valence (VB) and conduction (CB) bands, the produced electrons and holes are ultimately transported to the external circuit. By oxidizing or reducing water and producing O_2 or H_2, the WOC or the HEC replenish the dye, accordingly [14]. There are three different types of DS-PECs:

- DS-PEC with a dye-sensitized photo anode and a passive cathode.
- DS-PEC with a dye-sensitized photocathode and a passive anode.
- Tandem DS-PEC with a dye-sensitized photoanode and photocathode.

The passive counter electrode in the first and second groups is often made of a metal, such platinum. The dye is covalently linked to the SC surface on the photoactive electrode. The catalyst can either be simply dispersed in the solution, covalently grafted to the SC, or even covalently linked to the dye itself, providing a dyad-sensitizer where all the major molecular components are integrated into one chemical species. (Figure 1).

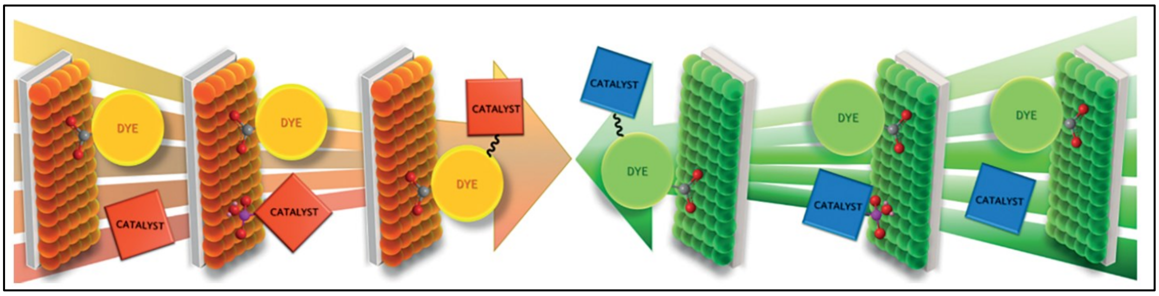

Figure 1: Schematic representation of the possible arrangements of the catalyst and the dye with respect to the electrode in a DS-PEC [23].

The most often employed molecular sensitizers up until now have been metal complexes like Ru(II) polypyridyl complexes. Designing metal-free organic dyes is a very young area of research that has only recently become relevant. This new field of study follows more established efforts in other areas of solar energy, such as dye-sensitized solar cells (DSSC), where record efficiencies employing this class of dyes have now been achieved and a vast literature has been made available during the past ten years [14], [15].

1.2.1. Metal-polypyridyl complexes

Metal complexes have been intensively investigated for DSSC applications for decades since the seminal work of Michael Grätzel in 1991, thanks to their broad absorption spectra and favorable photovoltaic properties [16]. In general, metal complex photosensitizers are composed of a central metal ion with ancillary ligands having at least one anchoring group. The absorption of light in the visible range of wavelengths is due to a metal to ligand charge transfer (MLCT). The overall characteristics of the complexes depend greatly on the central metal ion. Ancillary ligands, mainly bipyridines or terpyridines, can have their photophysical and electrochemical properties altered by adding various substituents (alkyl, aryl, heterocycle, etc.) to boost their photovoltaic performance. Anchoring groups are used to connect the dye and semiconductor and make it easier for the excited electron to be injected into the semiconductor's CB. To adjust the MLCT states' energy levels and to enhance the kinetics of the electron injection and dye regeneration, any component of the complex can be changed [17].

Ru complexes have demonstrated the best photovoltaic capabilities among the metal complexes, including a wide absorption spectrum, acceptable excited and ground state energy levels, a lengthy excited-state lifetime, and strong (electro)chemical stability. Under typical testing conditions, the solar cell efficiency of several Ru complexes utilized in DSSCs exceeded 10% [17]. The ligands of Ru complexes have undergone extensive modification over time in order to improve the photosensitizers. Extending the spectral response range of the sensitizer to the near-IR region is desirable to boost DSC efficiency even more.

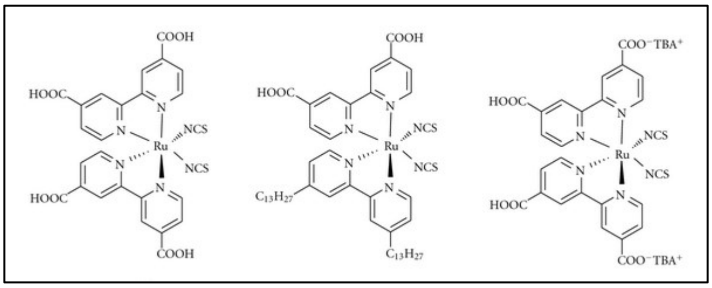

Figure 2: Examples of Ru-polypyridyl complexes utilized as sensitizers ind DSSCs [19].

In an effort to maximize and improve light absorption, in 2007 Thelakkat, Durrant, and co-workers developed Ru dyes with triarylamine-based electron donor groups at the bipyridyl ligands and studied charge recombination kinetics and solar cell performance [18]. When the triarylamine moiety is linked by a conjugated link to the metal center, a significant increase of the extinction coefficient is observed (about 2-fold). Rapid intramolecular hole transfer from the Ru center to the donor is seen upon excitation of the dye and electron injection, and a long-lasting charge separation between photoinjected electrons and the oxidized donor group was noticed. This strategy seems to be effective for raising solid-state DSC efficiency.

1.2.2. Porphyrins

Porphyrin-based dyes are a representative of another significant group of metal-containing DSSC sensitizers [19]. Two strong optical absorptions, the Soret band between 400 and 500 nm and the Q-band between 550 and 750 nm, define a porphyrin's optical behavior [19]. The functionalization of the macrocycle that makes up the structure of the porphyrin enables the tuning of these two bands to produce panchromatic dyes appropriate for DSSC applications. Tetrakis(4-carboxyphenyl)porphyrin and TiO_2 undergo a charge transfer process that, according to a significant study published in 2000, is fast and kinetically similar to that of photosensitizers based on ruthenium [20]. The preparation and investigation of several porphyrin-based compounds as DSSC sensitizers were made possible thanks to this paper. An important drawback of porphyrin dyes is the tendency to aggregate on the TiO_2 surface, leading to a self-quenching of the absorbed photon before the desired electron injection in the semiconductor. Co-adsorbates are frequently used to lessen aggregation with the goal of maintaining the physical separation of the molecules [21]. In order to functionalize the macrocycle core and prevent aggregation, a lengthy alkyl chain can be used. This also shields TiO_2 from unfavorable interactions with the electrolyte.

Porphyrin-based sensitizers have a low absorption between 500 and 600 nm, which is one of their key downsides. To increase the power conversion efficiency of the DSSC device, it can be useful to combine two or more distinct sensitizers having complimentary absorption qualities. Co-sensitization has a dual positive impact on DSSC performance: on one hand, it increases photo-generated current by increasing the number of solar photons captured. Additionally, improved semiconductor surface coverage decreases the negative charge recombination processes between the injected electron and the redox couple [22]. Co-sensitization can be accomplished using one of two methods: the stepwise strategy involves the sequential adsorption of the two distinct dye solutions, whereas the cocktail approach performs co-sensitization by combining two sensitizer solutions with a particular molar ratio.

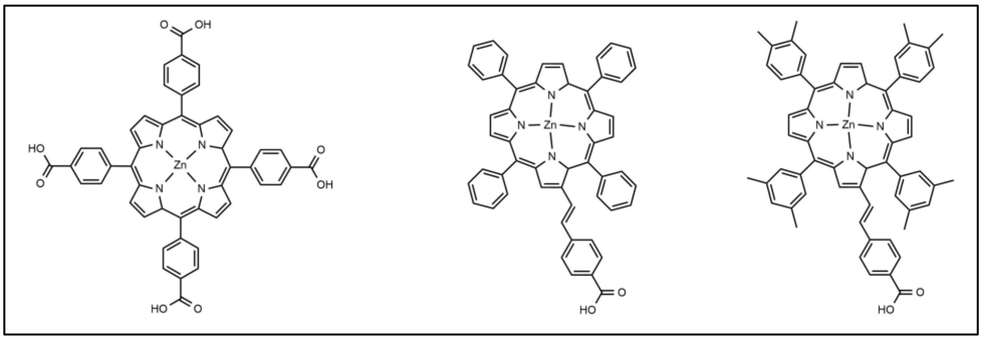

Figure 3: Examples of porphyrin-based structures used as sensitizers in DSSCs [19].

1.2.3. Metal-free sensitizers

The third important class of photosensitizers for DSSC is composed of metal-free organic dyes. Compared to ruthenium-based sensitizers, they offer a more straightforward tunability of the chemical structure by utilizing the well-established synthetic techniques used in the chemistry of dyes. The modulation of the chemical properties then has a significant impact on the optical properties, allowing for the preparation of sensitizers with a broad spectral absorption. Metal-free sensitizers are also typically characterized by larger molar extinction coefficients and this aspect is particularly relevant for electrolyte-free solid-state DSSC, where a semiconductor thickness not exceeding 2–3 mm is desirable to allow an optimal charge collection [19].

i. Perylene derivatives

This type of dyes has been actively used in DSSC and DS-PEC application because of their strong absorption in the visible range of the solar spectrum and their proper HOMO energy level for water oxidation [23]. However, they often exhibited very low overall power conversion efficiencies (1–2%) [24]. Nevertheless, their synthetic chemistry has a potentially wide range of flexibility for altering properties such as color and redox potentials. As for porphyrins, perylene derivatives tend to aggregate as well, hence functionalization with bulky groups or long alkyl chains could be useful.

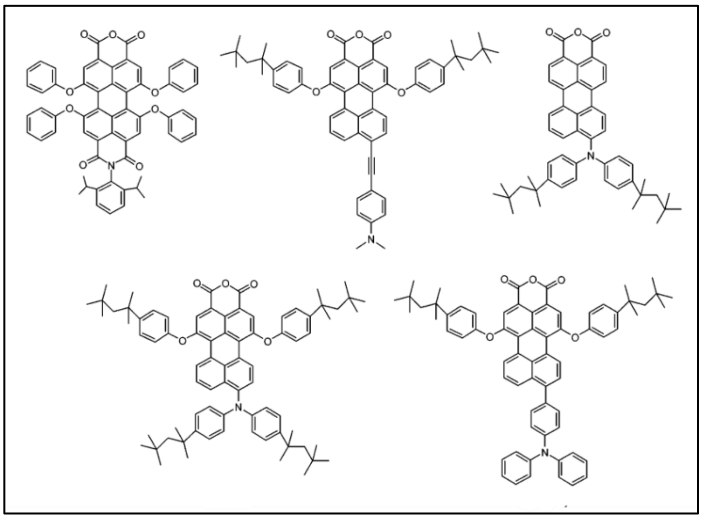

Figure 4: Examples of perylene-based structures used as sensitizers in DSSCs [19].

ii. Donor-acceptor D-π-A molecules

Another class of metal-free sensitizers is based on a push-pull structure D-π-A where an electron donor (D) group is linked to an electron acceptor (A) through a π-conjugated bridge (π). Usually, the anchoring group that holds the dye to the semiconductor surface is the electron acceptor. This type of structure is advantageous because it makes it easier to separate photoinduced charges: upon photoexcitation, an electron density shift occurs from the donor part of the molecule, where the HOMO is primarily localized, toward the electron acceptor side, where the LUMO is primarily localized. This promotes electron injection into the conduction band of TiO_2, while also preventing the deleterious process of charge recombination between the semiconductor and the oxidized dye. The investigation of various electron donors and π linkers, as well as, to a lesser extent, electron-withdrawing anchoring moieties, has been the main focus of the rational design of innovative metal-free sensitizers. These studies aimed to obtain systems with acceptable optical absorption, particularly in the NIR region of the spectrum, well-aligned electrical levels to reduce losses, and good stability during device operation [25].

Triphenylamine (TPA) and its derivatives are by far the most researched among the donor units [25]. In 2004, a triphenylamine donor was first employed. Dye **44** was used as a photosensitizer in a traditional DSSC device based on iodine electrolyte and provided a promising efficiency of 5.30% [26].

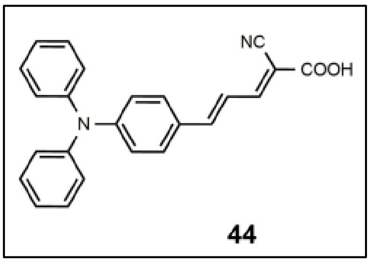

44

Figure 5: Molecular structure of dye 44 from [19].

Numerous studies have been conducted on the electron-rich thiophene rings as part of the conjugated bridge of the metal-free DSSC sensitizers. Liu proposed a number of TPA dyes with thiophene derivatives in their chemical backbone in 2008 [27]. Sensitizer **46**, which contains the 3,4-ethylendioxythiophene group (EDOT), showed the highest efficiency of these dyes thanks to its wide spectrum response and high molar extinction coefficient (24,500 M^{-1} cm^{-1}). This dye sensitized a device with an extremely interesting efficiency of 7.30%.

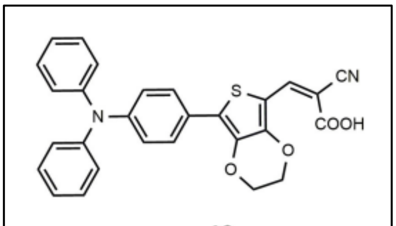

46

Figure 6: Molecular structure of dye 46 from [19].

In order to increase the efficiency of the DSSC and avoid undesirable charge recombination reactions at the semiconductor/electrolyte interface, bulky alkyl or alkoxy tails can be used, as was previously discussed for Ru- and porphyrin-based photosensitizers. In this context, one of the most effective donors in metal-free sensitizers for high-performance DSSCs is TPA functionalized with dihexyloxy (DHO). Hexyloxy tails also have the effect of improving the TPA group's capacity as an electron donor.

The molecular backbone of dyes **50** and **51**, respectively, shows a thienothiophene group and a bisthienothiophene group [28].The addition of these electron-rich heterocycles enhances the dyes' ability to absorb light, resulting in molar extinction values of 42,000 M^{-1} cm^{-1} for **50** at 516 nm and 47,000 M^{-1} cm^{-1} for **51** at 524 nm. The efficiency of the devices sensitized with **51** was marginally higher than that of the devices sensitized with **50** (8.02 vs. 7.54%). Device sensitized with **51** offered a remarkable 9.8% efficiency. The same dye was employed as the sensitizer in a solvent-free DSSC, which provided an efficiency of 8.1% and outstanding stability: after 1,000 hours of one solar soak, the device still maintained 96% of its initial performance.

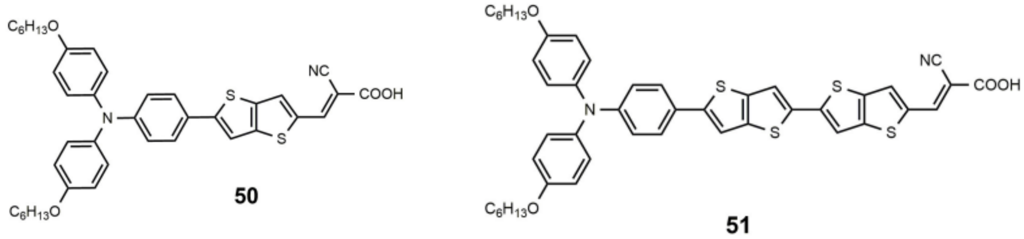

50

51

Figure 7: Molecular structures of dyes 50 and 51 from [19].

The development of a D-A-π-A structure by inserting an electron-poor moiety into the π-bridge is an alternative strategy that has been investigated. Particularly promising for achieving high extinction coefficients, extending the absorption spectrum, and enhancing the photo/thermal stability of organic sensitizing dyes, this sort of structure has recently grown in popularity. Several organizations investigated the inclusion of a benzothiadiazole group in the bridge and found some intriguing outcomes [29].

The standard metal-free push-pull photosensitizer has a cyanoacrylic moiety as its anchoring group, which also happens to be the dye's electron acceptor portion. While many different anchoring groups have been explored, including pyridine, phosphonic acid, benzoic acid, tetrazole, and triazole derivatives, the best-performing organic sensitizers up until recently had a cyanoacrylic-like anchoring group [30].

However, the Kakiage group looked into the alkoxysilyl moiety as a potential substitute anchoring group and created new photosensitizers with exceptional abilities. When used in a DSSC, the dye **68** provided an efficiency of up to 12.5%. The same dye was combined with dye **69** in a co-sensitized DSSC, and the efficiency ranged from 11.1% to 14.3% depending on the electrolyte utilized [31]. This number indicates the organic-based DSSC's current efficiency record.

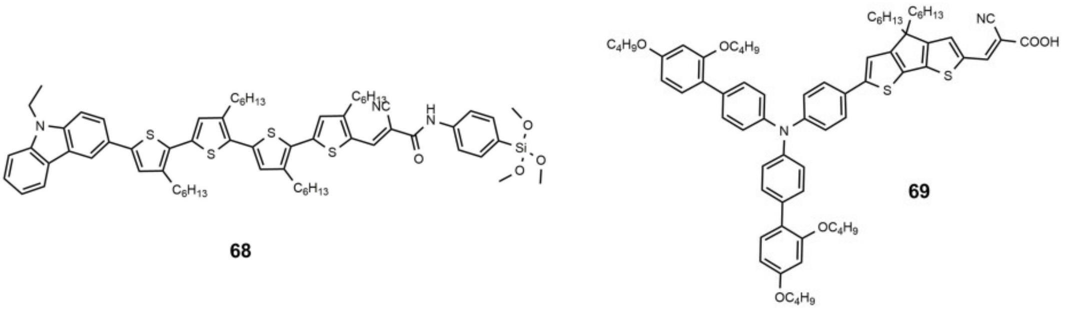

Figure 8: Molecular structures of dyes 68 and 69 from[19].

Due to a strong propensity for aggregation and improperly matched energy levels for electron injection, the number of highly effective DSSCs using blue photosensitizers is quite constrained (typically, the absorption at higher wavelengths is the result of the LUMO stabilization).

1.3. D-π-A molecules preparation

1.3.1. Miyaura borylation

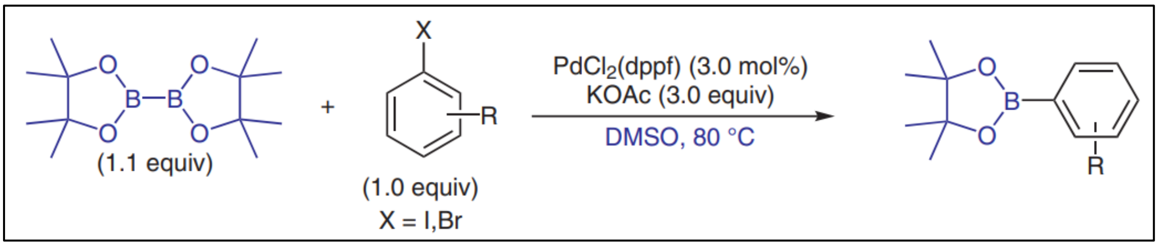

Figure 9: General scheme of reaction representing a Miyaura borylation between an aryl halide and bis(pinacolato)diboron.

The Miyaura borylation is a palladium catalyzed cross-coupling reaction which allows the synthesis of boronates by cross-coupling bis(pinacolato)diboron (B_2pin_2) with aryl halides or vinyl halides. Borylated products obtained from B_2pin_2 are stable to air and allow for regular workup, including chromatographic purification. Pinacol esters are challenging to hydrolyze, but they can act as coupling partners in reactions like the Suzuki Coupling and others without being hydrolyzed first.

The selection of a suitable base is essential for the borylation reaction's effectiveness since a high activation of the product allows for the competitive Suzuki coupling. The Miyaura group actually screened a variety of reaction conditions before deciding to employ KOAc and KOPh [32].

Since bis(pinacolato)diboron is a poor Lewis acid as a starting material, ^{11}B-NMR analysis of KOAc and B_2bin_2 in DMSO-d_6 reveals no indication of the coordination of the acetoxy anion to a boron atom leading to a tetrahedral activated species (compared to Suzuki coupling) [32]. However, the reaction rate of the transmetalation phase is affected by the creation of a (acetato)palladium(II) complex following the oxidative addition of the halide.

Compared to a Pd-X (X=Br, I) bond, the Pd-O bond, which consists of a hard Lewis base and a soft Lewis acid, is more reactive. The strong oxophilicity of boron must also be taken into account as a catalyst for the transmetalation process, which involves an acetato ligand. The proposed catalytic cycle is reported in the figure below.

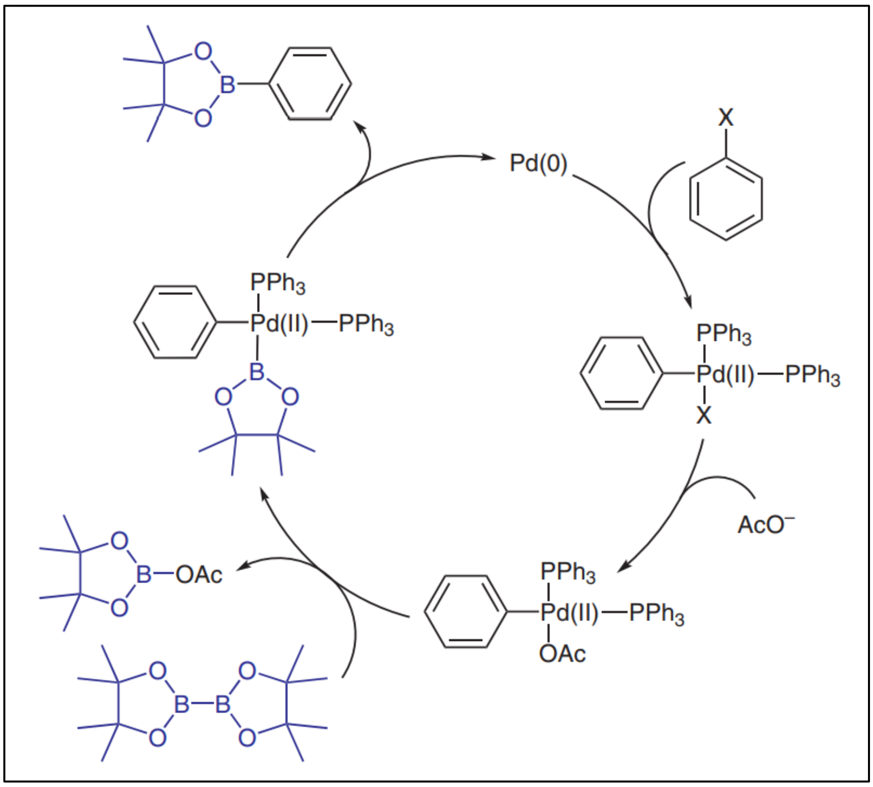

Figure 10: Schematic representation of the catalytic cycle in Miyaura borylation.

Because of the mild reaction conditions, boronates that are not accessible via lithium or Grignard intermediates and subsequent borylation can be prepared. Similar reactions can be carried out in large-scale synthesis when HBPin is used instead of B_2Pin_2, which also tolerates a variety of reducible functional groups. However, side products may form when the aryl halide is dehalogenated.

1.3.2. Suzuki-Miyaura coupling

The Suzuki-Miyaura condensation consists in the coupling of an aryl-boronic acid with an aryl halide by a palladium(0) complex. The reaction is widely used for the formation of selective C-C bonds between two aromatic rings. It was first published in 1979 by Akira Suzuki and Norio Miyaura [33].

The cross-coupling reaction of organoboron compounds follows a catalytic cycle involving (1) oxidative addition of organic halides or other electrophiles to give palladium(II) R^1-Pd-X complex; (2) transmetallation between R^1-Pd-X and R^2-$B(OH)_2$ with the help of a base; and (3) reductive elimination of R^1-R^2 to regenerate the palladium (0) complex [33].

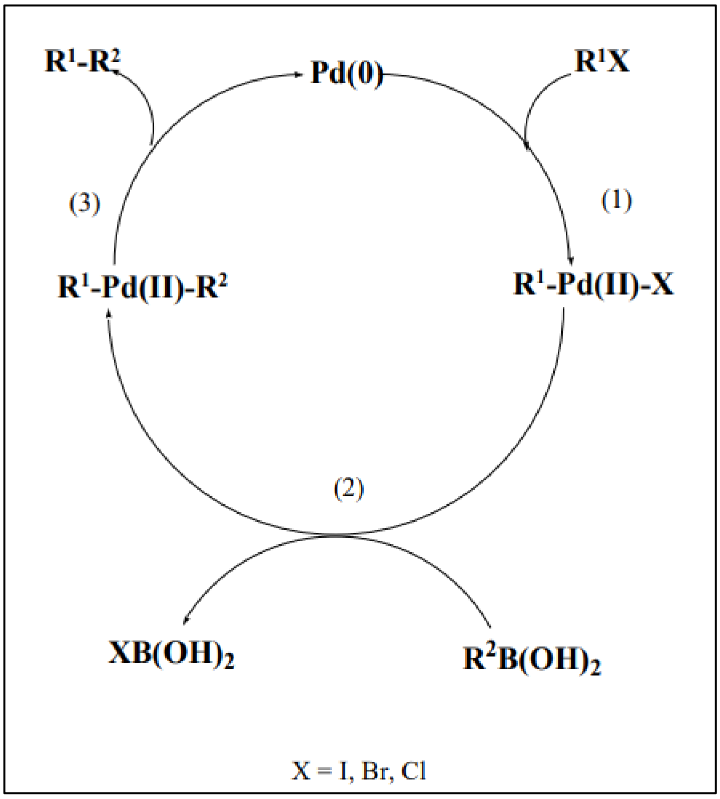

Figure 11: Schematic representation of the catalytic cycle in a Suzuki-Miyaura cross-coupling reaction.

Although the two steps of oxidative addition and reductive elimination are reasonably well understood, little is known about the transmetallation process. Based on the available information, it is believed that there are several processes involved in the transfer of the organic group in the R^1-Pd-X complex. The addition of sodium hydroxide or other bases causes a significant acceleration in the transmetallation between R^1-Pd-X and alkylborates or organoboronic acids, which is quite different from the effect it has in other organometallic reactions [34].

The quaternarization of the boron atom by a negatively charged base increases the nucleophilic nature of the organic group on the boron atom towards the alkylation of R^1-Pd-X. A hydroxylborate anion $R^2B(OH)^{3-}$, which is present in equilibrium with free boron acid, could alkylate R^1-Pd-X.

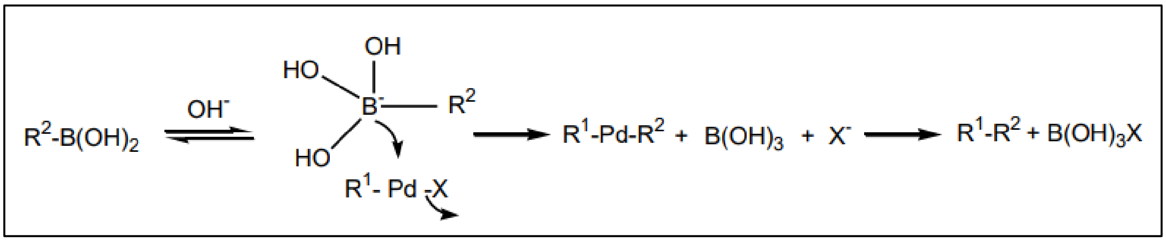

Figure 12: Proposed mechanism of transmetallation between R1-Pd-X and organoboronic acids, promoted by the presence of hydroxyl groups.

The principle on which the reaction for the formation of carbon-carbon bonds is based is the formation of intermediates in which both reagents coordinate with palladium by simple Pd-C bonds (oxidative addition). Then the catalytic cycle involves the formation of the C-C bond with restoration of the initial oxidation state of palladium (reductive elimination). Palladium's ability to oxidize and reduce rapidly and reversibly during the cross-coupling reaction is hence key to the process efficiency. Traditionally, the Suzuki reaction is conducted using palladium complexes with phosphine ligands, due to their high efficiency. Phosphines have two functions: on the one hand, due to their high basicity, they favor the oxidative addition stage, on the other, by stabilizing Pd(0) in solution, they prevent precipitation [35]. However, the use of phosphine ligands also has a number of disadvantages such as instability in air and at high temperatures, and in some cases they can react with the palladium precursor hence reducing its catalytic activity [36].

The cross-condensation reaction of organoboron compounds with organic halides requires the presence of a negatively charged base, such as an aqueous solution of carbonate, phosphate or sodium hydroxide. Although anhydrous inorganic bases can mediate the reaction as a suspension in organic solvents, the presence of water or the use of hydrated inorganic bases can accelerate the reaction [37].

Although Na_2CO_3 is a weak base, it is effective for a large group of coupling reactions of arylboronic acids, but it's not suitable for reagents with steric hindrance such as various ortho-substituents. Transmetallation involves nucleophilic displacement of R^1-Pd-X with $ArB(OH)_3M$, producing R^1-Pd-R^2, $B(OH)_3$ and MX. The reaction can be accelerated with a counter ion (M^+) that has a high stability constant for the outgoing halide ion ($Ag^+ > Tl^+ \gg Ba^+ > Cs^+ > K^+$) [38].

Electron withdrawing substituents (e.g. -CO, -COOH, -COR, -NO_2, -CN etc.) conjugated at the attack position of the aryl halide are considered activators of the reaction as they contribute, by resonance effect, to decrease the density of charge favoring the nucleophilic attack in the transmetallation process; as shown by the resonance forms.

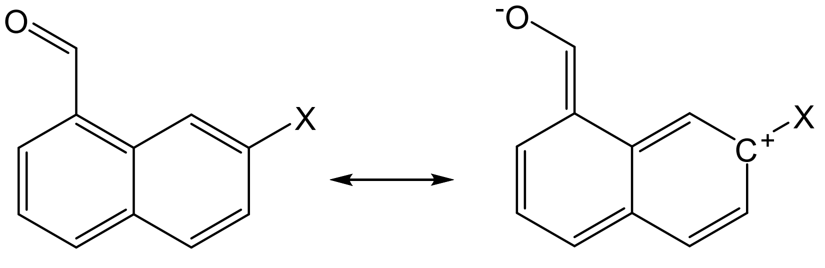

Figure 13: Resonance forms in the presence of electron withdrawing substituents, which decrease the density of charge on the attack position, favouring the nucleophilic attack in the transmetallation process.

Positive charges, or partly positive carbons by resonance effect, in the aromatic ring near the halo-substituted carbon act similarly, but in this case by inductive effect. These effects are shown in the following figure.

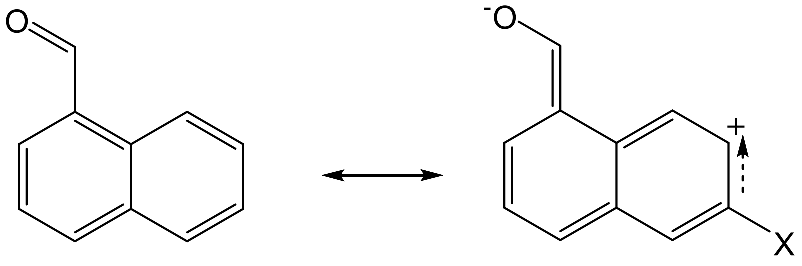

Figure 14: Inductive effect of a halo-substituted carbon atom near the attack position.

Some side reactions can be involved in the mechanism.
The metathesis of R-Pd-X to R^1M and MX produces both dimers when the transmetallation step is relatively slow due to the low nucleophilicity of the organometallic reagent.

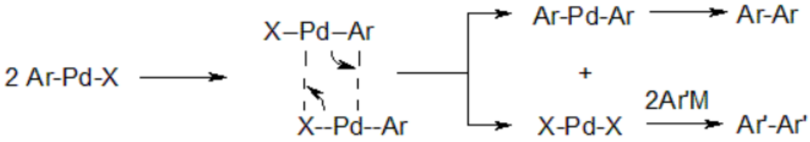

Figure 15: Mechanism of metathesis of R-Pd-X.

Triphenylphosphines are excellent ligands for the stabilization of palladium species; nevertheless, an undesired aryl-aryl interexchange can occur between aryl-palladium and aryl-phosphine complexes. A phenyl-coupling product is an important side product for electron-rich halides, while it is obtained in very small quantities with electro-deficient halides.

In many cases a large degree of homocondensation has been reported. In these cases, careful consideration should be given to oxygen (see diagram below). When the reaction mixture is exposed to air, arylboronic acids can easily produce homocondensation products. The reaction is slow under neutral conditions but is very rapid in the presence of aqueous bases.

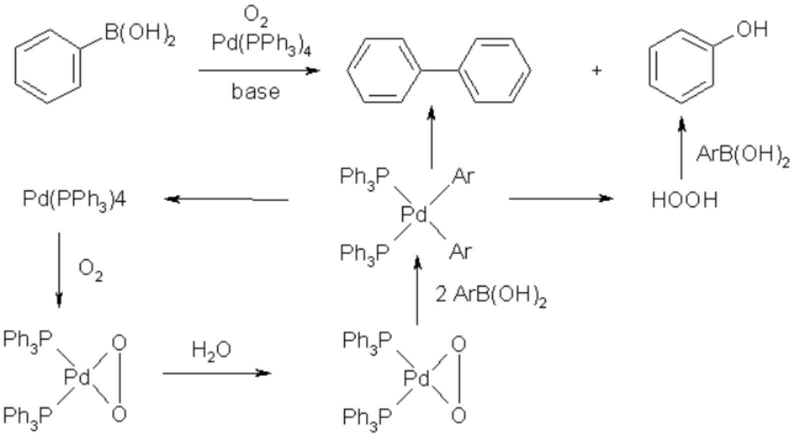

Figure 16: Mechanism of homocondensation in Suzuki-Miyaura cross-coupling.

Coupling reactions often result in the dehalogenation of organic halides (RX → RH), particularly when alcohols are used as a solvent. Dimethylformamide can also be blamed for its role as a hydride donor in the presence of a base.

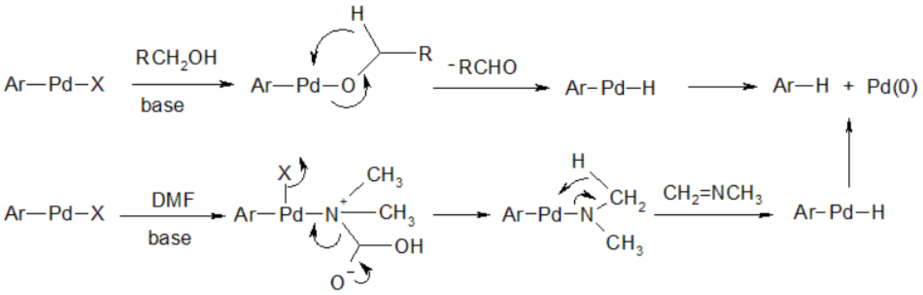

Figure 17: Mechanism of dehalogenation of organic halides.

1.3.3. Knoevenagel condensation

The Knoevenagel condensation was first demonstrated by Emil Knoevenagel in 1896 [39]. It's a modification of the aldol condensation and it consists of a nucleophilic addition of an active hydrogen compound to a carbonyl group in the presence of a basic catalyst, resulting in a double C=C bond formation. The active hydrogen compound contains a C–H bond which can be deprotonated by the basic catalyst, often a secondary amine as the piperidine. The reaction is usually followed by spontaneous dehydration resulting in an unsaturated product [40].

One of the general features of this reaction is that aldehydes react much faster than ketones. Additionally, the active methylene groups require two electron withdrawing groups, with typical examples including malonic esters, acetoacetic esters, malonodinitrile or acetylacetone. Both the nature of the catalyst and the solvent employed are important.

Since the by-product of the reaction is water, removing the generated water by azeotropic distillation or by the addition of molecular sieves helps to shift the equilibrium to favor the formation of the product [40].

The proposed mechanism in which piperidine acts as organo-catalyst involves the corresponding iminium intermediate as the acceptor:

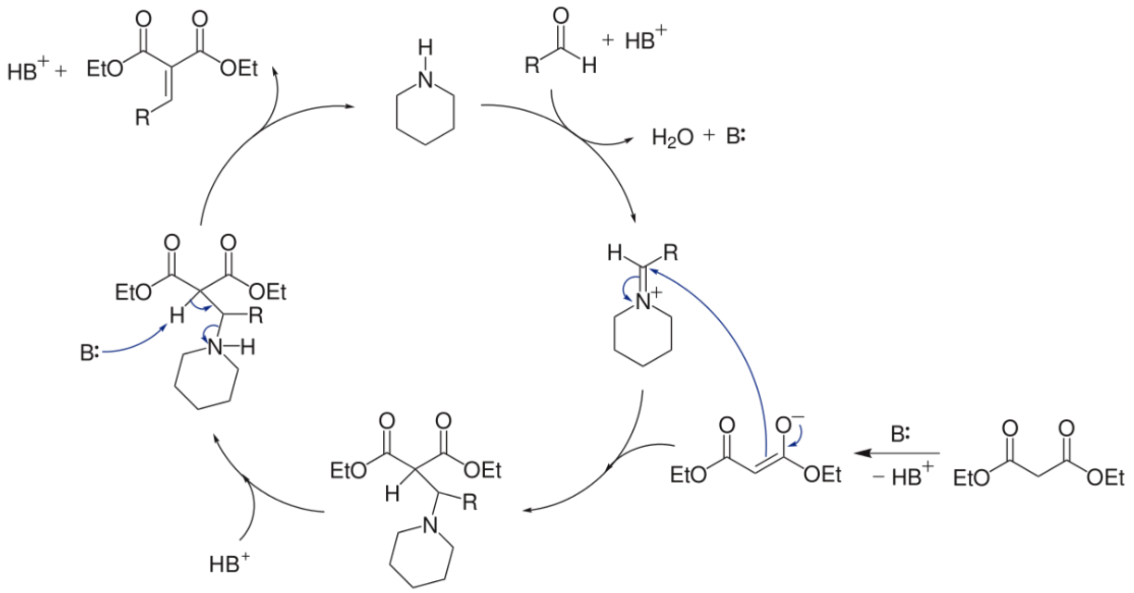

Figure 18: Schematic representation of the catalytic cycle in the Knoevenagel condensation between an active hydrogen compound and a carbonyl group.

1.3.4. Steglich esterification

The esterification of Steglich was presented for the first time by Wolfgang Steglich in 1978, during his research in introducing ester moieties for the synthesis of sugars and amino acids [41]. It can also be employed for the preparation of amides.

This reaction utilizes a carbodiimide together with N-(dimethylamino)pyridine (DMAP) in order to activate a carboxylic acid and promote the ester formation [41]. As first thing, the acid is activated by the carbodiimide to form an O-acylisourea intermediate. To synthesize an ester, the use of DMAP is necessary to minimize the formation of the acyl migration byproduct, which is inactive and competitive with the nucleophilic attack of the alcohol on the O-acylisourea intermediate. Under these conditions, an acyl pyridinium intermediate is formed, which then is able to react with the alcohol, releasing the urea byproduct, regenerating DMAP and forming the desired ester [42], [43]. This kind of couplings, involving the use of carbodiimide, are usually performed in anhydrous chlorinated solvents or dimethylformamide under inert atmosphere.

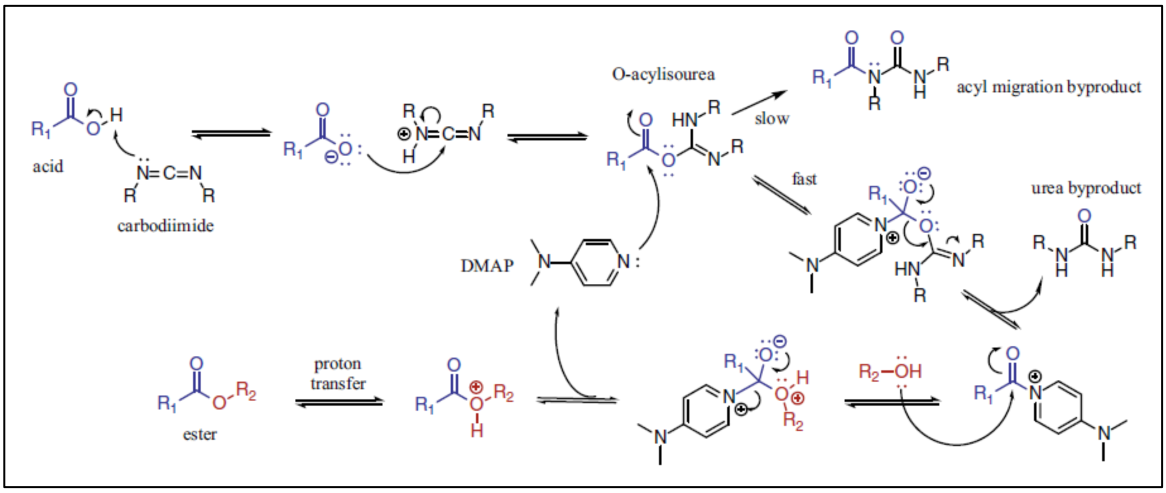

Figure 19: General mechanism or reaction of Steglich esterification.

Different carbodiimides are reported in the literature. Historically, the first used was DCC (dicyclohexyl carbodiimide), employed for peptide synthesis since 1955 [44]. It's prevalently used for amide bonds formation and it's insoluble in water, being a waxy solid at room temperature. This could introduce a challenge for the isolation of the reaction product. Active ester synthesis with DCC typically is carried out in organic solvent and therefore does not have the hydrolysis problems of water-soluble EDC-formed esters [44]. The isourea byproduct of a DCC-initiated reaction, dicyclohexyl urea (DCU), is also water insoluble.

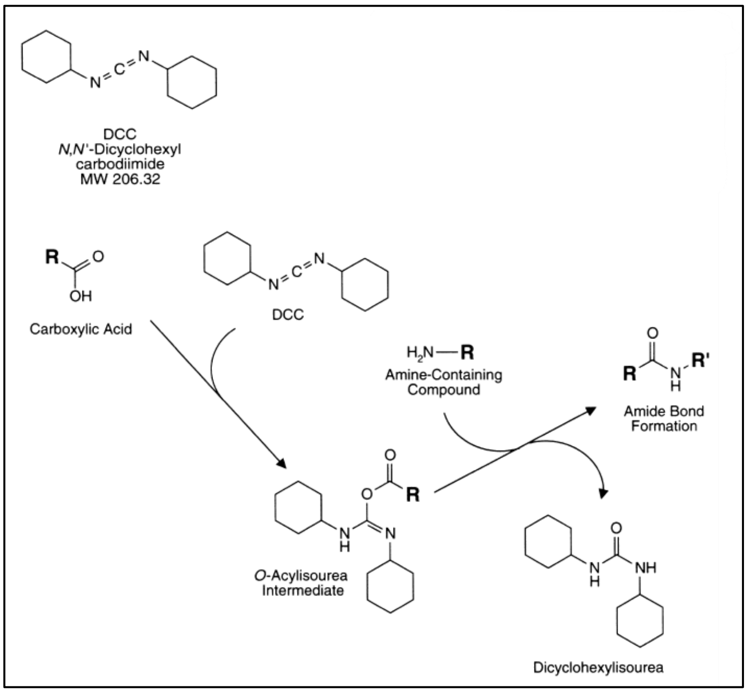

Figure 20: Mechanism of Steglich esterification using DCC as carbodiimide.

A potential undesired effect of DCC coupling is represented by the spontaneous rearrangement of the O-acylisourea to the inactive N-acylurea, which sequestrates DCC from the reaction. This rearrangement's rate is enormously increased in aprotic organic solvents, like DMF.

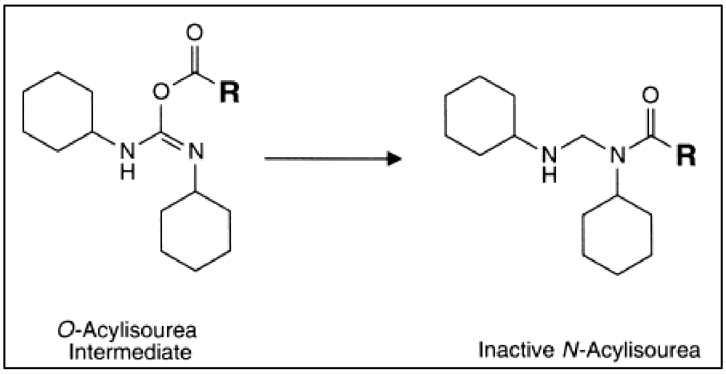

Figure 21: Spontaneous rearrangement of O-acylisourea to the inactive N-acylurea using DCC.

The activation efficiency of DCC is however extraordinarily high. If DCC is added to an excess of carboxylic acid, without the presence of alcohol or amine target molecule, the activated carboxylate may react with another carboxylic acid to yield a symmetrical anhydride, which is, however, another activated form that can then lead to products [44].

Another frequently used carbodiimide is DIC (diisopropyl carbodiimide), which is water-insoluble too. It has some advantages over DCC: it's a liquid at room temperature and hence easier to manipulate and disperse than DCC. The byproducts of DIC, diisopropylurea and diisopropyl-N-acylurea, are more soluble in organic solvents than DCU byproduct of a DCC reaction. DIC reacts similarly to DCC, forming an active O-acylisourea intermediate with a carboxylic acid group. This active species may then react with a nucleophile such as an amine or an ester [44].

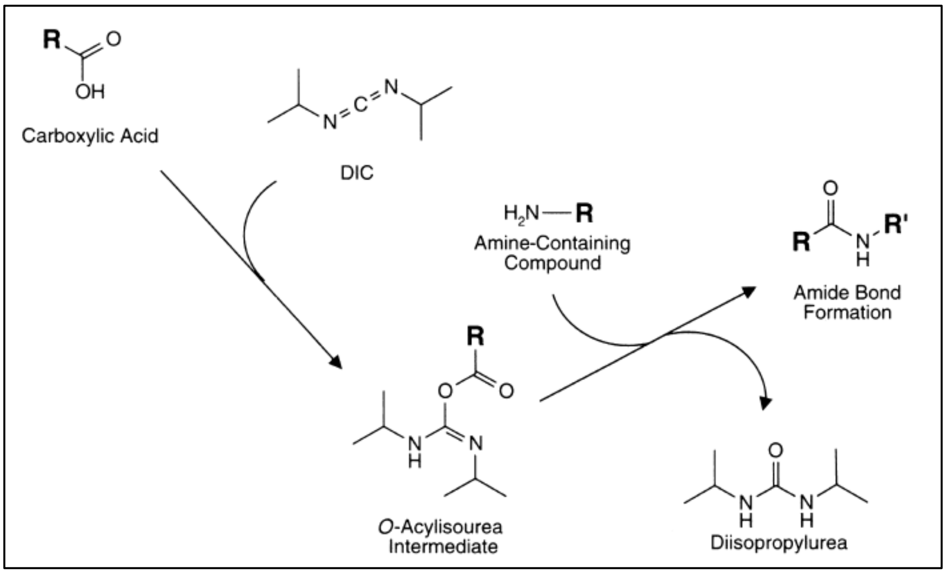

Figure 22: Mechanism of Steglich esterification using DIC as carbodiimide.

EDC (or EDC-HCl, 1-ethyl-3-(3-dimethylaminopropyl) carbodiimide hydrochloride) is probably the most popular carbodiimide used for this kind of condensations. It has some advantages compared to DCC and DIC. Both the reagent itself and the isourea formed as the byproduct are water soluble and may be removed easily by dialysis or gel filtration. However, the reagent is labile in the presence of water, especially when in acidic solutions. EDC can react with carboxylic acids to form highly reactive O-acylisourea intermediates which readily react with a nucleophile such as an amine or alcohol. Other nucleophiles are also reactive. Sulfhydryl groups may attack the active species and form thiol ester linkages.

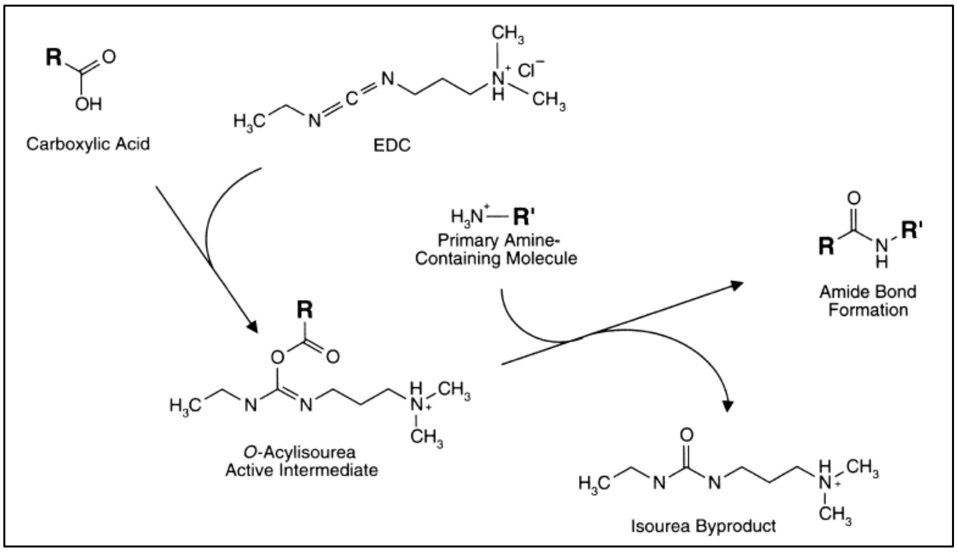

Figure 23: Mechanism of Steglich esterification using EDC as carbodiimide.

In aqueous solutions, hydrolysis by water is the major competing reaction, cleaving off the activated ester intermediate, forming an isourea, and regenerating the carboxylate group.

Performing an EDC-mediated reaction in aqueous solution presents a number of potential side reactions that can occur in addition to the desired product. The mechanism begins with protonation on one of the nitrogen atoms on the imide group of EDC, which forms a carbocationic intermediate. At this point, the modified carbodiimide can hydrolyze in the presence of water forming an inactive isourea which can no longer participate in the reaction. Alternatively, it can react with a carboxylate group to form the desired O-acylisourea reactive intermediate. This ester can accept a second proton to form a second carbocation on the central atom, and this form of the reactive ester can undergo reaction with an amine or alcohol to afford the product. However, this intermediate also can undergo hydrolysis to yield the same inactive isourea derivative. Reaction with water can hence inactivate EDC in two major steps of the mechanism. If hydrolysis is avoided, there are at least three reactions that can happen, including the desired amid or ester bond formation. If a carboxylate group is present in close proximity to the O-acylisourea, an anhydride intermediate can form. The anhydride is however reactive and it can lead to products. In addition, if EDC is in large excess over the amount of carboxylate, then the intermediate ester may exist long enough to rearrange by reacting with its neighboring secondary amines in the carbodiimide, thus forming an N-acylisourea derivative, which is inactive, permanently attaches the EDC derivative to the carboxylate, effectively sequestrating carboxylic compound from the reaction mixture. Finally, the EDC-reactive ester can also react with the desired amine or alcohol to yield products [44].

Despite the number of potential side reactions, EDC-mediated coupling can be done with reproducibility and its water solubility often makes it the first choice as carbodiimide activator.

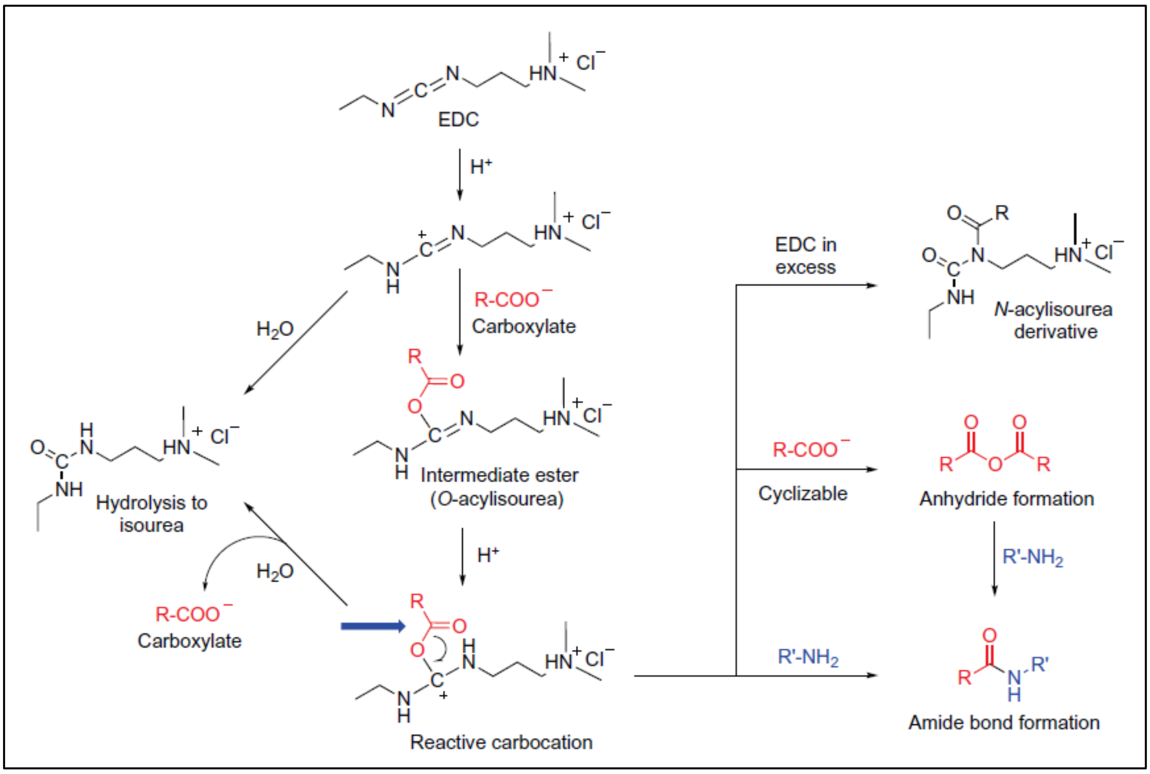

Figure 24: Schematic representation of all the possible undesired side reactions using EDC as carbodiimide in a Steglich esterification.

1.4. Molybdenum disulfide

The molybdenum disulfide utilized in this thesis work was provided by the research group of Dr. Teresa Gatti at the Institute of Physical Chemistry Justus-Liebig-University Giessen, Germany.

Numerous intriguing characteristics of MoS_2 make it useful as a lubricant, 2D transistor, hydrodesulfurization catalyst, and, for our purposes, HER catalyst. Curiously, early research on the electrochemistry of bulk MoS_2 crystals by Tributsch and others revealed that this material is not an active HER catalyst, but further investigations have demonstrated that nanostructuring it can considerably boost its HER activity, reigniting interest in the material [45].

Bulk MoS_2 has a layered hexagonally packed structure, similar to graphite, with a 6.5 Å van der Waals gap separating each sheet. MoS_2 has a number of different surface sites due to its crystal structure, and its electron and hole mobilities are 2200 times higher along a basal plane than perpendicularly to the sheets. The thermodynamically preferred basal plane sites, which are catalytically inert, dominate the surface of bulk MoS_2. On the other hand, MoS_2 layer edges have strong HER activity [45].

Using density functional theory (DFT), Hinnemann and colleagues determined in their foundational work on MoS_2 as HER catalyst that the Mo(1010) edge has a hydrogen binding energy of about 0.08 eV with 50% H coverage, which is extremely close to the ideal value of 0 eV [45]. This binding energy is comparable to that of precious metal catalysts, such as platinum. Enzymes like hydrogenases and nitrogenases, which are both efficient catalysts for generating hydrogen, served as the basis for this investigation [46]. Both these enzymes are extremely active, with hydrogen binding energies close to zero, and active sites that incorporate Mo, Ni, and Fe with under-coordinated sulfur.

Experimentalists synthesized MoS_2 on a carbon black substrate with a high surface area in order to expose a significant number of edge sites, guided by the MoS_2 edge site prediction [45]. They used a membrane electrode assembly setup to achieve 10 mA/cm^2 at roughly 175 mV overpotential, making it the most active, acid-stable nonprecious metal catalyst for the HER at the time. The membrane electrode assembly setup reduced protons to make hydrogen at the cathode and oxidized hydrogen at the anode.

By placing single monolayer MoS_2 nanoparticles on Au(111) through physical vapor deposition of Mo in an H_2S atmosphere, it was experimentally proven in 2007 that the MoS_2 edges are active catalysts for the HER.

Scanning tunneling microscope measurements of the nanoparticle area and edge length were followed by measurements of the HER activity, which demonstrated that the reaction rate scaled with perimeter length rather than area. MoS_2 edges had extremely high turnover frequency, although it was still 50–100 times lower than that of Pt [47].

Theoretical and fundamental experimental research yielded important insights, which in turn inspired major efforts targeted at creating MoS_2 catalysts with increased activity approaching that of platinum surfaces.

1.4.1. Structure and polymorphs of MoS_2

MoS_2 in the bulk form consists of layers presenting an arrangement of one Mo atom surrounded by six S atoms. Adjacent layers are associated through weak Van der Waals forces which allow the layers to slide on each other. MoS_2 shows polymorphism, having three different configurations such as 1T, 2H and 3R, belonging to point groups D_{6d}, D_{6h} and C_{3v}, respectively. In these notations, the first digit represents how many layers are present in the arrangement and the letter indicate the crystallographic configuration: T represents trigonal, H hexagonal and R rhombohedral arrangement. Different allotropes can be obtained by applying some alterations in the synthesis procedure, such as 3D (flowers, snowflakes, and dandelion), 2D (nanosheets, nanostripes, and nanoribbons), 1D (nanowires and nanorods) and 0D (nanoplatelets). Thermodynamically stable and naturally occurring MoS_2 is 2H with 3% of 3R [48].

2H-MoS_2 is considered to be the most stable configuration. It behaves like an n-type semiconductor and it's stable until 1200°C, when it transforms to Mo_2S_3. Various methods are used to synthesize 2H-MoS_2, such as chemical vapor deposition, hydrothermal methods, ball milling and chemical exfoliation. When heated above 800°C, its features change from semiconducting to metallic. Moreover, its semiconducting properties can get converted into superconducting by doping it with rubidium. 2H-MoS_2 has promising applications in removing sulfur from fuels and organic compounds, acting as a hydrodesulfurization catalyst. It is also employed to catalyze the hydrogen evolution reaction from water. In the UV–Vis spectrum, it shows two significant peaks at ($\lambda \sim 580$ nm) and at ($\lambda \sim 640$ nm). In Raman scattering, it displays four characteristic vibration modes i.e. E_{2g}^1 (Strong mode, 383 cm^{-1}), A_{1g} (strong mode, 409 cm^{-1}), E_{1g} (weak mode, 287 cm^{-1}) and E_{2g}^2 (weak mode, 33 cm^{-1}) [48].
Another metastable state of MoS_2 is 1T. It shows a paramagnetic as well as metallic nature. 1T-MoS_2 is synthesize by electron beam.

3R-MoS_2 is an additional stable form of MoS_2, which is naturally occurring and present in molybdenite in percentage of about 3% and gets converted completely into 2H when heated. As 3R, it finds applications in non-linear optical devices. Mechanical exfoliation is used to obtain mono and multilayer 3R-MoS_2 [48].

1.4.2. Properties as HER catalyst

Molybdenum disulfide has many properties which make it suitable for a variety of applications, ranging from solid lubricant, hydrodesulfurization catalyst, microelectronics, superconductors, water splitting catalyst. For what is our concern, we'll focus on the exploitation of MoS_2 features as a catalyst for the hydrogen evolution reaction from water.

The HER occurs either via the Volmer-Heyrowsky mechanism or the Volmer-Tafel mechanism, reported in the figure below. Anyway, the reaction proceeds through an adsorption of hydrogen atoms onto the surface of the catalyst. Hence, the rate of the overall reaction is influenced by the free energy of hydrogen adsorption [47].

Volmer step	$H^+ + e^- \rightarrow H_{ad}$
Heyrovsky step	$H^+ + H_{ad} \rightarrow H_2$
Tafel step	$2H_{ad} \rightarrow H_2$

Figure 25: Possible steps in the hydrogen evolution reaction on the surface of a catalyst, from [47].

If the bond of the hydrogen atoms to the surface is too weak, then the absorption step will be limiting the overall rate. If, at the contrary, the hydrogen to surface bond is too strong, the desorption step will be the limiting step. Optimal HER catalysts have hydrogen adsorption free energies close to 0, binding the hydrogen atoms neither too strongly nor too weakly. This relationship gives rise to the “volcano” graph shown in the figure below, which shows HER exchange current, which is a measure of the catalytic activity, as a function of free energy. In order to maximize the rate of the HER, a catalyst must have the appropriate surface properties. DFT calculations have shown that MoS_2 has a value of hydrogen adsorption energy of 0.08, similar to what is observed for active precious metal catalysts, including platinum [47].

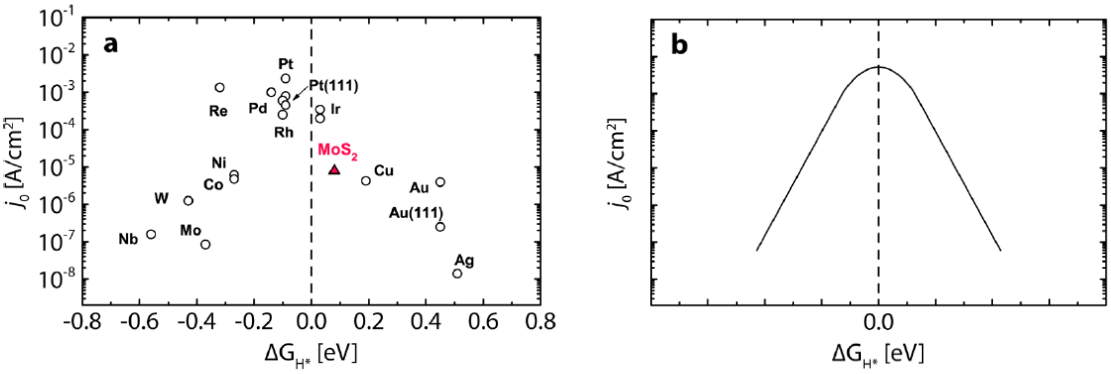

Figure 26: Exchange current density as a function of hydrogen adsorption free energy for various HER catalyst materials. (a) The experimental “volcano plot” for the HER is shown and Pt, with slightly negative hydrogen absorption energy, has the highest HER activity. (b) The theoretical HER volcano predicts catalysts with hydrogen binding energy equal to zero will have the highest activity. From [47]

Unique optical and electronic properties emerge when bulk MoS_2 is thinned to a single layer, making MoS_2 monolayers particularly attractive. Photoluminescence is observed in MoS_2 monolayers due to quantum confinement and the associated change from indirect band gap (1.3 eV) to direct band gap (1.8 eV) is recognized. This is interesting for HER catalysis, since in the monolayer form MoS_2 appears to have the necessary band gap to promote the evolution of hydrogen [49].

It has been demonstrated that the active sites for HER in MoS_2 are present in the edges of the layers, while the basal planes are catalytically inert [49], [50]. Sulfur vacancies present in these regions promote the catalysis of the reaction and allow the MoS_2-based material to express strong catalytic properties [50]. Different studies have been published with the aim to enhance the amount of sulfur vacancies in order to activate the basal planes towards the catalysis of HER. Various methods have been explored, ranging from plasma treatments, electron beam irradiation, chemical reduction [51]–[55].

1.4.3. Exfoliation method

The molybdenum disulfide was exfoliated by the research group of Dr. Teresa Gatti. The exfoliated molybdenum disulfide was exfoliated using an optimized literature methodology using sodium dodecyl sulfate (SDS) and water (H_2O) as surfactant and exfoliating media respectively [56]–[58]. As shown in *Figure 27*, the procedure consists in pre dispersing the material in the desired media and applying an external force using a Tip Sonicator for 4 hours. The as produced suspension is then centrifugated twice at 1500 rpm and 3000 rpm in order to select and narrow flakes size, using the liquid cascade centrifugation methodology (LCC). This methodology produced a stable green suspension with a Zeta Potential of -39 mV, pointing at a long-term stable ink.

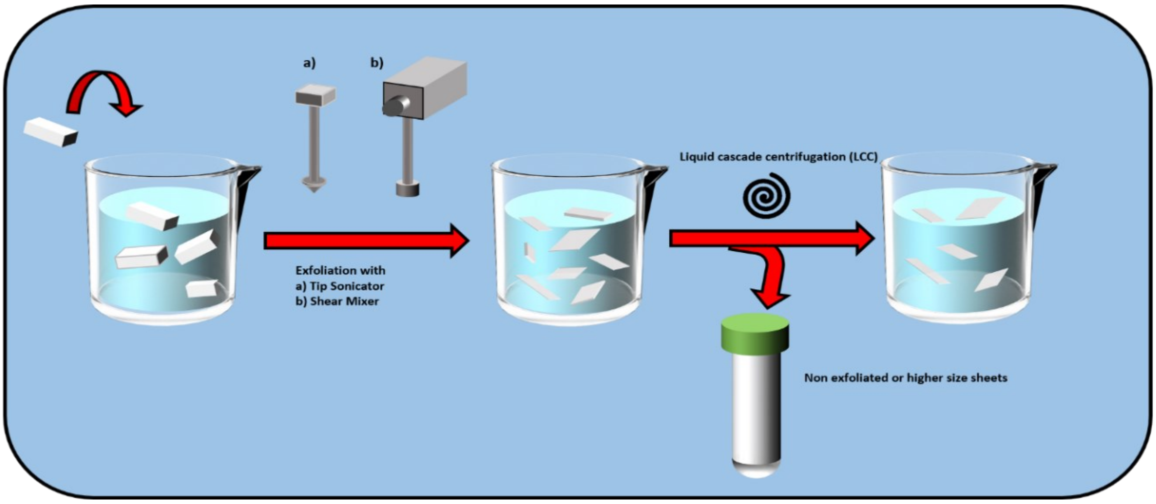

Figure 27: Schematic representation of the exfoliation method employed to obtained few-layers molybdenum disulfide.

In order to assess the exfoliation quality, the as produced material was, then, characterized via Raman spectroscopy, UV-Vis spectroscopy and via TEM images. UV-Vis was the first methodology used and it is possible to observe a shift in the UV spectra of the material: in *Figure 28a* is possible to recognize the A and B exciton's peaks at circa 690 and 640 nm in the bulk material, shifting towards lower wavelength, first clue of an effective exfoliation. It is also possible to observe an increase in steepness of the curve: this can be further addressed to the thinning of the material and therefore to the exfoliation, where a very steep curve between the B exciton and the peak at circa 450 nm can be attributed to mono- or few- layered material [59], [60].

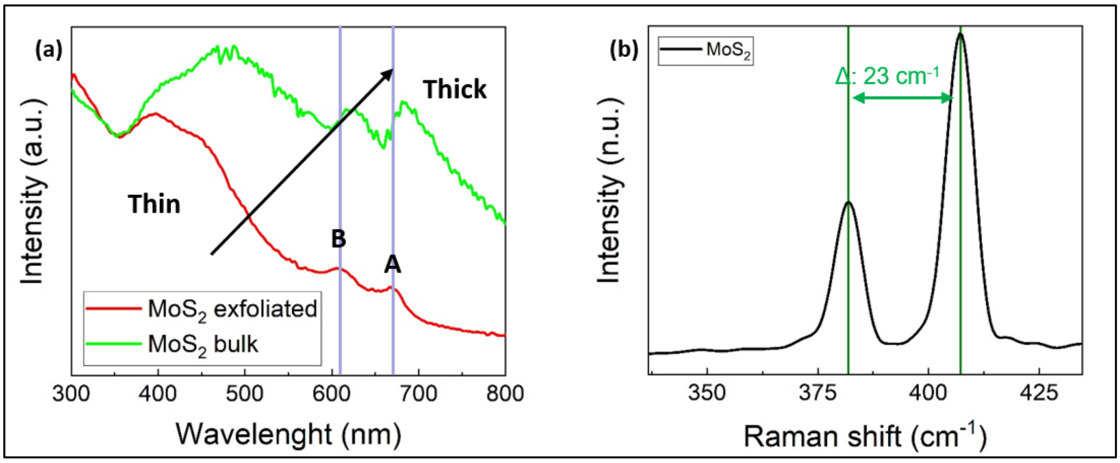

Figure 28: (a) Uv-Visible absorption spectra of bulk and exfoliated MoS_2. (b) Raman shifts of the exfoliated sample, accounting for 2-3 layers material.

To further confirm this hypothesis, Raman spectroscopy was performed. It is possible to estimate the number of layers by analyzing the E_{2g} (around 380 cm^{-1}) and A_{1g} (around 406 cm^{-1}) peak distance. In the as synthesized material, it is possible to observe a shift toward higher number of the E_{2g} while a shift in the opposite direction of the A_{1g}, assessing their position at 382 and 405 respectively, with a distance between the two of 23 cm^{-1}. This value corresponds to 2-3 layers materials, while the value for bulk material is around 25.6 cm^{-1}, index of an efficient exfoliation using the aforementioned technique [61], [62], [63].

Lastly, TEM images were performed to confirm the indirect method used to assess thickness of the material. In *Figure 29* it is possible to easily recognize few layers, especially at the edges, where it is most clear the overlapping of 1 or 2 layers, where the dark areas correspond to areas were the material have an increasing number of layers. This can be attributed to a restacking in the layer deposition of the material on the TEM grids, since a not effective exfoliation would have had the same behavior extended to entire particles.

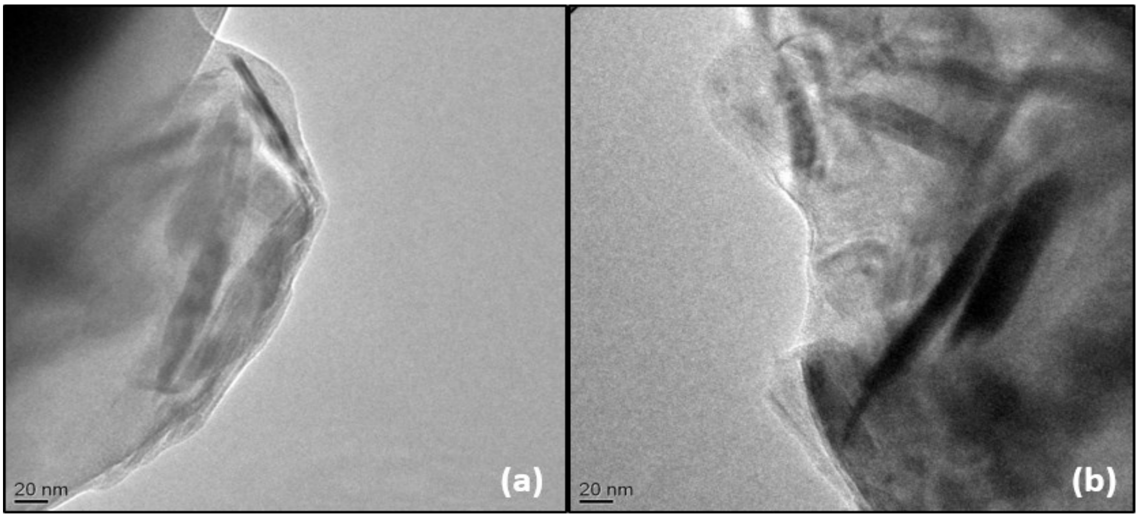

Figure 29: TEM images of the exfoliated material.

1.4.4. Functionalization approach

The functionalization of the MoS_2 presented in this thesis has the goal to enhance the light absorption properties of the semiconductor, allowing it to cover a vast part of the solar emission spectrum. Moreover, the charge separation that should take place in the push-pull dye upon absorption of a photon could inject an electron in the MoS_2, promoting the catalysis of the HER. Functionalization of molybdenum disulfide with thiol terminating dyes should take place by filling the sulfur vacancies present in the semiconductor, both in the edges and on the basal planes [49]. The latter may come from the exfoliation process that the MoS_2 experienced prior to functionalization, or from post-treatments designed to create more sulfur vacancies, hence activating the inert basal planes [49]. However, the actual nature of the interaction between the MoS_2 and the organic thiols is still unclear, as some claim that a physisorption of the dyes with the thiol termination facing the surface of the semiconductor is occurring [64].

It is also reported that, since the active sites for the HER are the very undercoordinated Mo atoms, filling the vacancies of sulfur with thiols may reduce the catalysis capabilities of MoS_2 [49]. Nevertheless, our intention is not to obtain an extensive and complete functionalization of the molybdenum disulfide, but rather to achieve a diffused presence of dye on the surface of the MoS_2, just enough to enhance its properties.

1.5. Characterization of materials

1.5.1. Fluorescence spectroscopy

Fluorescence spectroscopy is an electromagnetic spectroscopy technique that examines fluorescence from a sample. It uses of a beam of light to excite the electrons of the molecules and cause them to release light. It usually, but not always, operates in the UV-visible range of the electromagnetic spectrum.

Molecules possess various energy levels. Fluorescence spectroscopy is primarily concerned with the study of electronic and vibrational states. In general, the species of interest has a ground electronic state and an excited electronic state at higher energies. Withing these, various vibrational states are present. In fluorescence, the species is excited by interaction with an incident beam of light. Absorbing a photon, the molecule is promoted from its ground electronic state to one of the various vibrational states in the excited electronic state. Collisions with other molecules cause the excited fluorophore to lose vibrational energy until it reaches the lowest vibrational state of the excited electronic state. This process is often visualized with a Jablonski diagram. After this non-radiative relaxation, the molecule drops down to one of the vibrational levels of the ground electronic state, emitting a photon in the process. Since molecules can drop into any of several vibrational levels in the ground state, the emitted photons will have different frequencies. By studying the different frequencies of the emitted light, the structure of the various vibrational levels of the ground electronic state can be determined.

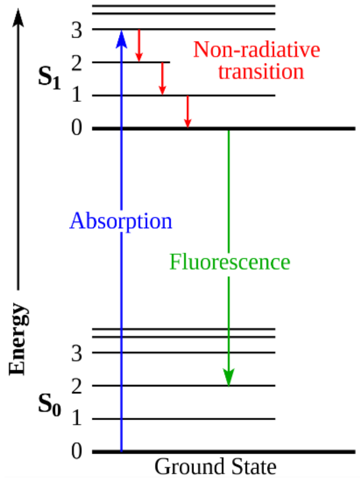

Figure 30: Simplified Jablonski diagram representing the absorption and fluorescence emission processes.

In a typical fluorescence emission measurement, the excitation wavelength is kept constant, and the detection wavelength varies, while in a fluorescence excitation measurement the detection wavelength is fixed, and the excitation wavelength is varied across the spectral region to be investigated.

For what concerns the instrumentation used, spectrofluorometers are more diffused and accurate than filter fluorometers, and use diffraction grating monochromators to isolate incident and emitted light. The light from the excitation source passes through a monochromator which selects one define wavelength, and then it strikes the sample. The incident light is in part absorbed by the sample, and some molecules of it fluoresce. The fluorescent light is emitted in all directions. Some of this light passes through a second monochromator and reaches a detector, usually placed at 90° to the incident light to avoid being reached by transmitted or reflected light. As excitation sources, many can be used, including lasers, LEDs, lamps such as xenon arcs and mercury vapor lamps. A laser emits light of high irradiance at a very narrow wavelength interval, making the use of a monochromator often unnecessary. However, this involves having different lasers for different excitation wavelengths. A mercury vapor lamp is a line lamp, emitting nearly peak-like wavelengths. By contrast, a xenon arc has a continuous emission, with almost constant irradiance in the range of 300-800 nm. To select the wavelength to excite the sample with, a monochromator is needed. It transmits light of an adjustable wavelength with an adjustable tolerance. The most common type of monochromator utilizes a diffraction grating: collimated light illuminates a grating and exits with different angles depending on the wavelength. Constructive or destructive interference select one wavelength and eliminates all the others. The monochromator can then be adjusted to select which wavelengths to transmit. The emitted light is often measured at a 90° angle relative to the incident light. This is done in order to avoid interference of the transmitted excitation light. With this configuration, in fact, only the scattered light from the sample can cause stray light. This results in a much better signal-to-noise ratio, compared to the 180° geometry, lowering the detection limit of approximately a factor of 10^4.

The most versatile fluorimeters can record both an excitation spectrum and a fluorescence spectrum. When measuring fluorescence spectra, the wavelength of the excitation light is kept constant, preferably at a wavelength of high absorption, and the emission monochromator scans the spectrum. For measuring excitation spectra, the wavelength passing through the emission filter or monochromator is kept constant and the excitation monochromator is scanning. The excitation spectrum is usually identical to the absorption spectrum, since the fluorescence intensity is proportional to the absorption.

i. Fluorescence lifetimes

When a photon of appropriate energy is absorbed by a molecule, a chain of photophysical events arises: internal conversion or vibrational relaxation (energy loss in absence of emission of light), fluorescence, intersystem crossing (from a singlet to a triplet state), phosphorescence. Each of these processes occurs with a certain probability, which can be expressed by a decay rate constant (k). Theory says that the average length of time τ for a given number of molecules to decay from one state to another is reciprocally proportional to the rate of that decay: $\tau=1/k$. This average length of time is called the lifetime of that process. In other words, it can be shown that the lifetime of a photophysical process is the time required by a population of N excited molecules to be reduced by a factor of e. In the case of fluorescence, one lifetime is the time required by a population of electronically excited molecules to decrease exponentially to N/e through the loss of energy via fluorescence emission. Lifetimes of photophysical processes can vary widely, from femtoseconds of internal conversion to nanoseconds for fluorescence or evens seconds for phosphorescence.

Fluorescence lifetime is an interesting and useful parameter, as it is largely independent of the fluorescence intensity or the fluorophore concentration. It’s correlated to an electronic state which is energetically unstable, hence it can be sensitive to a great variety of internal factors, such as the fluorophore molecular structure, and external factors, including temperature, polarity, presence of quenchers, interaction with nanostructures or other molecules.

For what concerns data acquisition, two main methods exist, time-domain and frequency-domain. The instrumentation and the acquisition of lifetime measurements is different for the two techniques, but both methods are mathematically equivalent, and their results can be interconverted through Fourier transform. For our goals, the time-domain approach is more interesting. The sample, in a cuvette, is excited with short pulses of light, in the order of nanoseconds, from flash lamps, pulsed lasers, diodes or LEDs, with sufficient delay between pulses. Many detection methods are available for lifetime measurements, but the advent of time-correlated single photon counting (TCSPC) vastly simplified data collection and enhanced the quality of the experiments. Avalanche photodiodes or photomultiplier tubes are employed to record the time-dependent distribution of emitted photons after each excitation pulse. A typical emission decay obtained from TCSPC method is shown in the figure below. Fluorescence lifetime is calculated from the slope of the decay curve, according to Equation 2:

$$F(t) = F_0 e^{-t/\tau} \qquad (2)$$

where F_0 is the fluorescence intensity at t_0, t is the time after the absorption, and τ is the fluorescence lifetime. In the example reported in *Figure 31*, an instrument response function (prompt, in the image) reflects the distribution of photons from the excitation pulse in a nonfluorescent media able to scatter incident light. In the presence of a fluorophore the slope of the decay is less steep because of the existence of a finite excited emitting state. Hence, fluorophores with longer lifetimes have larger slopes (in the example reported in the figure, ICG has τ ≈ 0.97 ns; pyrropyrrole cyanine presents a longer lifetime τ ≈ 4.02 ns).

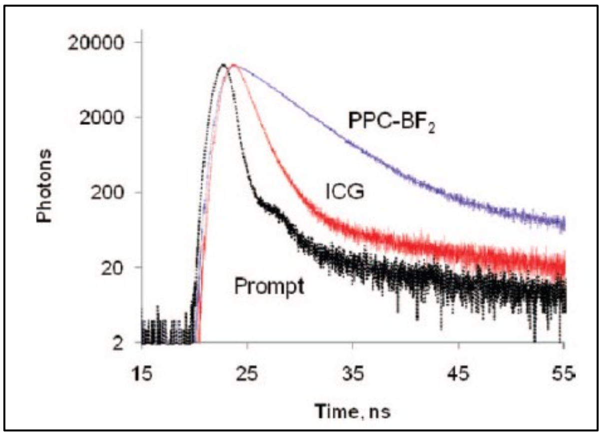

Figure 31: Lifetime decays of ICG, PPC-BF2 and instrument response.

The presence of a mono-exponential or multi-exponential decay can be indicator of different quenching processes being happening to the emitting fluorophore. A multi-exponential decay can indicate that different pathways are possible for the dye to reach the ground state emitting a photon, or that different populations of the emissive molecule in the solution are experiencing different environments, as for interaction with the solvent, with other molecules of the same type or different molecules present in the medium.

Time-Correlated Single Photon Counting is an immensely powerful technique for recording lifetime measurements. The principle of TCSPC is the detection of single photons and the measurement of their arrival times with respect to a reference signal, usually the light source. TCSPC is a statistical method requiring a high repetitive pulsed light source to accumulate enough photon events for a required statistical data precision. TCSPC electronics can be compared to a fast stopwatch. The clock is started by the START signal pulse and stopped by the STOP signal pulse. The time measured for one START – STOP sequence will be represented by an increase of a memory value in a histogram, in which the channels on the x-axis represent time. With a high repetition rate light source millions of START – STOP sequences can be measured in a brief time. The resulting histogram counts versus channels will represent the fluorescence intensity versus time. Generally, one of the inputs to the TCSPC electronics (either START or STOP) will be a pulse generated by a single photon. Single photons can be detected by photodetectors with intrinsically high gain. Most of those photodetectors are photomultipliers or micro-channel plate photomultipliers, but also single photon avalanche photodiodes. For statistical reasons it is important to ensure no more than one single photon event per light flash is detected. Multi-photon events will affect the histogram statistics and will yield to erroneous measurement results. This is known in literature as the “pulse pile-up problem”. To ensure that only one photon per light flash is detected, the recorded photon rate is kept low in comparison to the rate of the exciting lamp, usually 5% or lower.

TCSPC can be used to measure lifetimes ranging from approximately 5 ps to over 50 ms (over 7 orders of magnitude).

1.5.2. Thermogravimetric analysis (TGA)

Thermogravimetry (TG) or thermogravimetric analysis (TGA) is an experimental material characterization technique within the wider family of thermal analyses. The technique consists in the continuous measurement over time of the mass change of a sample of material as a function of time (isotherm) or temperature (heating/cooling ramp), under controlled, inert, reducing, or oxidizing atmosphere conditions. The result of this analysis, generally referred to as Thermogram or Thermal Decomposition Curve, is a graph in which the change in weight (Y axis), in absolute value or percentage, as a function of time or temperature (X axis) is shown. Further information can generally be obtained from the derivative of this signal [65].

The main components necessary for carrying out this analysis can be summarized as follows:

- Thermal balance: key component to monitor the weight of the analyzed sample. The commonly used technology is based on the employment of an electronic photodiode monitoring system, used for the continuous detection of the position of the two arms of the balance: one inserted in the furnace containing the sample and one on which an empty reference sample holder is placed. A change in the mass of the sample produces a deflection of the yoke which interposes a shutter between the lamp and one of the two photodiodes. The resulting variation of the photodiode current is amplified and sent to a coil located between the poles of a permanent magnet. The magnetic field generated by the current in the coil returns the yoke to its original position. The current amplified by the photodiodes is measured and translated into mass or mass loss via the processing system.

- Furnace: generally made of a refractory material like alumina (melting temperature >2000 °C), quartz (melting temperature >1700°C), etc. to ensure the achievement of high temperatures without risk of damage to the material itself.
- Crucibles: containers used for sample insertion and as a reference counterweight; generally made of an inert material, the most common ones are made of steel (applications for temperatures below 600-650°C), platinum or alumina.
- Temperature control system: fundamental to ensure the correct realization of different thermal programs, from the maintenance of a constant temperature (isotherm) to concatenated heating/cooling processes (temperature ramp), thermal steps and much more. The continuous temperature measurement is carried out by using thermocouples, generally in platinum coated with ceramic material, placed inside the furnace near the sample subjected to analysis.
- Ventilation and gas recirculation system: useful to condition and keep a controlled atmosphere inside the furnace and eliminate any gases produced as a result of the degradation of the analyzed material.
- Continuous sample weight recording system.

Nowadays, all the listed components are enclosed in a single machine. The recording and storage of the data is carried out inside the machine itself or by means of a computer, also used for the subsequent processing of the data [65].

The currently available thermobalances allow to analyze quantities of material in the order of milligrams (1-20 mg), but allow to reach up to 1 g. The average sensitivity of these components, thanks to the technology of the photodiodes, turns out to be of the order of the micrograms, that is approximately thousand times inferior to the average amount of material analyzed [65].

The available material properties and processing technologies, in standard application cases, allow to explore a temperature range generally between 23-25°C (room temperature) and 1000-1200°C. Thanks to relatively recent advances in the field of electronics and control systems, in the last decade machines capable of carrying out much more complex thermal programs have been developed; in these programs to the classic thermal program a sinusoidal signal of arbitrary amplitude is superimposed, selectable by the user depending on the specific application. This configuration is called modulated thermogravimetry or high resolution thermogravimetry. This analysis makes it possible to distinguish, as a function of time or temperature, phenomena which are not easily or completely separable by means of a traditional thermogravimetric analysis [65].

Gases commonly used for atmosphere conditioning in the furnace can be divided into two main categories:

- Inert gases: nitrogen, helium and argon are commonly used in different degrees of commercially available purity.
- Reactive gases: oxygen, carbon dioxide, nitrogen monoxide and many others. Often mixtures in different proportions are also used depending on the specific application.

The technique finds a wide range of applications in different fields: from scientific research to corporate quality control, from water analysis to agribusiness and many others. The general applications in which the technique is widely used and for which it was originally developed are the study of degradation kinetics, more generally the reaction kinetics of materials both in an inert environment (nitrogen, helium or argon) than in oxidative environment (technical air, oxygen).

Thermogravimetry is often associated and combined with other techniques of characterization and analysis of materials with the aim of obtaining detailed information about the behavior of the material as a function of temperature and other variables. The two most used combinations are:

- Thermogravimetry combined with differential scanning calorimetry (DSC): this combination allows to obtain information, carrying out a single analysis, on all the phase transitions to which the material is subject (e.g. glass transition for polymeric materials) and ensures the correct attribution of the DSC signal to physical phenomena occurring in the material as a function of temperature. This coupling is commonly identified as Simultaneous Thermal Analysis (STA).
- Thermogravimetry combined with gas analysis by infrared spectroscopy (IR), gas chromatography (GC) or mass spectrometry (MS): in this configuration it is possible to obtain information in real time or retrospectively, collecting the gases produced by the degradation of the material under analysis. This coupling is called Evolved Gas Analysis (EGA).

In our laboratory, TGA is used to determine the degradation of organic molecules grafted onto inorganic matrixes or carbon nanotubes.

1.5.3. Transmission electron microscopy (TEM)

The transmission electron microscopy (TEM) is a type of electron microscopy. In TEM, the electrons that make up the beam pass through a section in which a vacuum was previously created and then completely pass through the sample. This, therefore, must have an extremely low thickness, between 50 and 500 nm. The power of resolution (the minimum distance between two points for which they can be distinguished as such and not as just one) is about 0.2 nm. This type of microscope is provided, along the electro-optical axis, with complex systems that exploiting the modification of electric and magnetic fields, are able to drive electrons through magnetic "lenses" to enlarge the electron beam, already passed through the sample, to make the image larger. The sample consists of very thin sections, resting on a small copper or nickel disk (a few millimeters in diameter) usually fenestrated so that the section can be observed between its meshes without interposition of glass (unlike what happens in the optical microscope) that would not be crossed by electrons. The electron beam then hits a fluorescent screen projecting on it a real and strongly magnified image of the previously crossed sample portion. This microscope provides the images in black and white, but they can be subsequently digitally processed to improve the quality of the images and add colors.

1.5.4. Raman spectroscopy

Raman spectroscopy is a material analysis technique based on the phenomenon of diffusion of a monochromatic electromagnetic radiation by the analyzed sample.

Raman spectroscopy is widely used in the study of materials, both solid and liquid state or in the gas phase. It is a non-destructive technique, which gives answers in a short time, which does not require special conditions for the execution of the measurement and can be carried out directly on the sample without any preparation. In a Raman scattering experiment, the sample to be analyzed is struck by monochromatic electromagnetic radiation from a laser source. The electromagnetic radiation interacting with the electrons of the molecules induces on them an oscillating electric dipole responsible for the diffusion process of the incident radiation. By analyzing the diffuse radiation, components with different energies can be distinguished. The Rayleigh component that represents almost all the diffused radiation, comes from a process of elastic diffusion that does not involve exchange of energy with the system and has the same energy as the incident radiation. Stokes components that have lower energies and anti-Stokes components that have higher energies than incident radiation come from inelastic diffusion processes.

It's a technique which can be considered complementary to the infrared absorption. In fact, both allow to obtain information on the vibrational levels of the material under analysis, but the selection rules for the two techniques are different. For a vibrational mode, to be Raman active, it’s necessary that the incident electromagnetic radiation causes a change in the polarizability of the molecule, while for it to be infrared active it needs to change its dipolar moment.

Raman spectroscopy can be used to characterize samples of molybdenum disulfide for what concerns their thickness, number of layers and defects present. Off resonance, it is possible to see four first-order Raman active modes in bulk MoS_2 at 32 cm^{-1} (E_{2g}^2), 286 cm^{-1} (E_{1g}), 383 cm^{-1} (E_{2g}^1), and 408 cm^{-1} (A_{1g}). The E_{2g}^2 mode is produced when an S-Mo-S layer vibrates against surrounding layers. In a basal plane back-scattering experiment, the E_{1g} mode is prohibited. While the A_{1g} mode is connected to the out-of-plane vibration of just S atoms in opposite directions, the in-plane E_{2g}^1 mode is caused by the opposite vibration of two S atoms with regard to the Mo atom [66].

1.6. Aim of the thesis

This thesis work aims to synthesize an organic dye as sensitizer and to graft it to the semiconductor, which in our case will be molybdenum disulfide, to obtain an active hybrid material to be used in a PEC. The chosen sensitizer structure is D-π-A, because of its great potential in terms of variability of structures. The donor moiety is constituted of a triphenylamine derivative, the π-bridge consists of a thiophene, and the acceptor group is a cianoacrylic derivative, esterified with a thiol to present a sulfur atom at the end for functionalization of the MoS_2. This molecular structure represents a benchmark, which will be compared to a second sensitizer comprehending a secondary acceptor group, thus being a D-A-π-A dye. The auxiliary acceptor is constituted of a benzothiadiazole, and it should bring many advantages overall, such as improved light absorption, broadening its working wavelength range, acting as an electron trap, facilitating the transfer to the primary acceptor and injection in the semiconductor.

The functionalization of the exfoliated molybdenum disulfide will be performed in situ, employing a protecting group on the thiol terminating dyes, which will be removed in the presence of the MoS_2, exposing the free thiol for a direct interaction with the undercoordinated Mo atoms.

The hybrid materials hence obtained will be characterized by means of TGA, TEM, UV-Vis absorption and fluorescence emission, looking for an evidence of the occurred functionalization and any possible interaction being present between the sensitizing dye and the nanostructured semiconductor.

2. Results and discussion

2.1. Choice of dye structure

The purpose of the sensitizer is to absorb a significant portion of the visible spectrum, converting all photons absorbed into electron-hole pairs, to strongly bind to the surface of the photoelectrode (anode or cathode), and to have an appropriate redox potential to drive the catalytic redox reaction of water in conjunction with the appropriate catalysts (WOC or HEC). In current DS-PEC investigations, the two half-cells are often optimized separately before being joined in tandem devices with both photoactive electrodes. The photosensitizer needs to be functionalized with a specific anchoring site, like a carboxylic, phosphonic, or hydroxamic acid, in order to form a stable binding with the SC. The majority of the anchoring groups in DS-PEC are carboxylic acids, however the dye-SC ester bond may be rapidly hydrolyzed in water. The hydroxamic and phosphonic groups offer a more durable long-term connection with the SC surface in aqueous solutions [15]. The dye's structure varies depending on the electrode it must sensitize, and its electrical properties are modified depending on the application. To speed up the proton reduction reaction in photocathodes, the dye must receive electrons from the p-type SC and transfer them to the HEC. In photoanodes, the dye must transfer the excited electron to the n-type SC. In addition to the basic requirements, photoanode dyes need to have LUMO energies that are greater than the SC CB and HOMO energies that are lower than the WOC potentials in order to permit reduction of the oxidized dye [67]. The HOMO level of the sensitizer must be lower than the p-type SC VB and the LUMO level must be higher than the potential of HEC when it comes to the photocathode dye [68].

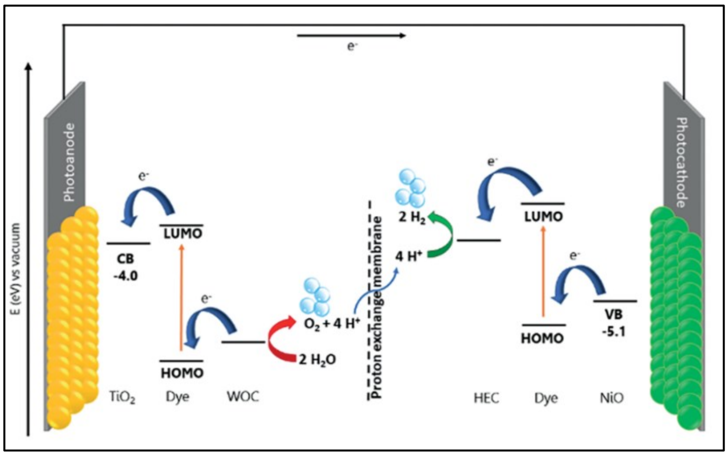

Figure 32: Energy levels of the key components of a DS-PEC, from [23].

The dyes must have a charge transfer excited state with long-life being competitive with the recombination process in both electrodes and be photo(electro)chemically stable. Three main types of molecules have been reported to be employable as organic sensitizers in DS-PEC: porphyrins, perylene derivatives, and donor-acceptor (or push-pull) D-π-A molecules.

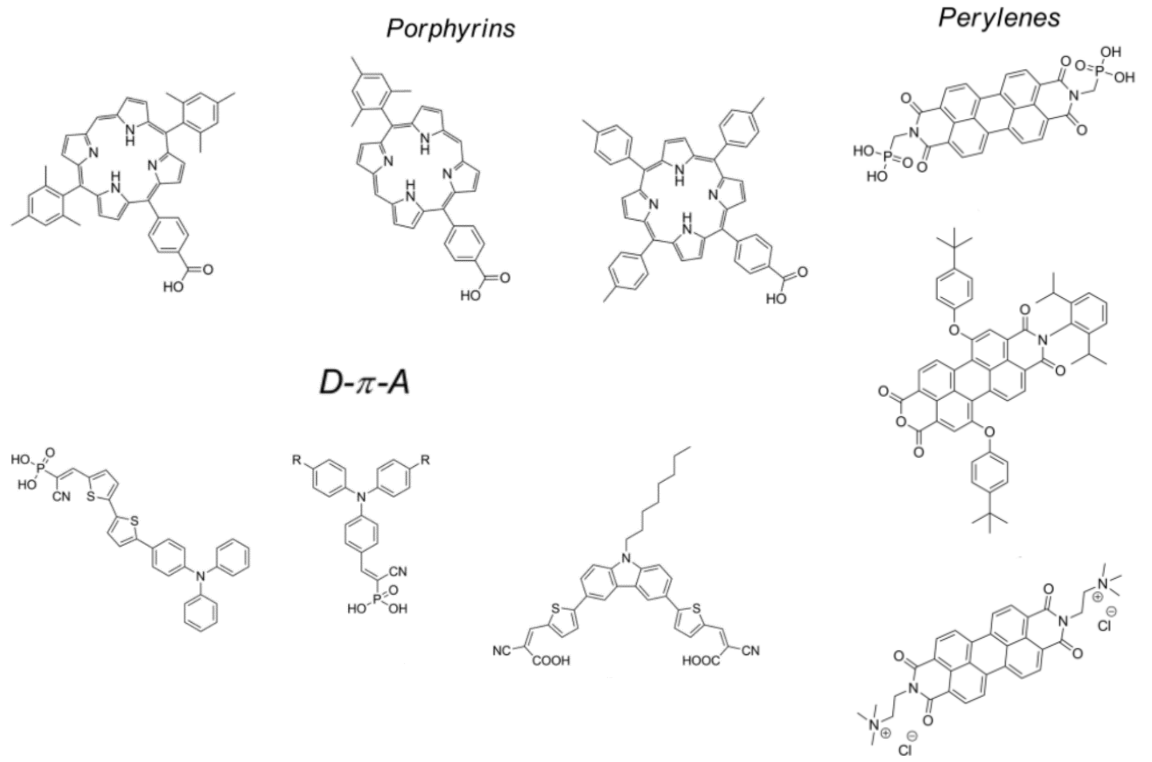

Figure 33: Example of dyes and their structures used as sensitizers in DS-PECs, from [23].

In the blue region of the Vis spectrum, porphyrins have strong Soret (or B) bands with a molar extinction value of roughly 10^5 $M^{-1}cm^{-1}$, while at longer wavelengths they show slightly less intense Q bands (ca. 10^4 $M^{-1}cm^{-1}$) [69]. As a result, the solar emission spectrum is effectively overlapped by their absorption spectra. Research on perylene dyes has focused on their intense visible light absorption. Due to their durability, strong absorption in the visible region, low cost, and thermal and chemical stability in the air, the class of perylene dyes has been extensively employed as sensitizers in numerous sectors, including on an industrial scale. The most popular D-π-A design has a linear or branched architecture with an electron-rich group (D), a conjugated spacer (π), and an electron-withdrawing moiety (A) [8]. The anchoring group, which is employed to covalently attach the dye to the SC surface, is either a functionalization of the A (n-type) or the D moiety (p-type), depending on the kind of sensitizer (p-type or n-type).

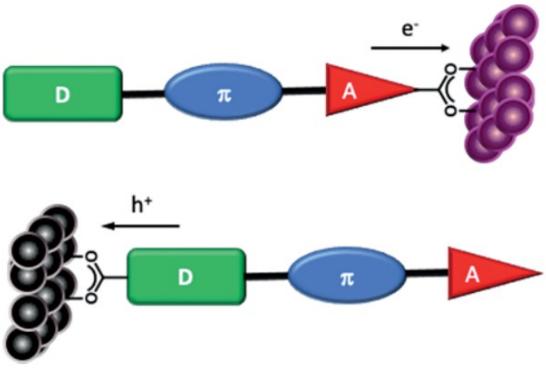

Figure 34: Schematic representation of (top) n-type and (bottom) p-type D-π-A dyes, from [23].

The dye is stimulated by light to undergo an ICT transition from D to A, which is where the charge separation takes place. The electron is moved from the A group to the SC in the case of n-type dyes; otherwise, the hole is moved from the D group to the SC in the case of p-type. The most prevalent D, π, and A groups are based on triphenylamine, thiophene, cyano-acrylic acid (n-type) or dicyanovinyl end groups (p-type) [70]. Thanks to their virtually infinite design variety, the wide availability of D, π, and A libraries, their simplicity in preparation and purification, the low costs of lab-scale and industrial manufacturing, and, most importantly, their adaptable tunability of optical and electrochemical properties, D-π-A dyes have attracted a lot of interest in DSSC and photocatalytic hydrogen generation over the past ten years [8].

For these numerous reasons, in this thesis it was chosen to synthesize a D-π-A molecule, to study its spectroscopic properties and attempt its grafting on the semiconductor. More specifically, the dye under examination is composed of a triphenylamine as donor group, a thiophene as π spacer and cyanoacetic acid as acceptor. Since the semiconductor onto which it will be grafted is molybdenum disulfide, the carboxylic end of the dye will be esterified with a thiol, to present a sulfur atom at its termination. Moreover, a variation of this molecule, to be considered as a benchmark, will be explored, by introducing a secondary acceptor in the π bridge. In fact, it was demonstrated that introducing an electron-withdrawing additional acceptor, such as a benzothiadiazole unit, can act as an "electron trap", bringing several beneficial effects. Some of these are facilitating the electron transfer from the donor to the acceptor moiety, conveniently tailoring the solar cell performance with a facile structural modification on the additional acceptor, tuning the molecular energy gap, modulating the light-harvesting range of the dye with new absorption bands, and improving the photo-stability of the sensitizer [29].

In general, the overall water splitting reaction

$$H_2O \rightarrow H_2 + {}^{1}\!/_{2}\, O_2 \qquad (3)$$

can be broken down into two semi-reactions, the hydrogen evolution reaction (HER), which takes place at the cathode, and the oxygen evolution reaction (OER), which takes place at the anode. These reactions are shown below as they occur in acidic electrolyte:

$2H^+ + 2e^- \rightarrow H_2$ (4) HER reaction

$H_2O \rightarrow {}^1/_2\, O_2 + 2H^+ + 2e^-$ (5) OER reaction

To split water efficiently, catalysts are required for both the HER and the OER. In this thesis we focus on the HER, and between many possibilities, molybdenum disulfide is among the materials which offer the lower activation energy for this reaction, in its nanostructured form. Therefore, MoS_2 could be a promising material for this kind of applications, also given its low economical cost and high abundancy [47]. Bulk MoS_2 is structurally similar to graphite, with a hexagonally packed layer structure. Due to this crystal structure, it has different surface sites, and the mobility of electrons and holes are about 2000 times faster along basal planes than between sheets. The edges of the layers have high activity towards HER, while the basal planes are catalytically inert [47].

Functionalization of molybdenum disulfide with organic thiols should be possible, thanks to the numerous sulfur vacancies present on the surface and on the edges of the semiconductor [71]. These vacancies are inherently present on the layered MoS_2 once it's chemically exfoliated and can be physically or chemically enhanced by some post-exfoliation treatments [52], [54]. It's interesting to note that these exact sulfur vacancies have shown to also be crucial for the catalysis of the HER, since it's right in this sites that the reduction of protons to molecular hydrogen occurs [50]. The approach to functionalization consists in exploiting the sulfur atoms present at the edge of the organic sensitizers to heal the vacancies present in the semiconductor [71]. As reported in literature, this would affect the photoluminescence properties of the hybrid material, enhancing them, but it would cause a dramatic decrease in HER catalytic activity [49]. Nevertheless, the goal is not to completely heal the sulfur vacancies but rather just enough to allow charge separation and injection into the material.

2.2. Synthesis of the dyes

The first part of the thesis is focused on the synthesis of two D-π-A molecules. This class of molecules has been chosen to be studied because of their facile structure modification, high extinction coefficients and low cost with respect to classical ruthenium polypyridine complexes [72].

Both molecules are composed of a donor group, represented by a triphenylamine, a conjugated π bridge, in our case a thiophene, and an acceptor moiety, expressed by a cyanoacetic group. To the carboxylic edge of the molecule, an esterification reaction, namely a Steglich esterification, is performed to provide a thiolated anchor point to the final product to attach to the molybdenum disulfide. Said thiol moiety is inserted in the molecule as trityl-protected, to avoid reactions between two thiols yielding disulfide dimers, which would prevent their interaction with the molybdenum disulfide. Differently from the first, the second molecule will present a second acceptor group, consisting of a benzothiadiazole, between the acceptor and the π bridge (thus being a D-A-π-A dye). The insertion of a second acceptor group has proved to facilitate the charge separation inside the dye after photoexcitation, helping the charge transfer to the main acceptor, to increase the photostability of the sensitizer, to tune the HOMO-LUMO gap and to broaden

the absorption spectra to cover as much as possible the wavelength range emitted by the sun [72], [73].
The reaction paths for the two dyes are depicted in the figures below:

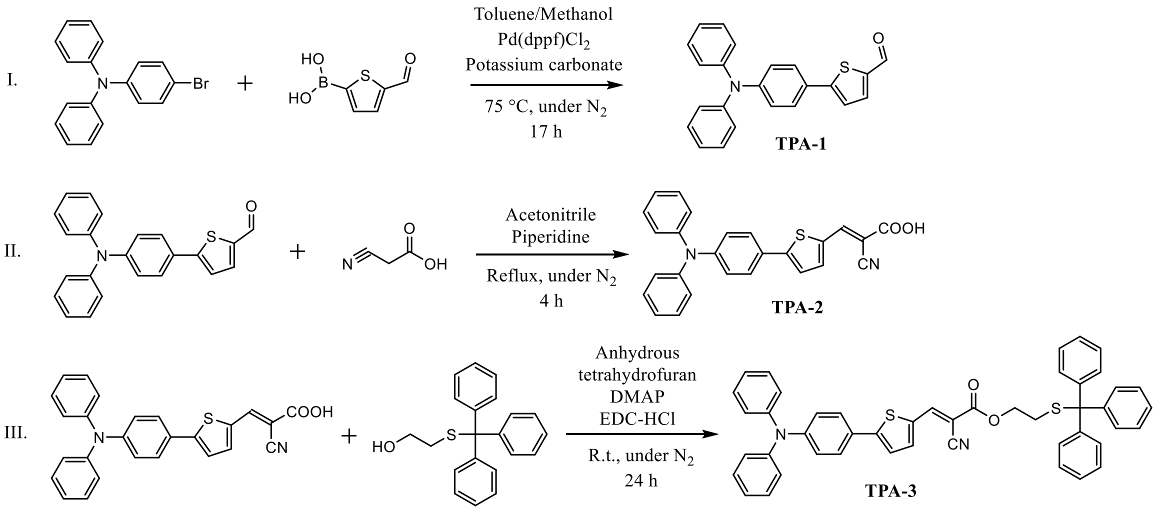

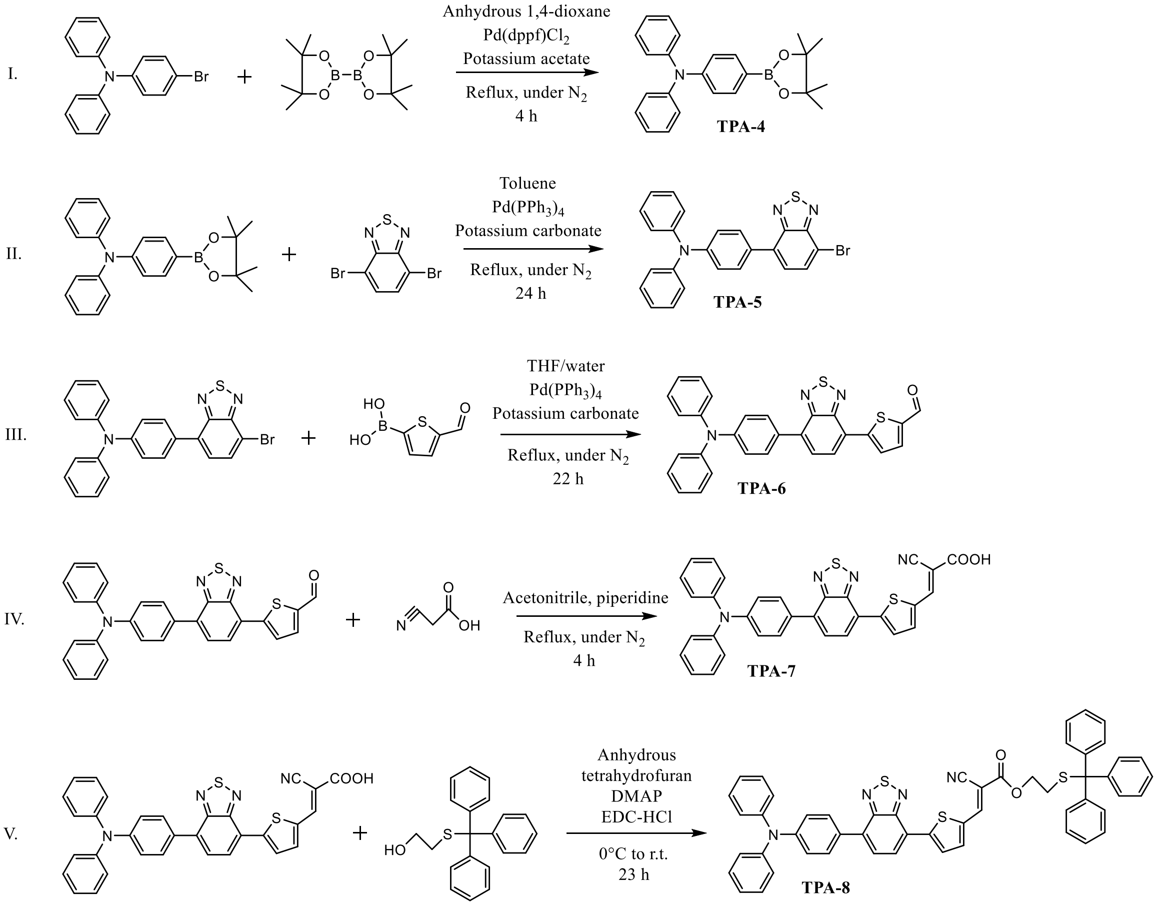

2.2.1. Synthesis of D-π-A dye

i. Synthesis of TPA-1

To begin with, a Suzuki-Miyaura coupling is performed to link the acceptor group, a brominated triphenylamine, to the π bridge, which building block consists of 5-formyl-2-thienylboronic acid, as previously reported in the literature [74], [75]. The reaction is performed using toluene/methanol (1/1) as solvent, at 75°C under nitrogen, to avoid the presence of oxygen in the reaction mixture. The building blocks are added together with the palladium catalyst and potassium carbonate as base. After 17 hours, 4-bromotriphenylamine seems completely reacted, being the limiting reagent, and at least one brightly colored spot is noticeable in TLC with a value of Rf of about 0.3. The reaction time is in agreement with the literature [75]. A TLC analysis of the crude product reveals the presence of numerous spots, index that many species are present, not only the wanted product. Chromatographic purification is performed, using hexane/ethyl acetate in 5/1 ratio as eluent. The separation results however very challenging, due to the heavy presence of by-products.

To purify the product further, a different approach is used: recrystallization. The product is precipitated from hot ethyl acetate/hexane, yielding white, inflorescence-like crystals which are readily filtered. After drying, NMR analysis is performed and it reveals an optimal level of purity, compared with the product obtained by column chromatography, as witnessed by the figure below: it reports the aldehydic portion of the NMR spectrum, where the green trace is the product collected from the column, while the red trace is obtained from the crystals. The presence of impurities is obvious in the first case, whereas it's clear that the recrystallization afforded a high purity final product.

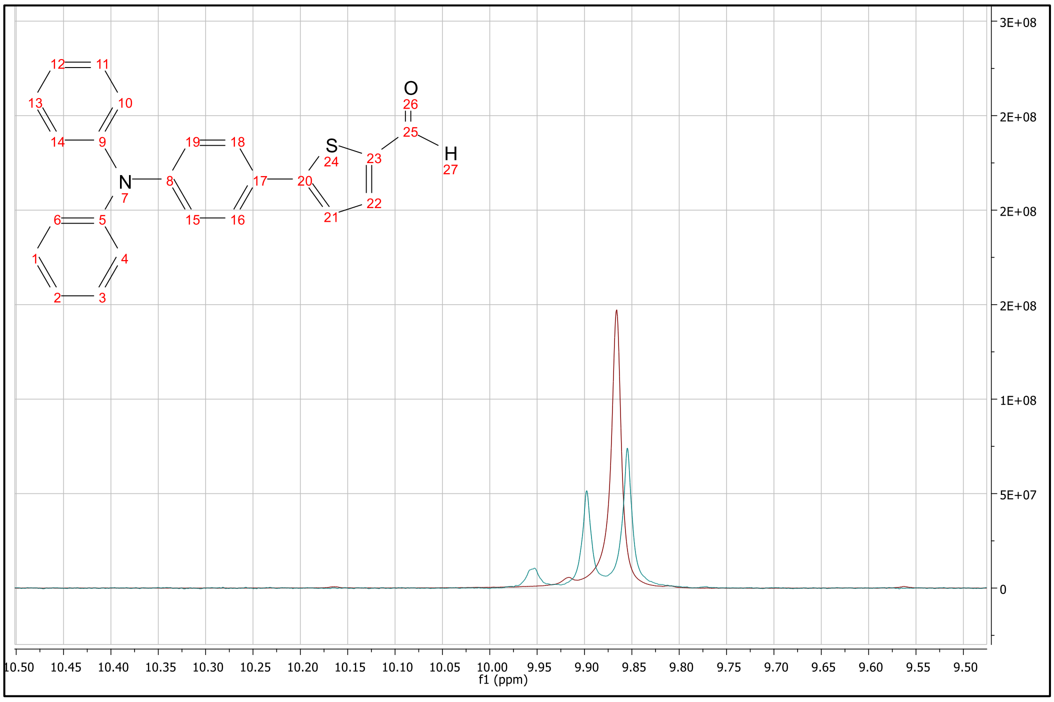

Figure 35: H-NMR of TPA-1 in the ppm range of aldehydic protons.

The overall yield of the reaction is 64% and the total obtained product accounts for 1.2162 grams.

ii. Synthesis of TPA-2

Once the aldehyde is obtained, a Knoevenagel condensation is performed, as previously reported in the literature [76], between the aldehydic moiety introduced with the previous reaction and a cyanoacetic group. The reaction is carried out in acetonitrile/piperidine at reflux under nitrogen atmosphere. After four hours, the reaction is quenched by evaporation of the solvent. Unlike what is reported in the literature, the solid resulted insoluble in dichloromethane once acid is added to perform the work-up. It was then executed by dissolving the solid in THF and adding a solution of hydrochloric acid; the organic solvent was eliminated and the solid filtered. The procedure was repeated three times, at the end of which a red solid was collected. A chromatographic separation is performed in dichloromethane/ethyl acetate 7/3, switching to dichloromethane/methanol 9/1 when all the impurities left the column. Once again, the separation is not perfect, due to tailing of some impurities inside of the column. Recrystallization is explored, with hexane as antisolvent and tetrahydrofuran as solvent. Nevertheless, the crystallization doesn't come about. A second chromatographic column is run, this time in ethyl acetate with 0.5% of acetic acid in gradient; the separation is efficient, and the product is obtained pure, as confirmed by the NMR spectrum below. The most deshielded singlet at 8.46 ppm corresponds to the proton attached to the carbon 25, and it shows a clean and well isolated signal. The presence of an isolated single signal indicates the formation of solely the trans isomer, as reported in the literature [77], [78]. The total obtained mass from the reaction is 970 mg and 67% of yield.

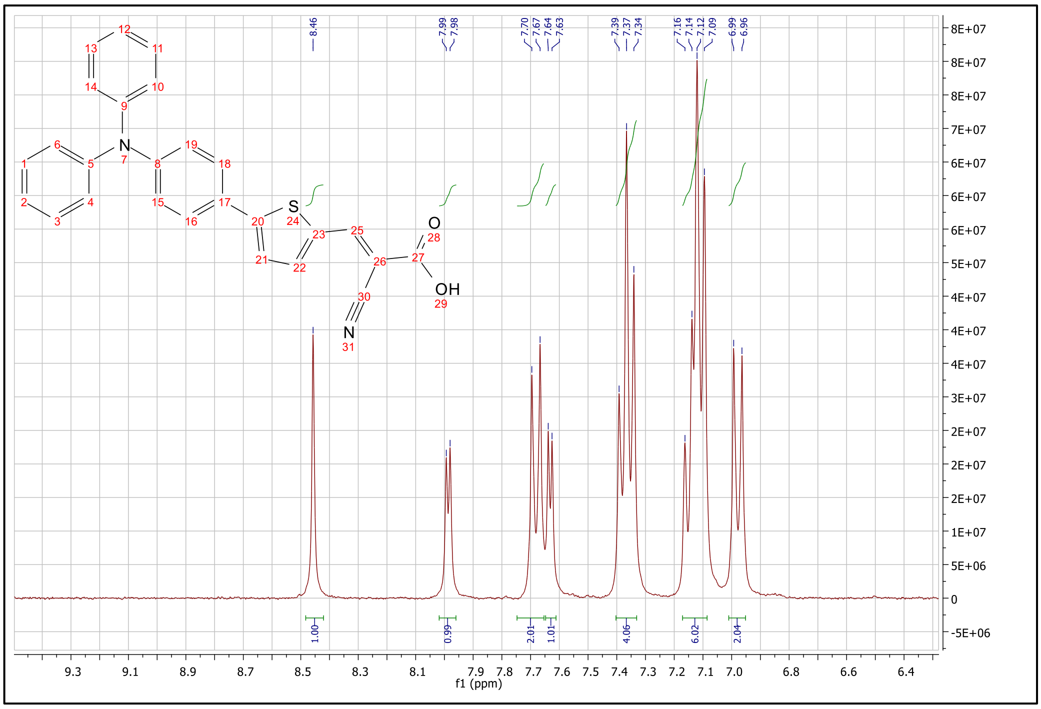

Figure 36: H-NMR spectrum of TPA-2.

iii. Synthesis of TPA-3

Having the cyanoacetic acid moiety inserted in the molecular structure, to be able to eventually link it to the molybdenum disulfide, the inclusion of a thiol group via a Knoevenagel esterification is needed. The procedure used is basically the one suggested by W. Steglich in 1978, with some amendments [41]. In its seminal work, W. Steglich suggests the use of dicyclohexylcarbodiimide (DCC) to activate the esterification of carboxylic acids with alcohols or thiols [41]. Despite this, nowadays the use of different carbodiimides is rather common [79]. Using 1-etil-3 (3-dimetilaminopropil) carbodiimide, commonly EDC-HCl, presents numerous advantages, maybe the most useful of which is the water solubility of its isourea by-product, affording a much easier work-up than using DCC [80]. The by-product of DCC, in fact, is not water soluble and it results also insoluble in most organic solvents, making it difficult to eliminate from the crude product [80].

Since it's important to work in anhydrous conditions, to avoid hydrolysis of the active intermediate with consequent inactivation of EDC, to perform this reaction all glassware was dried in an oven at 120°C overnight prior utilization [81]. TPA-2 results poorly soluble in dichloromethane, common solvent for Steglich esterification, so anhydrous tetrahydrofuran is chosen [82]. Together with TPA-2, the partner alcohol and DMAP are dissolved with 40 mL of tetrahydrofuran in a round-bottomed flask under inert nitrogen atmosphere, and the system is placed in an ice bath to reach 0°C before adding EDC, to avoid common rearrangements of the reactive intermediate which can sequestrate a large portion of the acid making it non-reactive [80]. Once EDC is added at 0°C, the temperature is slowly risen to room temperature. After many hours, both reagents are still visible on TLC, so 0.4 equivalents of EDC are added to force the reaction and it's left overnight. No reaction with an equivalent substrate is reported in the literature, however, it's often a non-quantitative reaction due to different side-reactions that are possible due to carbodiimide rearrangements during the mechanism [81], [83]. To force the reaction progress, some suggest using large excess of the alcohol or extending reaction times to days [83]. Nevertheless, after a total of 22 hours, the reaction is quenched by removing the solvent under reduced pressure. After work-up, chromatographic separation is performed using hexane/ethyl acetate 7/1 as eluent.

High purity of the product is confirmed by NMR spectroscopy, where the protons of the aliphatic bridge on carbon atoms 30 and 31 are well visible and isolated at 3.98 and 2.55 ppm, as shown below. The mass of the obtained product accounts for 164 mg, equal to a yield of 17.3%.

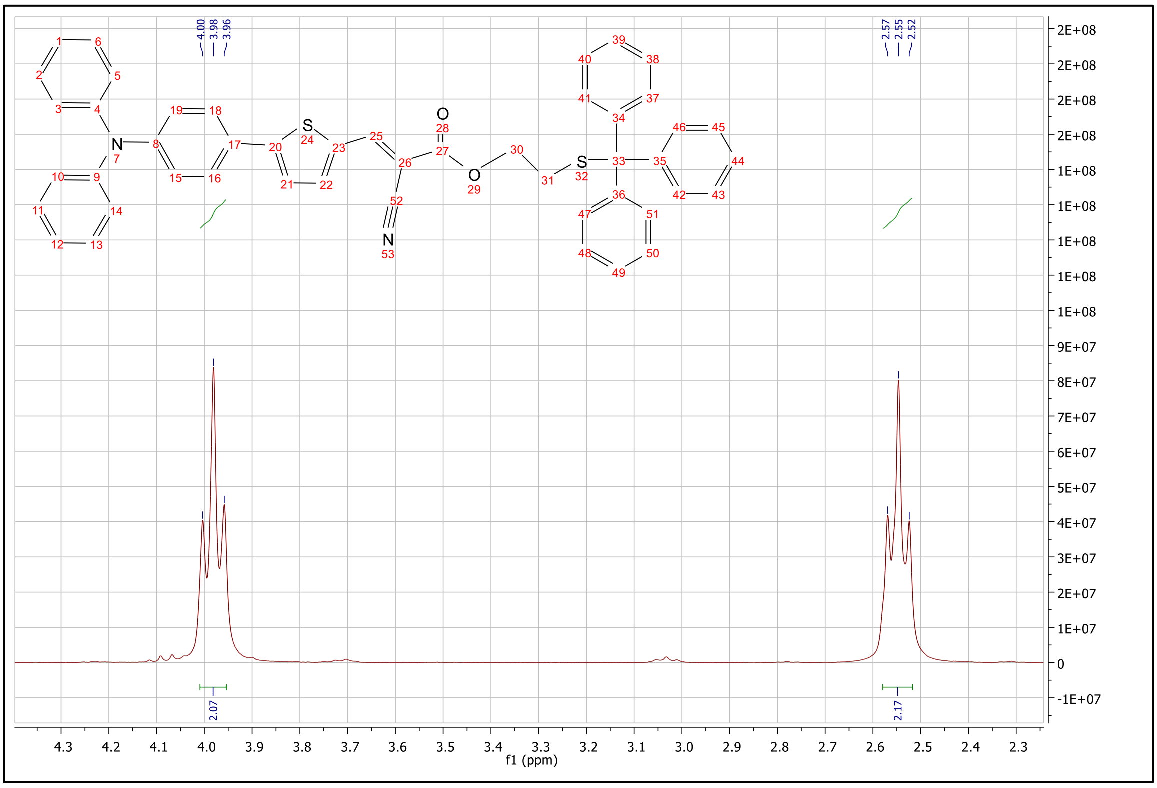

Figure 37: H-NMR spectrum of TPA-3 in the ppm range of the alyphatic bridge protons (C30-C31).

iv. **Deprotection of TPA-3 yielding D-π-A**

The molecule which will be used to functionalize the molybdenum disulfide is TPA-3**,** in its protected-thiol form. Nevertheless, since the actual form grafted on the semiconductor is the free thiol, it's interesting to have the molecule in this form, to accurately compare its spectroscopic properties with the functionalized material. Every time some spectroscopy analyses are made, TPA-3 is deprotected and purified over chromatography column the day before. This is done in order to be sure to have a sample of pure, free thiols, with little risk of oxidation and dimerization, to resemble as closely as possible the system grafted onto the molybdenum disulfide.

To perform the deprotection, TPA-3 is dissolved in degassed dichloromethane, together with triisopropylsilane, which acts as carbocation scavenger once the trityl cation leaves the molecule, and trifluoroacetic acid as acidic medium to actually cleave the S-C bond. The reaction time is about two hours. After removing the solvent under reduced pressure, flash chromatography (dichloromethane/hexane 3/2) yields the desired free thiol with good purity.

2.2.2. Synthesis of D-A-π-A dye

i. Synthesis of TPA-4

To start the synthesis of the D-A-π-A dye it’s necessary to introduce a boronic ester function into the triphenylamine, to be able to link the benzothiadiazole building block, which is purchased as dibromide, in the next step.

The reaction is performed as described by precedent literature [84]–[86]. Using dry glassware, the reagents are mixed together with anhydrous 1,4-dioxane, adding the palladium catalyst last. The mixture is left stirring under inert atmosphere at gentle reflux. After four hours, B_2pin_2 is still visible on the TLC plate, while it seems to confirm the absence of TPA-Br. Consequently, the reaction is quenched by removing the solvent under reduced pressure, the solid is dissolved in dichloromethane and it’s washed with water and brine. Once dried over anhydrous sodium sulfate, the solvent is evaporated and what’s left is a dark brown oil. Flash chromatography (ethyl acetate/hexane 1/30) and evaporation of the solvent to dryness yields 1.048 grams of product as tacky off-white solid (61%). The relatively low yield is compatible with what is reported in the literature [84], [85]. However, NMR analysis confirmed a pure product is obtained, as witnessed by the singlet at 1.27 ppm, which accounts for 12 protons, and it corresponds to the protons of the boronic ester residue attached to the triphenylamine, namely the protons connected to the carbon atoms 25-26-27-28.

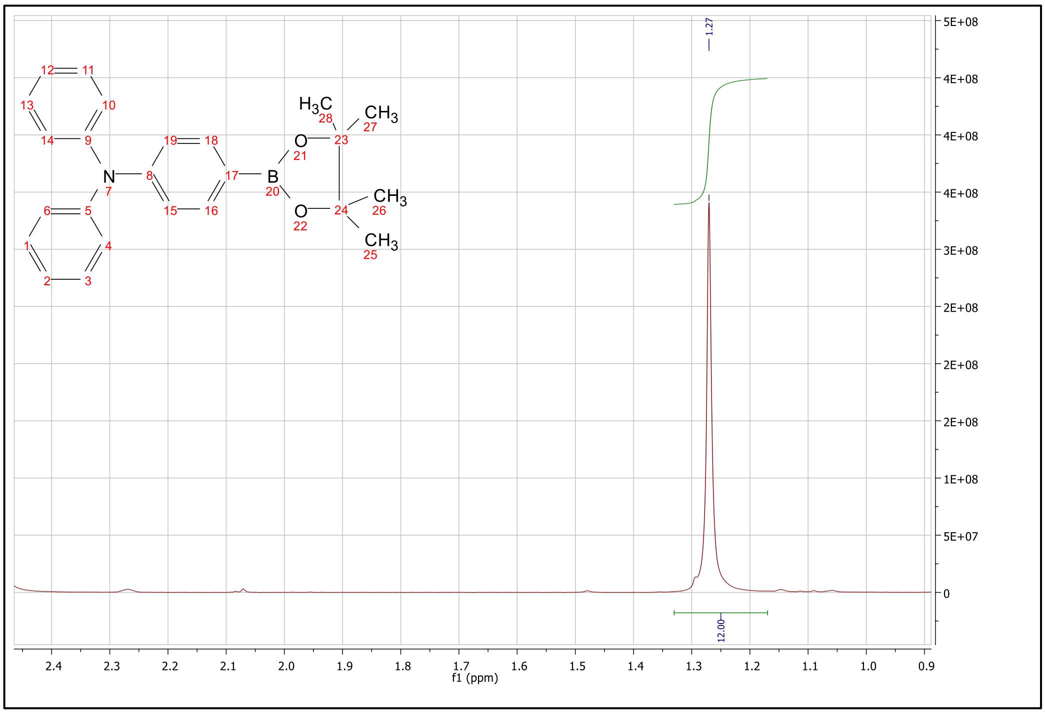

Figure 38: H-NMR spectrum of TPA-4 showing the singlet of the 12 methyl protons.

ii. Synthesis of TPA-5

The following step in the synthesis of the dye consists in a $Pd(PPh_3)_4$-assisted Suzuki-Miyaura coupling, exploiting the boronic ester moiety just introduced to react with a brominated derivative of benzothiadiazole. By taking a look at the reagents, it's inevitable to note that hypothetically the brominated benzothiadiazole could react with two molecules of TPA derivative, hence yielding the product of the double coupling. It's chosen to work with 1 to 1 equivalents of the reagents to statistically avoid this inconvenience.

The reaction is performed as described in the literature [87], [88], in toluene at reflux under inert atmosphere for 24 hours. Flash chromatography (dichloromethane/hexane 4.5/5.5) yields a dark yellow solid. ESI-MS analysis confirmed the product (m/z: 458) but highlighted the presence of BTD (m/z: 295, BTD+H^+). The NMR analysis of the product proved the presence of BTD, as confirmed by the singlet at 7.96 ppm visible in the figure below, compatible with the BTD spectrum reported in the literature [89]. The formation of the product is however confirmed by the presence of the two doublets at 8.09 and 7.75 nm, corresponding to the protons of the BTD in the product, linked to carbons 21 and 22 in the figure below, now differentiated from the equivalent protons present in the BTD alone.

Therefore, the product is recrystallized from hot toluene/hexane. The obtained crystals are considered of sufficient purity to continue the synthesis, yielding 647 mg (53%), in accordance with what is reported in the literature [87].

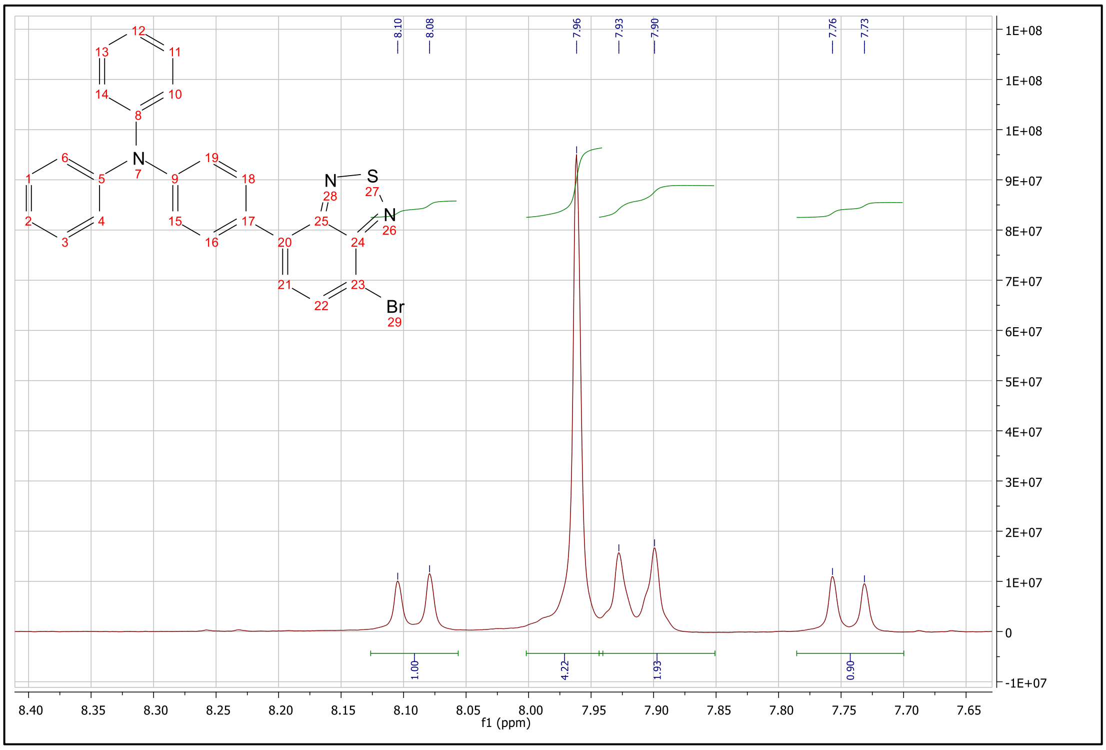

Figure 39: H-NMR spectrum of TPA-5 contaminated by BTD, as confirmed by the singlet at 7.96 ppm.

iii. Synthesis of TPA-6

The next step involves another Suzuki-Miyaura coupling, again $Pd(PPh_3)_4$-assisted, to connect the product of the previous synthesis to 5-formyl-thienylboronic acid, in order to insert the thiophene moiety as a π-spacer into the dye.

The reaction is carried out in tetrahydrofuran/water solution, using potassium carbonate as base, in inert atmosphere of nitrogen, as reported in the literature [90]. After 18 hours, TPA-5 seems to still be present, therefore palladium catalyst and 5-formyl-thienylboronic acid is added in excess to force the reaction. After 22 hours the reaction is quenched and flash chromatography using dichloromethane/petroleum ether (7/1) as eluent yields 321 mg of product as a deep red solid (47%). NMR analysis confirms the obtained product, as highlighted by the aldehydic proton as singlet at 9.98 ppm, in excellent purity.

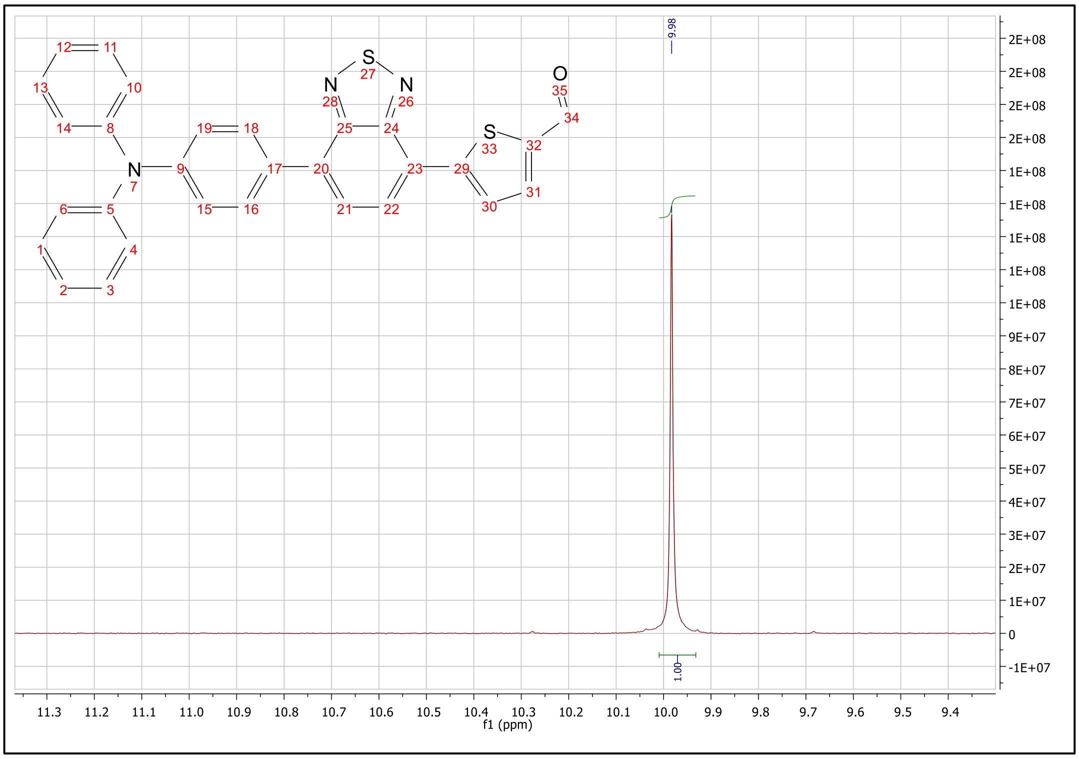

Figure 40: H-NMR spectrum of TPA-6, confirming the obtained product with the singlet at 9.98 ppm, corresponding to the aldehydic proton.

iv. Synthesis of TPA-7

The subsequent stage of the synthesis lies in exploiting the aldehydic moiety just introduced to perform a Knoevenagel condensation to obtain a cyanoacetic derivative. The cyan moiety represents the main acceptor group of the dye, and it's responsible for the separation of charge inside the molecule once it's photoexcited.

The procedure followed for this reaction is the same as for TPA-2 [76]. After the reaction was complete, it is quenched by evaporating the solvent under reduced pressure. Like with TPA-2, the work-up results quite challenging due to the poor solubility of the acid in many organic solvents, once it’s protonated. To wash the product from the water soluble contaminants, as protonated piperidine and excess of cyanoacetic acid, it’s dissolved in THF and washed with acidic water. After solid is recovered, a TLC (toluene/ethyl acetate 3/1) is performed to evaluate the presence of contaminants, and an intense spot is visible with very high retention factors. NMR analysis shows the presence of singlets at 6.87, 6.62, 2.18 and 1.35 ppm (the last one being very intense, comparable with the solvent residual signal, figure below). Apart from this, the product seems pure.

These signals weren’t present in the NMR spectrum of the crude product pre-workup.

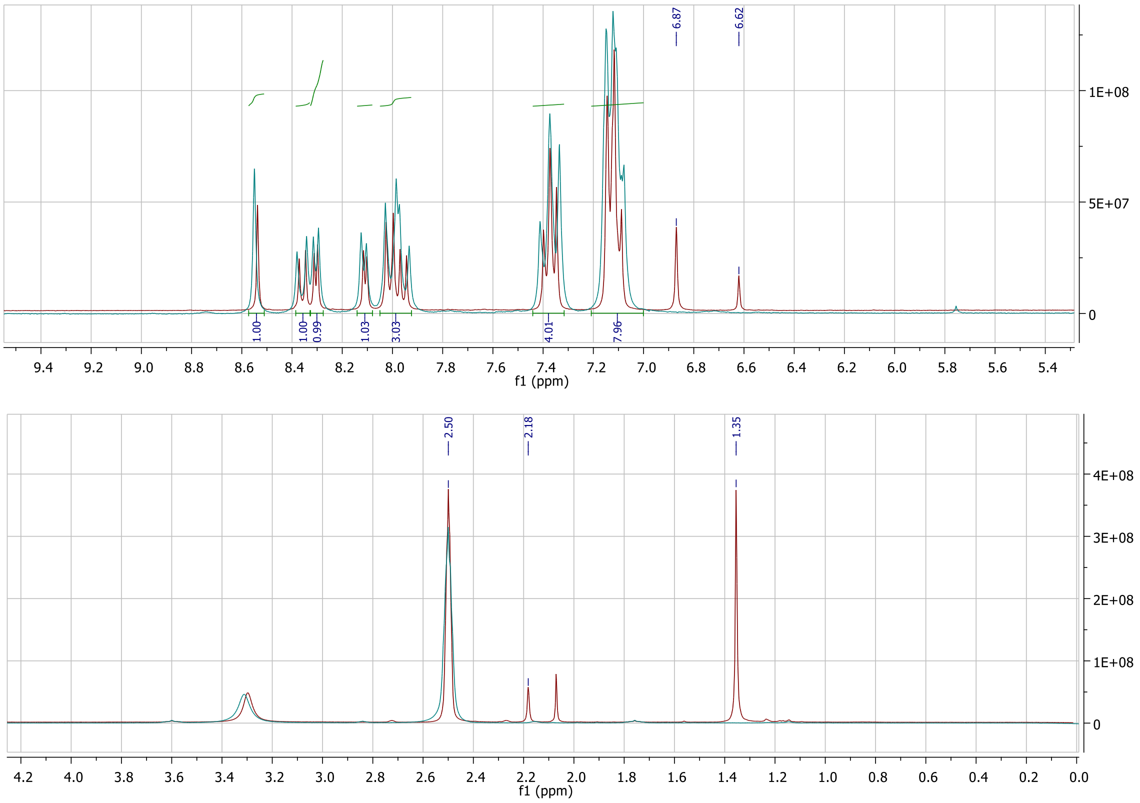

Figure 41: H-NMR of TPA-7, contaminated by BHT, as confirmed by the singlets at 6.87, 6.62, 2.18 and 1.35 ppm.

An NMR spectrum of cyanoacetic acid is collected, but it does not correspond with the observed additional signals observed in the product. The conclusion is that the supplementary signals, all singlets, are ascribable to BHT, butylated hydroxytoluene, present in tetrahydrofuran as peroxide inhibitor at concentrations of 250 ppm. Being high boiling (b. p. 265°C), it’s not eliminated through simple in vacuo evaporation, and it concentrates in the product. Having washed the crude product with not negligible amounts of tetrahydrofuran, it’s more than plausible to have large quantities of this contaminant in the final product. Being aware of this, isopropanol washings are used to attempt to wash away the BHT. The obtained product is still contaminated with BHT, so flash chromatography (toluene/ethyl acetate 3/1 with acetic acid in gradient to 5%) yields 308 mg of pure product, as a dark red solid (84%).

v. Synthesis of TPA-8

Once the carboxylic species has been obtained and isolated, to promote the effective functionalization of the molybdenum disulfide it is mandatory to introduce a thiol group in the molecule. It's the sulfur atom in the molecule, in fact, responsible for the functionalization, as it's going to heal a sulfur vacancy in the exfoliated defective material. To do this, a Steglich esterification can be carried out, similarly to the approach used for TPA-3.

The reaction is carried out as previously [41], [79]–[81]. Better results seem to be obtained by introducing the reagents in THF leaving out the EDC-HCl, and placing the flask in a salt and ice bath to reach temperatures around -10°C. After 10 minutes, EDC is added, the solution is kept at -10°C and it's left to slowly rise to room temperature. In this way less counterproductive rearrangements should have the chance to happen, leading to a purer product in higher yields. After five hours, it's clear that reagents are still present in large amounts, so other 0.75 equivalents of EDC are added to force the reaction and it's left overnight. After the reaction is considered complete, THF is removed and the obtained solid is washed with acidic and basic water. Once the work up is complete, flash chromatography (toluene/hexane 95/5) yields highly pure product with low yield (15%).

vi. Deprotection of TPA-8 yielding D-A-π-A

As we did for the D-π-A molecule, it is necessary to have the dye in its free thiol form to perform any reliable analysis to compare its spectroscopic features to the functionalized nanomaterial. This is mandatory to be done to have a free molecule that is as similar as possible to the one which actually is linked to the nanostructure, in order to accurately differentiate contributes from the two components of the hybrid material. To prevent dimerization in long-stored samples and the formation of disulfides which could supposedly have different spectroscopic and electronic properties, the free thiol form of the dye is prepared and purified in small amounts roughly the day before a measurement will be performed.

The reaction is a simple removal of the trityl protecting group. It's carried out in degassed dichloromethane as solvent, in the presence of triisopropylsilane as carbocation scavenger to sequestrate the trityl cation which will be released and trifluoroacetic acid as acidic medium to promote the cleavage of the S-C bond, in nitrogen atmosphere for about two hours. After removing the solvent under reduced pressure, flash chromatography (dichloromethane/hexane 3/2) yields the desired free thiol with good purity.

2.3. Functionalization of molybdenum disulfide

Once the dyes in their protected thiol forms are ready, they can be employed for the functionalization of molybdenum disulfide. Despite being often depicted as perfect lattices, MoS_2 sheets commonly present sulfur vacancies, which are a crucial prerogative in its uses as catalyst [91]. It's been demonstrated that simply stirring chemically exfoliated MoS_2 with thiol-terminating polyethylene glycol ligands causes them to interact with the inorganic semiconductor [92]. Some studies support the idea of a covalent interaction, while others claim that rather a physisorption is occurring [64], [71]. The theory of the nature of the interaction is still quite blurry, nevertheless the mostly accepted version consists of a repair or passivation of the sulfur vacancies on the MoS_2 by the thiol bearing molecules [49].

In this second part of the thesis, the aim is to functionalize, as efficiently as possible, small aliquots of molybdenum disulfide. Moreover, in the literature many different ways are reported to artificially create strain and defects in the pristine material, including sulfur vacancies. The main strategies can be divided into introduction of defects during the production of the material, for example through CVD, or after the material is exfoliated into nanosheets from the bulk [93]. This second approach consists of physical methods, like treating the exfoliated molybdenum disulfide with argon or hydrogen plasma or γ-rays, and chemical methods, such as reduction with sodium borohydride or hydrazine, which strips sulfur atoms from the structure of the semiconductor, leaving behind vacancies and defects [51]–[55], [94]–[97]. In this thesis, a sample of MoS_2 is treated with sodium borohydride prior to functionalization, in an attempt to enhance the present sulfur vacancies and hence the possible degree of functionalization [52]. The time needed to obtain a homogeneous functionalization is still under debate in the literature [49], [64], [71].

A total of four materials were prepared, in order to investigate the different effect of time of functionalization, artificial introduction of vacancies and defects on the MoS_2 surface and different sensitizers utilized:

- MoS_2 functionalized with the D-π-A dye for 1 day (MoS_2@D-π-A_1).
- MoS_2 functionalized with the D-π-A dye for 7 days (MoS_2@D-π-A_7).
- MoS_2 treated with $NaBH_4$, functionalized with the D-π-A dye for 7 days (MoS_2@$NaBH_4$@D-π-A_7).
- MoS_2 functionalized with the D-A-π-A dye for 7 days (MoS_2@D-A-π-A_7).

i. Functionalization of MoS_2@D-π-A_1

A first functionalization of molybdenum disulfide was carried on with the D-π-A dye. This first hybrid material serves a dual purpose: to evaluate the effectiveness of this functionalization approach, and to set a benchmark to be compared with future functionalization strategies of different type.

To carry out the functionalization, molybdenum sulfide is dispersed in a solution of dichloromethane and trifluoroacetic acid (3/1), together with the protected thiol and triisopropylsilane, under inert atmosphere of nitrogen and left stirring at room temperature for 24 hours. Being quite hard to quantify even an approximate amount of sulfur vacancies in the semiconductor, the quantity of thiol to be used is considered to be 0.5 equivalents of the molybdenum disulfide, taking its molecular weight as the mass of the formula unit "MoS_2" (equal to 160.07 mg/mol). This is just a rough evaluation of the maximum required amount, based on an overestimation of the sulfur vacancies on the surface of molybdenum disulfide. Nevertheless, an excess of thiol is certainly needed to force the interaction between the two partners. After 24 hours, the reaction mixture is subjected to several sonication/centrifugation cycles. Sonication is performed in dichloromethane, to disperse as much non-linked molecule as possible, and then an equal amount of methanol is added to promote precipitation of functionalized molybdenum disulfide during the centrifugation. Washings are repeated, until the collected supernatants stop showing UV-Vis absorption bands ascribed to the free dye. On the other hand, further washings would cause a rise in the baseline of the spectra, indicating that small portions of the nanomaterial are being taken out. At this stage, the solid product is collected and dried under nitrogen flux.

ii. Functionalization of MoS_2 with D-π-A dye for 7 days: MoS2@D-π-A_7

To investigate if a longer treatment time could improve the functionalization, the same functionalization process is repeated extending time from 1 to 7 days.

iii. Functionalization of NaBH4-treated MoS2 with the D-π-A dye for 7 days: MoS2@NaBH4@D-π-A_7

According to the literature, it should be possible to increase the amount of sulfur vacancies on exfoliated molybdenum disulfide through treatments with sodium borohydride [52]. This, in turn, should result in an improved thiol functionalization.

To verify this hypothesis, a batch of molybdenum disulfide is treated with sodium borohydride and then used in a functionalization process as described before. The reducing treatment is performed by dispersing the MoS_2 in some Milli-Q water together with a large amount of sodium borohydride and the suspension obtained is stirred for five hours. After recovering it and drying it under nitrogen flux, the defected molybdenum disulfide is functionalized with the D-π-A dye, it's washed and dried. Interestingly, for this particular hybrid much fewer washing steps than before were required to obtain a clean product: about 8, compared to 15-20.

iv. Functionalization of MoS2 with the D-A-π-A dye for 7 days: MoS2@D-A-π-A_7

Since the one-day functionalization didn't do well with the fluorescence studies, for the dye with the secondary acceptor (D-A-π-A) it is chosen to directly proceed with the functionalization for 7 days, performed as described earlier.

2.4. Characterization of the dyes and the hybrid materials

During the synthesis of the two dyes, for each step a ^{1}H-NMR and an ESI-MS analysis are performed to assure the desired intermediate is obtained before advancing with the following reaction. For the final products, also a ^{13}C-NMR spectrum is collected. For what concerns the hybrid materials, TGA, TEM, Raman spectroscopy, UV-Vis and fluorescence spectroscopy are used to characterize them. Each time a spectroscopic measurement is performed on a functionalized material, the same analysis is done also on the pristine MoS_2 and on the corresponding sensitizer in its free thiol form.

2.4.1. Thermal gravimetric analysis

Thermal gravimetric analysis is a destructive technique that allows one to subject the sample to a temperature ramp in order to accurately quantify the mass loss during the test. In particular, for the hybrid materials, it would be desirable to see a degradation step in a temperature range consistent with the deterioration of the organic molecules interacting with the semiconductor. All the analyses are performed in nitrogen atmosphere to avoid oxidation of the molybdenum disulfide which would lead to formation of mixed phases of oxides of molybdenum. The temperature program is the same for all the samples tested and involves a stabilization at 100°C for 10 minutes to reach a stable weight and to eliminate any solvent traces, after which a constant increase by 10°C/minute is operated until reaching 1000°C.

Firstly, a TGA of the pristine molybdenum disulfide is recorded. As visible in the figure below, a constant degradation is observed, without evident peaks in the derivative (green trace).

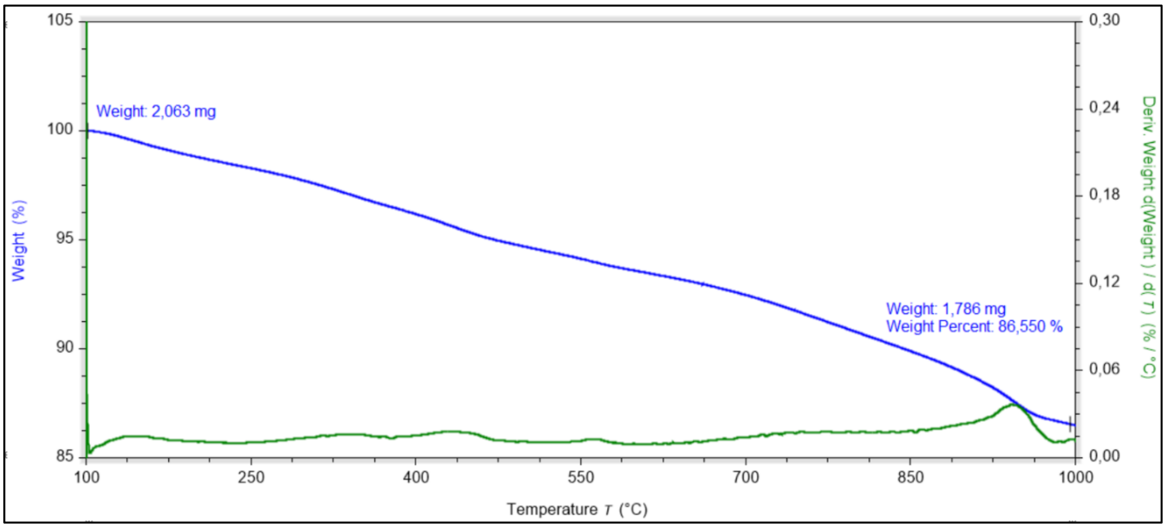

Figure 42: Thermogram of pristine molybdenum disulfide, recorded from 100°C to 1000°C, with a constant increase in temperature of 10°C/min.

The rather constant degradation of the nanostructure is due to the intrinsic defects of the material, which lead to the presence of energetic points that promote decomposition, such as stripping of sulfur atoms at high temperatures. Said punctual defects could be vacancies of S or Mo atoms, self-interstitial atoms, substitutional impurity atoms or interstitial impurity atoms (see figure below).

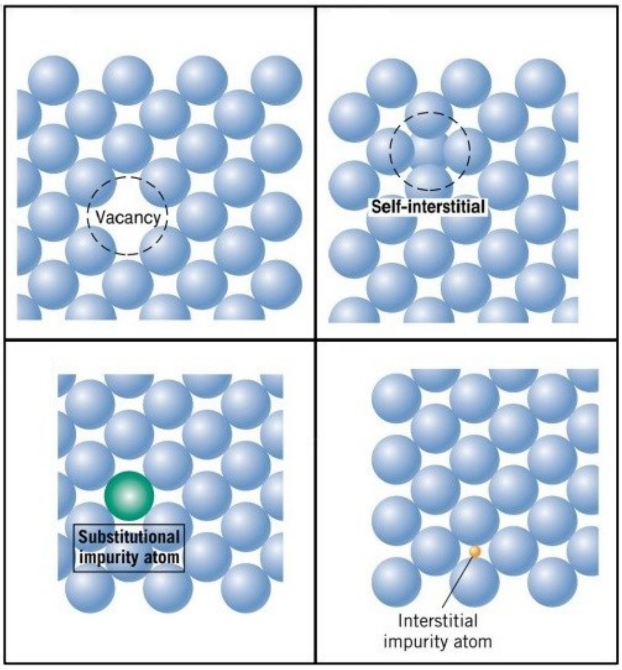

Figure 43: Common types of defects in molybdenum disulfide [102].

After that, speaking of the functionalization with the D-π-A dye, a TGA of the organic molecule is performed, and as visible in the figure below two main degradation steps are recognizable, around 250°C and 300°C. As it should be expected, at 1000°C no residue is left, index that all the dye has been decomposed.

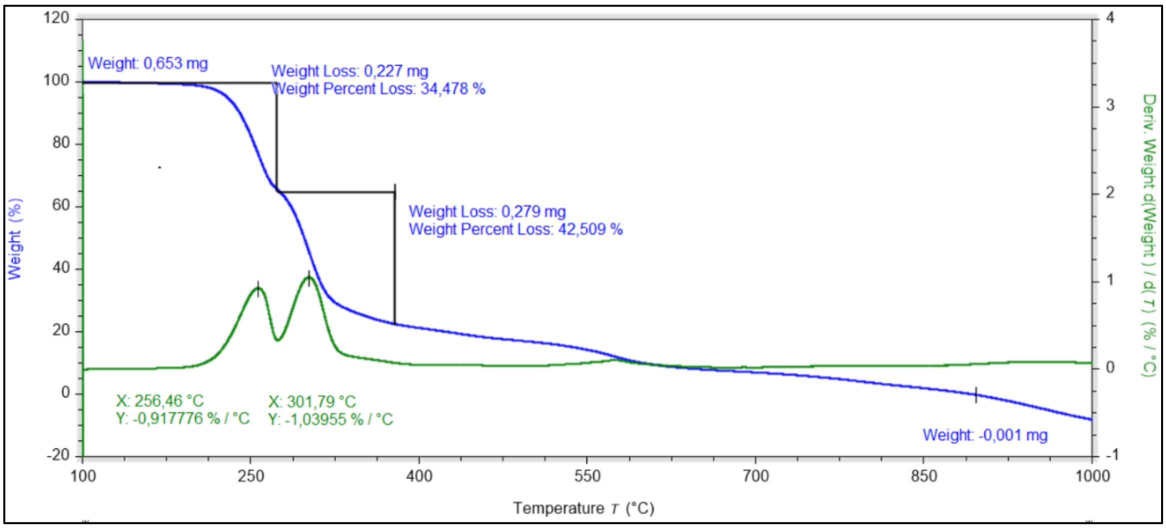

Figure 44: Thermogram of TPA-3, recorded from 100°C to 1000°C, with a constant increase in temperature of 10°C/min.

An analysis of two hybrids, MoS_2@D-π-A_1 and MoS_2@D-π-A_7 is then recorded, and the results are quite interesting. As shown below, for the 1-day functionalization only one broad yet pronounced degradation step is observable, at around 400°C, with a weight loss of about 4.5%. For the 7-days functionalization, two broad degradations are visible, at roughly 300°C and 550°C, accounting for 6.0% and 4.8% of weight loss. The remaining weight at the end of the treatment is for the two samples 79.7% and 73.8%, respectively.

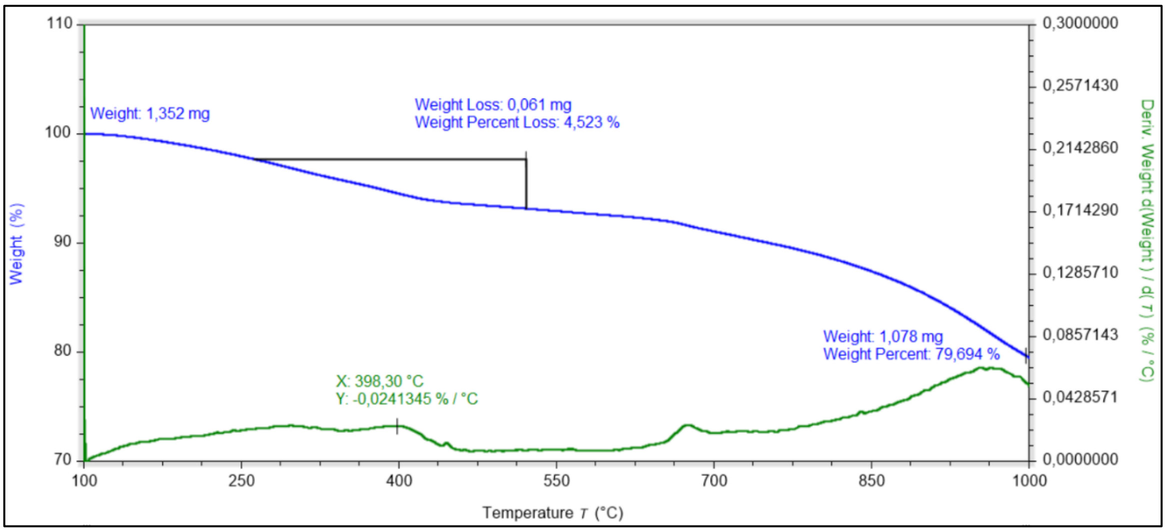

Figure 45: Thermogram of MoS2@D-π-A_1, recorded from 100°C to 1000°C, with a constant increase in temperature of 10°C/min.

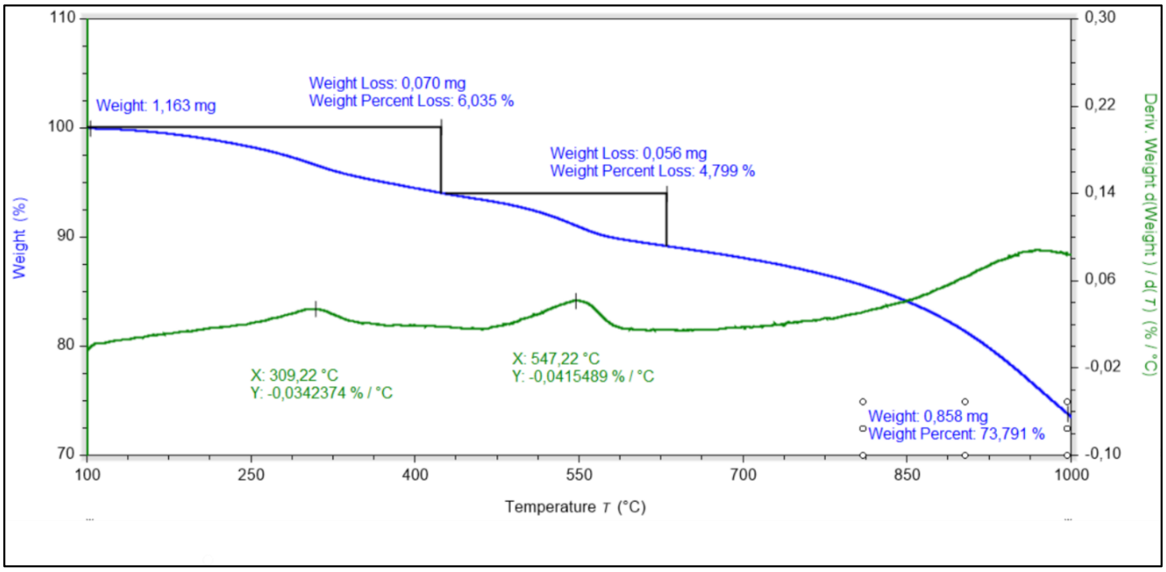

Figure 46: Thermogram of MoS2@D-π-A_7, recorded from 100°C to 1000°C, with a constant increase in temperature of 10°C/min.

It's compelling noticing how in the longer functionalization there is one degradation step roughly in the same temperature range of the shorter functionalization, which however accounts for 1.5% of weight loss more than the 1-day test. Moreover, a second degradation is present, which account for 4.8% of weight loss. Both these features could be explained with a more extensive functionalization of the molybdenum disulfide, which then is more heavily loaded with organic matter. The second degradation could be justified by the fact that a larger scale functionalization would introduce strain effects in the structure of the molybdenum disulfide, hence making it less stable against high temperature decomposition. The figure below reassumes the degradation profiles of these three samples: pristine molybdenum disulfide, MoS_2@D-π-A_1 and MoS_2@D-π-A_7.

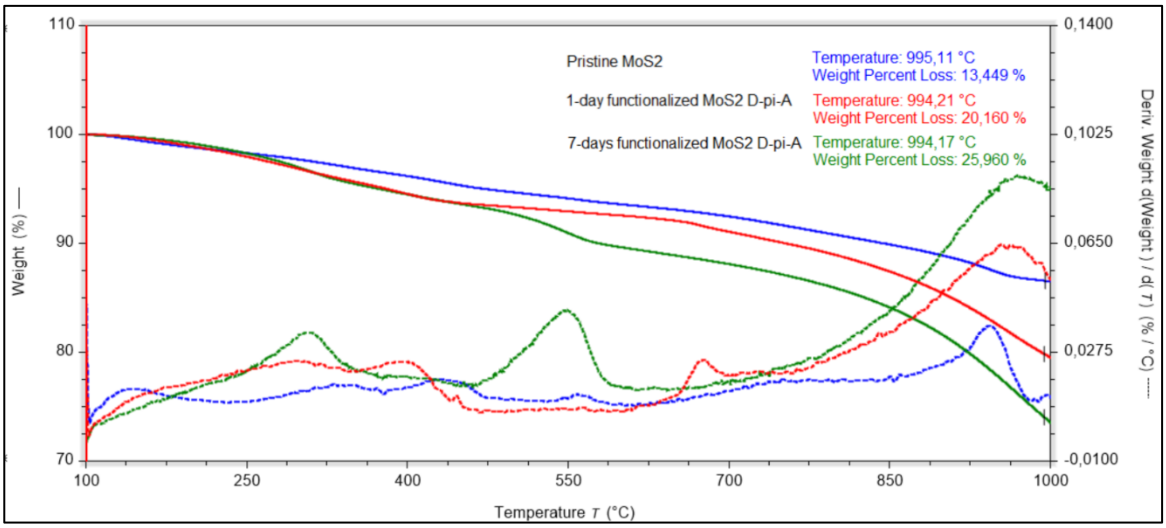

Figure 45: Thermogram of pristine molybdenum disulfide, MoS2@D-π-A_1, and MoS2@D-π-A_7, recorded from 100°C to 1000°C, with a constant increase in temperature of 10°C/min.

2.4.2. Transmission electron microscopy analysis

TEM imaging can help to visually assess the shape and size of the pristine and functionalized molybdenum disulfide present in this study, as reported by the figures below (pristine and MoS_2@D-π-A_7).

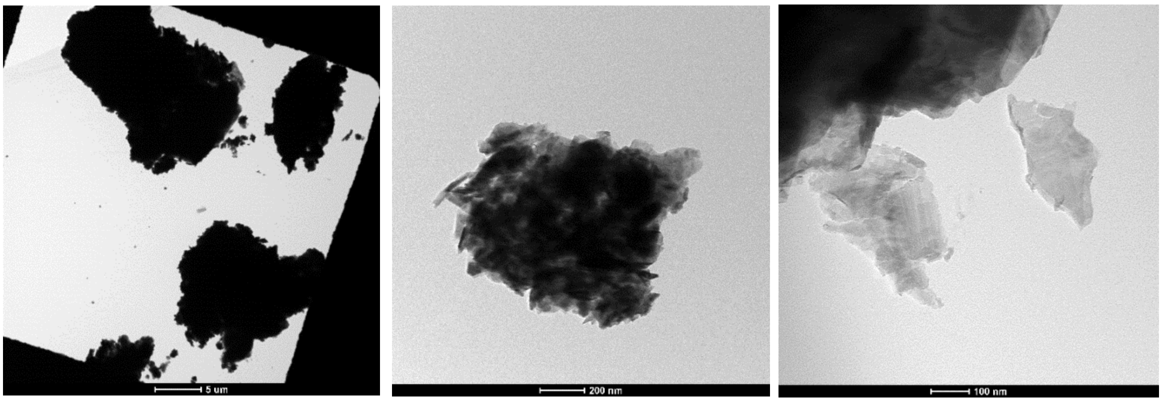

Figure 46: TEM images of pristine molybdenum disulfide with different magnifications (5 µm, 200 nm and 100 nm) .

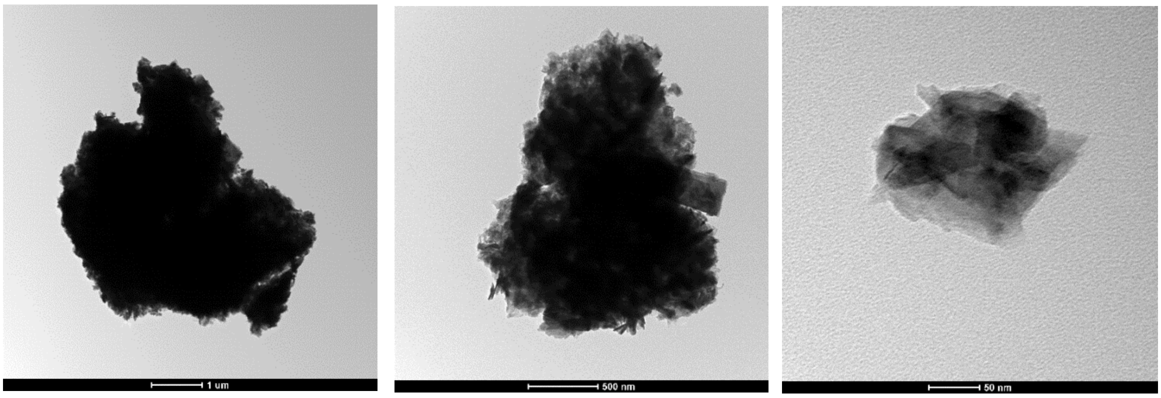

Figure 47: TEM images of MoS2@D-π-A_7 with different magnifications (1 µm, 500 nm and 50 nm).

It's clear from this analysis that the transition metal dichalcogenide is present in the form of flakes, whose dimensions can be quite variable, ranging from some micrometers to hundreds of nanometers. There are no significant differences for what concerns the shape and size of the functionalized and the pristine flakes, as a proof that functionalization does not introduce relevant modifications in the structure and aggregation state of MoS_2.

2.4.3. Raman spectroscopy

Raman spectroscopy is a useful technique which can be employed in the study of nanomaterials. In particular, for what concerns its application with molybdenum disulfide, it could give some insight into the presence and extension of defects in the pristine and treated materials [98]. Moreover, Raman spectroscopy could be used to shine light on the average number of layers of the pristine and treated materials [66], [99], [100].

As reported in the literature, the non-resonant Raman spectrum of MoS_2 is dominated by two main vibrational modes: E_{2g}^1, which is due to the in-plane vibration of two sulfur atoms with respect to a molybdenum atom, and A_{1g}, which corresponds to the out-of-plane vibrations of two sulfur atoms in opposite directions [100]. Previous literature works report that with excitation at 532 nm (non-resonance) strong signals are evident for both in-plane E_{2g}^1 mode and out-of-plane A_{1g} mode, at around 400 cm^{-1} [101]. Interestingly, the E_{2g}^1 vibration softens (red shifts), while the A_{1g} vibration stiffens (blue shifts) with increasing sample thickness. For samples of six or more layers, the frequencies of both modes converge to bulk values [101]. It's also interesting to notice that the rate variation is twice as large for the A_{1g} mode as for the E_{2g}^1 mode. In the figure below the differences in vibration frequency of the two modes as a function of the number of layers [101].

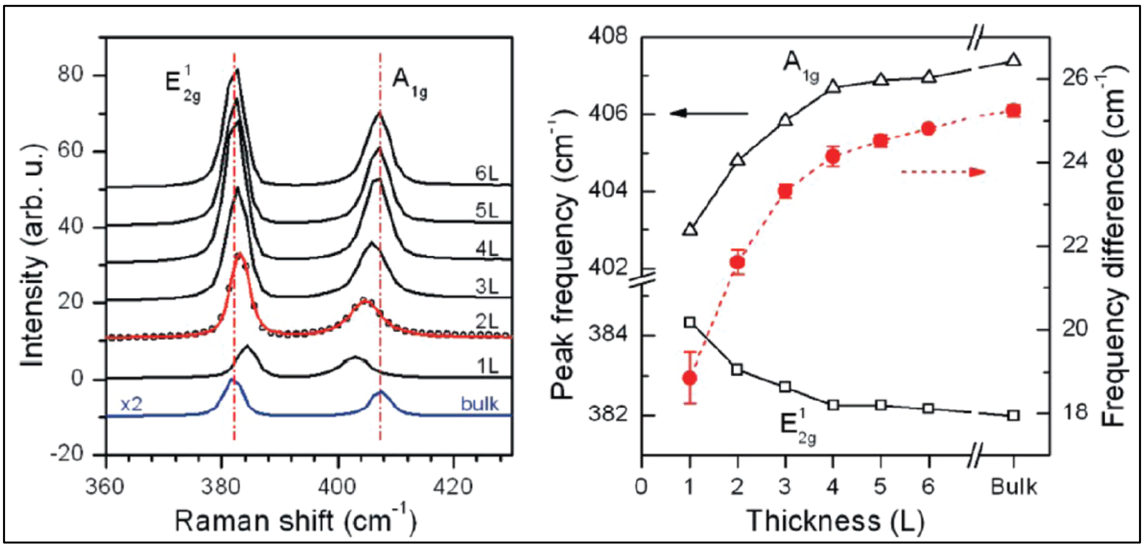

Figure 48: (left) Raman spectra of thin (nL) and bulk MoS_2 films. (right) Frequencies of E^1_{2g} and A_{1g} Raman modes (left vertical axis) and their difference (right vertical axis) as a function of layer thickness [101].

Considering the classical model for coupled harmonic oscillators, the two vibrational modes are expected to stiffen as additional layers are added, because of the interlayer Van der Waals interactions increase the restoring forces acting on the atoms. Hence both modes should blue shift while increasing the number of layers. While the A_{1g} mode's shift agrees with this prediction, the E_{2g}^1 peak shows a red-shift, instead of a blue-shift, suggesting that the increased interlayer Van der Waals forces play a minor role while stacking-induced structure changes or long-range Coulombic interlayer interactions in multilayer MoS_2 may dominate the change of atomic vibration [66], [101].

To investigate our samples and verify if a similar relationship occurs, and also to try to determine the average number of layers, three Raman spectra are recorded for the pristine MoS_2, MoS_2@$NaBH_4$@D-π-A_7 and MoS_2@D-π-A_7. For each sample three spectra are collected, in different areas, and the results are mediated on the three recordings. The excitation wavelength used is 532 nm.

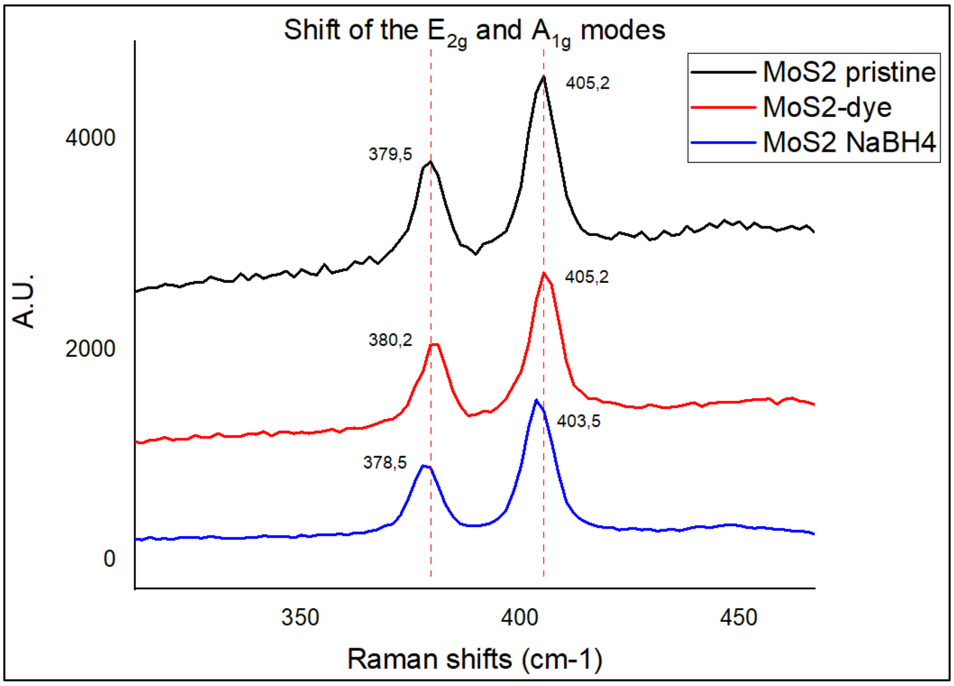

Figure 49: Frequencies of E^1_{2g} and A_{1g} Raman modes in the prepared samples: pristine MoS_2 (black), MoS_2@D-π-A_7 (red) and MoS_2@$NaBH_4$@D-π-A_7 (blue).

The obtained results show an average shift for the A_{1g} mode of 405 nm and of 380 nm for the E^1_{2g} mode, in the pristine molybdenum disulfide, which only slightly change once the material is functionalized with thiols or treated with sodium borohydride. While this drops the idea of working with single-layer structures, it also confirms an exfoliated material, probably in average between three and six layers.

As mentioned earlier, Raman spectroscopy could also be used to verify the presence of defects in the material, which are crucial for both the catalytic activity of the molybdenum disulfide and the thiol functionalization [50], [102]. In fact, chemical treatments designed to produce new defects, like the sodium borohydride reduction, are supposed to cause some variations in Raman spectra of MoS_2 [94]. In particular, a red-shift of the E^1_{2g} mode and a blue-shift of the A_{1g} mode indicate the presence of sulfur vacancies in the molybdenum disulfide [98]. According to theory, increasing sulfur vacancies concentration should reduce Mo-S bonds involved in the in-plane vibrations, and thus the restoring force constants of the E^1_{2g} mode is weakened, hence its frequency should red-shift. For the A_{1g}mode the mechanism is different: due to its different vibration pattern, its restoring force constant is only slightly reduced with sulfur vacancies, in comparison with the E^1_{2g} mode. However, here the total mass of the system plays a more important role in the calculation of the vibration intensity. There are hence two competitive factors deciding the shift of the A_{1g} mode, which should first upshift slightly and then downshift with increasing sulfur vacancies, as reported in the figures below (grey and black dots are calculated shifts, blue and sky blue are experimental ones) [98].

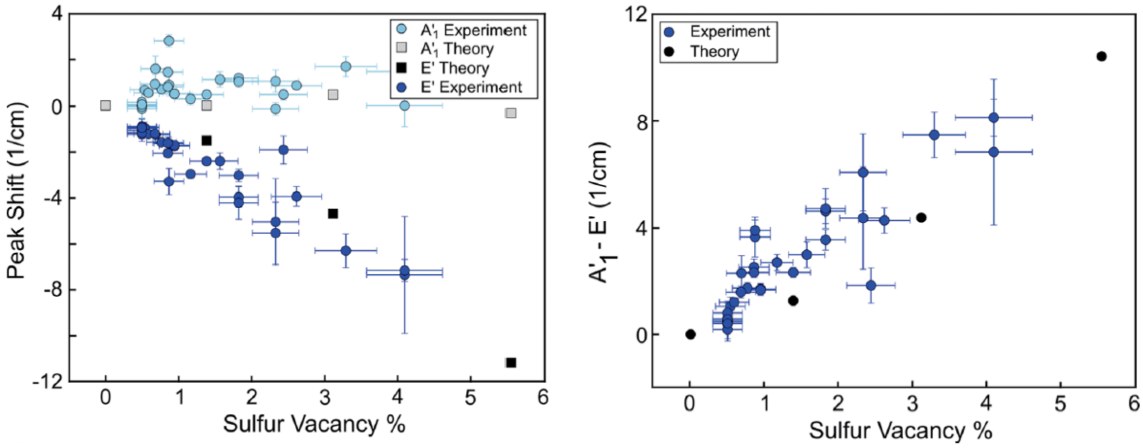

Figure 50: Raman peak shift vs S vacancy: experiment and theory. (left) Experimental and theoretical individual peak shifts of the E' and A'$_1$ modes as a function of sulfur vacancy percentage. DFT calculations are shown in gray and black. (right) Change in separation between the E' and A'$_1$ Raman modes as a function of defect concentration. From [98].

Since the E_{2g}^1 mode experiences a more intense shift with increasing sulfur vacancies, it seems to possibly afford a more reliable evaluation of the presence of sulfur vacancies. Looking at our samples, we can see that the vibration shift of the E_{2g}^1 mode only slightly decreased, roughly 1 cm^{-1}. This could be an indicator of a very mild introduction of sulfur vacancies, of the order of 1 % or less. It would be desirable to introduce as many vacancies as possible, without ruining and compromising the structural integrity of the material, as their presence is favorable for both its catalytic properties and its functionalization degree. A more extensive vacancy introduction could perhaps be achieved using different chemical treatments or, more probably, with physical approaches, such as plasma or electron beam irradiation [51], [53], [94], [96], [97].

Raman spectroscopy can also be useful to identify the presence of organic molecules interacting with the molybdenum disulfide. For example, looking at the complete scans from 200 cm^{-1} to 2000 cm^{-1}, we can see many features in the functionalized MoS_2 in the region between 1000 and 1700 cm^{-1}, that are not present in the pristine or $NaBH_4$ treated material. The scans reported below are averages of three recorded scans per each sample, using 532 nm as exciting wavelength. In particular, the moderate intensity signal around 1200 cm^{-1} could be assigned to a C-S bond, indication of the presence of organic molecules linked to the disulfide. Furthermore, strong signals at 1435 and 1570 cm^{-1} are attributable to the CH_2 and CH_3 stretches and to aromatic rings vibrations respectively. In addition, no strong signals are discernible in these areas in the pristine and reduced material scans. These altogether are strong indicators that some organic molecules are effectively anchored on the surface of the MoS_2.

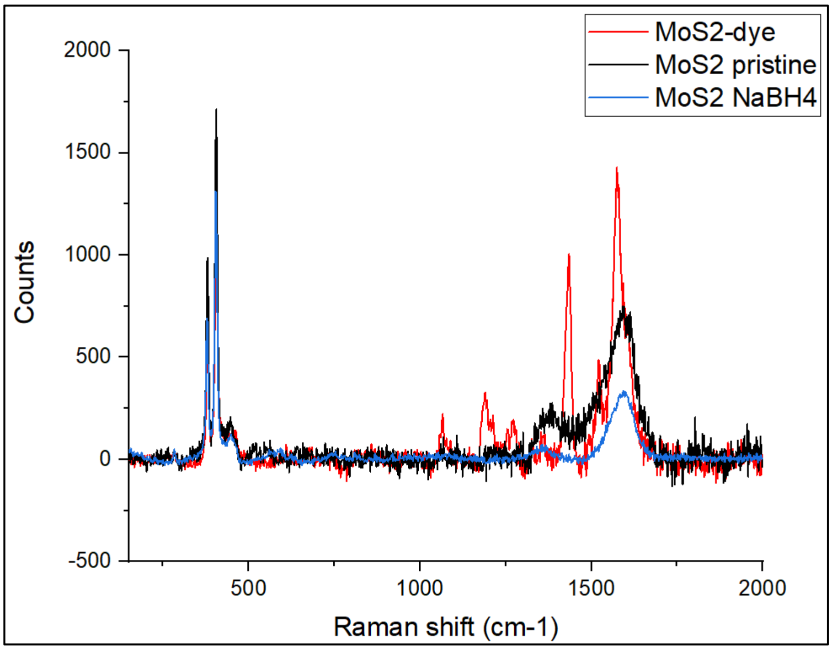

Figure 51: Raman spectra of pristine MoS_2 (black), MoS_2@$NaBH_4$@D-π-A_7 (blue) and MoS_2@D-π-A_7 (red), recorded from 200 to 2000 cm^{-1}.

2.4.4. Computational models

A computational approach is considered fundamental to assess the feasibility of a project like the one here reported, which includes energy transitions and energy transfers. It's no less interesting and important to fully understand the theoretical background of the molecules here tested, and where their energy levels place compared to the ones of molybdenum disulfide.

The simulations are performed using the software Gaussian, while the isodensity surfaces are displayed with GaussView and the spectral data with GaussSum. The calculations are of DFT type, using CAM-B3LYP method and 6-311G** as basis set. Energetic levels are determined through Time Dependent approach, and the solvation effects of the solvent, tetrahydrofuran, are modeled using the polarizable continuum model (PCM).

The results for computed (CAM-B3LYP/6-311G**) isodensity surface plots of HOMO and LUMO orbitals are reported in the figures below, together with the calculated UV-Vis absorption spectrum in tetrahydrofuran and the electronic transitions for the D-π-A molecule. As it can be seen, the CH_2-CH_2 bridge linking the carboxylic moiety to the thiol is not interested in the electronic delocalization. This could prevent a complete energy transfer to the molybdenum disulfide, and it's something to keep in mind.

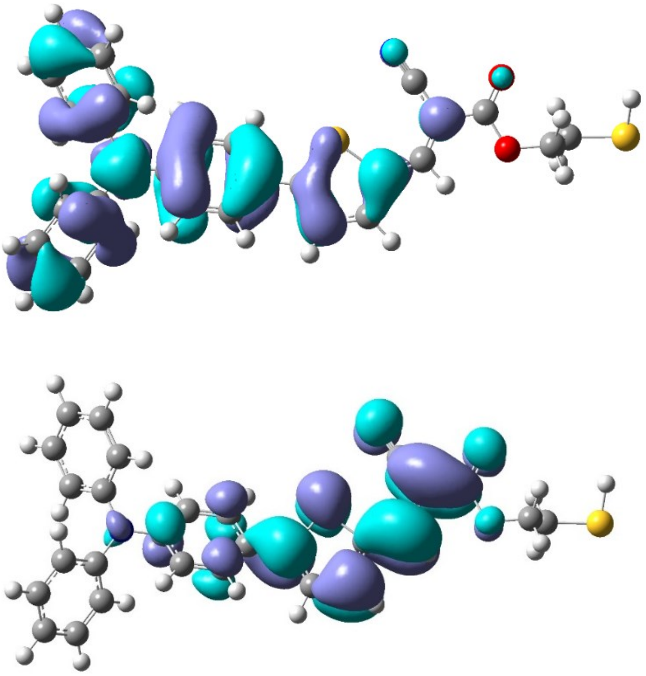

*Figure 54: Computed (CAM-B3LYP/6-311G**) isodensity surface plots of HOMO (top) and LUMO (bottom) orbitals of D-π-A.*

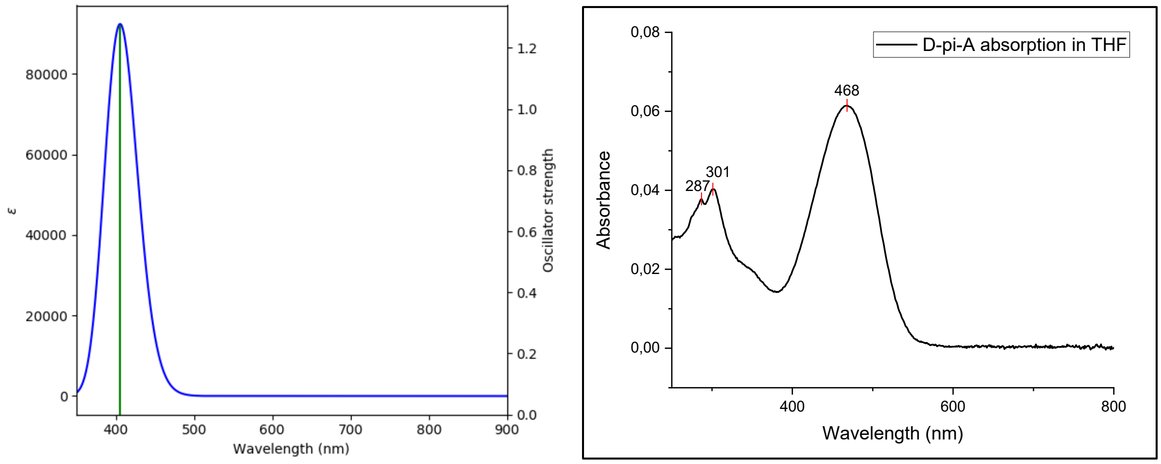

*Figure 55: (left) Computed UV-vis absorption spectrum (TD DFT: CAM-B3LYP/6-311G**/PCM, geometry optimized at CAM-B3LYP/6-311G**) in THF of D-π-A. (right) Recorded absorption spectrum of D-π-A in THF.*

*Table 1: Computed electronic transitions (TD DFT: TD DFT: CAM-B3LYP/6-311G**/PCM, geometry optimized at CAM-B3LYP/6-311G**) in THF.*

No.	Energy (cm^{-1})	Wavelength (nm)	Osc. Strength	Symmetry	Major contribs	Minor contribs
1	24656	405,6	1,2749	Singlet-A	H-1->LUMO (15%), HOMO->LUMO (78%)	HOMO->L+1 (4%)
2	33059	302,5	0,1213	Singlet-A	H-1->LUMO (67%), HOMO->L+1 (12%)	H-8->LUMO (4%), H-7->LUMO (3%), HOMO->LUMO (8%)
3	34588	289,1	0,0246	Singlet-A	HOMO->L+2 (84%)	

As it can be seen, the calculated electronic transition in the visible range falls at 405.6 nm, while in tetrahydrofuran the same transition appears at around 468 nm, with a discrepancy of about 60 nm. It's not a small difference, probably due to the fact that the calculations consider transitions between mono-electronic theoretical boxes, while experimentally we deal with an electronic distribution diffused on the whole molecule. The shape of the transition, however, is consistent. As depicted in the table above, said transition shows predominantly a HOMO → LUMO character, with a non-negligible HOMO-1 → LUMO contribution and a small HOMO → LUMO+1 character.

There is very good correspondence between the higher energy calculated transitions and the experimental spectrum, where the software provides values of 302.5 and 289.1 nm, which are in good accordance with the recorded spectrum, 301 and 287 nm.

For what concerns the D-A-π-A molecule, the results for computed (CAM-B3LYP/6-311G**) isodensity surface plots of HOMO and LUMO orbitals are reported in the figures below, together with the calculated UV-Vis absorption spectrum in tetrahydrofuran and the electronic transitions expected. Not differently from the previous example, the HOMO and LUMO configurations do not include the aliphatic CH_2-CH_2 bridge at the end of the molecule. As before, this is something important to keep in mind, which could, in theory, affect the capabilities of the dye to transfer energy to the molybdenum disulfide, as the electronic conjugation does not extend until its surface.

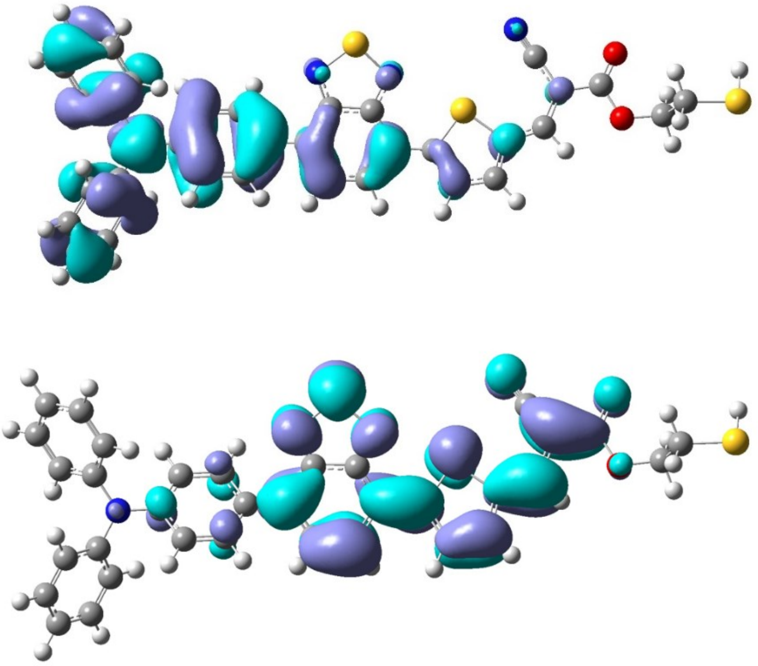

*Figure 52: Computed (CAM-B3LYP/6-311G**) isodensity surface plots of HOMO (top) and LUMO (bottom) orbitals of D-A-π-A.*

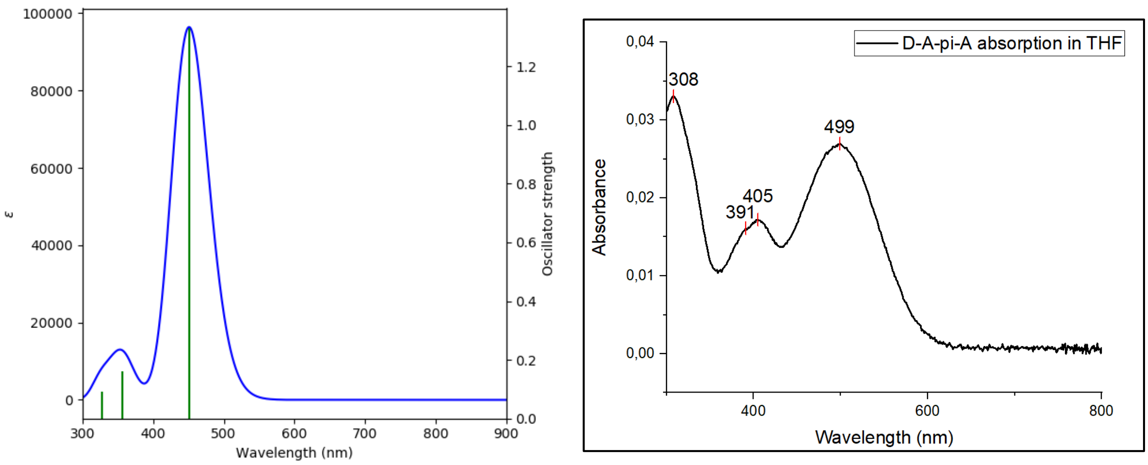

*Figure 53: (left) Computed UV-vis absorption spectrum (TD DFT: CAM-B3LYP/6-311G**/PCM, geometry optimized at CAM-B3LYP/6-311G**) in THF of D-A-π-A. (right) Recorded absorption spectrum of D-A-π-A in THF.*

*Table 2: Computed electronic transitions (TD DFT: TD DFT: CAM-B3LYP/6-311G**/PCM, geometry optimized at CAM-B3LYP/6-311G**) in THF.*

No.	Energy (cm^{-1})	Wavelength (nm)	Osc. Strength	Symmetry	Major contribs	Minor contribs
1	22174	451,0	1,3308	Singlet-A	H-1->LUMO (25%), HOMO->LUMO (66%)	HOMO->L+1 (4%)
2	28029	356,8	0,1622	Singlet-A	H-1->LUMO (54%), HOMO->LUMO (12%), HOMO->L+1 (17%)	H-2->LUMO (5%), H-1->L+1 (4%)
3	30482	328,1	0,0908	Singlet-A	H-1->LUMO (12%), H-1->L+1 (40%), HOMO->LUMO (11%), HOMO->L+1 (30%)	HOMO->L+2 (3%)

This time, the main calculated transition in the visible range falls at 451.0 nm, with additional bands at 356.8 and 328.1 nm. The experimental absorption spectrum reproduces the shape of the predicted one, with a shift in wavelengths, similar to what it has been seen in the case of the D-π-A dye. The recorded spectrum shows absorption maxima at 499, 405, 391 and 308 nm, hence calculations are affected by a blueshift discrepancy of about 45-50 nm, as seen before. The composition of the main band is mainly described by HOMO → LUMO transition, with some minor character of HOMO-1 → LUMO and HOMO → LUMO+1. The composite band around 400 nm is ascribable to π−π* electronic transitions of the sensitizer, while the longer wavelength band corresponds to ICT [73].

Comparing the two dyes, a red shift in absorption for the main band is expected for the D-A-π-A molecule, since the introduction of a benzothiadiazole unit as second acceptor lowers the HOMO-LUMO band gap, thus shifting the ICT absorption peak [90]. Simultaneously, the absorption onset is extended by 70 nm from 560 nm (D-π-A) to 630 nm (D-A-π-A) in diluted solutions in THF. Consequently, the benzothiadiazole unit can efficiently decrease the bandgap and optimize energy levels, resulting in a better spectral response to longer wavelengths and a more solid absorption at higher energies, which are beneficial characteristics to light-harvesting and efficiency [90].

2.4.5. UV-Visible spectroscopy

In order to investigate the spectroscopic properties of the dyes and the hybrid systems, some absorption measurements are required. Firstly, it is crucial to find a solvent able to readily dissolve the dyes and afford stable suspensions of the hybrids and the pristine nanomaterial. Few solvents proved suitable, and, among them, THF seemed to be the most promising. For this reason, absorption and fluorescence measurements were performed in spectroscopy grade THF. To avoid absorption interferences due to the trityl protecting group and considering the absence in the final functionalized material, all the measurements were performed employing the free thiol form of the sensitizer, prepared by deprotection of the trityl-capped dye. For every measurement session, the deprotection was performed the day before of the analysis, with subsequent chromatographic purification, as described in the *Experimental section*. Because of the difficulty of preparing different solutions with the same concentration (due to the small amounts of hybrid materials prepared that makes it practically impossible to weight it accurately and repeatedly), we opted to prepare solutions with values of absorbance below 0.1 at the maximum in order to minimize optical issues and to have a direct comparison of the fluorescence spectra, so that no optical corrections are needed [103].

To begin with, the absorption properties of the dye were explored. For the D-π-A dye the absorption spectrum was collected in a diluted solution of THF. The main absorption peak corresponds to 468 nm and it's ascribable to an intramolecular charge transfer state [90]. Moving to shorter wavelengths the spectrum shows a minimum, followed by two absorptions at 301 and 287 nm, which can be related to π−π* electronic transitions [90].

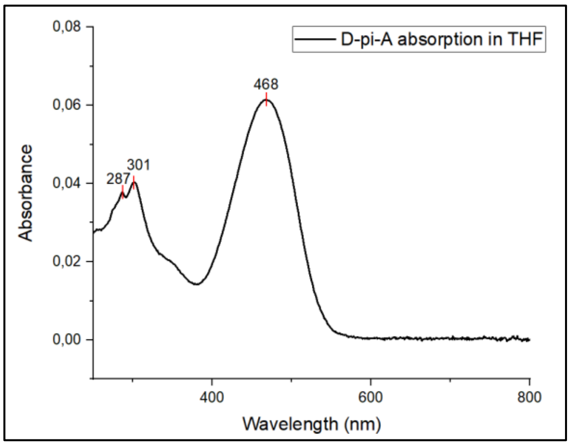

Figure 54: Absorption spectrum of D-π-A in THF, recorded from 250 nm to 800 nm.

In the case of the D-A-π-A dye, the absorption maximum is redshifted to a value of about 500 nm, as expected due to the introduction of a benzothiadiazole unit as secondary acceptor. The depression in absorbance visible in the spectrum of the D-π-A sensitizer is not visible anymore, and instead it's replaced by a wide peak composed by two absorptions at 405 and 391 nm. These are separated by 14 nm, which is the exact same difference that we find in the peaks at about 300 nm in the D-π-A dye, therefore most likely they both represent the same π−π* electronic transitions which become red-shifted thanks to the presence of the benzothiadiazole. In the new sensitizer, in addition to the three peaks of the simple D-π-A dye, a new peak is present at 308 nm, which is not detectable in the dye without the secondary acceptor, probably because too much in the UV region of the spectrum where the solvent cut-off the signal. Moreover, it's brought to longer wavelengths thanks to the benzothiadiazole unit.

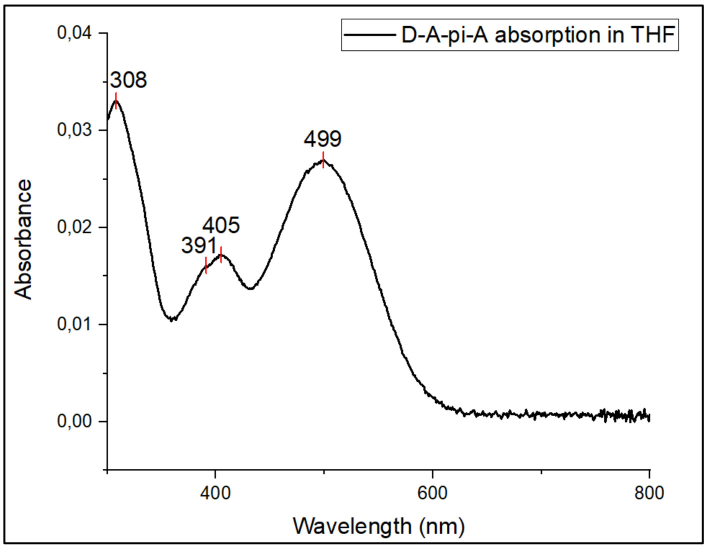

Figure 55: Absorption spectrum of D-A-π-A in THF, recorded from 300 nm to 800 nm.

Since the two sensitizers show a different absorption profile, a comparison with the solar emission spectrum to evaluate which one can better act as light harvester is a key point to success the goal of this Master Thesis project. The solar spectrum changes throughout the day and with location, therefore standard reference spectra are defined to allow the performance comparison of photovoltaic devices from different manufacturers and research laboratories. Two standards are defined for terrestrial use. The AM1.5 Global spectrum is designed for flat plate modules and has an integrated power of 1000 W/m^2. The AM1.5 Direct (+circumsolar) spectrum is defined for solar concentrator work. It includes the direct beam from the sun plus the circumsolar component in a disk 2.5 degrees around the sun. The direct plus circumsolar spectrum has an integrated power density of 900 W/m^2. For our comparison the AM1.5 Global spectrum is used. Information and data on the solar spectra are taken from the website of the National Renewable Energy Laboratory (NREL). In the figure below the solar emission spectrum is compared with the absorption spectra of the two dyes. The absorption spectra are normalized on the maxima in the visible range. Importantly, the D-A-π-A sensitizer extends its absorption to longer wavelengths, effectively covering a wider portion of the solar spectrum, which is obviously a desirable feature in a light harvesting device.

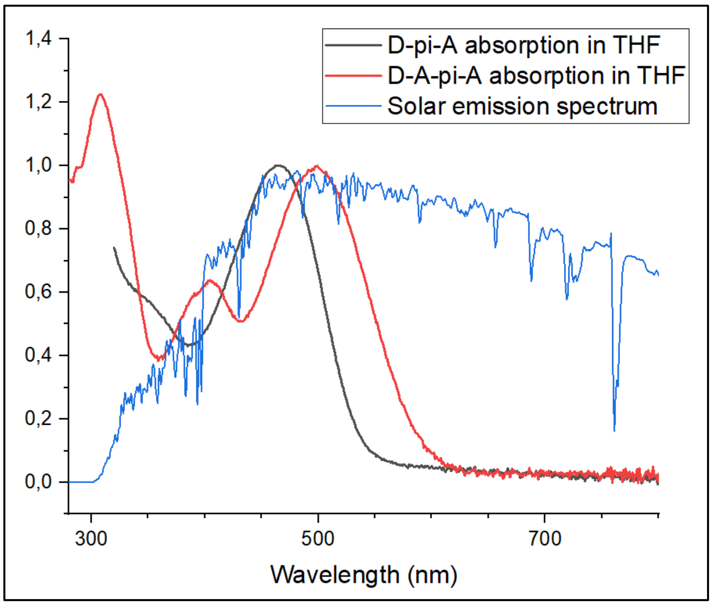

Figure 56: Comparison between the absorption spectrum of D-π-A and D-A-π-A with the AM1.5 Global solar emission spectrum.

Additionally, an absorption spectrum of the pristine MoS_2 is recorded, in order to have a reference to be compared with the functionalized material. Specifically, what is collected is an extinction spectrum since it contains contributions from both absorbance and scattering of the nanomaterial [104]. In fact, scattering is known to be significant for dispersions of nanosheets, especially for those with large lateral size [105]. However, it has been proved that for $\lambda < 700$ nm the scattering contribution is broadly similar in shape to the absorbance contribution, and so, as a result, the absorbance spectrum and the extinction spectrum are also similar in shape [104]. This indicates that, even though scattering is always present, information encoded in an absorption spectrum can be effectively extracted from the extinction spectrum, at least at a qualitative level [104]. Interestingly, the shape of the spectrum of our pristine exfoliated MoS_2 corresponds to what can be find in the literature for flakes of large lateral size [104]. Moreover, TEM measurements confirmed that the pristine material used presents various flake dimensions, reaching hundreds of nanometers. The excitons A and B are well visible and are marked in the figure below.

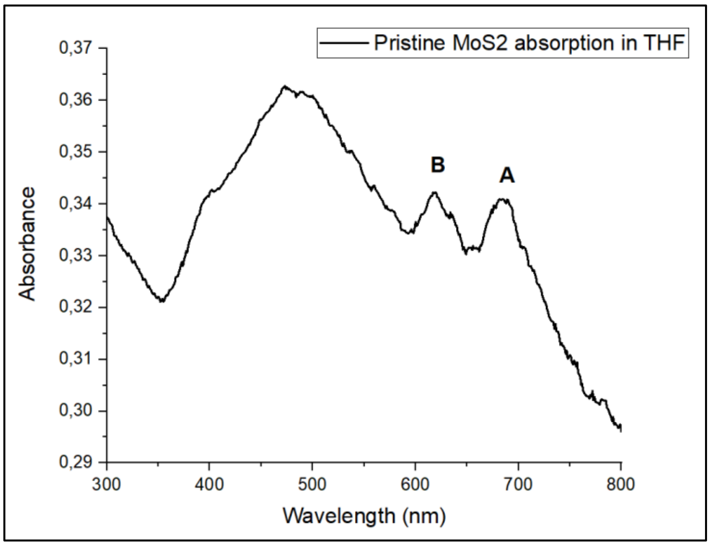

Figure 57: Absorption spectrum of pristine MoS_2 in THF, recorded from 300 to 800 nm.

Our attention was then focused on the hybrid materials. All the four prepared samples were analyzed in order to investigate the influence of different variables, like a diverse functionalization time, an attempt to enhance the amount of sulfur vacancies prior to the functionalization, and the change in sensitizer.

Speaking of MoS_2@D-π-A_1, the shape of the absorption spectrum resembles the one of the pristine MoS_2. However, while the two excitons are clearly visible at 615 and 675 nm, the area that overlaps with the absorption of the dye, between 400 and 500 nm, shows a clear enhancement as it can be noticed looking at the diminished depth of the dip at 350 nm and at the augmented absorption between 400 and 500 nm, compared to the baseline at 800 nm. It is evident that in the hybrid material MoS_2 is surely present, due to the scattering trend and the presence of the two excitons; however, a second feature also exists, attributable to the organic dye. This new peak is in accordance with the absorption spectrum of the free molecule, showing a maximum at 468 nm.

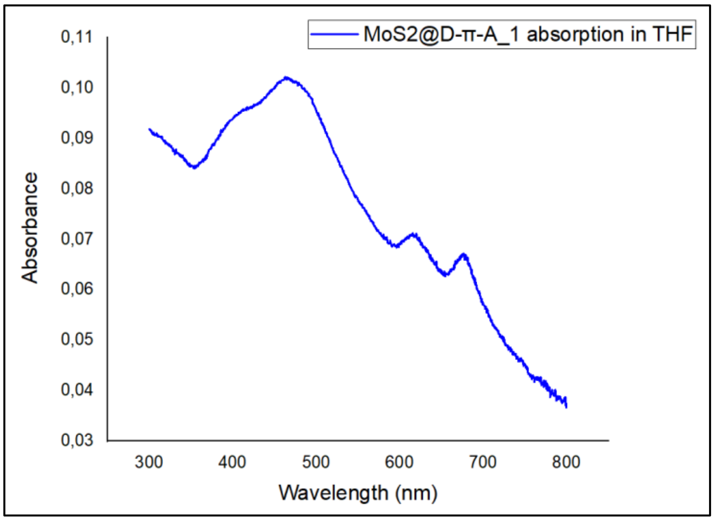

Figure 58: Absorption spectrum of MoS_2@D-π-A_1 in THF, recorded from 300 to 800 nm.

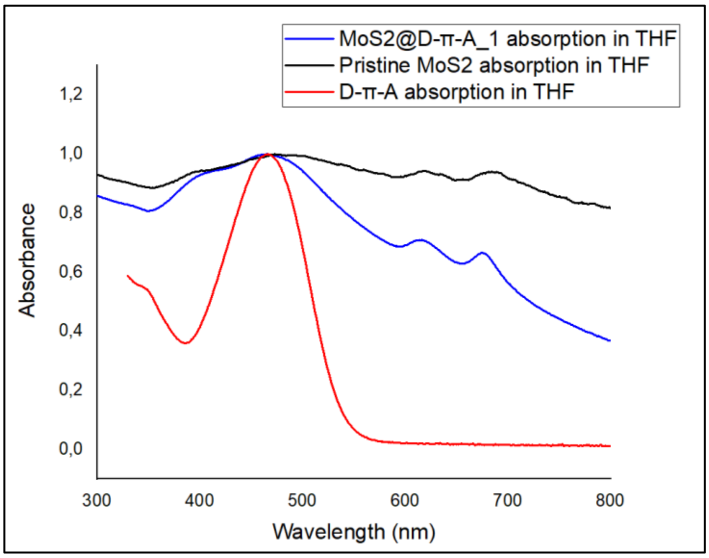

Figure 59: Comparison between the absorption spectra of pristine MoS_2 (black), MoS_2@D-π-A_1 (blue) and D-π-A (red) in THF.

Moving the attention to MoS_2@D-π-A_7, once again scattering is present, since the baseline does not move to zero at longer wavelengths as in the free dye. This is coherent with the presence of nanostructured material in suspension. MoS_2@D-π-A_7 this time shows a broad absorption at 480 nm, while D-π-A presents the usual maximum at 468 nm and another peak in the blue, at 302 nm, which region is lost in the spectra of the materials due to scattering and solvent's cut-off. It is also important to note a large shift is present in this sample in comparison with the hybrid material and the free sensitizer of about 12 nm. By using the absorption spectrum of pristine MoS_2 as baseline, we imposed the recorded traces to have a value of zero at 1000 nm in order to highlight the contribution of the organic dye in the absorption of the functionalized material, as reported in *Figure 64*. This feature suggests that a hybrid has been obtained, which shows, at least for what concerns absorption properties, features of both the inorganic and organic components, with a more evident shift in absorption maxima. This larger shift in the maximum could be a proof of a more extensive degree of functionalization, since the functionalization

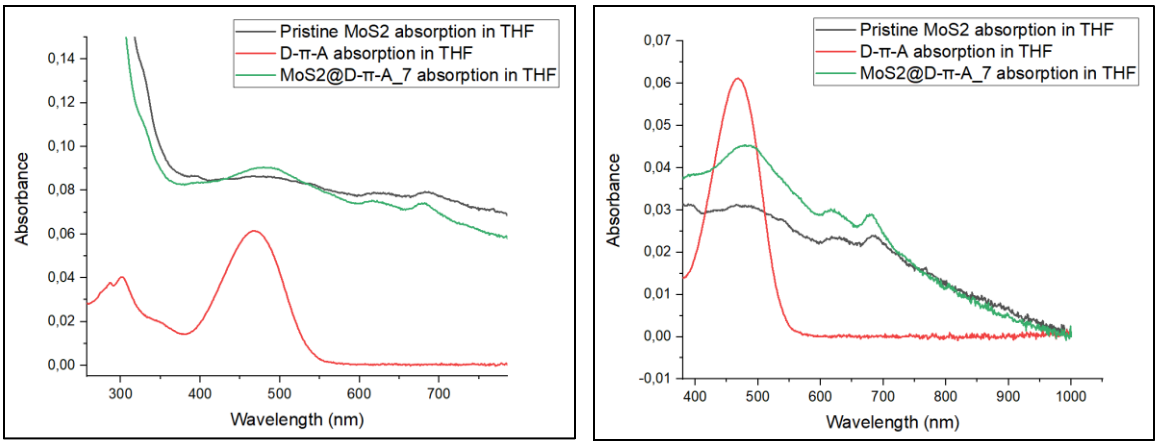

Figure 60: (left) Absorption spectra of pristine MoS_2 (black), MoS_2@D-π-A_7 (green) and D-π-A (red), as recorded in THF. (right) Same absorption spectra normalized to reach zero absorbance values at long wavelengths.

time was extended from one to seven days. Moreover, it could be a hint that some kind of electronic interaction takes place between the two components.

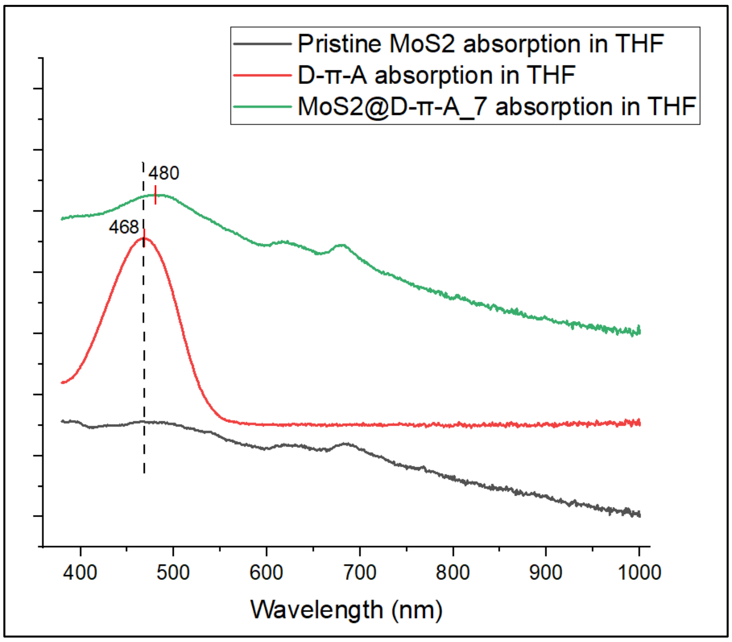

Figure 61: Absorption spectra of pristine MoS2 (black), MoS2@D-π-A_7 (green) and D-π-A (red), shifted on the Y-axis, to highlight the shift present between the red and green trace.

Moving on to MoS_2@$NaBH_4$@D-π-A_7, it's interesting to see whether the treatment with $NaBH_4$ provides any benefit. The sample MoS_2@D-A-π-A_7 could give an insight about how the absorption of MoS_2 varies with functionalization with a different sensitizer. These two hybrids are compared with the respective free dyes and the corresponding pristine nanomaterials. As usual, scattering is present in all the samples containing nanostructured materials, as it can be understood from the high baseline and the greater contribution with shorter wavelengths.

The dyes present the usual expected absorptions at 466 nm for D-π-A and 497, 404 and 308 nm for D-A-π-A.

Comparing now MoS_2@$NaBH_4$@D-π-A_7 with its corresponding free sensitizer, it can be seen that the maximum of absorbance in the hybrid shifts from 466 nm to 498 nm, with a remarkable shift of about 30 nm. As reported in *Figure 67*, it's evident the appearance of a strong absorption due to the presence of the dye. Interestingly, this band is placed 30 nm red-shifted from the band of the free sensitizer, most probably due to a better functionalization compared to the previous case, thanks to the pre-treatment with $NaBH_4$, and it could be a hint of a stronger communication between the inorganic matrix and the dye.

For what concerns MoS_2@D-A-π-A_7, a similar trend is observed: with respect to the maximum of D-A-π-A, placed at 497 nm, the hybrid shows a band at 530 nm, again with a shift of about 30 nm. Interestingly, the peak of the dye at 404 nm is present in the hybrid basically unaffected, while the band at 308 nm shifts to 320 nm in the functionalized material. A comparison of MoS_2@D-A-π-A_7 and the pristine MoS_2, once the absorbance has been corrected to zero at longer wavelengths, shows that the shifted bands of the sensitizer are emerging and differentiating from the extinction of the pristine material. Once again, these preliminary tests seem to confirm the occurrence of functionalization of the molybdenum disulfide, which seems more efficient for longer time of functionalization and pre-treatment with a reducing agent. Moreover, the red shift of the sensitizers peaks in the hybrid materials seems to suggest that an electronic communication between the two component is taking place.

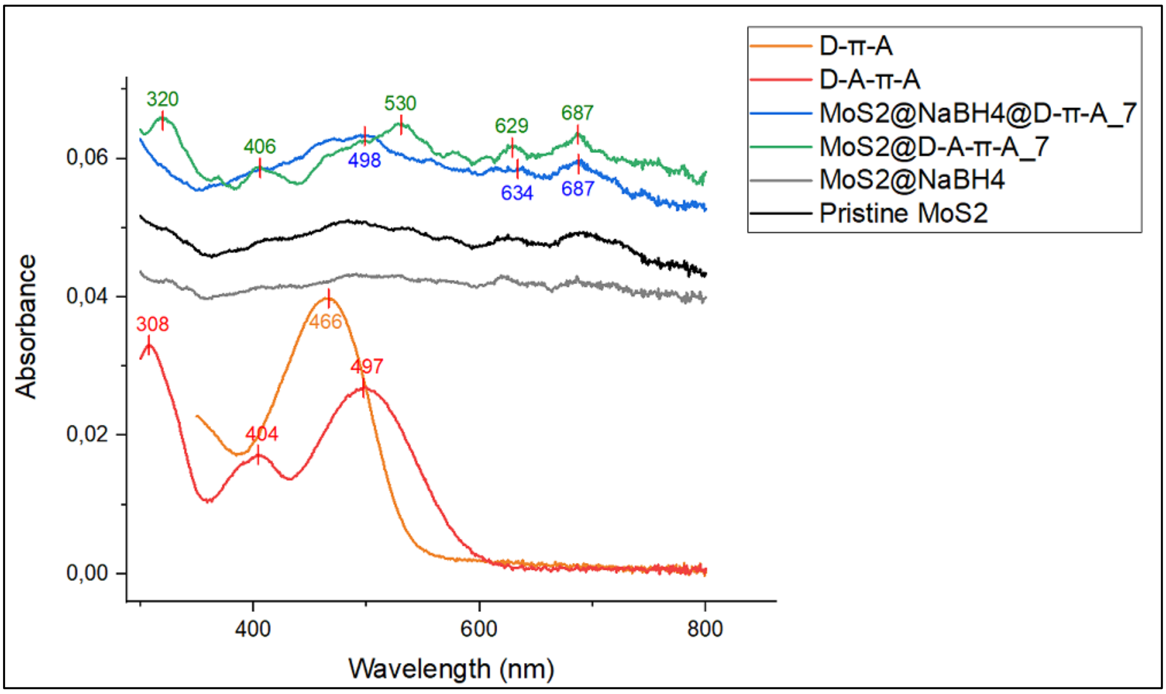

Figure 62: Summary of the absorption spectra recorded for the samples under investigation, in THF.

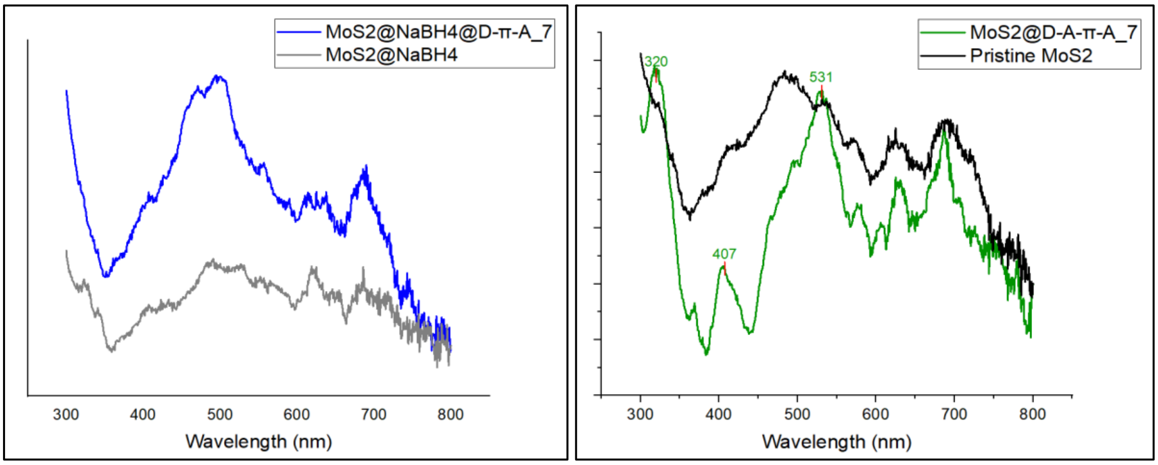

Figure 67: (left) Correction at long wavelengths for the absorption spectra of $MoS_2@NaBH_4@D$-π-A_7 (blue) and $MoS_2@NaBH_4$ (grey). (right) Correction at long wavelengths for the absorption of $MoS_2@D$-A-π-A_7 (green) and pristine MoS_2 (black).

Finally, the effect of the solvent has been explored, conducting a set of new measurements in DMF. DMF was chosen because it can readily dissolve the sensitizer and can also form better molybdenum disulfide suspensions. For this test, MoS_2@D-π-A_7 was chosen, together with the pristine MoS_2 and D-π-A for comparison. The absorption spectra are reported in the figure below. With respect to the measurements in THF as solvent, a blue shift of the maximum absorption peak of the sensitizer is observed: in THF the maximum value was at 468 nm, while in DMF it shifted to 405 nm, highlighting an important solvatochromic behavior of the dye. The maximum of the hybrid material, however, seems to not be affected by the same shift, being placed at around 485 nm, coherently with the measurements recorded in THF, probably due to a shelter effect caused by the MoS_2 flakes in the hybrid materials. Anyway, once again the contribution of the dye in the absorption of the hybrid is evident, as witnessed by the figures below. The results seem consistent with what has already been discussed, with the particularity of the wide blue shift of the dye alone.

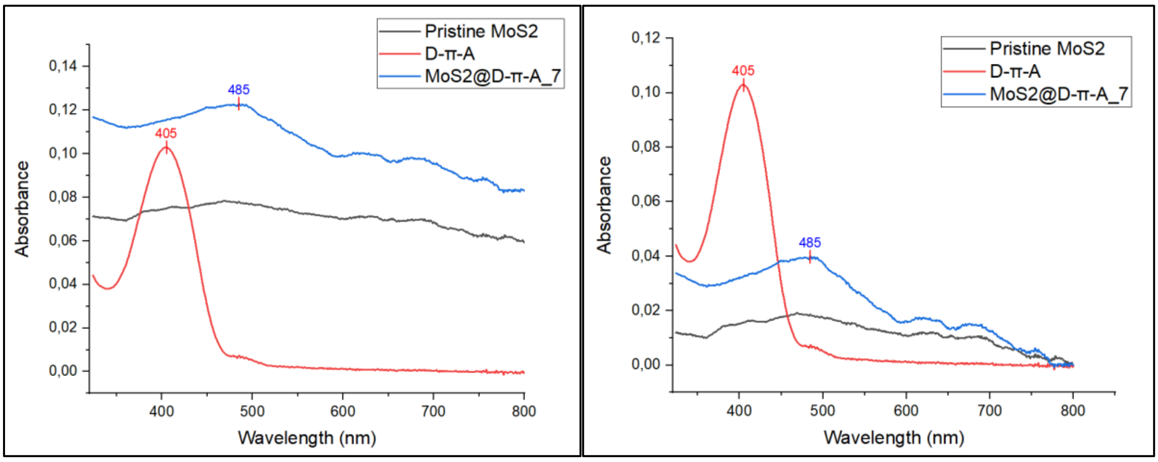

Figure 68: (left) Absorption spectra of pristine MoS_2 (black), D-π-A (red) and MoS_2@D-π-A_7 (blue) in DMF. (right) Absorption spectra of pristine MoS_2 (black), D-π-A (red) and MoS_2@D-π-A_7 (blue) in DMF corrected at long wavelengths.

In conclusion, interesting variations have been observed in the absorption spectra of the hybrid materials compared with the single precursors. In particular, a general red shift of the maximum in the functionalized materials is encountered, in comparison with the absorption of the sensitizers alone. The comparison of new features in the hybrid's spectra, resembling the shape of the sensitizer's absorption and their inherent shift that is observed could be explained by acknowledging the effective functionalization of the molybdenum disulfide with the organic dyes, and the modification of their electronic structure upon interaction with the semiconductor.

In the following table a summary of the absorption maxima of the analyzed samples is reported.

Table 3: Summary of the absorption maxima observed in the analyzed samples, in nanometers.

D-π-A in THF	468 (ICT)	301 (π-π*)	287 (π-π*)	
MoS_2@D-π-A_1 in THF	468			
MoS_2@D-π-A_7 in THF	480			
MoS_2@$NaBH_4$@D-π-A_7 in THF	498			
D-A-π-A in THF	499 (ICT)	405 (π-π*)	391 (π-π*)	308
MoS_2@D-A-π-A_7 in THF	530	406		320
D-π-A in DMF	405 (ICT)			
MoS_2@D-π-A_7 in DMF	485			

2.4.6. Fluorescence spectroscopy

For all the available samples, the fluorescence emissions were recorded by exciting at the maximum of absorption or other interesting wavelengths depending on the case. In some cases, excitation spectra were performed to obtain some insights of particular properties. For each sample, the excited state emission decay was recorded to estimate the correlated lifetimes.

i. MoS_2@D-π-A_1

Starting the study from MoS_2@D-π-A_1, and the corresponding dye D-π-A, the measurements were collected with diluted solutions, having absorbance values under 0.1, prepared in spectroscopy grade THF. The solution of the sensitizer was excited at 410 nm. While the absorption maximum stands at 468 nm, the emission shows a maximum at 630 nm, presenting a wide Stokes shift of about 160 nm.

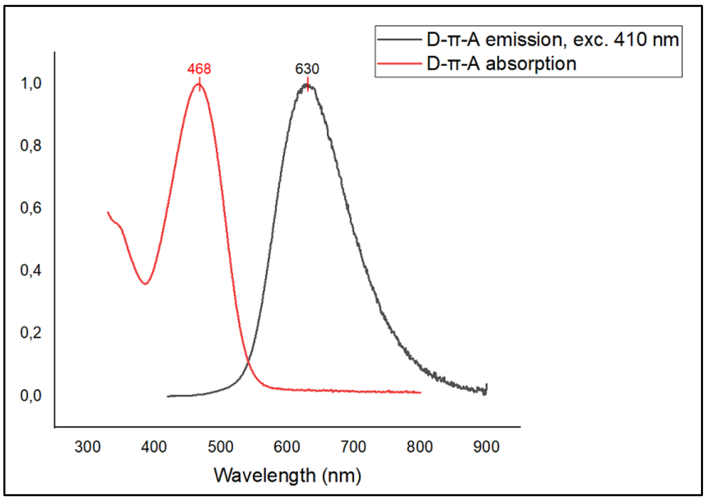

Figure 63: Absorption spectrum (red) and emission spectrum (black) of D-π-A, recorded in THF. Emission recorded exciting the sample at 410 nm.

Subsequently, the emission of the hybrid was recorded, exciting it at the same wavelength used for the free dye, i.e., 410 nm.

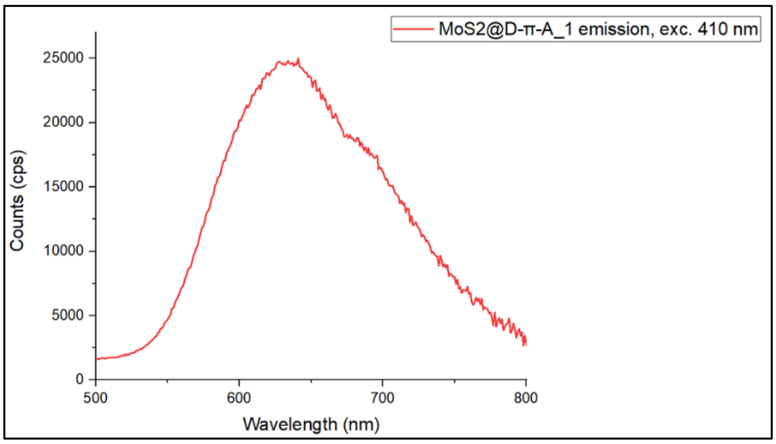

Figure 64: Emission spectrum of MoS_2@D-π-A_1, recorded exciting the sample at 410 nm, in THF.

Comparing the emissions of the dye alone and the hybrid material, an additional shoulder at around 685 nm can be seen in the MoS_2@D-π-A_1. Moreover, the maximum of emission in the material is placed at 635 nm, with a red shift from the emission of the sensitizer of about 5 nm (emission maximum of D-π-A results at 630 nm).

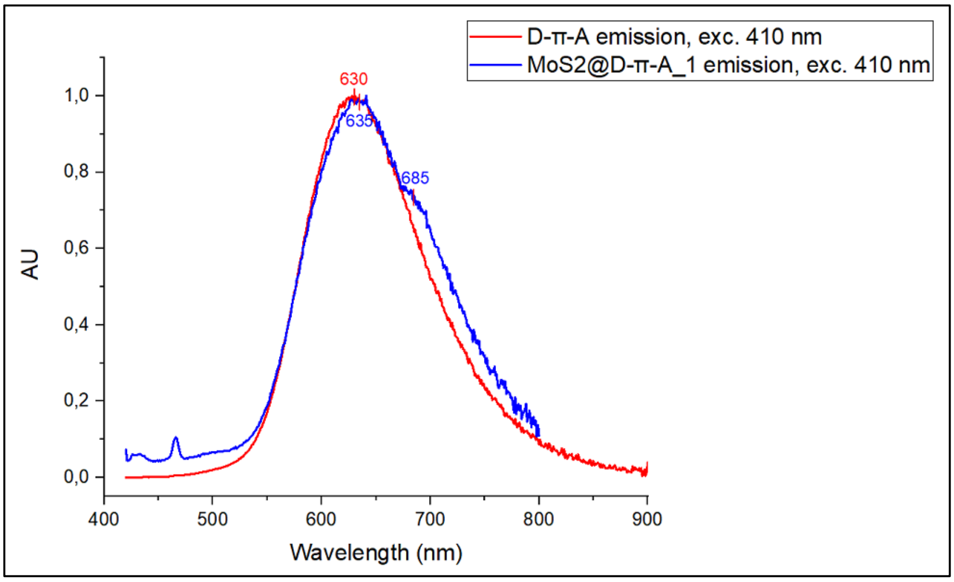

Figure 71: Overlap of the emission spectrum of D-π-A (red) and MoS_2@D-π-A_1 (blue), both excited at 410 nm.

To investigate the nature of the shoulder feature in the MoS_2@D-π-A_1 emission, an experiment of fluorescence excitation was performed, placing the emission monochromator at 635 and 685 nm and scanning with the excitation monochromator. The results obtained show that the two excitation profiles are perfectly stackable, and they are consistent with the absorption profile of the sensitizer alone, with a maximum at 468 nm. It can be concluded then that both the features in the emission spectrum of the hybrid are linked to the presence of the dye, and they are originated from the same excited state, thus denying the presence of two different emissive species in the hybrid suspension.

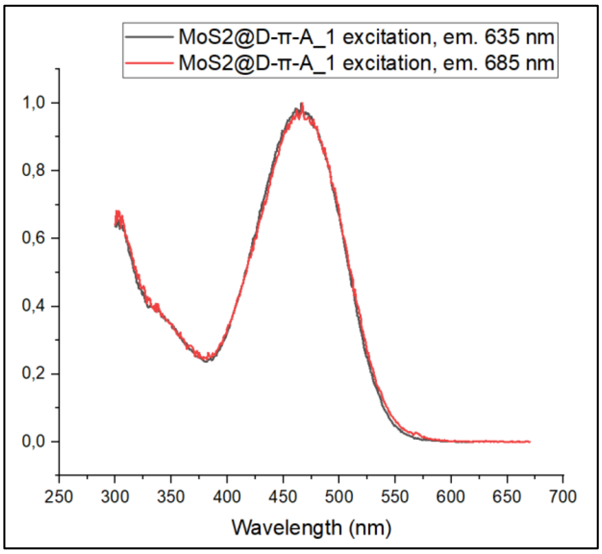

Figure 72: Fluorescence excitation spectrum of MoS_2@D-π-A_1, emission at 635 nm (black) and 685 nm (red).

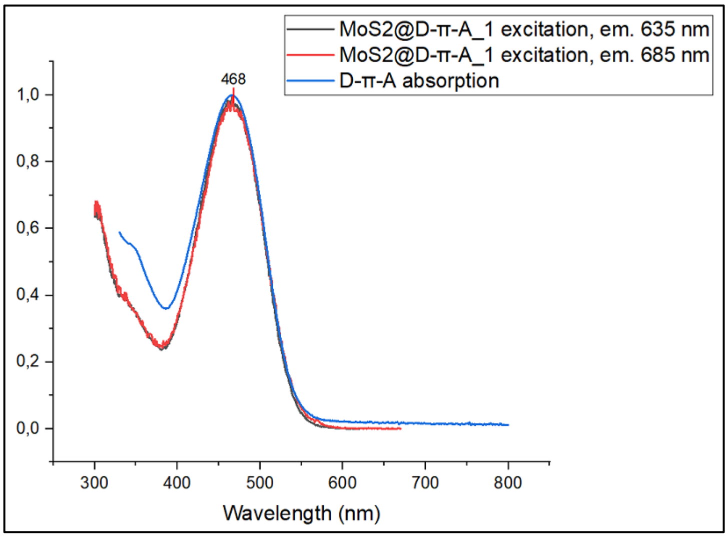

Figure 73: Comparison between the MoS2@D-π-A_1 fluorescence excitation spectra and the absorption spectrum of D-π-A.

The exclusion of the presence of different emitting species is interesting: in the hybrid material a double emission can be seen, and it's attributed to the same fluorophore. This result is not in contradiction with the presence of two excited states, S_1 and ICT, both populated and emissive. A double emission then arises, as reported in the literature, which actually varies between the free dye and the functionalized material [106]. It may be that the presence of the nanostructure in the hybrid modifies the populations of the excited states, since only one emits.

To prove the covalent interaction between the molybdenum disulfide and the dye, as well as to estimate the effective yield of this binding, time resolved emission measurements were conducted. Both D-π-A and MoS_2@D-π-A_1 show a mono-exponential decay, with lifetimes of 2.42 ns and 2.35 ns respectively. Pre-exponential factors for D-π-A and

MoS_2@D-π-A_1 were 0.375 and 0.370 respectively. For MoS_2@D-π-A_1 the lifetimes were measured at both peaks, 635 nm and 685 nm, obtaining the same value of 2.35 ns.

Table 4: Lifetime measurements for D-π-A and MoS_2@D-π-A_1 in THF.

D-π-A	τ = 2.42 ns B = 0.375	$\boldsymbol{k_r = Be^{-t/\tau}}$
MoS_2@D-π-A_1	τ = 2.35 ns B = 0.370	$k_r = Be^{-t/\tau}$

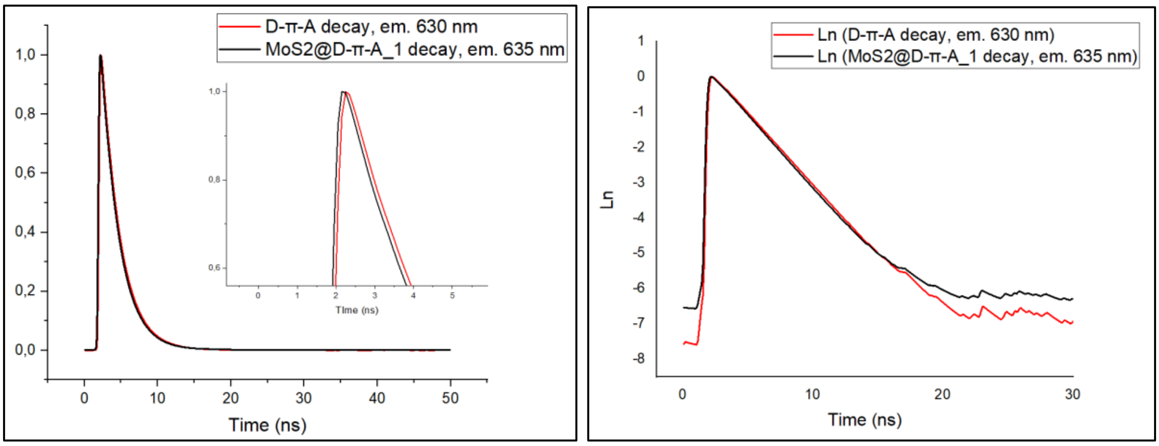

Figure 74: (left) Lifetime measurements of MoS2@D-π-A_1 and D-π-A. (right) Logarithm of the recorded decays.

Plotting the natural logarithm of counts against time in a graph we can see a linear dependence, confirming a mono-exponential decay. The presence of a mono-exponential decay suggests the presence of only one relaxation process, however, a difference in lifetimes exists, between D-π-A and MoS_2@D-π-A_1, which would be in agreement with a deactivation of the fluorescent molecule by energy transfer to the semiconductor. As perspective, a longer functionalization time (more than one day) could bring more molecules to the semiconductor, allowing to identify a difference in the functionalized material and the free molecule, concerning the lifetime.

ii. MoS_2@D-π-A_7

After these preliminary tests, the seven days functionalized material, MoS_2@D-π-A_7, was taken under consideration, together with its sensitizer, D-π-A, and a sample of pristine MoS_2 as reference. All the analyzed solutions were prepared in spectroscopy grade THF and they were diluted to have a maximum value of absorbance below 0.1. Focusing on D-π-A, the main absorption bands have maxima at 302 nm and 468 nm. Fluorescence emission is hence recorded by exciting the dye at these two wavelengths. The resulting spectra are perfectly stackable, index that the two absorptions contribute to populate the same excited state. The emission maximum is placed at 630 nm, perfectly consistent with older measurements.

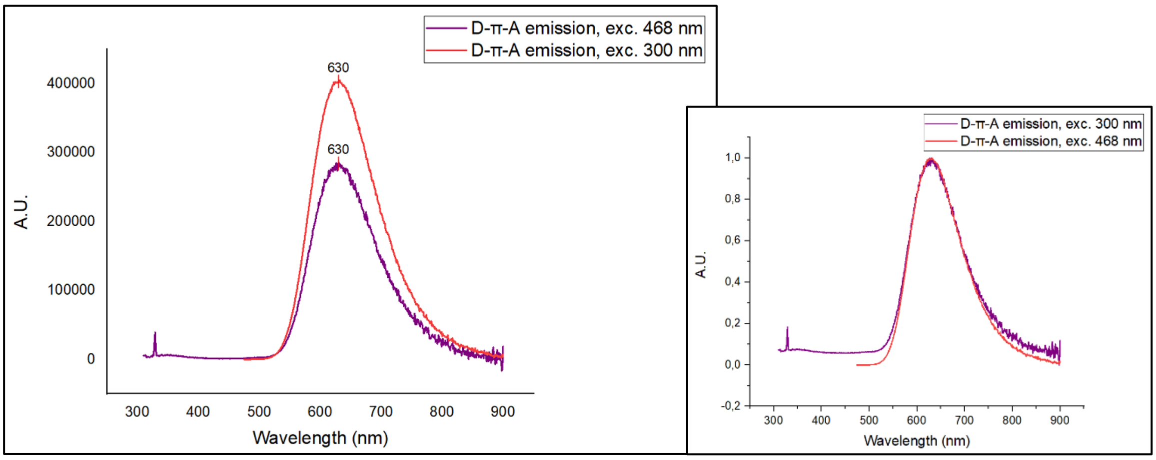

Figure 75: Emission spectra of D-π-A, exciting the dye at 468 nm (purple) and 300 nm (red). (inset) Normalization of the two spectra shows perfect stacking.

The fluorescence excitation spectrum confirms this hypothesis, since excitation at 630 nm provides the same trend of the absorption trace of D-π-A, stating that the excited state which emits at 630 nm is populated by both the two absorption bands located at 302 and 468 nm.

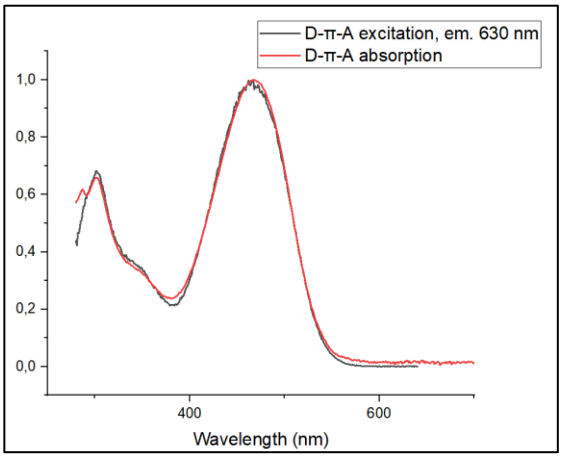

Figure 76: Excitation spectrum of D-π-A with emission at 630 nm (black), perfectly stackable to the absorption spectrum of the dye (red).

To ensure that the pristine MoS_2 does not contribute to the overall emission of MoS2@D-π-A_7, the pristine sample is excited at 468 nm, the wavelength at which the dye has the maximum of absorption, and it’s verified that it does not show any fluorescence.

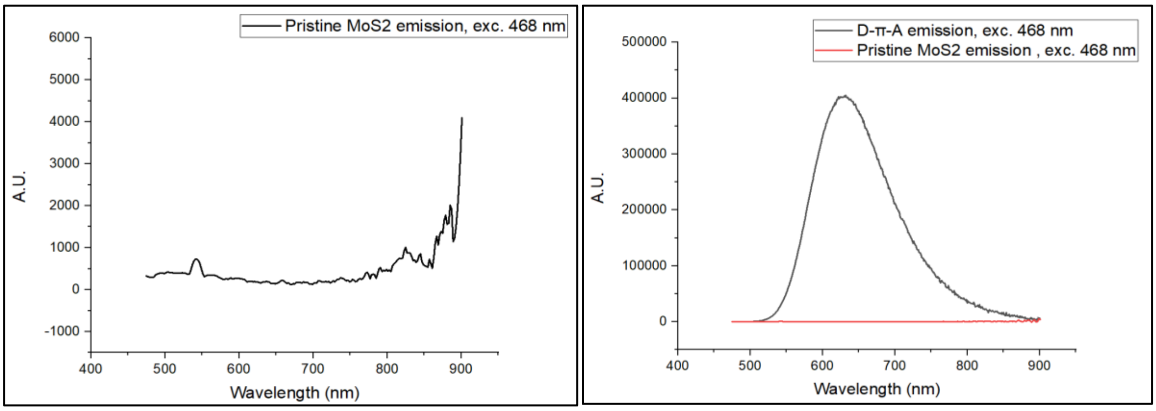

Figure 77: (left) Emission spectrum of pristine MoS_2, with excitation at the maximum of absorption of the dye, 468 nm. (right) Comparison of the emission intensity of pristine MoS_2 with the emission of the dye.

Moving the attention to MoS_2@D-π-A_7, an emissive signal obtained by excitation at 468 nm was observed, showing a comparable spectrum in shape to the dye, but slightly red shifted, as reported in *Figure 78*. MoS_2@D-π-A_7 shows a maximum at 637 nm, while the emission maximum of D-π-A is placed at 630 nm.

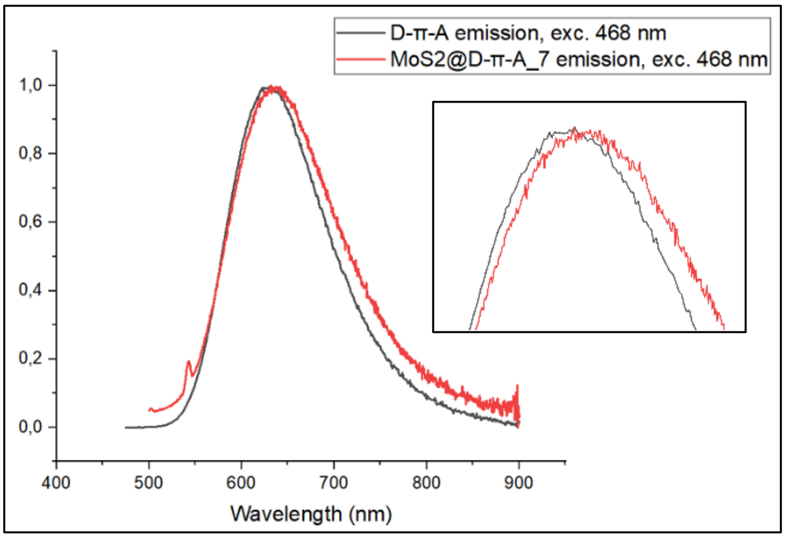

Figure 78: Emission spectrum of D-π-A (black) compared to the emission spectrum of MoS_2@D-π-A_7 (red), both recorded in THF, with excitation wavelength of 468 nm.

Recording the fluorescence excitation of MoS_2@D-π-A_7, with fixed emission at 650 nm, a stackable spectrum with the absorption of D-π-A is obtained, after a normalization. This confirms that the emissive entity in MoS_2@D-π-A_7 arises from D-π-A.

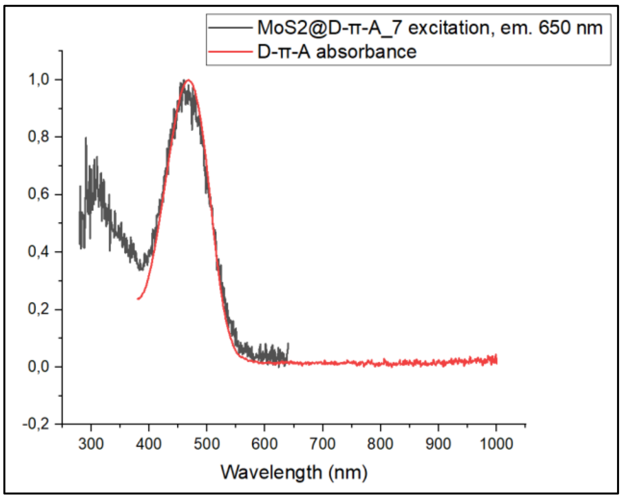

Figure 79: Fluorescence excitation of MoS_2@D-π-A_7 (black), compared to the absorption spectrum of D-π-A (red).

It is interesting to make a comparison between fluorescence emissions of pristine MoS_2, MoS_2@D-π-A_7 and D-π-A. The emission of the free thiol is several orders of magnitude greater than the hybrid material, but it's remarkable that from zero fluorescence of pristine MoS_2, a slight emission in MoS_2@D-π-A_7 is obtained, thanks to the functionalization with D-π-A.

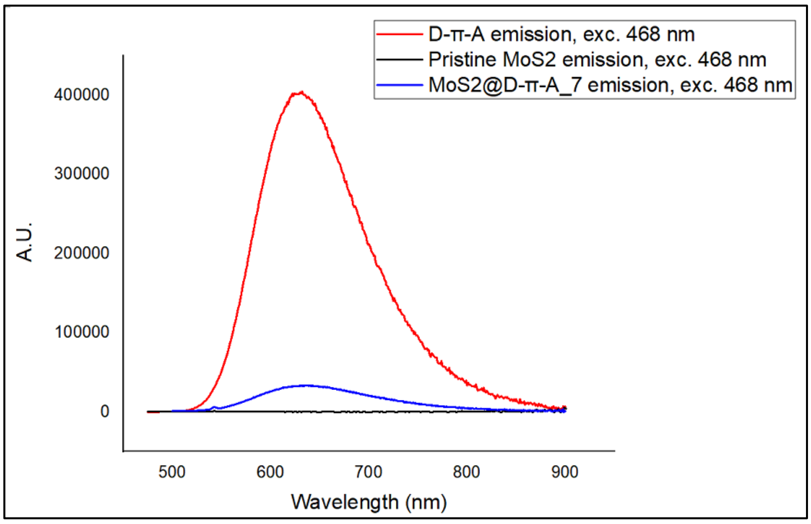

Figure 80: Emission spectra compared: MoS$_2$@D-π-A_7 (blue), D-π-A (red) and pristine MoS$_2$ (black).

It is noteworthy that the fluorescence profile can allow us to get rid of the scattering effect that is inevitably present in absorption. From the point of view of the emitting state it seems like no difference is detectable between MoS$_2$@D-π-A_7 and D-π-A, yet the decaying process seems to be slightly different.

Moving on to the lifetime measurements, MoS$_2$@D-π-A_7 decay results to be bi-exponential, while D-π-A shows a simple mono-exponential decay. The results are indeed encouraging: the free dye exhibits a fluorescence lifetime of 2.58 ns with a pre-exponential factor of 0.048, while MoS$_2$@D-π-A_7 shows two lifetimes, accounting for 0.88 ns and 2.54 ns, with pre-exponential factors of 0.027 and 0.024, respectively. Considering the average lifetime, mediated on the intensity of the signal, for the hybrid material a value of 2.07 ns is obtained. A sensible reduction in the lifetimes is hence appreciable in the functionalized nanomaterial compared to the free dye. This result would be in agreement with a partial quench of the sensitizer conjugated with the semiconductor due to energy transfer and/or electron transfer to the MoS$_2$. The longer deactivation time in MoS$_2$@D-π-A_7 is comparable with the one of D-π-A, therefore it points to the presence of dye molecules not covalently bonded to MoS$_2$ or anyway not electronically interacting with it. From the instrumental data elaboration, the faster decay of MoS$_2$@D-π-A_7 should account for about 28% of its emitting population, while the slower decay should account for 72%.

Table 5: Lifetime measurements for D-π-A and MoS$_2$@D-π-A_7 in THF.

D-π-A	τ = 2.57 ns B = 0.048	$\boldsymbol{k_r = Be^{-t/\tau}}$
MoS$_2$@D-π-A_7	τ_1 = 0.88 ns B = 0.027 28% τ_2 = 2.54 ns B = 0.024 72%	$k_r = B_1 e^{-t/\tau 1} + B_2 e^{-t/\tau 2}$

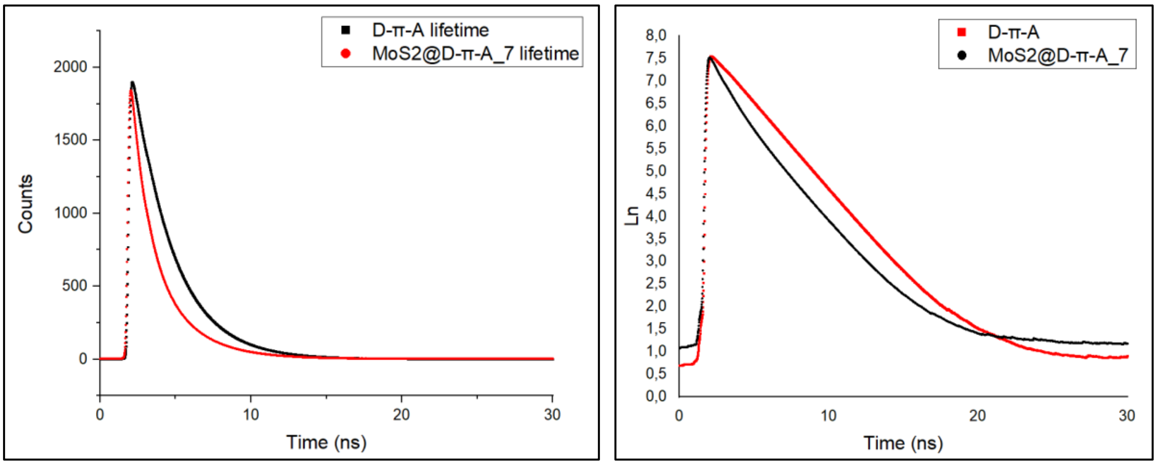

Figure 81: (left) Lifetime measurements of MoS2@D-π-A_7 and D-π-A. (right) Logarithm of the recorded decays.

Considering the recorded lifetimes and the red shift in emission two hypotheses can be drawn:

1. The functionalization of MoS_2 has been successful, and no free thiol is present in solution. This would translate in a non-massive functionalization of the material, and the dye molecules would be interacting with the molybdenum sulfide in different ways depending on whether they are physisorbed, chemisorbed or covalently bound. Another variable could be the physical place where functionalization takes place, that is usually along the edges or on the basal plane of MoS_2, as reported in the literature [71].

2. The functionalization of MoS_2 was successful, but free thiol is still present in solution. In this case all the recorded measurements would concern the contributions of both species, bonded and free dye, as it is not possible to selectively excite only one of them.

Due to the numerous washings made on the functionalized material and considering that no absorption attributable to the sensitizer was recorded in the supernatant, the second hypothesis seems to be less plausible. Nonetheless, the bonded dye seems to recognize MoS_2 as a trap on which excitation is dispersed, and it corresponds to the fraction with shorter lifetime. The other fraction, which is free in solution or bound to molybdenum disulfide in such a way that is still surrounded by the solvent, as on the edges, performs its de-excitation normally, regardless of the presence of MoS, maintaining its unaffected longer lifetime. In any case, we think that the direction of work is promising, since there are some functionalization and interaction evidences.

iii. MoS_2@$NaBH_4$@D-π-A_7

Moving on to MoS_2@$NaBH_4$@D-π-A_7, a similar course of analyses has been performed, recording the spectra in diluted solution prepared in THF. The emission spectrum of D-π-A is recorded and it's consistent with the previous measurements, with a broad band with a maximum at 628 nm, exciting it at 470 nm.

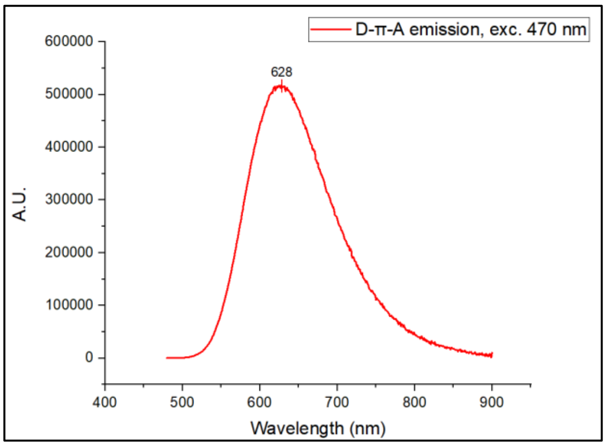

Figure 82: Emission spectrum of D-π-A, exciting the dye at its maximum of absorption.

As in the previous case, we verify that the pristine MoS_2 does not emit in the investigated spectral range, and the emission of MoS_2@$NaBH_4$@D-π-A_7 is reported in *Figure 81*.

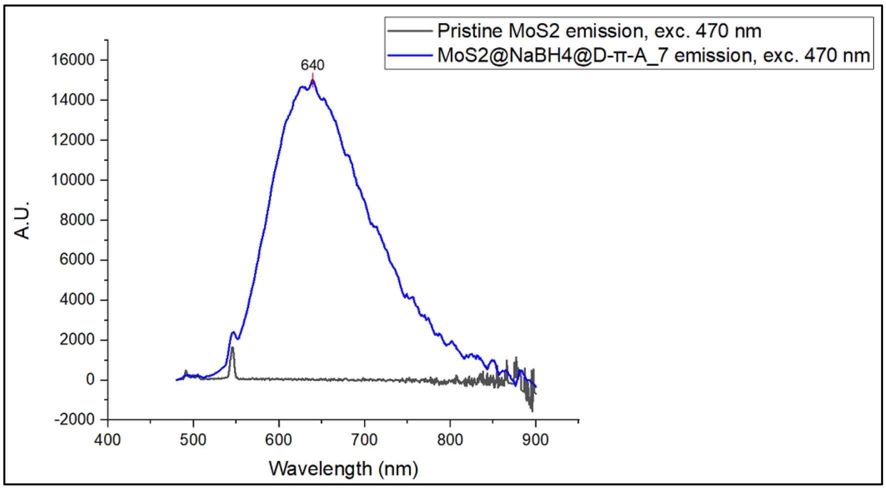

Figure 83: Emission spectrum of pristine MoS2 (black) and MoS_2@$NaBH_4$@D-π-A_7 (blue), exciting the samples at the maximum of absorption of the dye.

As it can be seen in *Figure 83*, the contribution of the pristine MoS_2 doesn't impact at all on the overall emission of the hybrid material. The maximum stands at about 640 nm, with a slight red shift compared to the emission of the free dye, as observed before. The peak at 550 nm consists of Raman modes and does not contain any information regarding emission properties.

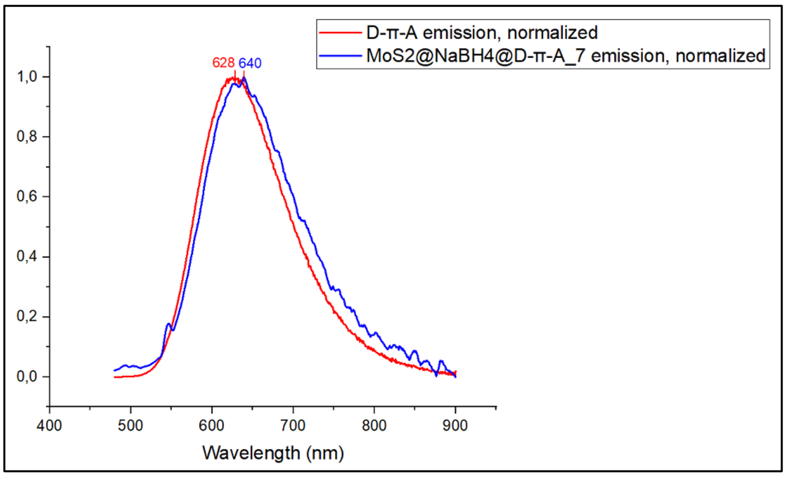

Figure 84: Emission spectra of D-π-A (red) and MoS_2@$NaBH_4$@D-π-A_7 (blue), normalized.

Once again, recording the fluorescence excitation of MoS_2@$NaBH_4$@D-π-A_7, with emission at 630 nm, a spectrum which is stackable to the absorption of D-π-A is obtained, once normalized. This confirms that the contribution to emission of MoS_2@$NaBH_4$@D-π-A_7 is represented by D-π-A.

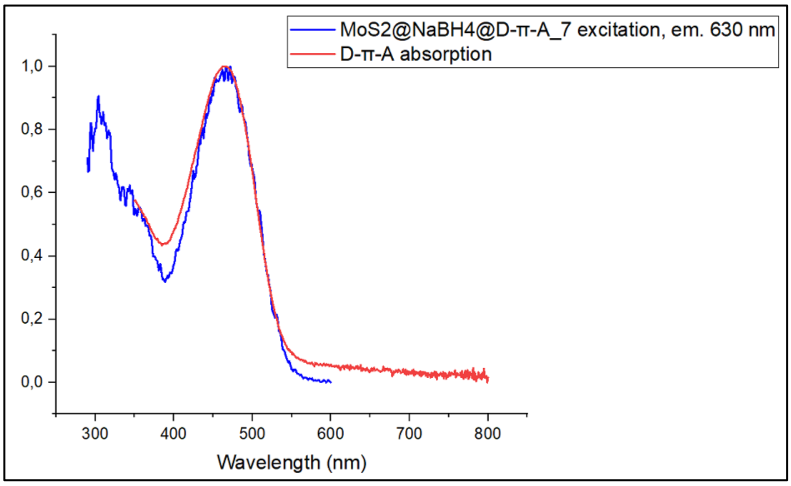

Figure 85: Excitation profile of MoS_2@$NaBH_4$@D-π-A_7 (blue), with emission at 630 nm, compared to the absorption profile of D-π-A (red), normalized.

The excited-state lifetime measurements of MoS2@$NaBH_4$@D-π-A_7 show a bi-exponential decay, while D-π-A shows a simple mono-exponential decay. These results are similar to MoS2@D-π-A_7: the free sensitizer exhibits a fluorescence lifetime of 2.47 ns, where MoS2@$NaBH_4$@D-π-A_7 shows two lifetimes, accounting for 0.94 ns and 2.29 ns. This feature suggests a good consistency with the previous measurements already discussed, proving that the functionalization procedure leads to reproducible data. In fact, a sensible reduction in decaying times is hence appreciable in the functionalized nanomaterial compared to the free dye. As for MoS2@D-π-A_7, this result would agree with a partial quench of the sensitizer due to energy transfer and/or electron transfer to the semiconductor. The second deactivation time in the functionalized material is comparable with the one of free dye, therefore it points out again the presence of dye molecules not covalently bonded to MoS_2 or that are interacting with the semiconductor in a different way. Anyway, they seem to perceive a different environment compared to the free one.

Table 6: Lifetime measurements for D-π-A and MoS_2@$NaBH_4$@D-π-A_7 in THF.

D-π-A	τ_1 = 2.47 ns B = 0.009	$\boldsymbol{k_r = Be^{-t/\tau}}$
MoS_2@$NaBH_4$@D-π-A_7	τ_1 = 0.94 ns B_1 = 0.0004 τ_2 = 2.29 ns B_2 = 0.0006	$k_r = B_1e^{-t/\tau1} + B_2e^{-t/\tau2}$

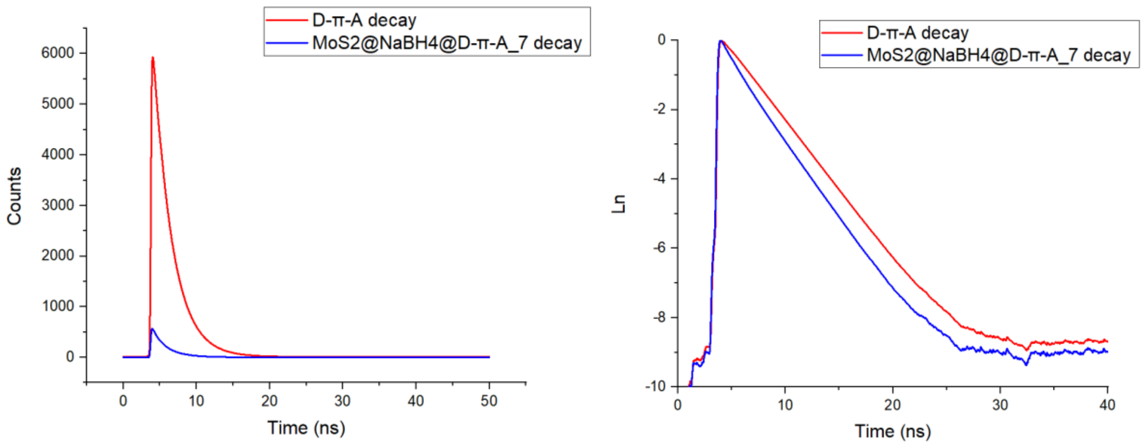

Figure 86: (left) Lifetime measurements of MoS_2@$NaBH_4$@D-π-A_7 and D-π-A. (right) Logarithm of the recorded decays.

To evaluate if the reducing treatment actually provided more sulfur vacancies and hence allowed a more efficient functionalization, quantitative measurements would be required, such as TGA or XPS. The results obtained for MoS_2@$NaBH_4$@D-π-A_7 are similar to and consistent with the results that MoS_2@D-π-A_7 provided. No difference in the emissive properties have been detected, and the lifetime measurements supplied about the same values for what concerns decay times.

iv. **MoS_2@D-A-π-A_7**

For MoS_2@D-A-π-A_7 the same set of measurements in spectroscopy grade THF has been recorded, using solutions which present an absorbance at the maximum less than 0.1.

The solution of sensitizer was excited at 500 nm to record its emission profile, which is reported in *Figure 87*. While the absorption maximum stands at 499 nm, the emission peaks at 710 nm, showing a Stokes shift even larger than the first sensitizer, accounting for more than 200 nm. Such a wide Stokes shift is interesting. A large value, such as in this case, could represent an important distortion of the excited state, which could be proof of the ICT nature of the emitting state. It's not yet clear how from the first excited state S_1 the molecule could reach the ICT, placed at lower energies, but proposed theories involve a structural relaxation of the excited configuration of the dye [106].

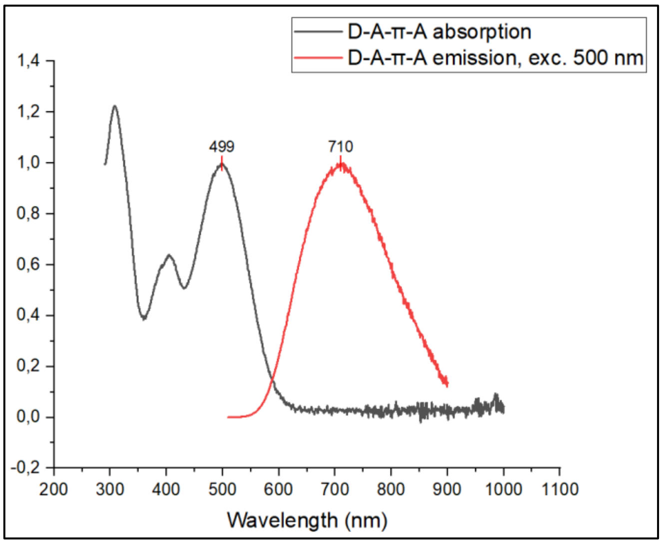

Figure 87: Absorption (black) and emission spectra (red) of D-A-π-A in THF.

Recording the fluorescence profile of D-A-π-A and comparing it with its absorption, it seems that the emission of the dye is mainly due to the absorption of two peaks, at 308 nm and 499 nm, with a small contribution of the absorption at 391 nm, while the band at 405 nm seems to not contribute to the fluorescence. It is interesting to see, however, how the excitation results slightly shifted from the absorption, in particular a red shift in the shorter wavelength region and blue shift in the long wavelength region of the spectrum has been observed.

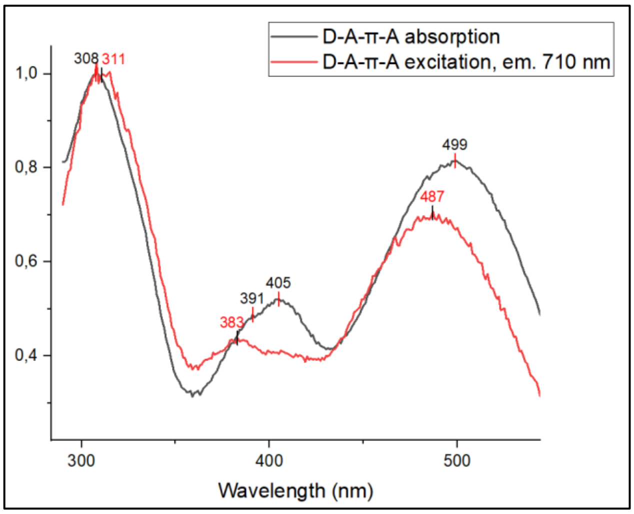

Figure 88: Absorption (black) and fluorescence excitation (red) spectra of D-A-π-A.

Subsequently, the emission of MoS_2@D-A-π-A_7 was recorded, exciting it at the same wavelength used for the free dye, 500 nm. As it can be seen from the figure below, the shape of the emission resembles the one of the dye alone, while the maximum is slightly red shifted. D-A-π-A in fact shows a maximum at 710 nm, while the hybrid material emits at 720 nm. As experienced before, this slight shift could be an indicator of some interaction being happening between the sensitizer and the molybdenum disulfide.

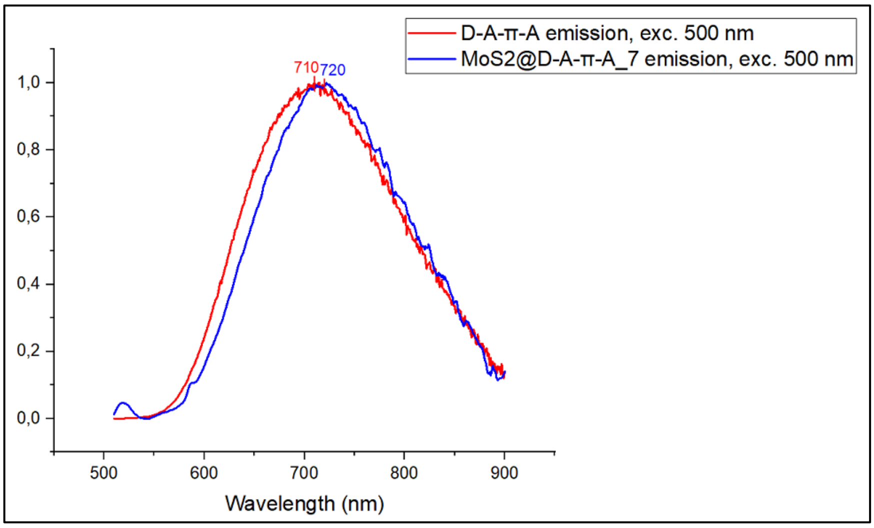

Figure 89: Emission spectra of D-A-π-A (red) and MoS_2@D-A-π-A_7 (blue), with excitation at 500 nm.

To try and shine light on this aspect, the fluorescence profile of MoS_2@D-A-π-A_7 is recorded and compared with the excitation and the absorption of the sensitizer alone.

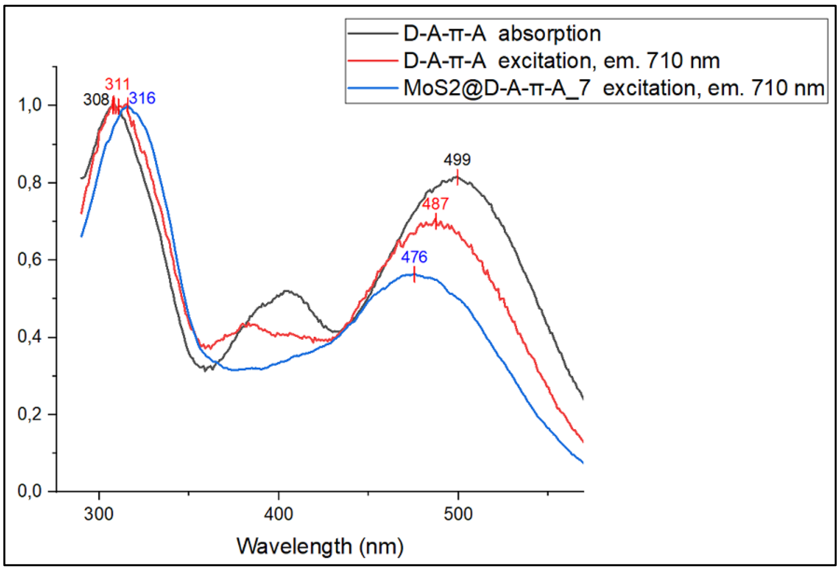

Figure 90: Absorption spectrum of D-A-π-A (black), compared to the excitation of the dye (red) at 710 nm and the excitation of MoS_2@D-A-π-A_7 (blue) at 710 nm.

A remarkable shift of the maxima among the absorption spectrum of the dye, the excitation of the dye at the maximum of emission, and the excitation of the hybrid at the same wavelength was observed. The bands at longer wavelengths move from 499 nm in absorption for the dye, to 476 nm for the excitation profile in the hybrid. In an opposite fashion, the band at 308 nm present in the sensitizer absorption spectrum blue shifts to 316 nm for the excitation of the hybrid. Another interesting feature is the disappearance of any contribution around 400 nm in the fluorescence profile of the hybrid, while a small band was present in the excitation spectrum of the sensitizer alone. All these particularities could be indicators of the fact that the organic species bonded to the semiconductor behaves differently than the same molecule in a free, non-constraining environment. Its absorption modes and characteristics seem to be modified upon linkage to the nanostructure, proving that an electronic communication is, in fact, happening.

To be sure that any emitting feature observed in the hybrid material is only due to the presence of the sensitizer, an emission spectrum of the pristine molybdenum disulfide was collected, and it's clear that no fluorescence is due to the MoS_2.

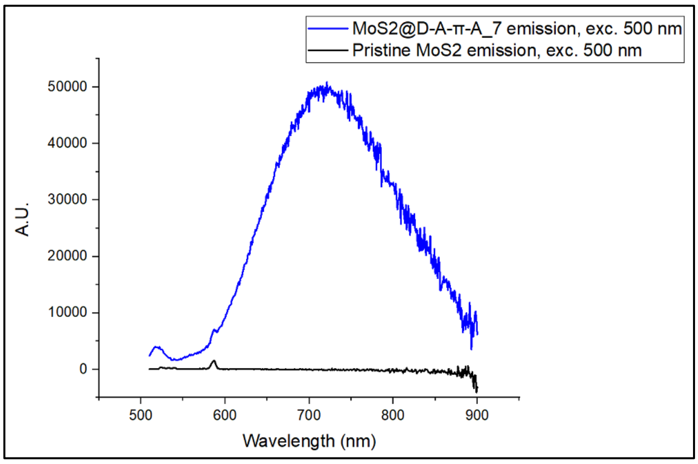

Figure 91: Emission of the pristine molybdenum disulfide (black) and MoS_2@D-A-π-A_7 (blue).

For what concerns lifetime measurements, they were performed exciting the sensitizer and the functionalized material at 400 nm. The presence of the secondary acceptor in the dye has an influence on the deactivation paths available. In fact, differently from D-π-A, in D-A-π-A a bi-exponential decay is observed, with two correspondent lifetimes of 1.62 ns and a longer one of 6.10 ns. The longer lifetimes of D-A-π-A compared with the sensitizer with no additional acceptor group is consistent with what expected by adding a benzothiadiazole unit in the molecular structure [90]. Moving the attention to MoS2@D-A-π-A_7, a bi-exponential decay is observed also, with lifetimes of 1.00 ns and 4.17 ns. A remarkable reduction in lifetime is hence appreciable in the hybrid material compared to the free sensitizer. Since the exponential order is the same between the two samples, it seems that the same types of dye populations are present in MoS2@D-A-π-A_7 and D-A-π-A. This is different from what was highlighted for D-π-A, where the functionalized material was showing one decaying process more than the dye alone. This could suggest that in the case of D-A-π-A the sensitizer is bonded to the semiconductor in only one mode, and this allows it to deactivate with the same number of decaying processes whether it's bonded to MoS_2 or free in solution. Moreover, the fact that the number of decaying processes is the same in the two samples, together with the presence of shorter lifetimes in the hybrid material, could be a proof that the bonded sensitizer finds a different, non-radiative, quenching process to decay, thanks to its interaction with the molybdenum disulfide. By looking at the graphs of the logarithm of the decay in function of time, it is evident the bi-exponential behavior of the two species and the difference with the simple D-π-A dye and its corresponding hybrid material.

Table 7: Lifetime measurements for D-A-π-A and MoS_2@D-A-π-A_7 in THF.

D-A-π-A	τ_1 = 1.62 ns τ_2 = 6.10 ns	B_1 = 0.009 B_2 = 0.001	$\boldsymbol{k_r = B_1 e^{-t/\tau 1} + B_2 e^{-t/\tau 2}}$
MoS_2@D-A-π-A_7	τ_1 = 1.00 ns τ_2 = 4.17 ns	B_1 = 0.002 B_2 = 0.0004	$k_r = B_1 e^{-t/\tau 1} + B_2 e^{-t/\tau 2}$

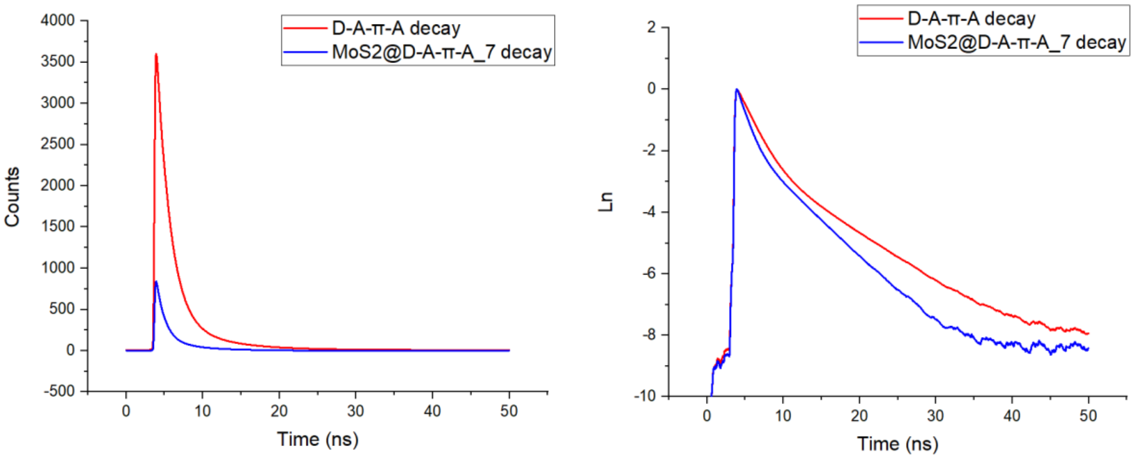

Figure 92: (left) Lifetime measurements of MoS_2@D-A-π-A_7 and D-A-π-A. (right) Logarithm of the recorded decays.

V. MoS_2@D-π-A_7 in DMF

To evaluate the effect of the solvent, another set of measurements was performed with MoS_2@D-π-A_7 and D-π-A in DMF. The emission of the dye falls at 545 nm, while the absorption at 405 nm, with a Stokes shift of about 140 nm, while in THF the fluorescence was standing at 630 nm and the absorption at 468 nm. The second maximum that was seen in THF at about 300 nm, now falls into the cutoff zone of the solvent and it is not possible to investigate it.

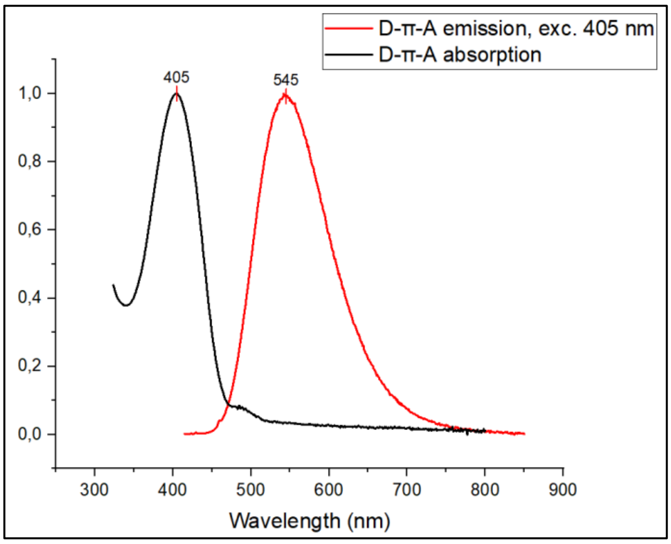

Figure 93: Absorption (black) and emission (red) spectra of D-π-A in DMF in DMF.

For what concerns the pristine MoS_2, the sample was excited in the spectral area of interest for the thiol, at 405 nm, and unlike in THF, there is a non-zero fluorescence contribution from MoS_2. It is possible that the DMF allows a better exfoliation of the MoS_2 flakes. Consequently, more thin layers stacks could be suspended, and as reported in the literature, few or single layers of MoS_2 show fluorescence properties [107]. Even if the contribution is small, the pristine material would contribute to the total fluorescence of the dye-functionalized system, and it will be taken into consideration in the lifetime contribution analysis.

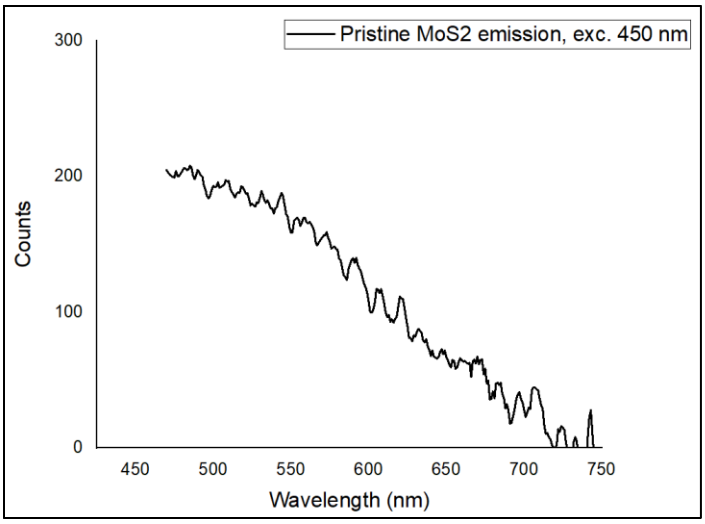

Figure 94: Emission of pristine MoS_2 in DMF.

Moving on to MoS_2@D-π-A_7, when one excites it at 405 nm, maximum of absorption of the sensitizer in DMF, the emissive signal of the dye is obtained, with a slight red shift. As already seen, D-π-A has the maximum of emission placed at 545 nm, while MoS_2@D-π-A_7's maximum stands at about 550 nm. Moreover, the emission of MoS_2@D-π-A_7 changes somewhat in shape, broadening to longer wavelengths. Peaks between 400 and 700 nm are Raman modes, not interesting for the aim of this study.

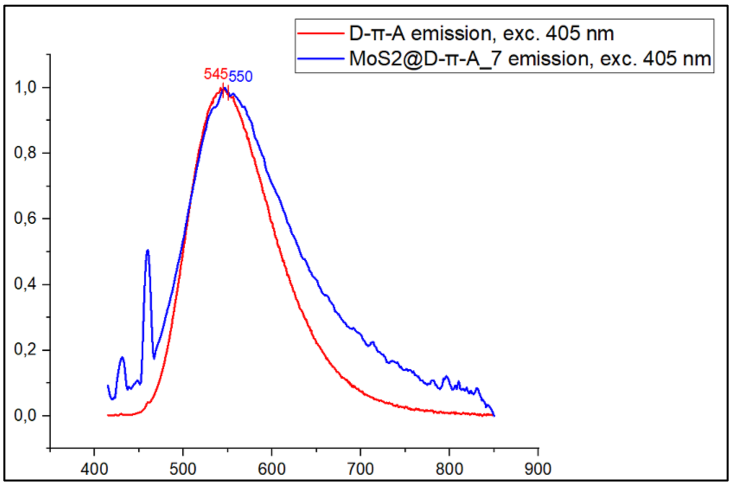

Figure 95: Emission spectra of D-π-A (red) and MoS_2@D-π-A_7 (blue) in DMF, with excitation at maximum of absorption of the dye.

Interesting is to compare the emission intensities of D-π-A, MoS_2@D-π-A_7 and pristine MoS_2. Even if emitting, the contribution of the pristine MoS_2 to the overall fluorescence is practically negligible.

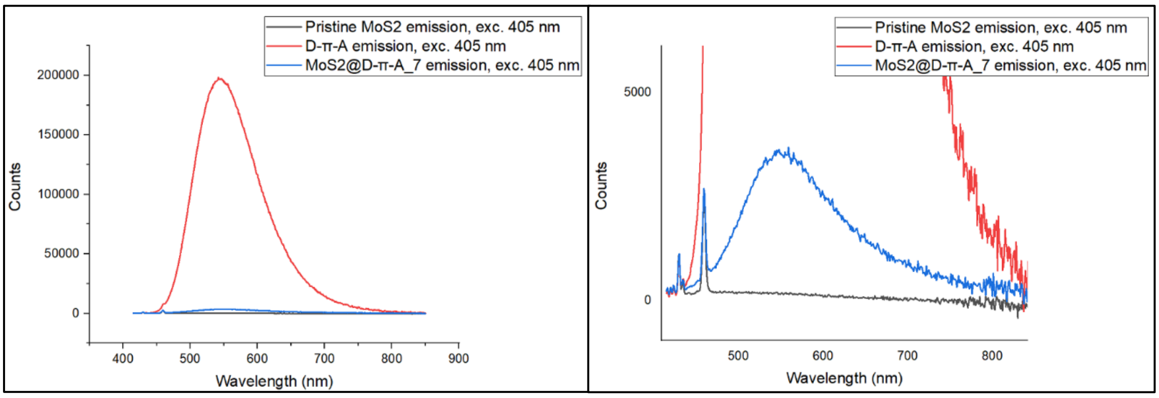

Figure 96: Comparison between the emission intensities of pristine MoS_2 (black), MoS_2@D-π-A_7 (blue) and D-π-A (red) in DMF.

By recording the fluorescence profile of MoS_2@D-π-A_7 at 550 nm, a spectrum which is stackable to the absorption of the dye is obtained, indicating that the emissive species in the hybrid is constituted by the sensitizer.

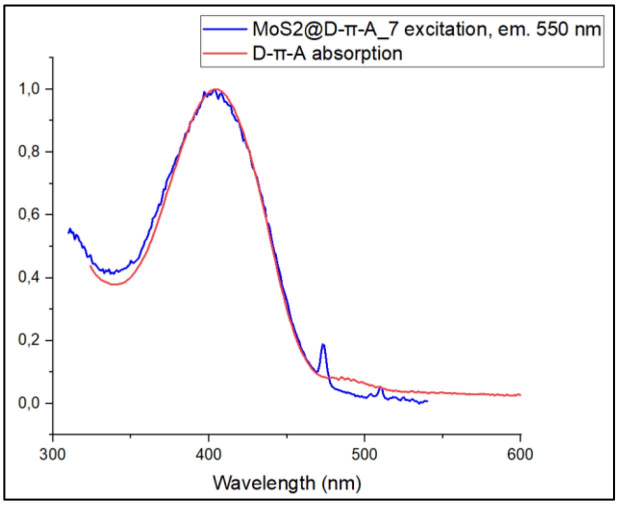

Figure 97: The absorption of D-π-A (red) results perfectly stackable to the fluorescence excitation of MoS_2@D-π-A_7 (blue) in DMF.

Lifetimes measurements have been performed on the samples under examination. In DMF, MoS_2@D-π-A_7 shows a tri-exponential decay, while D-π-A presents a bi-exponential decay. For MoS_2@D-π-A_7, the obtained lifetimes are 0.45 ns, 1.40 ns, and 3.84 ns, with pre-exponential coefficients of 0.16, 0.07 and 0.01, respectively. This would indicate that two faster decaying processes are present with a greater contribution, and a slower one with a much lower impact. Regarding D-π-A, 0.55 ns and 1.61 ns as lifetimes are obtained, with pre-exponential coefficients of 0.20 and 0.03, respectively. We also evaluated the decay of pristine MoS_2, verifying a bi-exponential decay, with lifetimes of 0.96 ns and 5.08 ns, and pre-exponential coefficients of 0.006 and 0.002, respectively.

Table 8: Lifetime measurements for D-π-A, MoS_2@D-π-A_7 and pristine MoS_2 in DMF.

D-π-A	τ_1 = 0.55 ns τ_2 = 1.61 ns	B_1 = 0.20 B_2 = 0.03	$\boldsymbol{k_r = B_1 e^{-t/\tau 1} + B_2 e^{-t/\tau 2}}$
MoS_2@D-π-A_7	τ_1 = 0.45 ns τ_2 = 1.40 ns τ_3 = 3.84 ns	B_1 = 0.16 B_2 = 0.07 B_3 = 0.01	$k_r = B_1 e^{-t/\tau 1} + B_2 e^{-t/\tau 2} + B_2 e^{-t/\tau 3}$
Pristine MoS_2	τ_1 = 1.00 ns τ_2 = 4.17 ns	B_1 = 0.006 B_2 = 0.002	$k_r = B_1 e^{-t/\tau 1} + B_2 e^{-t/\tau 2}$

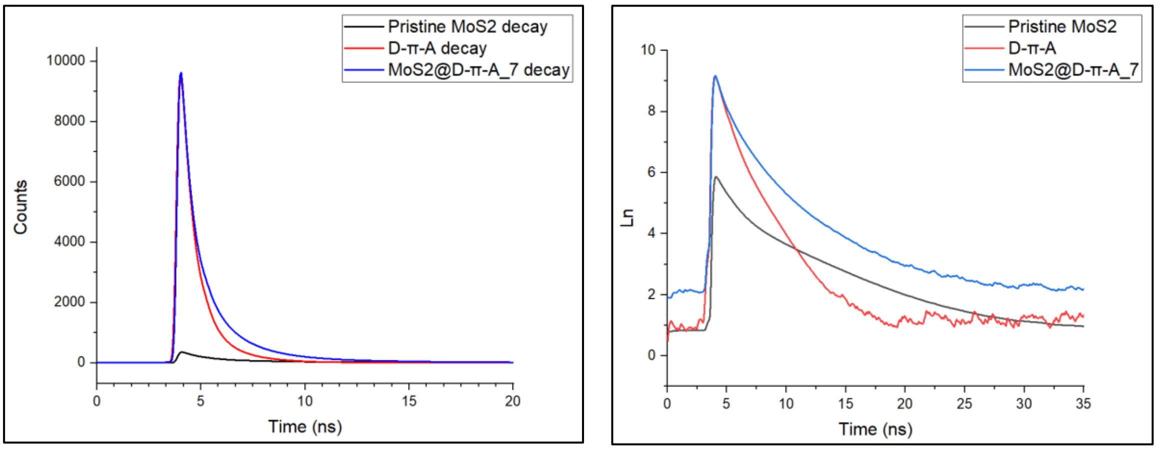

Figure 98: (left) Lifetime measurements of pristine MoS_2, MoS_2@D-π-A_7 and D-π-A in DMF. (right) Logarithm of the recorded decays.

In the following table a summary of the emission maxima of all the analyzed samples is reported.

Table 9: Summary of the emission maxima observed in the analyzed samples, in nanometers.

D-π-A in THF	630	
MoS_2@D-π-A_1 in THF	635	685
MoS_2@D-π-A_7 in THF	637	
MoS_2@$NaBH_4$@D-π-A_7 in THF	640	
D-A-π-A in THF	710	
MoS_2@D-A-π-A_7 in THF	720	
D-π-A in DMF	545	
MoS_2@D-π-A_7 in DMF	550	

From these results some conclusions can be drawn. It's plausible that DMF is able to promote a higher grade of exfoliation of the molybdenum disulfide, also in its pristine component. This would explain the observed fluorescence of the pristine MoS_2 in DMF, which was always not appreciable in THF. Moreover, two decaying processes, with a shorter lifetime of 0.96 ns and a longer one, of 5.08 ns have been identified. Since MoS_2 and D-π-A present two radiative decays each, for MoS_2@D-π-A_7 a decay composed by four contributions would be expected. The values τ are generated by a deconvolution process which fits the experimental data, and since τ_1 and τ_2 are in good agreement between the dye and the hybrid material, τ_3 could stem from an average of two different decays with similar lifetimes. The deactivations that characterize the MoS_2 could produce, if mediated by the weight of their contributions, the value of τ_3 in the hybrid, which is consistent with the hypothesis of having one of the three lifetimes of MoS_2@D-π-A_7 related to the exfoliated component of pristine MoS_2 present (i.e., 3.84 ns) and the other two to the functionalized component. Compared to THF, in DMF the lifetimes of D-π-A and MoS_2@D-π-A_7 change very little. In THF, D-π-A was showing a lifetime of 2.57 ns, while for MoS_2@D-π-A_7 the value drops to 0.88 ns (great variation). In DMF, the results were 0.55 and 1.61 ns for D-π-A and 0.45 and 1.40 ns for MoS_2@D-π-A_7 (small variation). It is possible that changing the solvent polarity results in a condition that no longer meets the thermodynamic requirement which allows the switching of excitation from the sensitizer to the molybdenum sulfide. In fact, in DMF a fast process in the hybrid compatible with a charge transfer or energy transfer is missing while it was present in the experiments carried out in THF. To shine light on this aspect and verify if changing the solvent actually turns in a missing thermodynamic requirement, more accurate measurements would be required. In particular, cyclic voltammetry or DFT calculations in which one changes the solvent under analysis would be necessary to support and verify these assumptions.

3. Conclusions

In this work, two sensitizers have been synthesized starting from commercially available precursors. Well known reactions have been employed, such as Miyaura borylation, Suzuki cross-coupling, Knoevenagel condensation and Steglich esterification, to yield two dyes terminating with a protected thiol moiety. The obtained dyes have been characterized through UV-Visible absorption and fluorescence spectroscopy. Both the sensitizers have been used to functionalize samples of chemically exfoliated molybdenum disulfide. Moreover, a reducing process with sodium borohydride was tested on a pristine molybdenum disulfide sample prior to functionalization, in an attempt to increase the density of sulfur vacancies on its surface to promote a more efficient grafting of the sensitizer. The obtained hybrid materials have been characterized by means of thermogravimetry, Raman, UV-Visible and fluorescence spectroscopy. The TGA highlighted the actual presence of an organic component in the hybrid, decomposing between 300 and 500°C, compared to the pristine material. In addition, the amount of organic matter grafted onto the MoS_2 seemed to increase with increasing functionalization times, from 1 to 7 days. If, in fact, the residue at 1000°C for the 1-day functionalization amounted to 80% of the initial weight, while for the 7-days functionalization it accounted for about 74%, indicating that more temperature-sensitive component was present. The Raman spectroscopy allowed to identify the A_{1g} and the E^1_{2g} modes of MoS_2 and to appreciate their slight shifts caused by modifications of the structure of the semiconductor, due to thiol functionalization or chemical reduction with sodium borohydride. It also allowed to identify peaks typically attributed to organic molecules, confirming the presence of the dyes on the surface of the hybrid material. A rough interpretation of the modes shifts hinted to a mild increase of sulfur vacancies after reducing treatment, in the order of 1%. In the future, if introduction of large amounts of sulfur vacancies will be necessary, it could be useful trying more aggressive approaches, such as stronger reducing agents or physical attacks like plasma or electron beam irradiation. For what concerns absorption and emission spectroscopies, they have provided some interesting insights about the possible electronic communication between the two components of the hybrid materials prepared. In absence of emissive contribution from the pristine MoS_2, the hybrids demonstrated a fluorescence emission ascribed to the organic sensitizer. The emission in the functionalized materials was slightly red shifted compared to the emission of the free thiols: this could be a hint that the sensitizer interacts with the nanostructure and that the interaction affects the excited state of the dye. The presence of a wide Stokes shift in the free sensitizers is not in contrast with the plausible presence of an ICT state which could communicate with the nanostructure once the dye is grafted onto the semiconductor.

To shine light on these aspects, accurate electrochemical measurements, namely cyclic voltammetry, on the dyes and the hybrids would be necessary, in order to properly understand the energy levels and states involved in the transitions.

Moreover, in the future it could be useful to estimate the amount of organic sensitizer grafted onto the surface of MoS_2, possibly through XPS measurements.

As for the progress of the study, thin films on conductive glass will be prepared with the hybrid materials, by means of drop casting or spray coating. These films will be tested for their catalytic properties and efficiencies and compared to the pristine exfoliated molybdenum disulfide.

4. Experimental section

4.1. Solvents and reagents

All solvents and reagents were used as purchased, without any further purification.

Solvent	Molecular Weight [g · mol^{-1}]	Density [g·mL^{-1}]	b.p. [°C]	Source
1.4-dioxane (anhydrous)	88.11	1.034	65-67	Sigma-Aldrich
Acetonitrile	41.05	0.786	82.0	Sigma-Aldrich
Dichloromethane	84.93	1.33	39.6	Sigma-Aldrich
Methanol	32.04	0.792	64.7	Sigma-Aldrich
Tetrahydrofuran	72.11	0.890	66.0	Sigma-Aldrich
Tetrahydrofuran (anhydrous)	72.11	0.889	65-67	Sigma-Aldrich
Toluene	92.14	0.867	110.6	Sigma-Aldrich
Water	18.02	1.00	100.0	Sigma-Aldrich

Reagent	Molecular Weight [g · mol^{-1}]	Density [g·mL^{-1}]	Source
4-bromotriphenylamine	324.22	/	Sigma-Aldrich
[1,1'-Bis(diphenylphosphino)ferrocene] dichloro palladium(II) [Pd(dppf)Cl$_2$]	731.71	/	Sigma-Aldrich
1-Ethyl-3-(3-dimethylaminopropyl) carbodiimide-HCl	191.70	/	Sigma-Aldrich
2-mercaptoethanol	78.13	1.11	Sigma-Aldrich
4,7-Dibromo-2,1,3-benzothiadiazole	293.96	/	Sigma-Aldrich
4-dimethylaminopyridine	122.17	/	Sigma-Aldrich
5-Formyl-2-thiopheneboronic acid	155.97	/	Sigma-Aldrich
Bis(pinacolato)diboron	253.94	/	Sigma-Aldrich
Cyanoacetic acid	85.06	/	Sigma-Aldrich
Molybdenum disulfide	160.07	/	Sigma-Aldrich
Piperidine	85.15	0.862	Sigma-Aldrich
Potassium acetate	98.15	/	Sigma-Aldrich
Potassium carbonate	138.21	/	Sigma-Aldrich
Sodium borohydride	37.83	/	Sigma-Aldrich
Tetrakis(triphenylphosphine) palladium(0) [Pd(PPh$_3$)$_4$]	1155.56	/	Sigma-Aldrich
Trifluoroacetic acid	114.02	1.49	Sigma-Aldrich
Triisoproprylsilane	158.36	0.773	Sigma-Aldrich

4.2. Instruments and characterizations

4.2.1. Thin Layer Chromatography (TLC)

TLC analyses were performed on Merck TLC Silica Gel plates 60 F254 (0.2 mm thick silica gel supported on aluminum sheets). Fluorescent spots were revealed using a UV lamp (254 nm and 365 nm). Non-visible and non-fluorescent spots were revealed using potassium permanganate or phosphomolybdic acid.

4.2.2. Nuclear magnetic resonance (NMR)

Nuclear magnetic resonance spectra were acquired with a Bruker AC-300 spectrometer, operating at 300 MHz for ^{1}H, or a Bruker AC-200, operating at 200 MHz for ^{1}H. ^{13}C spectra were acquired using a Bruker AC-400 instrument, operating at 400 MHz for ^{1}H and at 100 MHz for ^{13}C. All collected spectra were analyzed with the software MestReNova 6.0.2.

4.2.3. Mass spectroscopy (ESI-MS)

Mass spectra were obtained using a MSD SL Trap Mass Spectrometer by Agilent Technologies. The ion source was electrospray ionization. The samples were diluted in acetonitrile HPLC and 20 µL of solution were injected in acid acetonitrile. Flux rate was 0.05 mL/min, nebulizer was set at 20 psi, dry gas flux at 5 L/min, temperature set at 325 °C).

4.2.4. Bath sonication

When needed, or routinely to dissolve and disperse solids in solution, bath sonication was performed with a Bandelin SONOREX ultrasonic bath filled with deionized water.

4.2.5. Centrifugation

Centrifugation was performed using a ThermoScientific SL16 centrifuge.
50 mL and 12 mL plastic Falcon tubes were used.

4.2.6. Thermogravimetric analysis (TGA)

Thermogravimetric measurements were carried out on a TGA Q5000IR (TA instruments). Analyses were performed in nitrogen atmosphere, setting and isotherm at 100°C for 10 minutes to reach a constant weight, evaporating environmental water and residual solvents, followed by a 10°C/min ramp to 1000°C and a second isotherm at the final temperature in air for 5 minutes, to allow the instrument to clean the pan from any solid residue. Obtained thermograms were processed using the TRIOS software, provided by TA instruments.

4.2.7. UV-Vis spectroscopy

UV-Vis spectra were acquired between 250 nm and 800 nm using a Varian Cary 50 spectrometer at room temperature, with a 1.0 nm interval, scan speed of 600 nm/min and spectral bandwidth of 1.0 nm. Quartz cuvettes with 1 cm optical path were employed for all measurements. Obtained spectra were processed using Origin 2019b.

4.2.8. Fluorescence spectroscopy and lifetimes

Fluorescence tests were performed employing an Edinburgh Instruments FLS1000 photoluminescence spectrometer. The detectors utilized were the PMT850 for fast responses and the PMT980 for longer wavelength spectra. All measurements were performed on solutions having an absorbance value <0.1, assuring in this way a linearity between the obtained results. For each measurement, the Instrument Response Function (IRF) was measured using a 30wt. % suspension of silica in water (Ludox). Obtained spectra were processed using Origin 2019b.

4.2.9. Transmission electron microscopy (TEM)

TEM images were acquired with a Tecnai G2 (FEI) microscope operating at 100 kV. A small amount of solid sample was dispersed in tetrahydrofuran and a drop of suspension was deposited on a holey carbon paper. The solvent was evaporated, and the sample analyzed at the instrument.

4.2.10. Raman spectroscopy

Raman spectra were obtained with a microspectrophotometer Invia Renishaw, with 50x optics and a low power laser source (Physics 150m, Helium-Neon 532 nm). Samples were prepared either by drop casting on slides (Corning) and evaporating the solvent or by direct deposition of the solid product on the glass sheet.
Obtained spectra were processed using Origin 2019b.

4.3. Synthesis and characterizations

4.3.1. Synthesis of 5-(4-(diphenylamino)phenyl)thiophene-2-carbaldehyde (TPA-1) [reference: [74], [75]]

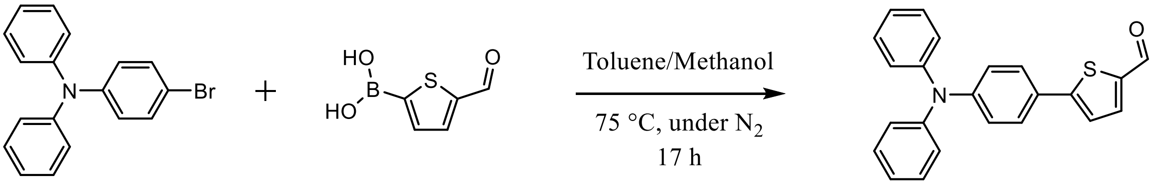

	Equivalents [eq]	**Molecular Weight** [g · mol^{-1}]	**Mass** [mg]	**Volume** [mL]	**Moles** [mmol]
4-bromotriphenylamine	1.0	324.22	1732	/	5.34
5-Formyl-2-thiopheneboronic acid	1.2	155.97	1000	/	6.41
Pd(dppf)Cl$_2$	0.10	731.71	391	/	0.534
Potassium carbonate	5	138.21	3692	/	26.7
Toluene (solvent)	/	92.14	/	100.0	/
Methanol (solvent)	/	32.04	/	100.0	/

A mixture of toluene and methanol (200 mL, 1/1) was degassed under a flux of nitrogen. 4-bromotriphenylamine (1732 mg, 5.34 mmol), 5-Formyl-2-thiopheneboronic acid (1000 mg, 6.41 mmol), potassium carbonate as base (3692 mg, 26.7 mmol) and Pd(dppf)Cl$_2$ (391 mg, 0.534 mmol) were added to the solution, which was heated to 75 °C and left under nitrogen and magnetic stirring for 17 hours. The reaction mixture was checked by TLC (hexane/dichloromethane : 2/3). Following the disappearance of 4-bromotriphenylamine, the solvent was eliminated by rotary evaporation and the solid obtained was dissolved in dichloromethane. Three aqueous washings with ammonium chloride were performed to remove palladium residues, after which the organic phase was collected, dried over anhydrous sodium sulfate, filtered, and concentrated under reduced pressure [108]. The crude product was purified by flash chromatography on silica gel using hexane/ethyl acetate (5/1) as eluent. The head and tail fractions of the product, presenting some contamination, were re-crystallized from ethyl acetate/hexane and the crystals thus obtained were filtered and collected.

***Yield**:* 64% (1216 mg)

***^{1}H NMR** (300 MHz, d6-DMSO, δ, ppm):* 9.87 (s, 1H), 8.00 (d, J = 3.0 Hz, 1H), 7.69 (d, J = 6.0 Hz, 2H), 7.60 (d, J = 6.0 Hz, 1H), 7.38-7.33 (m, 4H), 7.15-7.08 (m, 6H), 6.97 (d, J = 9.0 Hz, 2H)

4.3.2. Synthesis of 5-[4-(diphenylamino)phenyl]-thiophene-2-cyanoacrylic acid (TPA-2) [reference: [76]]

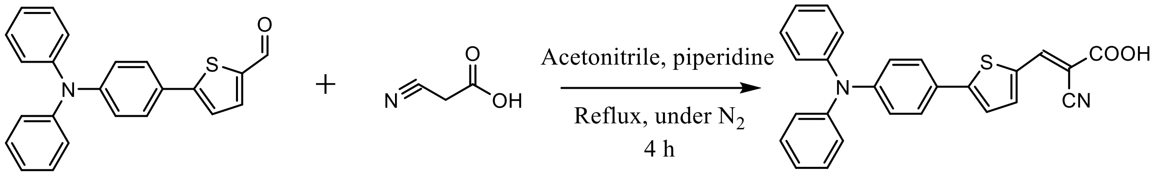

	Equivalents [eq]	**Molecular Weight** [g · mol^{-1}]	**Mass** [mg]	**Volume** [mL]	**Moles** [mmol]
TPA-1	1.0	355.46	1216	/	3.42
Piperidine	6.0	85.15	1748	2.03	20.53
Cyanoacetic acid	5.0	85.06	1454	/	17.10
Acetonitrile (solvent)	/	41.05	/	200.0	/

TPA-1 (1216 mg, 3.42 mmol), piperidine (2.03 mL, 20.53 mmol) and cyanoacetic acid (1454 mg, 17.10 mmol) were dissolved in 200.0 mL of acetonitrile. The solution was brought to reflux under nitrogen flux and the reaction proceeded for 4 hours. Every hour the reaction mixture was checked by TLC, using hexane/ethyl acetate (8/2) and dichloromethane/methanol (9/1) as eluent. After 4 hours, disappearance of the starting material and appearing of new spots on the TLC plates revealed the reaction was complete. After cooling, the solvent was eliminated under reduced pressure and the solid was dissolved in tetrahydrofuran. Addition of aqueous hydrogen chloride (1 M) caused the precipitation of a red solid. Tetrahydrofuran was removed under reduced pressure and the solid was filtered. The aqueous solution, still bright red, was extracted with three portions of ethyl acetate. The solid and the organic phases were recombined into one flask, the solvent removed. A purification by flash chromatography on silica gel was performed, using ethyl acetate with 0,5% of acetic acid in gradient up to 1.0% as eluent. The resulting product was a bright red solid.

***Yield**:* 67% (970 mg)

***^{1}H NMR** (300 MHz, d6-DMSO, δ, ppm):* 8.46 (s, 1H), 7.98 (d, J = 3.0 Hz, 1H), 7.68 (d, J = 6.0 Hz, 2H), 7.63 (d, J = 6.0 Hz, 1H), 7.39-7.34 (m, 4H), 7.16-7.09 (m, 6H), 6.97 (d, J = 9.0 Hz, 2H)

4.3.3. Synthesis of TPA-3 [reference: [41]]

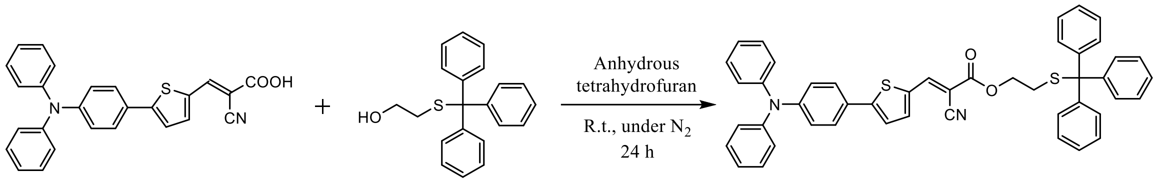

	Equivalents [eq]	**Molecular Weight** [g · mol^{-1}]	**Mass** [mg]	**Volume** [mL]	**Moles** [mmol]
TPA-2	1.0	422.50	552	/	1.31
2-(tritylthio)ethanol	1.2	320.46	503	/	1.57
4-dimethylaminopyridine (DMAP)	1.2	122.17	192	/	1.57
1-Ethyl-3-(3-dimethylaminopropyl) carbodiimide-HCl (EDC-HCl)	2.0	191.70	502	/	2.62
Tetrahydrofuran (anhydrous, solvent)	/	72.11	/	40.0	/

Oven-dried glassware was used to ensure anhydrous conditions. TPA-2 (552 mg, 1.31 mmol), 2-(tritylthio)ethanol (503 mg, 1.57 mmol), DMAP (192 mg, 1.57 mmol) were dissolved in 40.0 mL of anhydrous tetrahydrofuran in a round-bottomed flask. The mixture, under magnetic stirring and nitrogen flux, was placed in a ice bath and left to cool down for 15 minutes. EDC-HCl (502 mg, 2.62 mmol) was added and after 10 minutes the solution was brought back to room temperature. The progress of the reaction was followed through TLC. After 24 hours, the organic solvent was removed under reduced pressure, and the product was transferred into a Gooch filter (N°4). Here, it was washed thoroughly with a solution of hydrogen chloride (1M) for three times, following three basic washings with a solution of sodium bicarbonate. After drying, the crude product was purified through flash chromatography on silica gel using hexane/ethyl acetate (7/1) as eluent. A deep red solid was recovered.

Yield: 17% (164 mg)

^{1}***H NMR** (400 MHz, d-$CDCl_3$, δ, ppm):* 8.16 (s, 1H), 7.66 (d, J = 4.0 Hz, 1H), 7.49 (d, J = 8.0 Hz, 2H), 7.41-7.39 (m, 7H), 7.28-7.18 (m, 11H), 7.10-6.99 (m, 10H), 3.98 (t, J = 4.0 Hz, 2H), 2.54 (t, J = 4.0 Hz, 2H)

4.3.4. Synthesis of 4-(diphenylamino)phenylboronic pinacol ester (TPA-4) [reference: [109]]

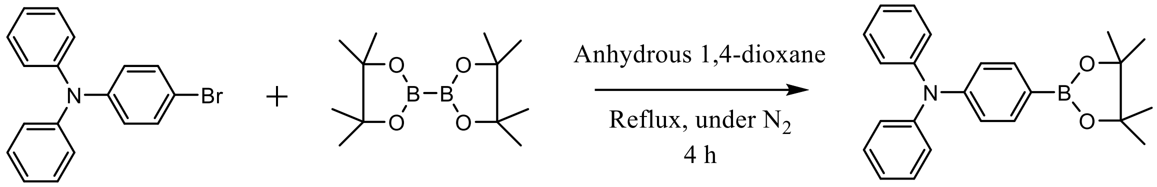

	Equivalents [eq]	**Molecular Weight** [g · mol^{-1}]	**Mass** [mg]	**Volume** [mL]	**Moles** [mmol]
4-bromotriphenylamine	1.0	324.22	1500	/	4.63
Bis(pinacolato)diboron	1.2	253.94	1410	/	5.56
Pd(dppf)Cl$_2$	0.035	731.71	119.0	/	0.162
Potassium acetate	4.0	98.15	1818	/	18.5
1,4-dioxane (anhydrous, solvent)	/	88.11	/	30.0	/

Anhydrous 1,4-dioxane (30 mL) was degassed under nitrogen for one hour using dry glassware. 4-bromotriphenylamine (1500 mg, 4.63 mmol), bis(pinacolato)diboron (1410 mg, 5.56 mmol) and potassium acetate (1818 mg, 18.52 mmol) were added to the solvent. The solution was magnetically stirred and after complete dissolution of the solids the palladium catalyst was added (119.0 mg, 0.162 mmol). The reaction mixture was then heated to gentle reflux and kept under nitrogen flux and magnetic stirring for 4 hours. The reaction was monitored through TLC using ethyl acetate/hexane (1/30) as eluent until disappearance of 4-bromotriphenylamine. After 20 hours, the reaction was quenched by elimination of the solvent by rotary evaporation. The crude product was dissolved in dichloromethane and washed with brine. The organic phase was recovered and dried over sodium sulfate. After filtration, evaporation under reduced pressure yielded a dark brown oil. Chromatographic purification over silica gel was performed employing ethyl acetate/hexane (1/30) as eluent. The product obtained after purification appeared a glassy-looking white solid.

Yield: 61% (1048 mg)

^{1}***H NMR*** *(300 MHz, d6-DMSO, δ, ppm):* 7.54 (d, J = 9.0 Hz, 2H), 7.33 (t, J = 9.0 Hz, 4H), 7.10 (t, J = 6.0 Hz, 2H), 7.05 (d, J = 9.0 Hz, 4H), 6.89 (d, J = 6.0 Hz, 2H), 1.27 (s, 12H)

ESI-MS *(acetonitrile/H$^+$, positive mode):* m/z: 371 [M$^+$]

4.3.5. **Synthesis of 4-(7-bromobenzo[c][1,2,5]thiadiazol-4-yl)-N,N-diphenylaniline (TPA-5) [reference:** [110]**]**

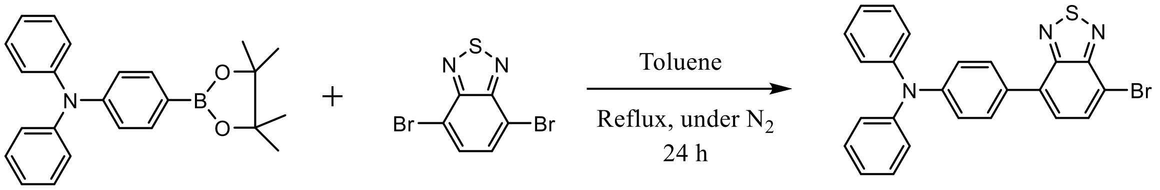

	Equivalents [eq]	**Molecular Weight** [g · mol^{-1}]	**Mass** [mg]	**Volume** [mL]	**Moles** [mmol]
TPA-4	1.0	371.29	1000	/	2.69
4,7-Dibromo-2,1,3-benzothiadiazole	1.0	293.96	792.0	/	2.69
Tetrakis(triphenylphosphine)palladium(0)	0.05	1155.56	155.0	/	0.135
Potassium carbonate 2 M	4.5	138.21	1660	6.0	12.0
Toluene (solvent)	/	92.14	/	18.0	/

6 mL of a solution of potassium carbonate in concentration 2 mol · L^{-1} (1660 mg, 12.0 mmol) was prepared. This solution was placed in a two-necks round-bottomed flask together with 18 mL of toluene. The mixture was degassed under nitrogen. TPA-4 (1000 mg, 2.69 mmol), 4,7-Dibromo-2,1,3-benzothiadiazole (792.0 mg, 2.69 mmol) and tetrakis(triphenylphosphine)palladium(0) (155.0 mg, 0.135 mmol) were transferred into the flask. The mixture was kept under magnetic stirring, nitrogen reflux and gentle reflux for 24 hours. The reaction progress was followed by TLC, using dichloromethane/hexane (4.5/5.5) as eluent. After completion of the reaction, it was quenched by adding water to the mixture. The organic phase was extracted with diethyl ether, washed with brine, and dried over sodium sulfate. After filtration, rotary evaporation yielded the crude product. Chromatographic purification over silica gel was performed using dichloromethane/hexane (4.5/5.5) as eluent.

Yield: 71% (873.7 mg)

^{1}***H NMR*** *(300 MHz, d6-DMSO, δ, ppm):* 8.09 (d, J = 9.0 Hz, 1H), 7.91 (d, J = 9.0 Hz, 2H), 7.75 (d, J = 9.0 Hz, 1H), 7.36 (m, 4H), 7.16-7.03 (m, 8H)

ESI-MS *(acetonitrile/H^{+}, positive mode):* m/z: 459 [M^{+}+1]

4.3.6. Synthesis of 5-[7-(4-diphenylaminophenyl)benzo[1,2,5] thiadiazol-4-yl]thiophene-2-carbaldehyde (TPA-6) [reference: [72]]

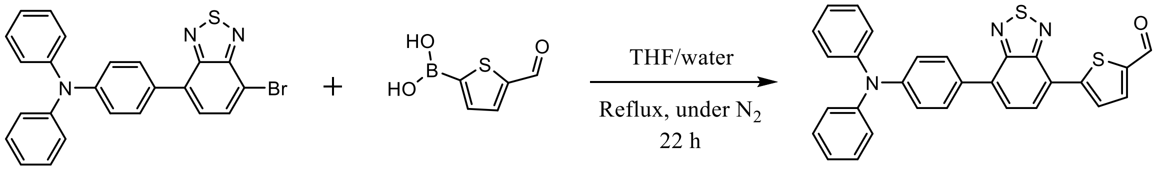

	Equivalents [eq]	**Molecular Weight** [g · mol^{-1}]	**Mass** [mg]	**Volume** [mL]	**Moles** [mmol]
TPA-5	1	458.38	647	/	1.41
5-Formyl-2-thiopheneboronic acid	1	155.97	219	/	1.41
Tetrakis(triphenylphosphine)palladium(0)	0.1	1155.56	162	/	0.14
Potassium carbonate	5	138.21	974	/	7.06
Tetrahydrofuran (solvent)	/	72.11	/	60.0	/
Water (solvent)	/	18.02	/	8.0	/

In a two-necks round-bottomed flask 60 mL of tetrahydrofuran together with 8 mL of water were degassed under nitrogen flux for an hour. TPA-5 (647 mg, 1.41 mmol), 5-Formyl-2-thiopheneboronic acid (219 mg, 1.41 mmol), potassium carbonate as base (974 mg, 7.06 mmol) and tetrakis(triphenylphosphine) palladium(0) (162 mg, 0.14 mmol) were added to the solution and the mixture was refluxed 22 hours under nitrogen and magnetic stirring. The reaction was followed by TLC, using tetrahydrofuran/hexane (1/30) and dichloromethane/hexane (1/1) as eluent. After termination of the reaction, tetrahydrofuran was eliminated by rotary evaporation, water was added and the product was extracted with dichloromethane three times. The combined organic layer was washed with water and brine, dried over anhydrous sodium sulfate, filtered and evaporated under reduced pressure. The crude product was purified by column chromatography on silica gel using dichloromethane/petroleum ether (7/1) as eluent to yield the product as a red solid.

Yield: 47% (321.0 mg)

***^{1}H NMR** (300 MHz, d-CDCl$_3$, δ, ppm):* 9.98 (s, 1H), 8.23 (d, J = 3.0 Hz, 1H), 8.06 (d, J = 9.0 Hz, 1H), 7.89 (d, J = 9.0 Hz, 2H), 7.85 (d, J = 3.0 Hz, 1H), 7.75 (d, J = 9.0 Hz, 1H), 7.34-7.28 (m, 4H), 7.22-7.18 (m, 6H), 7.11-7.06 (m, 2H)

4.3.7. Synthesis of 2-cyano-3-{5-[7-(4-diphenylaminophenyl)-2,1,3-benzothiadiazol-4-yl]thiophen-2-yl}acrylic acid (TPA-7) [reference: [72]]

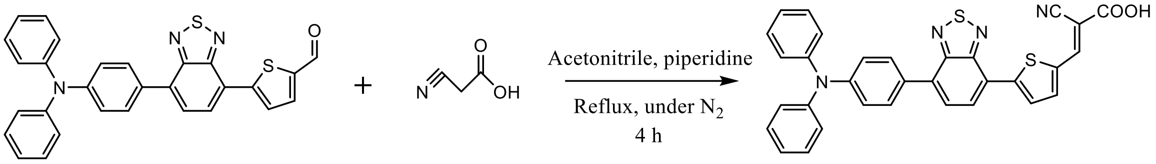

	Equivalents [eq]	**Molecular Weight** [$g \cdot mol^{-1}$]	**Mass** [mg]	**Volume** [mL]	**Moles** [mmol]
TPA-6	1.0	489.61	321	/	0.66
Piperidine	6.0	85.15	334	0.387	3.93
Cyanoacetic acid	5.0	85.06	279	/	3.28
Acetonitrile (solvent)	/	41.05	/	80.0	/

A mixture of TPA-6 (321 mg, 0.66 mmol) with cyanoacetic acid (279 mg, 3.28 mmol) and piperidine (387 µL, 3.28 mmol) in acetonitrile (80.0 mL) was refluxed for 4 hours. After cooling, the solvent was eliminated under reduced pressure; the obtained solid was dissolved in dichloromethane and it was washed three times with HCl 1M and finally with brine. The organic phase was dried over anhydrous sodium sulfate, filtered, and concentrated by rotary evaporation. The crude product was then purified by means of flash chromatography on silica gel using toluene/ethyl acetate (3/1) as eluent, adding up to 5% of acetic acid towards the end to collect the product, yielding a deep red powder.

***Yield**:* 84% (308.0 mg)

***^{1}H NMR** (300 MHz, d6-DMSO, δ, ppm):* 8.53 (s, 1H), 8.35 (d, J = 9.0 Hz, 1H), 8.29 (d, J = 3.0 Hz, 1H), 8.10 (d, J = 6.0 Hz, 1H), 8.00 (d, J = 9.0 Hz, 2H), 7.95 (d, J = 9.0 Hz, 1H), 7.40-7.34 (m, 4H), 7.14-7.08 (m, 8H)

***ESI-MS** (solvent, positive mode):* m/z: 597 [M+ACN]

4.3.8. Synthesis of TPA-8 [reference: [41]]

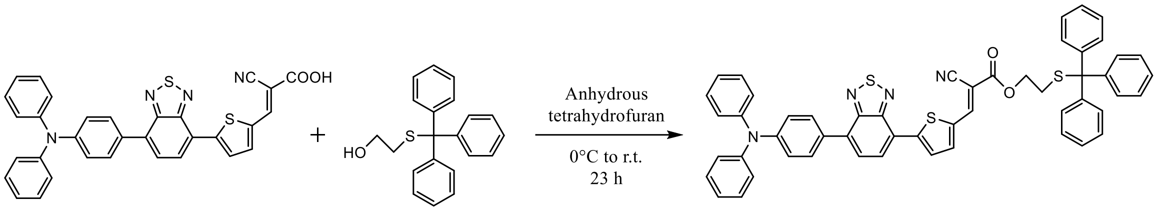

	Equivalents [eq]	Molecular Weight [g · mol^{-1}]	Mass [mg]	Volume [mL]	Moles [mmol]
TPA-7	1.0	556.66	100	/	0.180
2-(tritylthio)ethanol	1.2	320.46	69.0	/	0.216
4-dimethylaminopyridine (DMAP)	1.2	122.17	26.4	/	0.216
1-Ethyl-3-(3-dimethylaminopropyl) carbodiimide-HCl (EDC-HCl)	1.2	191.70	41.4	/	0.216
Tetrahydrofuran (anhydrous, solvent)	/	72.11	/	20.0	/

A mixture of TPA-7 (100 mg, 0.180 mmol), 2-(tritylthio)ethanol (69.0 mg, 0.216 mmol) and DMAP (26.4 mg, 0.216 mmol) was placed in a round-bottomed flask and under nitrogen atmosphere 20.0 mL of anhydrous tetrahydrofuran were added under magnetic stirring. The solution was cooled in an ice bath for 20 minutes and EDC-HCl (41.4 mg, 0.216 mmol) was added. After 15 minutes, the reaction mixture was brought back to room temperature and was followed by TLC using toluene and dichloromethane/methanol (9/1) as eluent. After 22 hours the reaction was considered complete due to the formation of numerous new spots and the disappearance of TPA-7. 20 mL of an acidic solution of hydrogen chloride (1M) was added to the flask and the organic solvent was removed by rotary evaporation. In aqueous conditions, a red solid started to precipitate; the suspension was transferred in a 50 mL centrifuge tube and was spun at 3000 RPM for 15 minutes. A clear, red solution above a deep red precipitate was observed: analysis via TLC established the absence of product in the aqueous phase, which was eliminated. The recovered solid was dissolved in tetrahydrofuran (20 mL) and hydrochloride acid (1M, 20 mL) was added. The organic solvent was evaporated, while the aqueous phase containing the product was transferred into a 50 mL centrifuge tube and spun again. After eliminating the aqueous phase, an analogous method was employed for basic and neutral washings. The red solid was collected and purified via flash chromatography, using toluene/hexane (9/1) as eluent.

***Yield**:* 35% (65.0 mg)

^{1}H NMR *(300 MHz, d-CDCl$_3$, δ, ppm):* 8.30 (s, 1H), 8.26 (d, J = 3.0 Hz, 1H), 8.08 (d, J = 9.0 Hz, 1H), 7.90 (d, J = 9.0 Hz, 1H), 7.74 (d, J = 6.0 Hz, 1H), 7.47-7.44 (m, 6H), 7.34-7.29 (m, 13H), 7.24-7.19 (m, 8H), 7.12-7.07 (m, 2H), 4.05 (t, J = 6.0 Hz, 2H), 2.62 (t, J = 6.0 Hz, 2H)

ESI-MS *(acetonitrile/H^+, positive mode):* m/z: 859 [M^+]

4.3.9. Synthesis of D-π-A

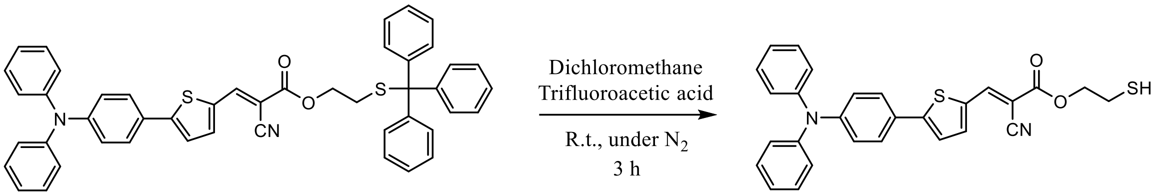

	Equivalents [eq]	**Molecular Weight** [g · mol^{-1}]	**Mass** [mg]	**Volume** [mL]	**Moles** [mmol]
TPA-3	1.0	724.94	20.0	/	0.028
Triisoproprylsilane	1.5	158.36	6.60	0.899	0.041
Dichloromethane (solvent)	/	84.93	/	3.00	/
Trifluoroacetic acid (solvent and acid medium)	/	114.02	/	1.50	/

Dichloromethane (3.00 mL) and trifluoroacetic acid (1.50 mL) are degassed under nitrogen flux for 30 minutes inside a round-bottomed flask. TPA-3 (20.0 mg, 0.028 mmol) and triisoproprylsilane (0.899 mL, 0.041 mmol) are added to the stirring solution and left under nitrogen for three hours at room temperature. The reaction is followed by TLC, using dichloromethane as eluent and potassium permanganate oxidation as revelation method. The disappearance of the protected thiol is almost immediate, as TLC testifies. After the reaction was considered complete, the mixture was washed with water and a chromatographic separation was performed, employing dichloromethane/hexane (2/1) as eluent.

4.3.10. Synthesis of D-A-π-A

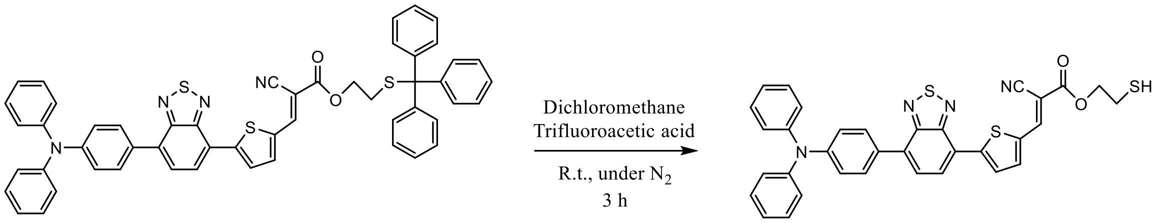

	Equivalents [eq]	**Molecular Weight** [g · mol^{-1}]	**Mass** [mg]	**Volume** [mL]	**Moles** [mmol]
TPA-8	1.0	859.12	20.0	/	0.023
Triisoproprylsilane	1.5	158.36	6.60	0.899	0.041
Dichloromethane (solvent)	/	84.93	/	3.00	/
Trifluoroacetic acid (solvent and acid medium)	/	114.02	/	1.50	/

Dichloromethane (3.00 mL) and trifluoroacetic acid (1.50 mL) are degassed under nitrogen flux for 30 minutes inside a round-bottomed flask. TPA-8 (20.0 mg, 0.023 mmol) and triisoproprylsilane (0.899 mL, 0.041 mmol) are added to the stirring solution and left under nitrogen for three hours at room temperature. The reaction is followed by TLC, using dichloromethane as eluent and potassium permanganate oxidation as revelation method. The disappearance of the protected thiol is almost immediate, as TLC testifies. After the reaction was considered complete, the mixture was washed with water and a chromatographic separation was performed, employing dichloromethane/hexane (2/1) as eluent.

***^{1}H NMR** (300 MHz, d-CDCl$_3$, δ, ppm):* 8.37 (s, 1H), 8.28 (d, J = 3.0 Hz, 1H), 8.09 (d, J = 6.0 Hz, 1H), 7.92 (d, J = 6.0 Hz, 1H), 7.90 (d, J = 6.0 Hz, 2H), 7.75 (d, J = 6.0 Hz, 1H), 7.33-7.29 (m, 4H), 7.22-7.19 (m, 8H), 4.44 (t, J = 6.0 Hz, 2H), 2.89 (t, J = 6.0 Hz, 2H)

4.3.11. Functionalization of MoS2 with TPA-3 exploiting in-situ deprotection: MoS$_2$@D-π-A_1 and MoS$_2$@D-π-A_7

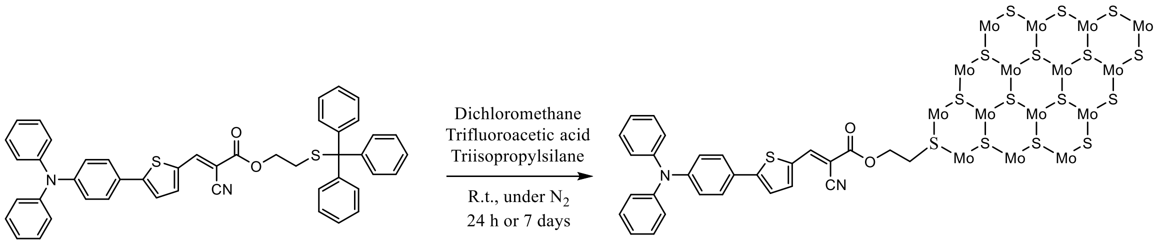

	Equivalents [eq]	**Molecular Weight** [g · mol^{-1}]	**Mass** [mg]	**Volume** [mL]	**Moles** [mmol]
Molybdenum disulfide	1.0	160.07	12.6	/	0.079
TPA-3	0.5	724.94	28.5	/	0.039
Triisoproprylsilane	0.5	158.36	6.24	0.0081	0.039
Dichloromethane (solvent)	/	84.93	/	15.00	/
Trifluoroacetic acid (solvent and acid medium)	/	114.02	/	5.00	/

Molybdenum disulfide was provided deposed on a microfilter. To disperse the material, the filter was placed into a 50 mL centrifuge tube, together with 5 mL of a solution of dichloromethane/trifluoroacetic acid (3/1), and it was sonicated in an ultrasonic bath for 10 minutes. The supernatant was collected, and 5 mL of fresh solution were added in the centrifuge tube with the filter, repeating the extraction. The procedure was iterated until 20 mL of suspension were collected in total. The suspension was then transferred to a 50 mL round-bottomed flask, and it was degassed for one hour under magnetic stirring and nitrogen flux. Subsequently, TPA-3 (28.5 mg, 0.039 mmol) and triisoproprylsilane (8.1 µL, 0.039 mmol) were added to the solution, which was left under magnetic stirring in nitrogen atmosphere for 24 hours (7 days). The reaction mixture was transferred to a 50 mL centrifuge tube and 20 mL of methanol were added. Sonication for 10 minutes was followed by centrifugation at 3500 RPM for 30 minutes. The supernatant was withdrawn, and a series of washing cycles was performed as follows: the solid was dispersed in dichloromethane (10 mL), sonicated for 10 minutes, methanol was added (10 mL), centrifugated at 4000 RPM for 10 minutes and at 7000 RPM for 30 minutes afterwards. For each washing, the supernatant was withdrawn and poured in a collection tube and then the procedure was repeated. Each washing was analyzed through UV-Vis spectrophotometry and after 14 cycles the obtained results of purity of the supernatant were considered satisfying. After the last washing cycle was performed, the obtained solid was dried under nitrogen flux.

4.3.12. Enhancement of sulfur vacancies on molybdenum disulfide basal plane through $NaBH_4$ treatment [reference: [111]]

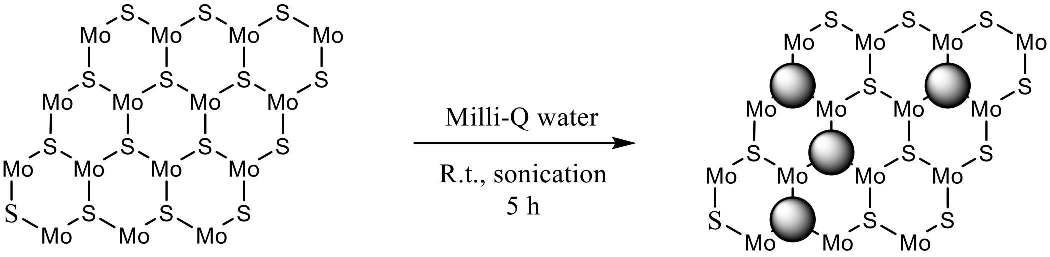

	Equivalents [eq]	**Molecular Weight** [g · mol^{-1}]	**Mass** [mg]	**Volume** [mL]	**Moles** [mmol]
Molybdenum disulfide	/	160.07	25	/	0.16
Sodium borohydride	/	37.83	190	/	5.0
Milli-Q water (solvent)	/	18.02	/	16	/

Molybdenum disulfide was provided deposed on microfilters. To disperse the material, two filters were placed into a 12 mL centrifuge tube, together with 4 mL of Milli-Q water and were sonicated in an ultrasonic bath for 10 minutes. The dispersion was transferred in a round-bottomed flask and the procedure was repeated into the centrifuge tube, other three times, collecting a total of 16 mL of suspension of molybdenum disulfide. Sodium borohydride (190 mg, 5.0 mmol) was added to the dispersion, and it was sonicated for five hours. After sonication time was over, the suspension was filtered on a polycarbonate microfilter (0,1 µm) and the collected solid was washed thoroughly with Milli-Q water. The filter was dispersed in a centrifuge tube using iso-propanol and a flux of nitrogen left overnight was used to dry the solid.

4.3.13. Functionalization of MoS_2 with TPA-8 exploiting in-situ deprotection: MoS_2@D-A-π-A_7

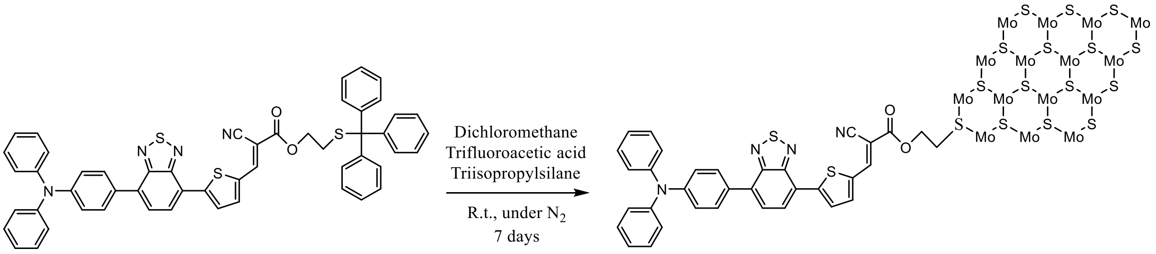

	Equivalents [eq]	**Molecular Weight** [g · mol^{-1}]	**Mass** [mg]	**Volume** [mL]	**Moles** [mmol]
Molybdenum disulfide	1.0	160.07	10.0	/	0.0625
TPA-8	0.5	859.2	26.8	/	0.0312
Triisoproprylsilane	0.5	158.36	4.9	0.0064	0.0312
Dichloromethane (solvent)	/	84.93	/	15.0	/
Trifluoroacetic acid (solvent and acid medium)	/	114.02	/	5.0	/

Molybdenum disulfide was provided deposed on a microfilter. 20 mL of a solution 3/1 in dichloromethane and trifluoroacetic acid was purged under nitrogen flux for 1 hour in a two-necks round-bottomed flask. After that, MoS_2 (10.0 mg, 0.0625 mmol), TPA-8 (26.8 mg, 0.0312 mmol) and triisoproprylsilane (6.4 µL, 0.0312 mmol) were added to the solution, kept agitated by magnetic stirring under nitrogen atmosphere for 7 days. The suspension was then transferred to a 50 mL centrifuge tube, 20 mL of methanol were added and centrifugation at 4500 RPM for 20 minutes followed. The supernatant was moved to a second tube, while the solid experienced a series of washings as follows: about 30 mL of a solution of dichloromethane and methanol (1/1) were added to the tube containing the solid, which was then centrifugated at 4500 RPM for 20 minutes. The supernatant was removed, replaced with fresh solution and the washing repeated. After 8 washings, since the supernatant was almost transparent, the solid was treated as follows: dispersed in 15 mL of dichloromethane, sonicated for 10 minutes in an ultrasonic bath, 15 mL of methanol were added and centrifugation at 4500 RPM for 20 minutes was performed. Transparent washings were checked with UV spectrometry until the dye peak, situated at 505 nm, reached values of 0.03 absorbance, and didn’t diminish with further washings; coincidentally, baseline started rising, indicating presence of nanostructure in the supernatant. Washings were stopped after 22 cycles. Obtained solid was dried under nitrogen flux.

4.3.14. Functionalization of $NaBH_4$-MoS_2 with TPA-3 exploiting in-situ deprotection: MoS_2@$NaBH_4$@D-π-A_7

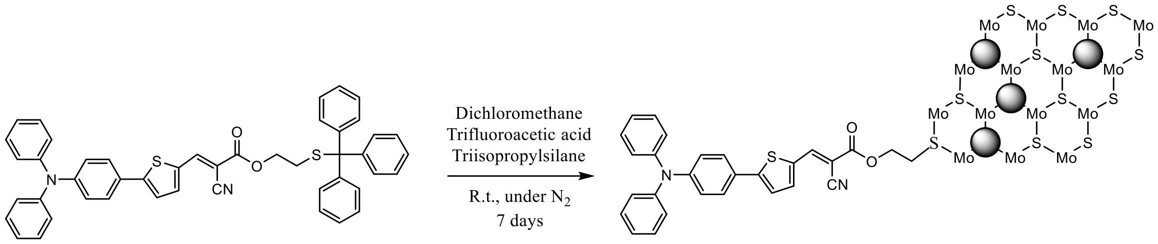

	Equivalents [eq]	**Molecular Weight** [g · mol^{-1}]	**Mass** [mg]	**Volume** [mL]	**Moles** [mmol]
Molybdenum disulfide	1.0	160.07	9.9	/	0.0621
TPA-3	0.5	724.94	22.5	/	0.0310
Triisoproprylsilane	0.5	159.36	4.9	0.0064	0.0310
Dichloromethane (solvent)	/	84.93	/	15.00	/
Trifluoroacetic acid (solvent and acid medium)	/	114.02	/	5.00	/

20 mL of a solution of dichloromethane/trifluoroacetic acid (3/1) were purged under nitrogen flux for about 1 hour in a two-necks round-bottomed flask. Then, $NaBH_4$-MoS_2 (9.9 mg, 0.0621 mmol), TPA-3 (22.5 mg, 0.0310 mmol), and triisopropylsilane (6.4 µL, 0.0310 mmol) were added to the stirring solution and left under nitrogen atmosphere for 7 days. After that, the suspension was transferred into a 50 mL centrifuge tube, 20 mL of methanol were added, and it was centrifugated at 4500 RPM for 20 minutes. The supernatant was placed into a second tube, while the solid obtained experienced a series of washings as follows: about 30 mL of a solution of dichloromethane/methanol (1/1) were added to the tube containing the solid, and it was spun at 4500 RPM for 20 minutes. The supernatant was removed, replaced with fresh solution and the washing was repeated. After 2 washings, the supernatant started fading in color, then the solid was treated as follows: 15 mL of dichloromethane were added to the tube, sonication in an ultrasonic bath for 10 minutes was performed, 15 mL of ethanol were added and centrifugation at 4500 RPM for 20 minutes was carried out. Transparent washings were checked through UV spectroscopy; the dye peak, placed at 480 nm, diminished until it reached values below 0.05 absorbance. At the same time, scattering arose in the spectra, indicating presence of nanostructure in the supernatant. Washings were stopped after 9 cycles. Obtained solid was dried under nitrogen flux.

5. Bibliography

[1] C. C. Elam, C. E. Gregoire PadrÃ, G. Sandrock, A. Luzzi, P. Lindblad, and E. Fjermestad Hagen, “Realizing the hydrogen future: the International Energy Agency’s eeorts to advance hydrogen energy technologies,” 2003. [Online]. Available: www.sciencedirect.comwww.elsevier.com/locate/ijhydene

[2] J. Hetland and G. Mulder, “In search of a sustainable hydrogen economy: How a large-scale transition to hydrogen may affect the primary energy demand and greenhouse gas emissions,” *Int J Hydrogen Energy*, vol. 32, no. 6, pp. 736–747, May 2007, doi: 10.1016/j.ijhydene.2006.08.011.

[3] R. H. Lin, Y. Y. Zhao, and B. D. Wu, “Toward a hydrogen society: Hydrogen and smart grid integration,” *Int J Hydrogen Energy*, vol. 45, no. 39, pp. 20164–20175, Aug. 2020, doi: 10.1016/j.ijhydene.2020.01.047.

[4] C. You and J. Kim, “Optimal design and global sensitivity analysis of a 100% renewable energy sources based smart energy network for electrified and hydrogen cities,” *Energy Convers Manag*, vol. 223, Nov. 2020, doi: 10.1016/j.enconman.2020.113252.

[5] B. Nastasi and G. lo Basso, “Hydrogen to link heat and electricity in the transition towards future Smart Energy Systems,” *Energy*, vol. 110, pp. 5–22, 2016, doi: 10.1016/j.energy.2016.03.097.

[6] D. F. Dominković, I. Bačeković, A. S. Pedersen, and G. Krajačić, “The future of transportation in sustainable energy systems: Opportunities and barriers in a clean energy transition,” *Renewable and Sustainable Energy Reviews*, vol. 82. Elsevier Ltd, pp. 1823–1838, Feb. 01, 2018. doi: 10.1016/j.rser.2017.06.117.

[7] Y. Wang *et al.*, “Mimicking Natural Photosynthesis: Solar to Renewable H2 Fuel Synthesis by Z-Scheme Water Splitting Systems,” *Chemical Reviews*, vol. 118, no. 10. American Chemical Society, pp. 5201–5241, May 23, 2018. doi: 10.1021/acs.chemrev.7b00286.

[8] B. Cecconi, N. Manfredi, T. Montini, P. Fornasiero, and A. Abbotto, “Dye-Sensitized Solar Hydrogen Production: The Emerging Role of Metal-Free Organic Sensitizers,” *European Journal of Organic Chemistry*, vol. 2016, no. 31. Wiley-VCH Verlag, pp. 5194–5215, Nov. 01, 2016. doi: 10.1002/ejoc.201600653.

[9] I. Dincer and C. Acar, “Innovation in hydrogen production,” *International Journal of Hydrogen Energy*, vol. 42, no. 22. Elsevier Ltd, pp. 14843–14864, Jun. 01, 2017. doi: 10.1016/j.ijhydene.2017.04.107.

[10] Grätzel Michael, “Photoelectrochemical cells,” *Nature*, vol. 414, pp. 338–344, 2001.

[11] K. Honda, “One and Two-dimensional Structure of Alpha-Helix and Beta-Sheet Forms of Poly(L-Alanine) shown by Specific Heat Measurements at Low Temperatures (1.5-20 K),” 1910.

[12] J. T. Kirner and R. G. Finke, “Water-oxidation photoanodes using organic light-harvesting materials: A review,” *J Mater Chem A Mater*, vol. 5, no. 37, pp. 19560–19592, 2017, doi: 10.1039/c7ta05709a.

[13] Mohammad Mahdi Najafpour, “APPLIED PHOTOSYNTHESIS NEW PROGRESS,” Rijeka, 2016.

[14] S. Zhang, H. Ye, J. Hua, and H. Tian, “Recent advances in dye-sensitized photoelectrochemical cells for water splitting,” *EnergyChem*, vol. 1, no. 3, p. 100015, Nov. 2019, doi: 10.1016/j.enchem.2019.100015.

[15] N. Queyriaux, N. Kaeffer, A. Morozan, M. Chavarot-Kerlidou, and V. Artero, “Molecular cathode and photocathode materials for hydrogen evolution in photoelectrochemical devices,” *Journal of Photochemistry and Photobiology C: Photochemistry Reviews*, vol. 25. Elsevier B.V., pp. 90–105, Dec. 01, 2015. doi: 10.1016/j.jphotochemrev.2015.08.001.

[16] M. Grätzel and B. O’Regan, “A low-cost, high-efficiency solar cell based on dye-sensitized colloidal TiO2 films,” *Nature*, pp. 737–740, 1991.

[17] A. Hagfeldt, G. Boschloo, L. Sun, L. Kloo, and H. Pettersson, “Dye-sensitized solar cells,” *Chem Rev*, vol. 110, no. 11, pp. 6595–6663, Nov. 2010, doi: 10.1021/cr900356p.

[18] C. S. Karthikeyan, H. Wietasch, and M. Thelakkat, “Highly efficient solid-state dye-sensitized TiO2 solar cells using donor-antenna dyes capable of multistep charge-transfer cascades,” *Advanced Materials*, vol. 19, no. 8, pp. 1091–1095, Apr. 2007, doi: 10.1002/adma.200601872.

[19] A. Carella, F. Borbone, and R. Centore, “Research progress on photosensitizers for DSSC,” *Frontiers in Chemistry*, vol. 6, no. SEP. Frontiers Media S.A., Sep. 01, 2018. doi: 10.3389/fchem.2018.00481.

[20] Y. Tachibana, S. A. Haque, I. P. Mercer, J. R. Durrant, and D. R. Klug, “Electron injection and recombination in dye sensitized nanocrystalline titanium dioxide films: A comparison of ruthenium bipyridyl and porphyrin sensitizer dyes,” *Journal of Physical Chemistry B*, vol. 104, no. 6. American Chemical Society, pp. 1198–1205, Feb. 17, 2000. doi: 10.1021/jp992774b.

[21] L. Zhang and J. M. Cole, “Dye aggregation in dye-sensitized solar cells,” *J Mater Chem A Mater*, vol. 5, no. 37, pp. 19541–19559, 2017, doi: 10.1039/c7ta05632j.

[22] N. V. Krishna, J. V. S. Krishna, M. Mrinalini, S. Prasanthkumar, and L. Giribabu, “Role of Co-Sensitizers in Dye-Sensitized Solar Cells,” *ChemSusChem*, vol. 10, no. 23. Wiley-VCH Verlag, pp. 4668–4689, Dec. 08, 2017. doi: 10.1002/cssc.201701224.

[23] C. Decavoli, C. L. Boldrini, N. Manfredi, and A. Abbotto, “Molecular Organic Sensitizers for Photoelectrochemical Water Splitting,” *European Journal of Inorganic Chemistry*, vol. 2020, no. 11–12. Wiley-VCH Verlag, pp. 978–999, Mar. 27, 2020. doi: 10.1002/ejic.202000026.

[24] T. Dentani, K. Funabiki, J. Y. Jin, T. Yoshida, H. Minoura, and M. Matsui, “Application of 9-substituted 3,4-perylenedicarboxylic anhydrides as sensitizers for zinc oxide solar cell,” *Dyes and Pigments*, vol. 72, no. 3, pp. 303–307, 2007, doi: 10.1016/j.dyepig.2005.09.004.

[25] S. Ahmad, E. Guillén, L. Kavan, M. Grätzel, and M. K. Nazeeruddin, “Metal free sensitizer and catalyst for dye sensitized solar cells,” *Energy and Environmental Science*, vol. 6, no. 12. pp. 3439–3466, Dec. 2013. doi: 10.1039/c3ee41888j.

[26] T. Kitamura *et al.*, “Phenyl-Conjugated Oligoene Sensitizers for TiO2 Solar Cells,” *Chemistry of Materials*, vol. 16, no. 9, pp. 1806–1812, May 2004, doi: 10.1021/cm0349708.

[27] W. H. Liu *et al.*, “Simple organic molecules bearing a 3,4-ethylenedioxythiophene linker for efficient dye-sensitized solar cells,” *Chemical Communications*, no. 41, pp. 5152–5154, 2008, doi: 10.1039/b808535h.

[28] G. Zhang *et al.*, “Employ a bisthienothiophene linker to construct an organic chromophore for efficient and stable dye-sensitized solar cells,” *Energy Environ Sci*, vol. 2, no. 1, pp. 92–95, 2009, doi: 10.1039/b817990e.

[29] Y. Wu and W. Zhu, “Organic sensitizers from D–π–A to D–A–π–A: Effect of the internal electron-withdrawing units on molecular absorption, energy levels and photovoltaic performances,” *Chem Soc Rev*, vol. 42, no. 5, pp. 2039–2058, Feb. 2013, doi: 10.1039/c2cs35346f.

[30] L. Zhang and J. M. Cole, “Anchoring groups for dye-sensitized solar cells,” *ACS Applied Materials and Interfaces*, vol. 7, no. 6. American Chemical Society, pp. 3427–3455, Feb. 18, 2015. doi: 10.1021/am507334m.

[31] K. Kakiage, Y. Aoyama, T. Yano, K. Oya, J. I. Fujisawa, and M. Hanaya, “Highly-efficient dye-sensitized solar cells with collaborative sensitization by silyl-anchor and carboxy-anchor dyes,” *Chemical Communications*, vol. 51, no. 88, pp. 15894–15897, Sep. 2015, doi: 10.1039/c5cc06759f.

[32] T. Ishiyama, M. Murata, and N. Miyaura, “Palladium(0)-Catalyzed Cross-Coupling Reaction of Alkoxydiboron with Haloarenes: A Direct Procedure for Arylboronic Esters,” *J. Org. Chem.*, vol. 60, no. 1, pp. 6313–6315, 1995, [Online]. Available: https://pubs.acs.org/sharingguidelines

[33] N. Miyaura, K. Yamada, and A. Suzuki, “A NEW STEREOSPECIFIC CROSS-COUPLING BY THE PALLADIUM-CATALYZED REACTION OF 1-ALKENYLBORANES WITH 1-ALKENYL OR l-ALKYNYL HALIDES,” OPergamon Press Ltd, 1979.

[34] S. Kotha, K. Lahiri, and D. Kashinath, “Recent applications of the Suzuki-Miyaura cross-coupling reaction in organic synthesis.”

[35] N. E. Leadbeater, “Fast, easy, clean chemistry by using water as a solvent and microwave heating: The Suzuki coupling as an illustration,” *Chemical Communications*, no. 23. Royal Society of Chemistry, pp. 2881–2902, Jun. 21, 2005. doi: 10.1039/b500952a.

[36] A. F. Littke *et al.*, “A Convenient and General Method for Pd-Catalyzed Suzuki Cross-Couplings of Aryl Chlorides and Arylboronic Acids,” *J. Colloid Interface Sci*, vol. 37, no. 24, pp. 3382–3387, 1998, [Online]. Available: http://www.wiley-vch.de/home/angewandte/or

[37] G. B. Smith, G. C. Dezeny, D. L. Hughes, and T. R. Verhoeven, “Mechanistic Studies of the Suzuki Cross-Coupling Reaction,” *J. Org. Chem.*, vol. 59, pp. 8151–8156, 1994.

[38] S. W. Wright, D. L. Hageman, and L. D. Mcclure, “Fluoride-Mediated Boronic Acid Coupling Reactions,” 1994.

[39] Knoevenagel Emil, “Condensation von Malondiure mit aromatiachen Aldehyden durch Ammoniak und Amine,” 1898.

[40] M. Smith and J. March, *March’s advanced organic chemistry : reactions, mechanisms, and structure.* Wiley-Interscience, 2007.

[41] B. Neises and W. Steglich, “Simple Method for the Esterification of Carboxylic Acids,” *Angewandte Chemie International Edition in English*, vol. 17, no. 7, pp. 522–524, 1978, doi: 10.1002/anie.197805221.

[42] B. Tsvetkova, J. Tencheva, and P. Peikov, “Esterification of 7-theophyllineacetic acid with diethylene glycol monomethyl ether,” *Acta Pharm.*, pp. 251–257, 2006.

[43] A. B. Lutjen, M. A. Quirk, A. M. Barbera, and E. M. Kolonko, “Synthesis of (E)-cinnamyl ester derivatives via a greener Steglich esterification,” *Bioorg Med Chem*, pp. 5291–5298, Oct. 2018, doi: 10.1016/j.bmc.2018.04.007.

[44] G. T. Hermanson, “Zero-Length Crosslinkers,” in *Bioconjugate Techniques*, Elsevier, 2013, pp. 259–273. doi: 10.1016/b978-0-12-382239-0.00004-2.

[45] B. Hinnemann *et al.*, “Biomimetic hydrogen evolution: MoS2 nanoparticles as catalyst for hydrogen evolution,” *J Am Chem Soc*, vol. 127, no. 15, pp. 5308–5309, Apr. 2005, doi: 10.1021/ja0504690.

[46] F. S. Moreira, R. G. Machado, B. B. Romão, F. R. X. Batista, J. S. Ferreira, and V. L. Cardoso, “Improvement of hydrogen production by biological route using repeated batch cycles,” *Process Biochemistry*, vol. 58, pp. 60–68, Jul. 2017, doi: 10.1016/j.procbio.2017.04.013.

[47] J. D. Benck, T. R. Hellstern, J. Kibsgaard, P. Chakthranont, and T. F. Jaramillo, “Catalyzing the hydrogen evolution reaction (HER) with molybdenum sulfide nanomaterials,” *ACS Catalysis*, vol. 4, no. 11. American Chemical Society, pp. 3957–3971, Oct. 08, 2014. doi: 10.1021/cs500923c.

[48] D. Gupta, V. Chauhan, and R. Kumar, “A comprehensive review on synthesis and applications of molybdenum disulfide (MoS2) material: Past and recent developments,” *Inorganic Chemistry Communications*, vol. 121. Elsevier B.V., Nov. 01, 2020. doi: 10.1016/j.inoche.2020.108200.

[49] Q. Ding *et al.*, “Basal-Plane Ligand Functionalization on Semiconducting 2H-MoS2 Monolayers,” *ACS Appl Mater Interfaces*, vol. 9, no. 14, pp. 12734–12742, Apr. 2017, doi: 10.1021/acsami.7b01262.

[50] L. Li *et al.*, “Role of sulfur vacancies and undercoordinated Mo regions in MoS2 nanosheets toward the evolution of hydrogen,” *ACS Nano*, vol. 13, no. 6, pp. 6824–6834, Jun. 2019, doi: 10.1021/acsnano.9b01583.

[51] J. Wang, X. Feng, D. Hedman, X. Wu, H. Pan, and Q. Zhang, “Enhancing the hydrogen evolution reaction on MoS2 flakes by cold plasma treatment,” *Electrochem commun*, vol. 137, Apr. 2022, doi: 10.1016/j.elecom.2022.107250.

[52] S. Geng, W. Yang, Y. Liu, and Y. Yu, “Engineering sulfur vacancies in basal plane of MoS2 for enhanced hydrogen evolution reaction,” *J Catal*, vol. 391, pp. 91–97, Nov. 2020, doi: 10.1016/j.jcat.2020.05.042.

[53] T. Liu *et al.*, “Plasma-Induced Fabrication and Straining of MoS2 Films for the Hydrogen Evolution Reaction,” *ACS Appl Energy Mater*, vol. 2, no. 7, pp. 5162–5170, Jul. 2019, doi: 10.1021/acsaem.9b00843.

[54] H. Li *et al.*, “Activating and optimizing MoS2 basal planes for hydrogen evolution through the formation of strained sulphur vacancies,” *Nat Mater*, vol. 15, no. 1, pp. 48–53, Jan. 2016, doi: 10.1038/nmat4465.

[55] S. García-Dalí *et al.*, “Activation of two-dimensional MoS2 nanosheets by wet-chemical sulfur vacancy engineering for the catalytic reduction of nitroarenes and organic dyes,” *Appl Mater Today*, vol. 20, Sep. 2020, doi: 10.1016/j.apmt.2020.100678.

[56] L. Karger *et al.*, “The Role of Additives in Suppressing the Degradation of Liquid-Exfoliated WS2 Monolayers,” *Advanced Materials*, vol. 33, no. 42, Oct. 2021, doi: 10.1002/adma.202102883.

[57] J. Kim *et al.*, “Direct exfoliation and dispersion of two-dimensional materials in pure water via temperature control,” *Nat Commun*, vol. 6, Sep. 2015, doi: 10.1038/ncomms9294.

[58] D. Zhang *et al.*, “Controllable synthesis and characterization of tungsten disulfide nanosheets as promising nanomaterials for electronic devices,” *Ceram Int*, vol. 45, no. 9, pp. 12443–12448, Jun. 2019, doi: 10.1016/j.ceramint.2019.03.177.

[59] C. Backes *et al.*, “Edge and confinement effects allow in situ measurement of size and thickness of liquid-exfoliated nanosheets,” *Nature Communications*, vol. 5, no. 1, pp. 1–10, Aug. 2014, doi: 10.1038/ncomms5576.

[60] S. Balendhran *et al.*, “Two-dimensional molybdenum trioxide and dichalcogenides,” *Advanced Functional Materials*, vol. 23, no. 32, pp. 3952–3970, Aug. 2013, doi: 10.1002/adfm.201300125.

[61] B. Chakraborty, H. S. S. R. Matte, A. K. Sood, and C. N. R. Rao, “Layer-dependent resonant Raman scattering of a few layer MoS2,” *Journal of Raman Spectroscopy*, vol. 44, no. 1, pp. 92–96, Jan. 2013, doi: 10.1002/JRS.4147.

[62] V. Paolucci *et al.*, “Sustainable Liquid-Phase Exfoliation of Layered Materials with Nontoxic Polarclean Solvent,” *ACS Sustainable Chemistry and Engineering*, vol. 8, no. 51, pp. 18830–18840, Dec. 2020, doi: 10.1021/acssuschemeng.0c04191.

[63] A. Hirsch and F. Hauke, “Post-Graphene 2D Chemistry: The Emerging Field of Molybdenum Disulfide and Black Phosphorus Functionalization,” *Angewandte Chemie International Edition*, vol. 57, no. 16, pp. 4338–4354, Apr. 2018, doi: 10.1002/anie.201708211.

[64] X. Chen, N. C. Berner, C. Backes, G. S. Duesberg, and A. R. McDonald, “Functionalization of Two-Dimensional MoS 2 : On the Reaction Between MoS 2 and Organic Thiols,” *Angewandte Chemie*, vol. 128, no. 19, pp. 5897–5902, May 2016, doi: 10.1002/ange.201510219.

[65] A. W. Coats and J. P. Redfern, “Thermogravimetric analysis. A review,” *Analyst*, vol. 88, no. 1053, pp. 906–924, 1963, doi: 10.1039/AN9638800906.

[66] H. Li *et al.*, “From bulk to monolayer MoS 2: Evolution of Raman scattering,” *Adv Funct Mater*, vol. 22, no. 7, pp. 1385–1390, Apr. 2012, doi: 10.1002/adfm.201102111.

[67] Z. Yu, F. Li, and L. Sun, “Recent advances in dye-sensitized photoelectrochemical cells for solar hydrogen production based on molecular components,” *Energy and Environmental Science*, vol. 8, no. 3. Royal Society of Chemistry, pp. 760–775, Mar. 01, 2015. doi: 10.1039/c4ee03565h.

[68] P. Xu, N. S. McCool, and T. E. Mallouk, “Water splitting dye-sensitized solar cells,” *Nano Today*, vol. 14. Elsevier B.V., pp. 42–58, Jun. 01, 2017. doi: 10.1016/j.nantod.2017.04.009.

[69] K. Kalyanasundaram and M. Neumann-Spallart, “Photophysical and Redox Properties of Water-Soluble Porphyrins in Aqueous Media,” 1982. [Online]. Available: https://pubs.acs.org/sharingguidelines

[70] Z. Ning and H. Tian, “Triarylamine: A promising core unit for efficient photovoltaic materials,” *Chemical Communications*, no. 37. Royal Society of Chemistry, pp. 5483–5495, 2009. doi: 10.1039/b908802d.

[71] S. Presolski and M. Pumera, “Covalent functionalization of MoS2,” *Materials Today*, vol. 19, no. 3. Elsevier B.V., pp. 140–145, Apr. 01, 2016. doi: 10.1016/j.mattod.2015.08.019.

[72] W. Zhu *et al.*, “Organic D-A-π-A solar cell sensitizers with improved stability and spectral response,” *Advanced Functional Materials*, vol. 21, no. 4. pp. 756–763, Feb. 22, 2011. doi: 10.1002/adfm.201001801.

[73] D. H. Roh *et al.*, “Strategy for Improved Photoconversion Efficiency in Thin Photoelectrode Films by Controlling π-Spacer Dihedral Angle,” *Journal of Physical Chemistry C*, vol. 120, no. 43, pp. 24655–24666, Nov. 2016, doi: 10.1021/acs.jpcc.6b08262.

[74] Y. Li, T. Ren, and W. J. Dong, “Tuning photophysical properties of triphenylamine and aromatic cyano conjugate-based wavelength-shifting compounds by manipulating intramolecular charge transfer strength,” *J Photochem Photobiol A Chem*, vol. 251, pp. 1–9, Aug. 2013, doi: 10.1016/j.jphotochem.2012.10.002.

[75] A. Aljarilla, L. López-Arroyo, P. de La Cruz, F. Oswald, T. B. Meyer, and F. Langa, “Organic dyes incorporating oligothienylenevinylene for efficient dye-sensitized solar cells,” *Org Lett*, vol. 14, no. 22, pp. 5732–5735, Nov. 2012, doi: 10.1021/ol302738k.

[76] D. P. Hagberg *et al.*, “Tuning the HOMO and LUMO energy levels of organic chromophores for dye sensitized solar cells,” *Journal of Organic Chemistry*, vol. 72, no. 25, pp. 9550–9556, Dec. 2007, doi: 10.1021/jo701592x.

[77] T. Parella and J. F. Espinosa, “Long-range proton-carbon coupling constants: NMR methods and applications,” *Progress in Nuclear Magnetic Resonance Spectroscopy*, vol. 73. Elsevier B.V., pp. 17–55, 2013. doi: 10.1016/j.pnmrs.2013.07.001.

[78] H. Cho, T. Iwashita, M. Hamaguchi, and Y. Oyama, “Stereochemistry of Knoevenagel condensation products from cyanoacetates and aromatic aldehydes,” *Chem. Pharm. Bull.*, vol. 39, no. 12, pp. 3341–3342, 1991.

[79] Greg T, “From: Comprehensive Heterocyclic Chemistry III,” 2008.

[80] M. Tsakos, E. S. Schaffert, L. L. Clement, N. L. Villadsen, and T. B. Poulsen, “Ester coupling reactions-an enduring challenge in the chemical synthesis of bioactive natural products,” *Natural Product Reports*, vol. 32, no. 4. Royal Society of Chemistry, pp. 605–632, Apr. 01, 2015. doi: 10.1039/c4np00106k.

[81] G. T. Hermanson, “Zero-Length Crosslinkers,” in *Bioconjugate Techniques*, Elsevier, 2013, pp. 259–273. doi: 10.1016/b978-0-12-382239-0.00004-2.

[82] Y. L. Tain *et al.*, “Synthesis and Characterization of Novel Resveratrol Butyrate Esters That Have the Ability to Prevent Fat Accumulation in a Liver Cell Culture Model,” *Molecules*, vol. 25, no. 18, Sep. 2020, doi: 10.3390/molecules25184199.

[83] G. Groeneveld, S. Kuijer, and M. de Puit, “Preparation of cyanoacrylate derivatives and comparison of dual action cyanoacrylate formulations,” *Science and Justice*, vol. 54, no. 1, pp. 42–48, Mar. 2014, doi: 10.1016/j.scijus.2013.09.002.

[84] Y. Im and J. Y. Lee, “Above 20% external quantum efficiency in thermally activated delayed fluorescence device using furodipyridine-type host materials,” *Chemistry of Materials*, vol. 26, no. 3, pp. 1413–1419, Feb. 2014, doi: 10.1021/cm403358h.

[85] G. Y. Ding *et al.*, “Administration of the D-A structure and steric hindrance effect to construct efficient red emitters for high-performance OLEDs with low efficiency roll-off,” *Dyes and Pigments*, vol. 192, Aug. 2021, doi: 10.1016/j.dyepig.2021.109398.

[86] M. K. Chini, R. Y. Mahale, and S. Chatterjee, “Effect of heterocycles on field-effect transistor performances of donor-acceptor-donor type small molecules,” *Chem Phys Lett*, vol. 661, pp. 107–113, Sep. 2016, doi: 10.1016/j.cplett.2016.08.073.

[87] P. Dutta, W. Yang, S. Hun Eom, W. H. Lee, I. Nam Kang, and S. H. Lee, “Development of naphtho[1,2-b:5,6-b′]dithiophene based novel small molecules for efficient bulk-heterojunction organic solar cells,” *Chemical Communications*, vol. 48, no. 4, pp. 573–575, Dec. 2012, doi: 10.1039/c1cc15465f.

[88] L. Wang, X. Yang, J. Zhao, F. Zhang, X. Wang, and L. Sun, “Efficient Organic Sensitizers with Pyridine-N-oxide as an Anchor Group for Dye-Sensitized Solar Cells,” *ChemSusChem*, vol. 7, no. 9, pp. 2640–2646, Sep. 2014, doi: 10.1002/cssc.201402208.

[89] S. Albrecht *et al.*, “Fluorinated copolymer PCPDTBT with enhanced open-circuit voltage and reduced recombination for highly efficient polymer solar cells,” *J Am Chem Soc*, vol. 134, no. 36, pp. 14932–14944, Sep. 2012, doi: 10.1021/ja305039j.

[90] W. Zhu *et al.*, “Organic D-A-π-A solar cell sensitizers with improved stability and spectral response,” *Advanced Functional Materials*, vol. 21, no. 4. pp. 756–763, Feb. 22, 2011. doi: 10.1002/adfm.201001801.

[91] R. R. Chianelli *et al.*, “Catalytic properties of single layers of transition metal sulfide catalytic materials,” *Catalysis Reviews - Science and Engineering*, vol. 48, no. 1. pp. 1–41, Jan. 2006. doi: 10.1080/01614940500439776.

[92] S. S. Chou *et al.*, “Ligand conjugation of chemically exfoliated MoS2,” *J Am Chem Soc*, vol. 135, no. 12, pp. 4584–4587, Mar. 2013, doi: 10.1021/ja310929s.

[93] W. Zhou *et al.*, “Intrinsic structural defects in monolayer molybdenum disulfide,” *Nano Lett*, vol. 13, no. 6, pp. 2615–2622, Jun. 2013, doi: 10.1021/nl4007479.

[94] S. Bae, N. Sugiyama, T. Matsuo, H. Raebiger, K. I. Shudo, and K. Ohno, “Defect-Induced Vibration Modes of Ar+ -Irradiated MoS2,” *Phys Rev Appl*, vol. 7, no. 2, Feb. 2017, doi: 10.1103/PhysRevApplied.7.024001.

[95] G. Ye *et al.*, “Defects Engineered Monolayer MoS2 for Improved Hydrogen Evolution Reaction,” *Nano Lett*, vol. 16, no. 2, pp. 1097–1103, Feb. 2016, doi: 10.1021/acs.nanolett.5b04331.

[96] Q. Ma *et al.*, “Controlled argon beam-induced desulfurization of monolayer molybdenum disulfide,” *Journal of Physics Condensed Matter*, vol. 25, no. 25, Jun. 2013, doi: 10.1088/0953-8984/25/25/252201.

[97] A. Singh and R. Singh, “γ-ray Irradiation-Induced Chemical and Structural Changes in CVD Monolayer MoS 2,” *ECS Journal of Solid State Science and Technology*, vol. 9, no. 9, p. 093011, Jan. 2020, doi: 10.1149/2162-8777/abb583.

[98] W. M. Parkin *et al.*, “Raman Shifts in Electron-Irradiated Monolayer MoS2,” *ACS Nano*, vol. 10, no. 4, pp. 4134–4142, Apr. 2016, doi: 10.1021/acsnano.5b07388.

[99] “Number of layers of MoS 2 determined using Raman Spectroscopy.” [Online]. Available: www.horiba.com/scientific

[100] K. Gołasa *et al.*, “Resonant Raman scattering in MoS2- From bulk to monolayer,” *Solid State Commun*, vol. 197, pp. 53–56, 2014, doi: 10.1016/j.ssc.2014.08.009.

[101] C. Lee, H. Yan, L. E. Brus, T. F. Heinz, J. Hone, and S. Ryu, “Anomalous lattice vibrations of single- and few-layer MoS2,” *ACS Nano*, vol. 4, no. 5, pp. 2695–2700, May 2010, doi: 10.1021/nn1003937.

[102] S. Saleem, M. Salman, S. Ali, Y. Ling, and M. Khan, “Electrocatalytic hydrogen evolution reaction on sulfur-deficient MoS2 nanostructures,” *Int J Hydrogen Energy*, vol. 47, no. 12, pp. 7713–7723, Feb. 2022, doi: 10.1016/j.ijhydene.2021.12.081.

[103] A. Credi and L. Prodi, “From observed to corrected luminescence intensity of solution systems: an easy-to-apply correction method for standard spectrofluorimeters,” 1998.

[104] C. Backes *et al.*, “Edge and confinement effects allow in situ measurement of size and thickness of liquid-exfoliated nanosheets,” *Nat Commun*, vol. 5, Aug. 2014, doi: 10.1038/ncomms5576.

[105] A. O’Neill, U. Khan, and J. N. Coleman, “Preparation of high concentration dispersions of exfoliated MoS 2 with increased flake size,” *Chemistry of Materials*, vol. 24, no. 12, pp. 2414–2421, Jun. 2012, doi: 10.1021/cm301515z.

[106] R. Misra and S. P. Bhattacharyya, *Intramolecular Charge Transfer*. Wiley, 2018.

[107] G. Eda, H. Yamaguchi, D. Voiry, T. Fujita, M. Chen, and M. Chhowalla, “Photoluminescence from chemically exfoliated MoS 2,” *Nano Lett*, vol. 11, no. 12, pp. 5111–5116, Dec. 2011, doi: 10.1021/nl201874w.

[108] A. P. Paiva, “Recycling of palladium from spent catalysts using solvent extraction—some critical points,” *Metals*, vol. 7, no. 11. MDPI AG, Nov. 16, 2017. doi: 10.3390/met7110505.

[109] G. Y. Ding *et al.*, “Administration of the D-A structure and steric hindrance effect to construct efficient red emitters for high-performance OLEDs with low efficiency roll-off,” *Dyes and Pigments*, vol. 192, Aug. 2021, doi: 10.1016/j.dyepig.2021.109398.

[110] P. Dutta, W. Yang, S. Hun Eom, W. H. Lee, I. Nam Kang, and S. H. Lee, “Development of naphtho[1,2-b:5,6-b′]dithiophene based novel small molecules for efficient bulk-heterojunction organic solar cells,” *Chemical Communications*, vol. 48, no. 4, pp. 573–575, Dec. 2012, doi: 10.1039/c1cc15465f.

[111] S. Geng, W. Yang, Y. Liu, and Y. Yu, “Engineering sulfur vacancies in basal plane of MoS2 for enhanced hydrogen evolution reaction,” *J Catal*, vol. 391, pp. 91–97, Nov. 2020, doi: 10.1016/j.jcat.2020.05.042.

6. Appendix

^{1}H-NMR spectrum in $CDCl_3$ of 5-(4-(Diphenylamino)phenyl)thiophene-2-carbaldehyde (TPA-1)

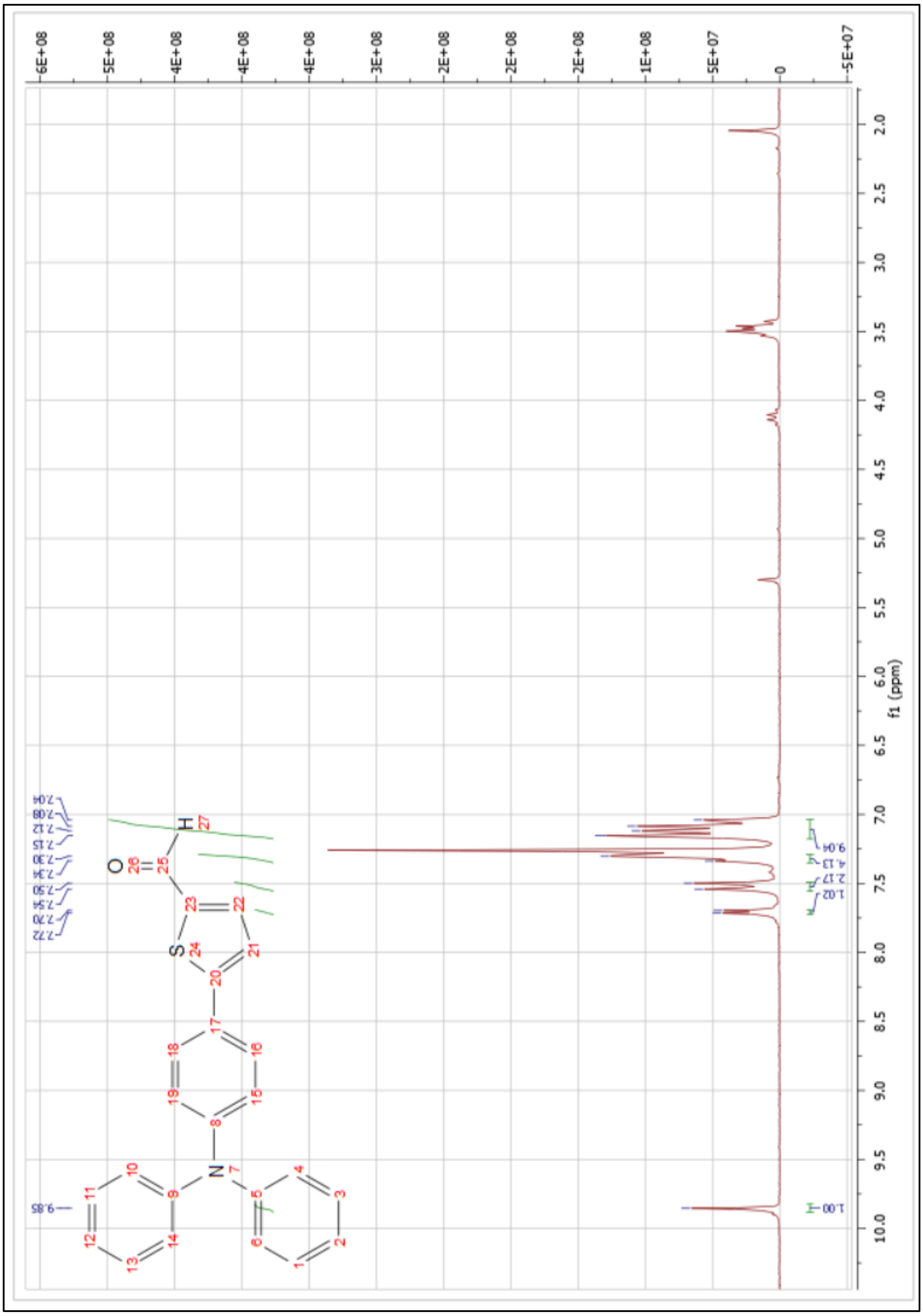

^{1}H-NMR spectrum in d_6-DMSO of 5-[4-(diphenylamino)phenyl]-thiophene-2-cyanoacrylic acid (TPA-2)

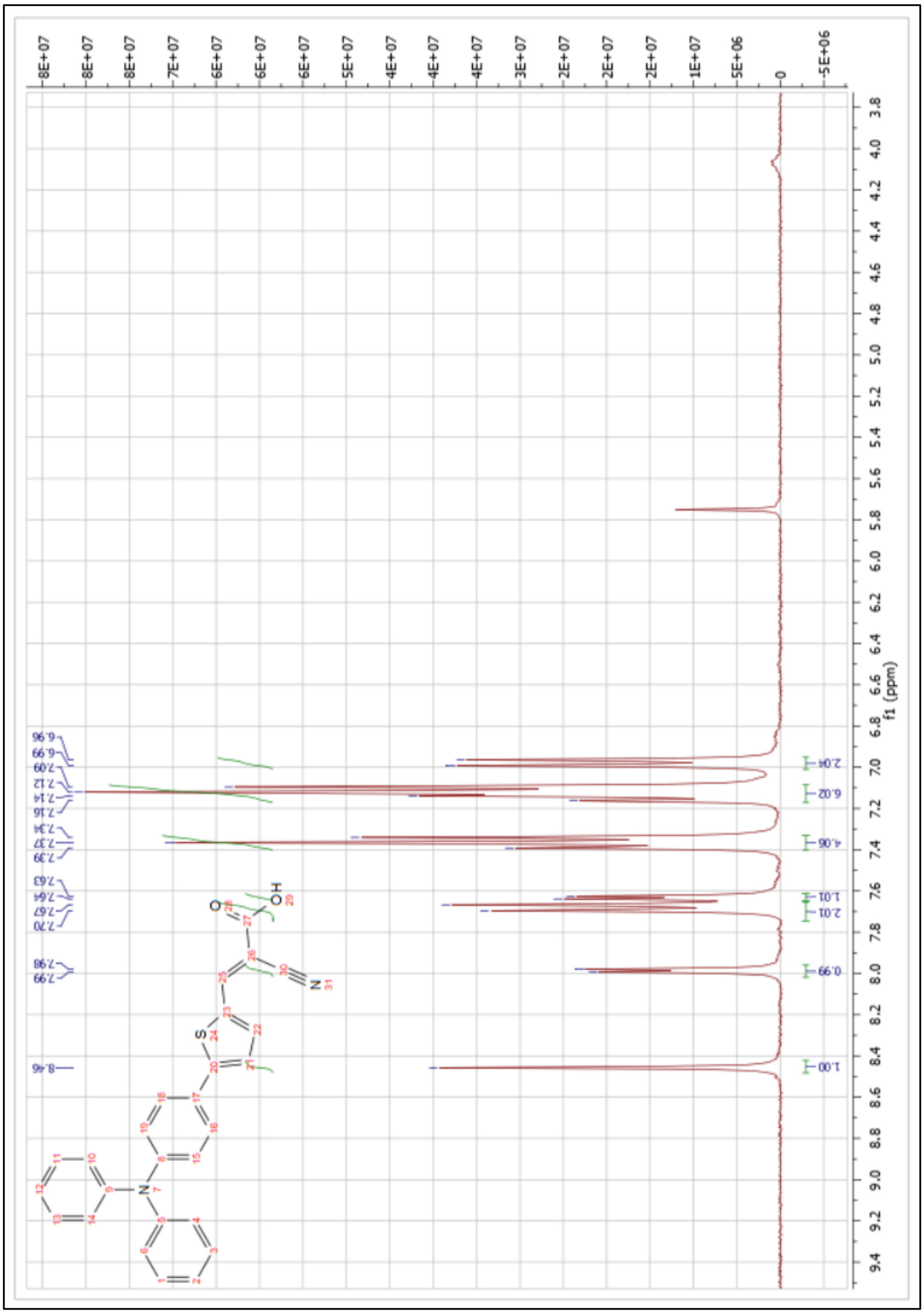

^{1}H-NMR spectrum in $CDCl_3$ of TPA-3

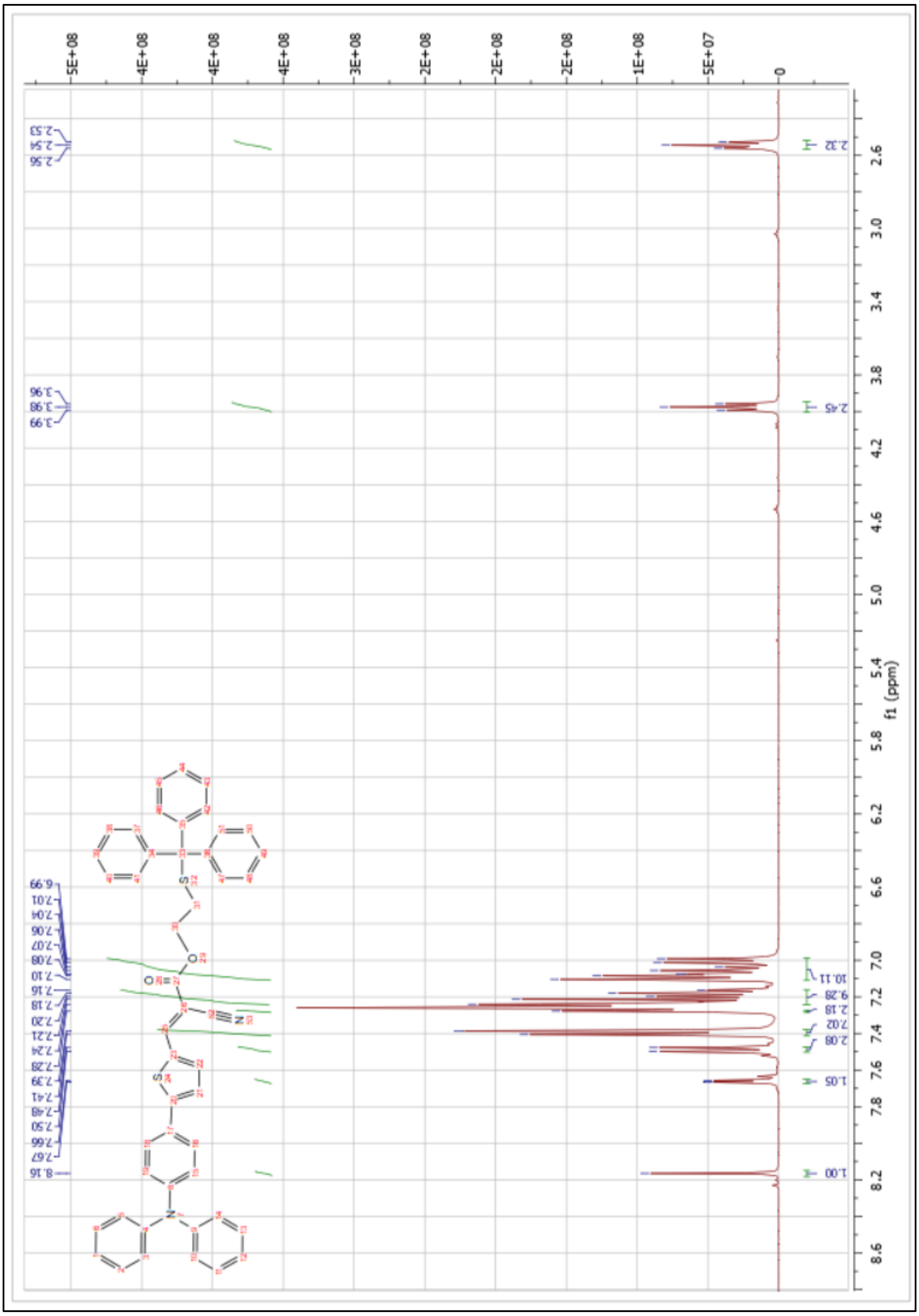

^{1}H-NMR spectrum in d_6-DMSO of 4-(diphenylamino)phenylboronic pinacol ester (TPA-4)

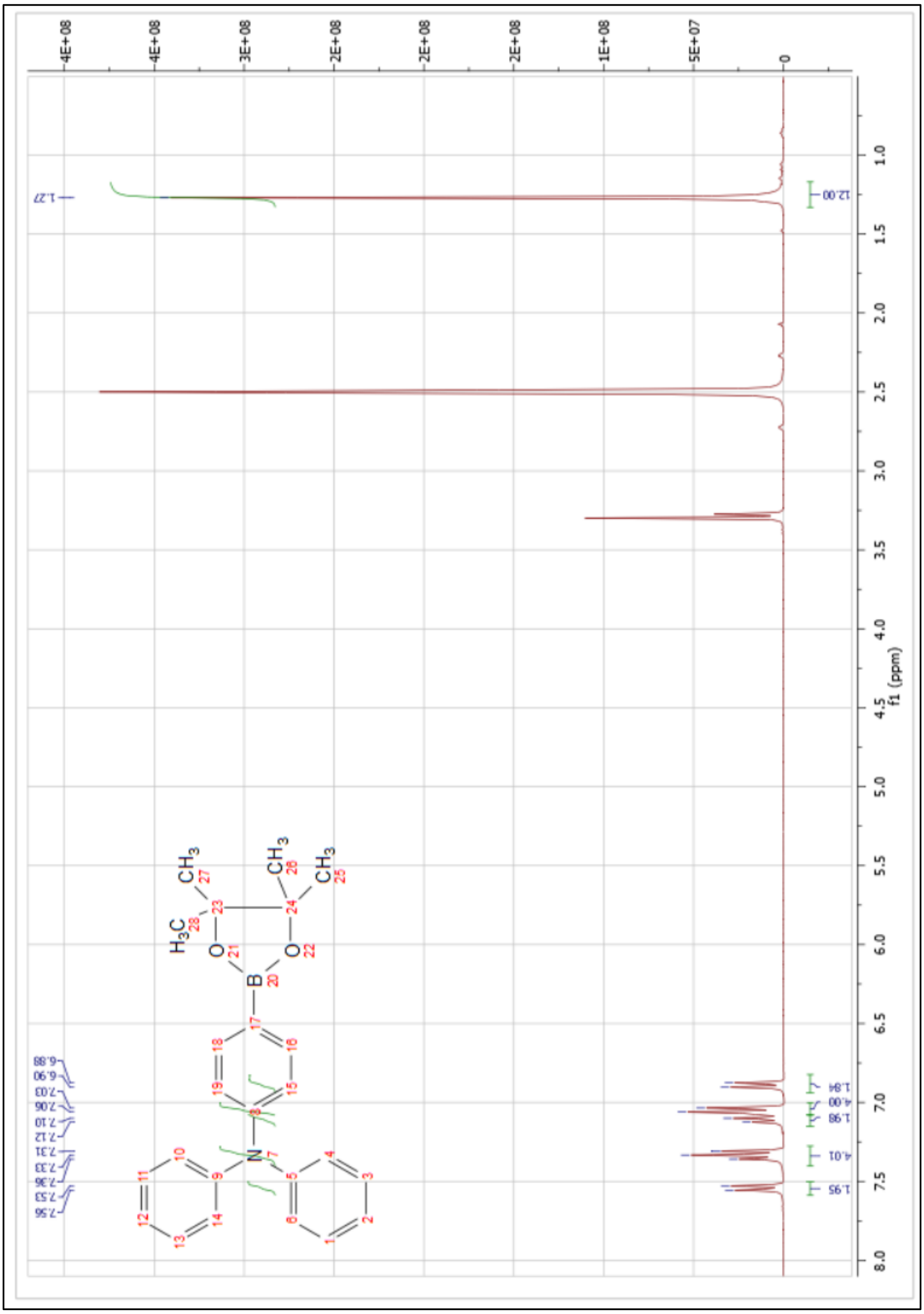

^{1}H-NMR spectrum in d_6-DMSO of 4-(7-bromobenzo[c][1,2,5]thiadiazol-4-yl)-N,N-diphenylaniline (TPA-5)

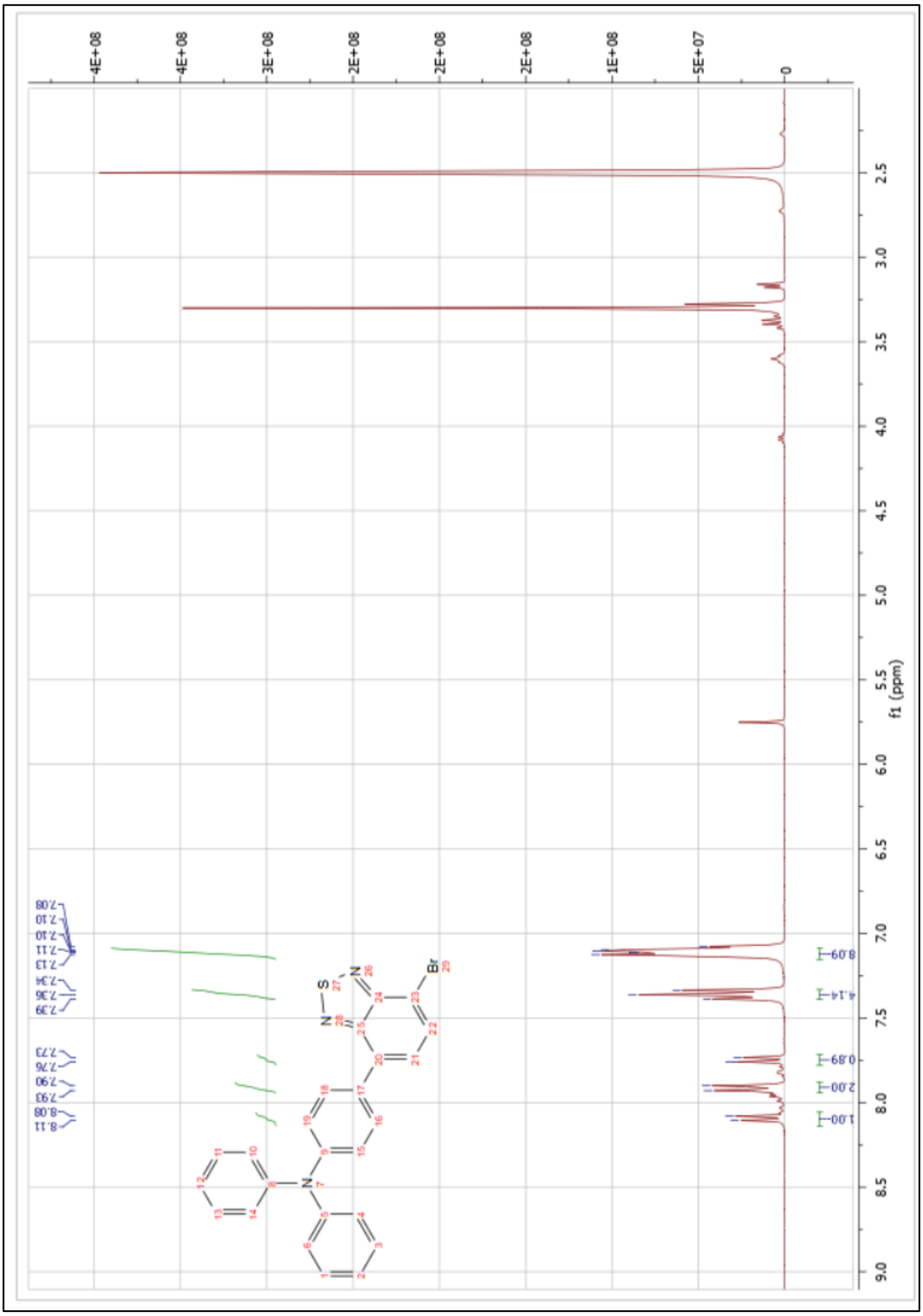

^{1}H-NMR spectrum in $CDCl_3$ of 5-[7-(4-diphenylaminophenyl)benzo[1,2,5]thiadiazol-4-yl]thiophene-2-carbaldehyde (TPA-6)

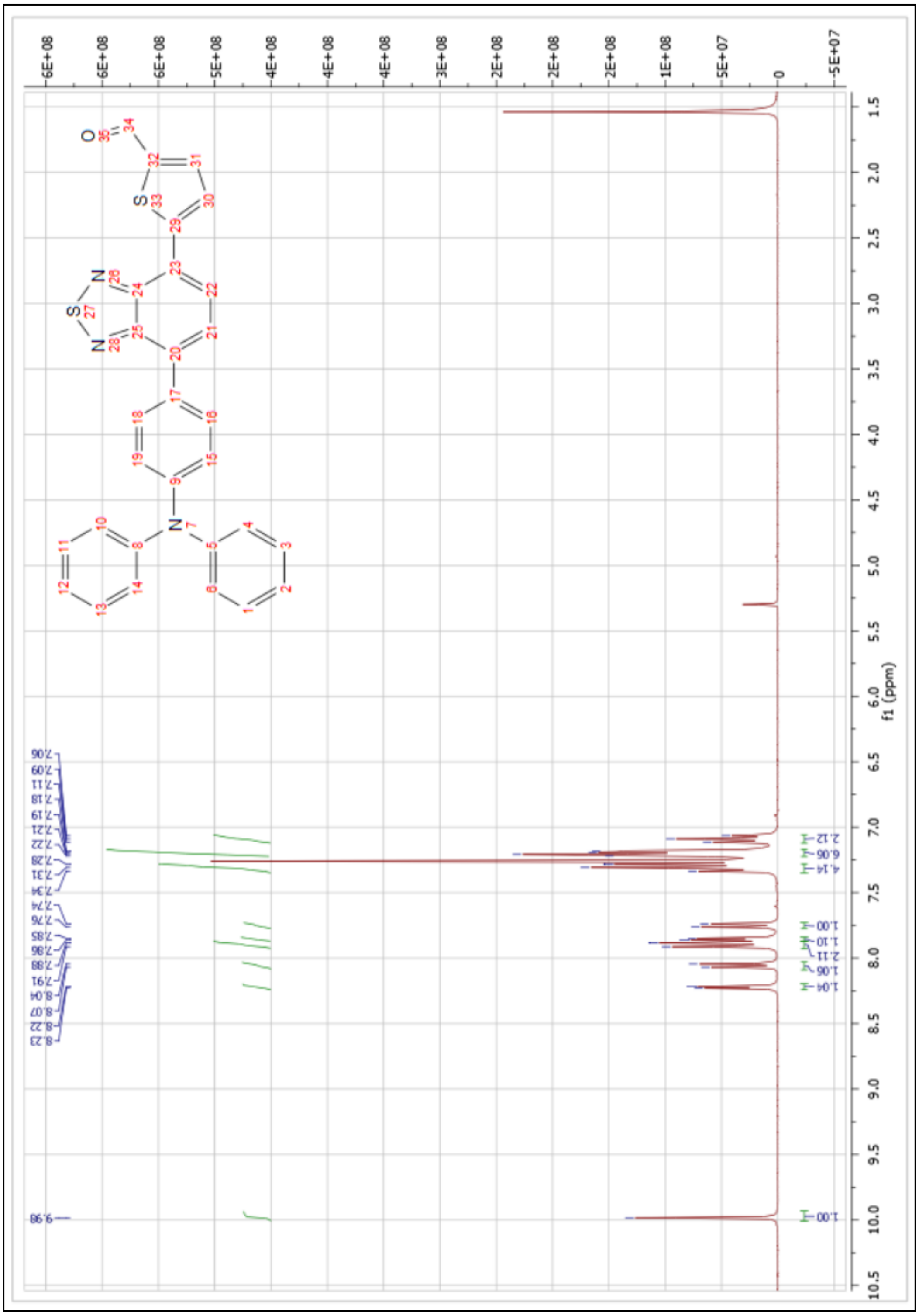

^{1}H-NMR spectrum in d_6-DMSO of 2-cyano-3-{5-[7-(4-diphenylaminophenyl)-2,1,3-benzothiadiazol-4-yl]thiophen-2-yl}acrylic acid (TPA-7)

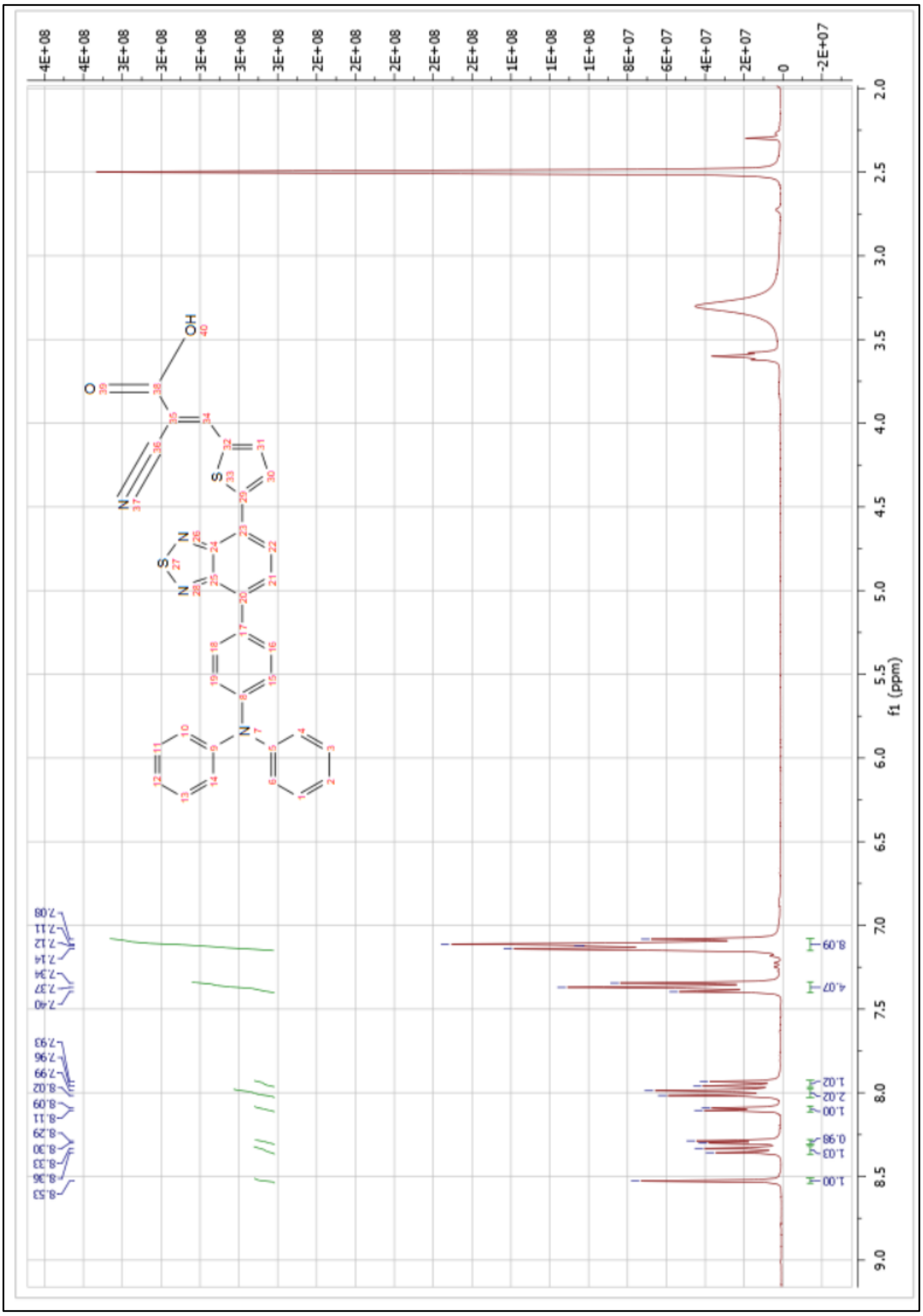

^{1}H-NMR spectrum in $CDCl_3$ of TPA-8

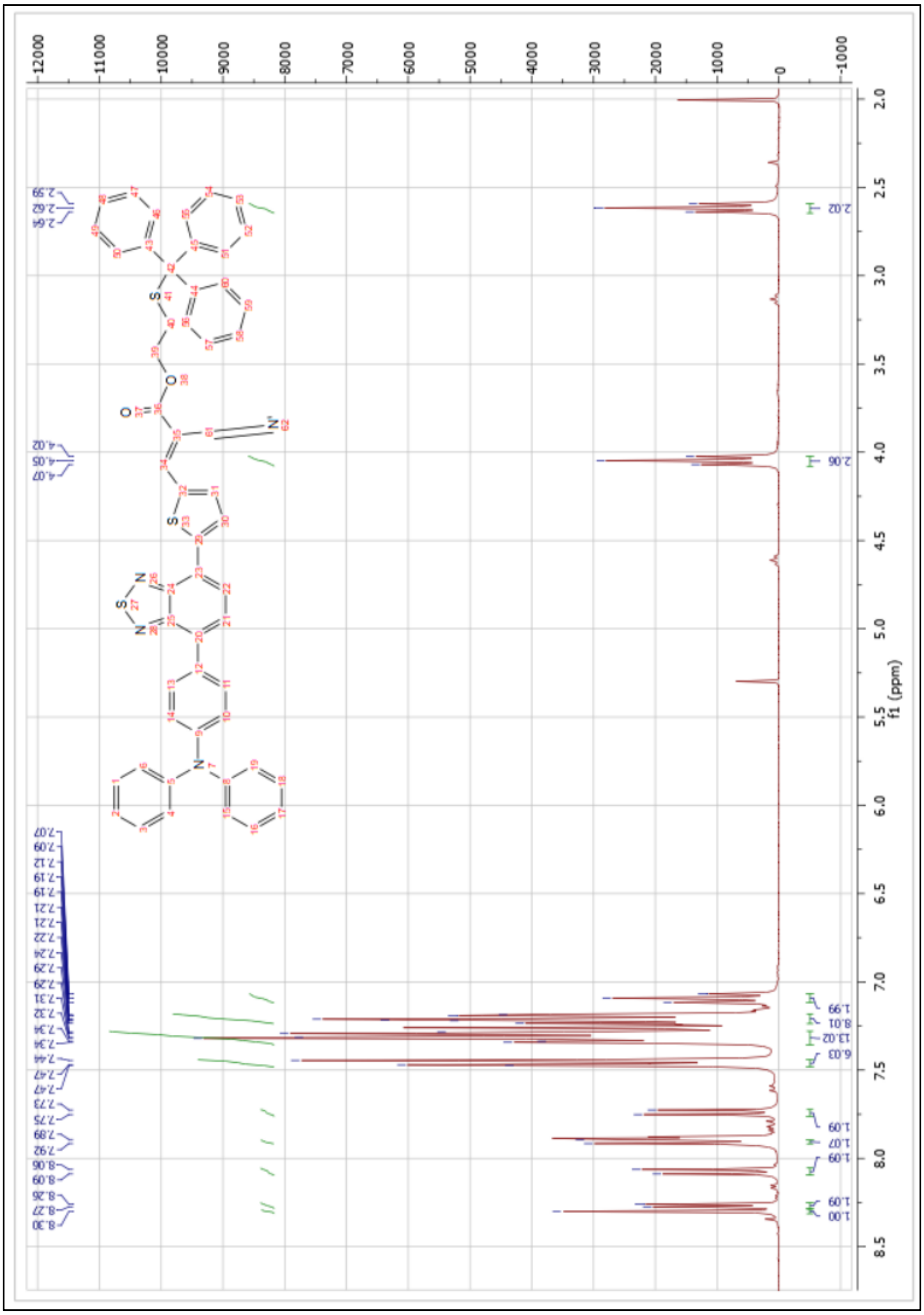

^{1}H-NMR spectrum in CDCl$_3$ of D-A-π-A

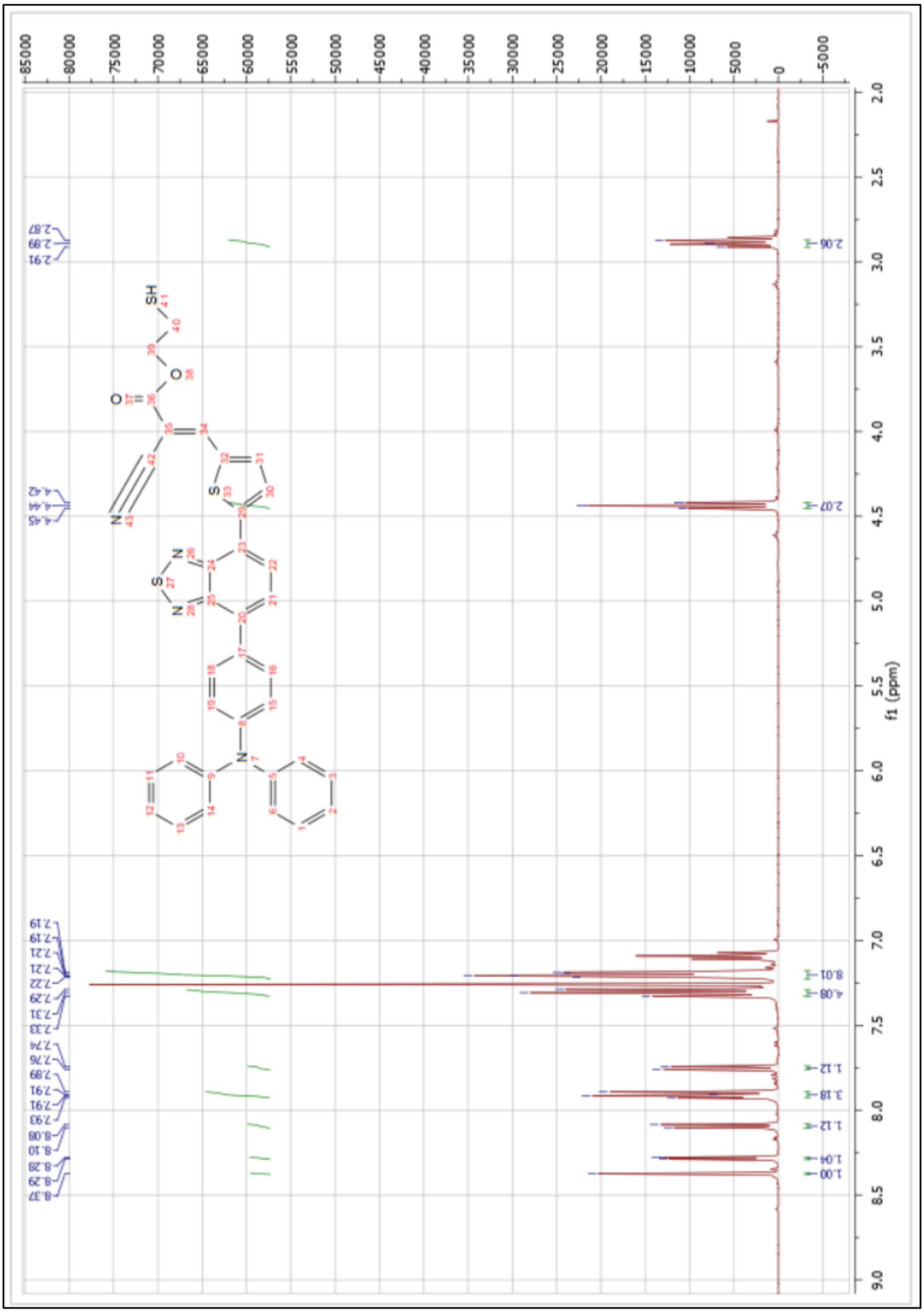

^{13}C-NMR spectrum in $CDCl_3$ of TPA-3

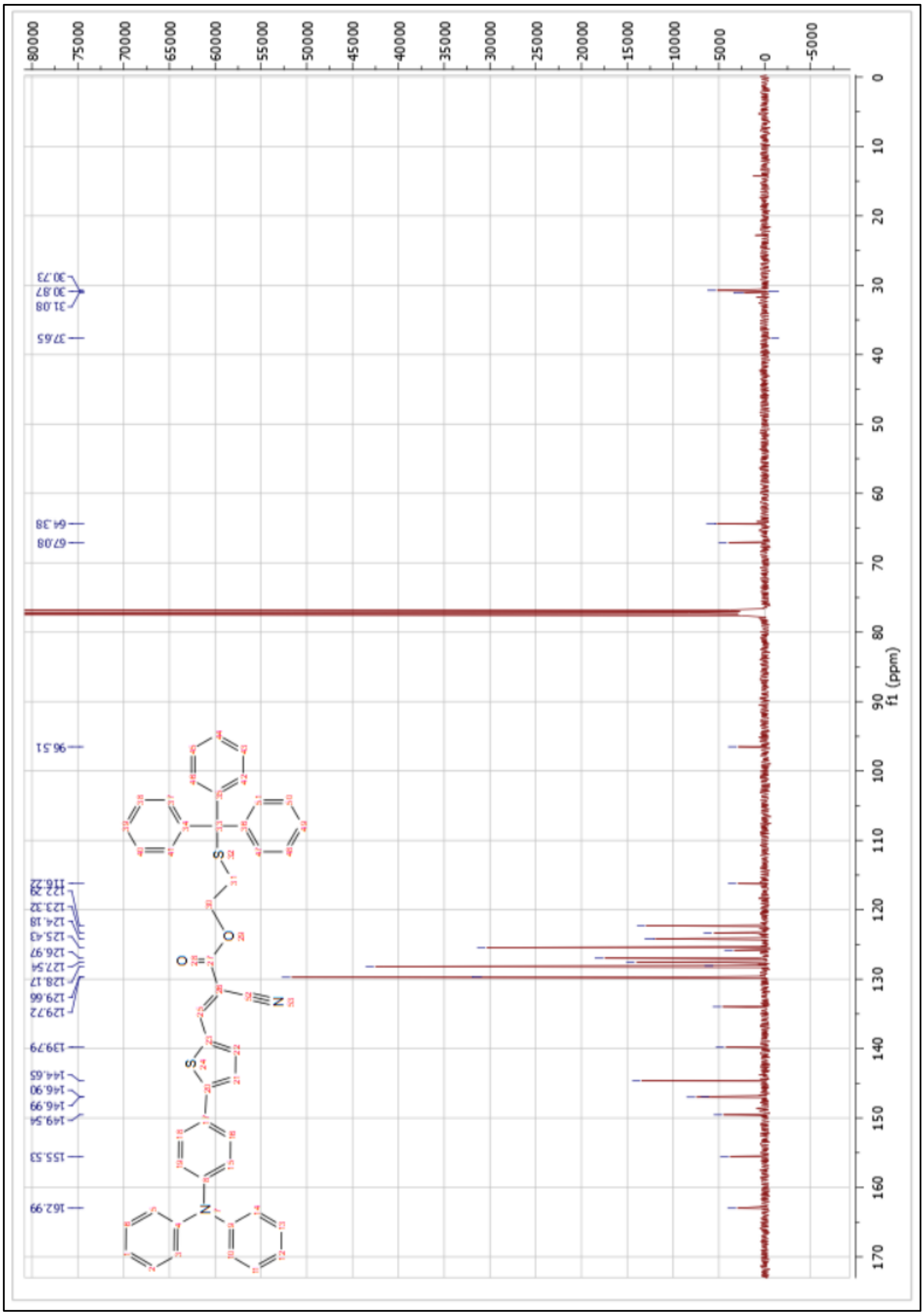

^{13}C-NMR spectrum in d$_6$-DMSO of TPA-8

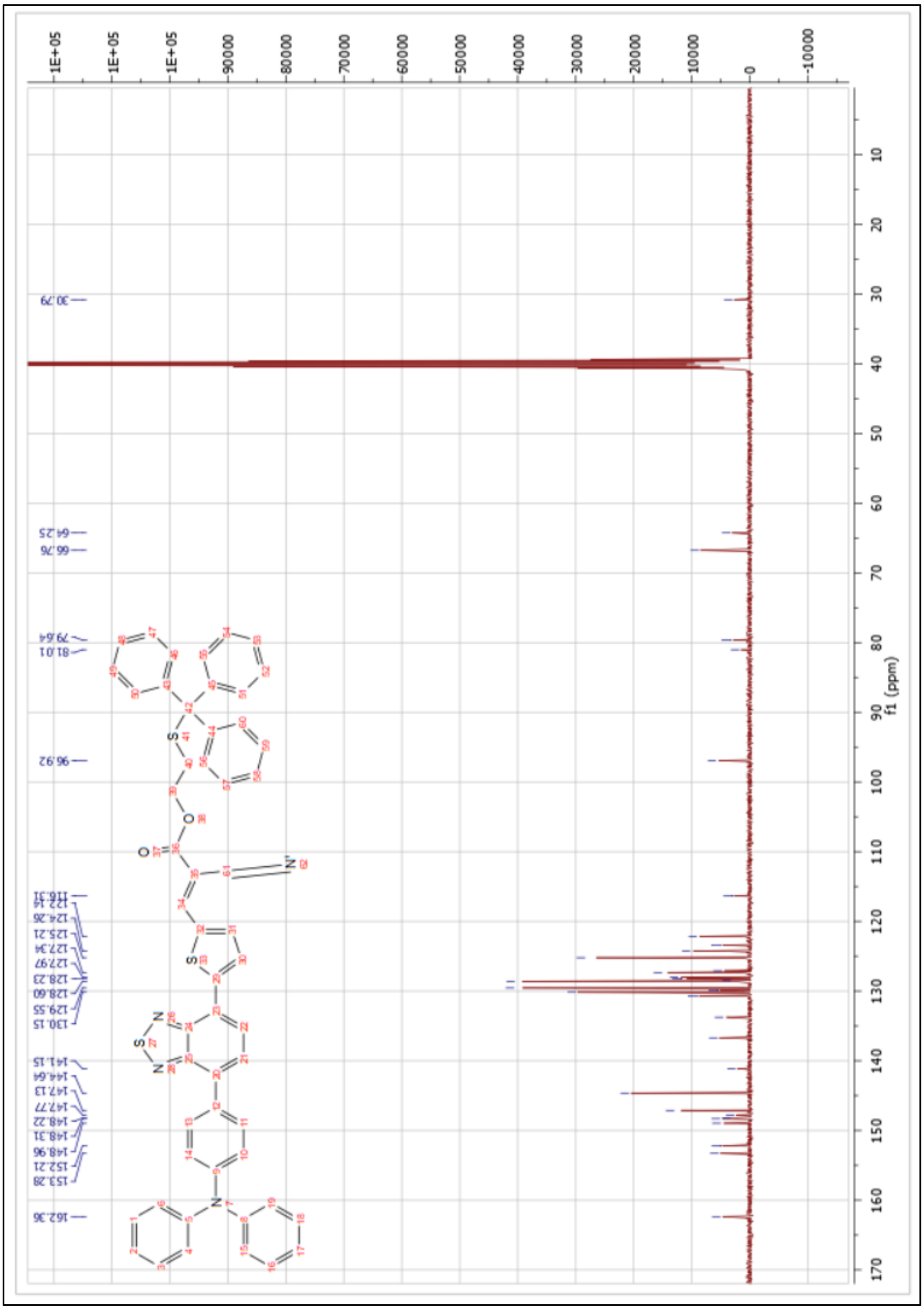

ESI-MS spectrum of TPA-4, in acidic acetonitrile, positive mode

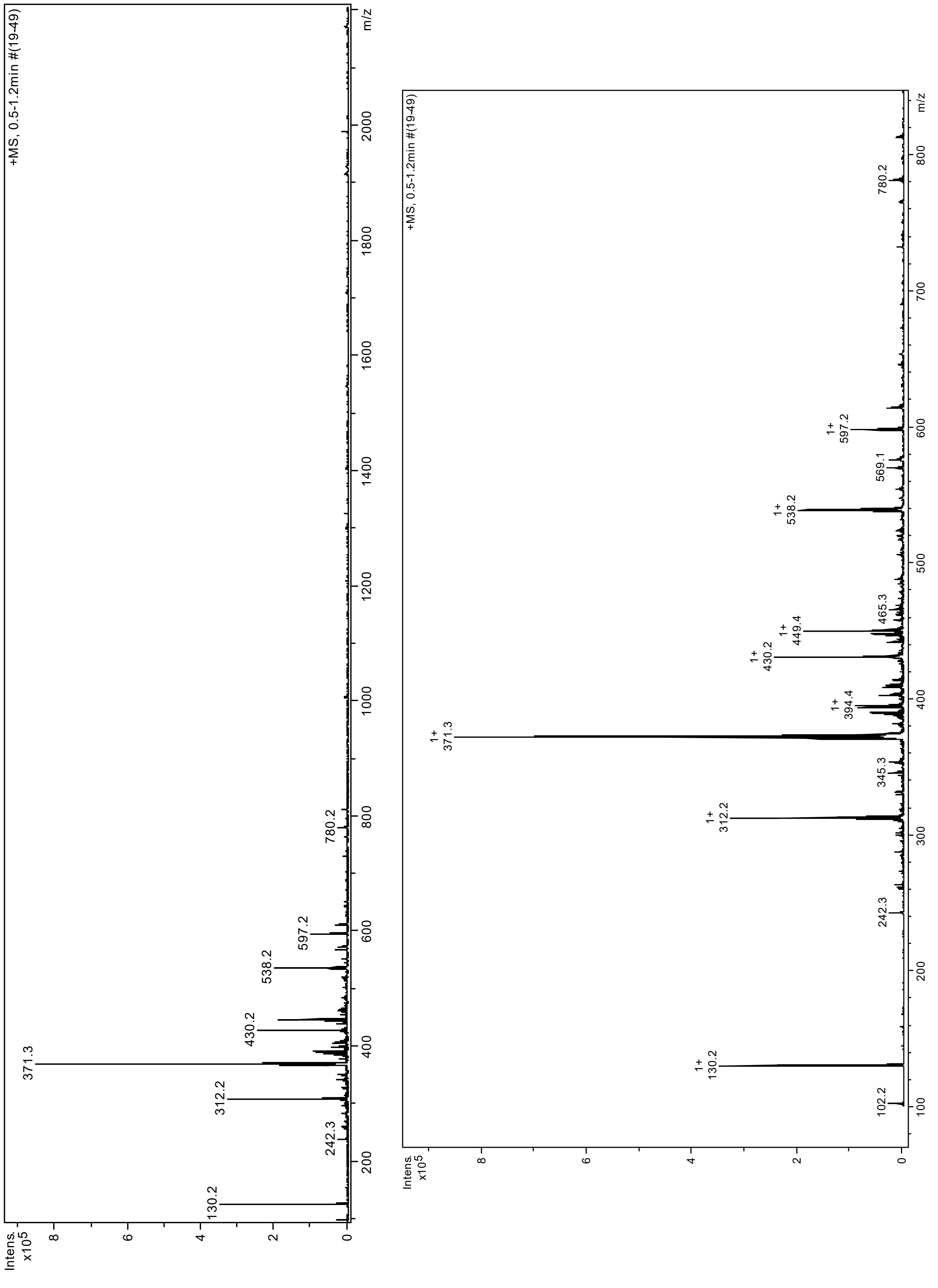

ESI-MS spectrum of TPA-5, in acidic acetonitrile, positive mode

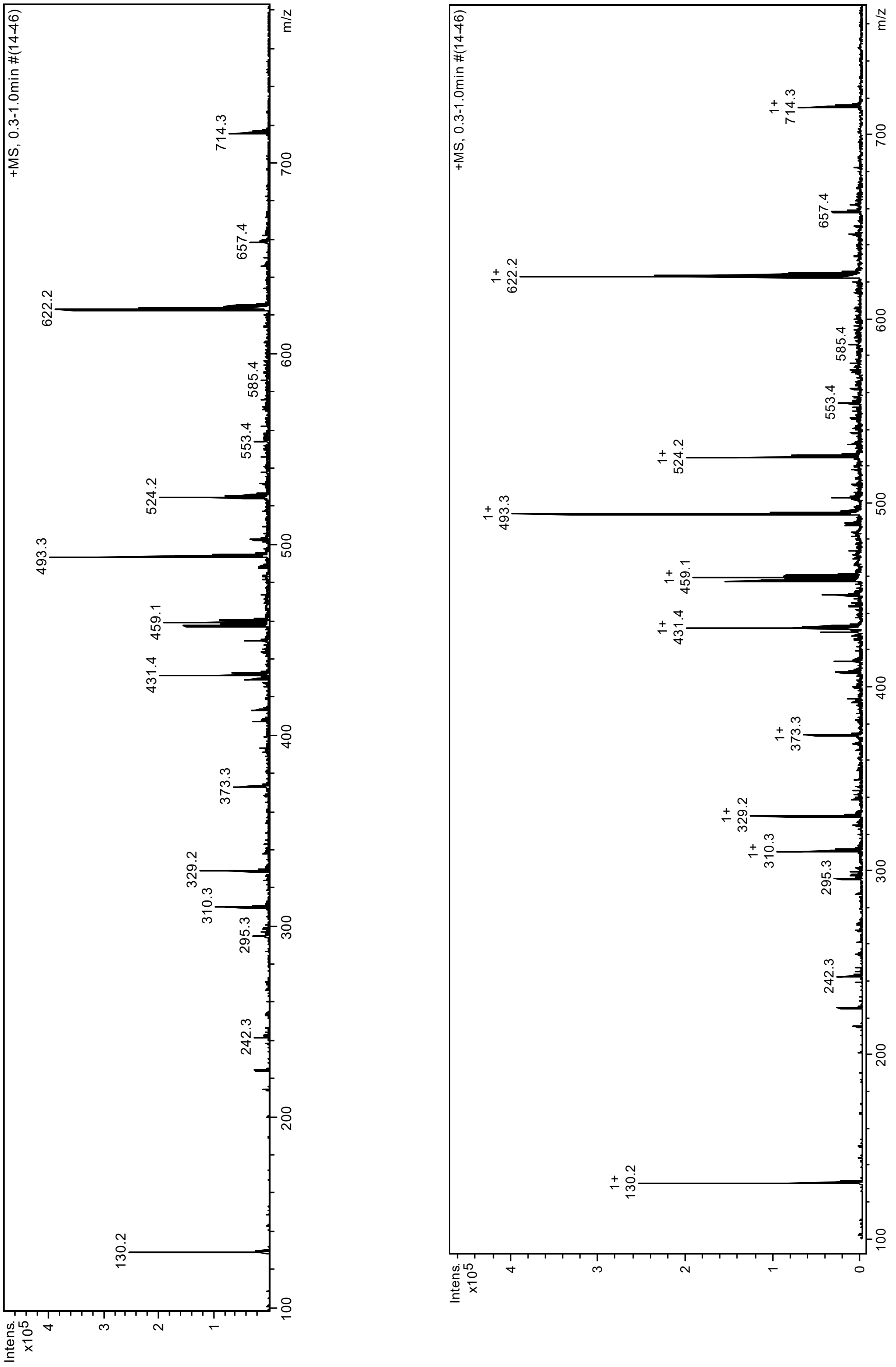

ESI-MS spectrum of TPA-7, in acidic acetonitrile, positive mode

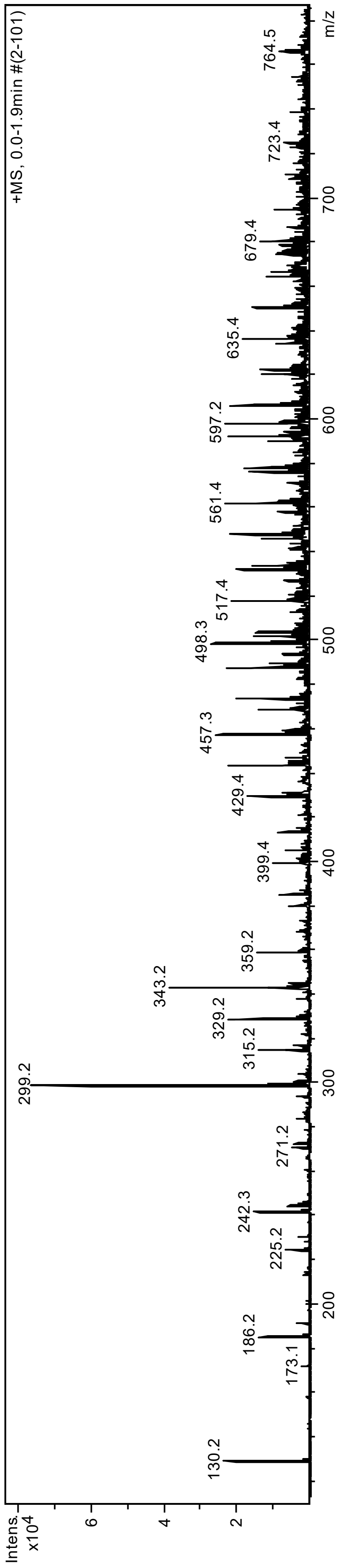

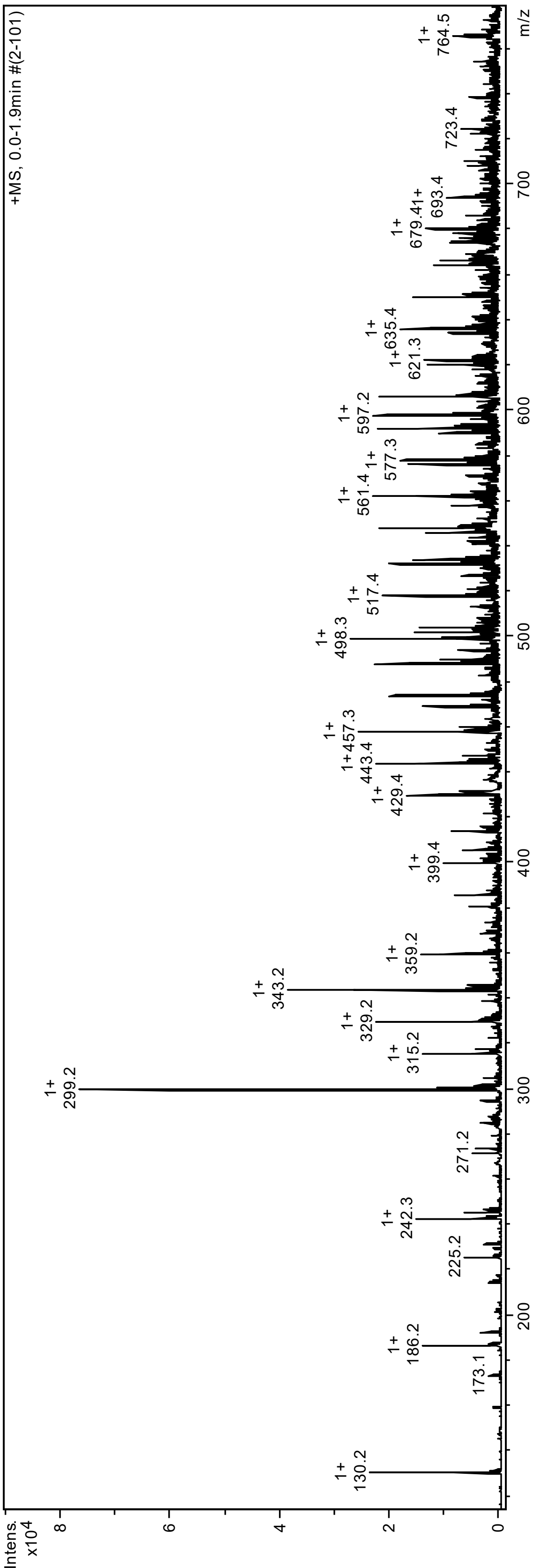

ESI-MS spectrum of TPA-8, in acidic acetonitrile, positive mode

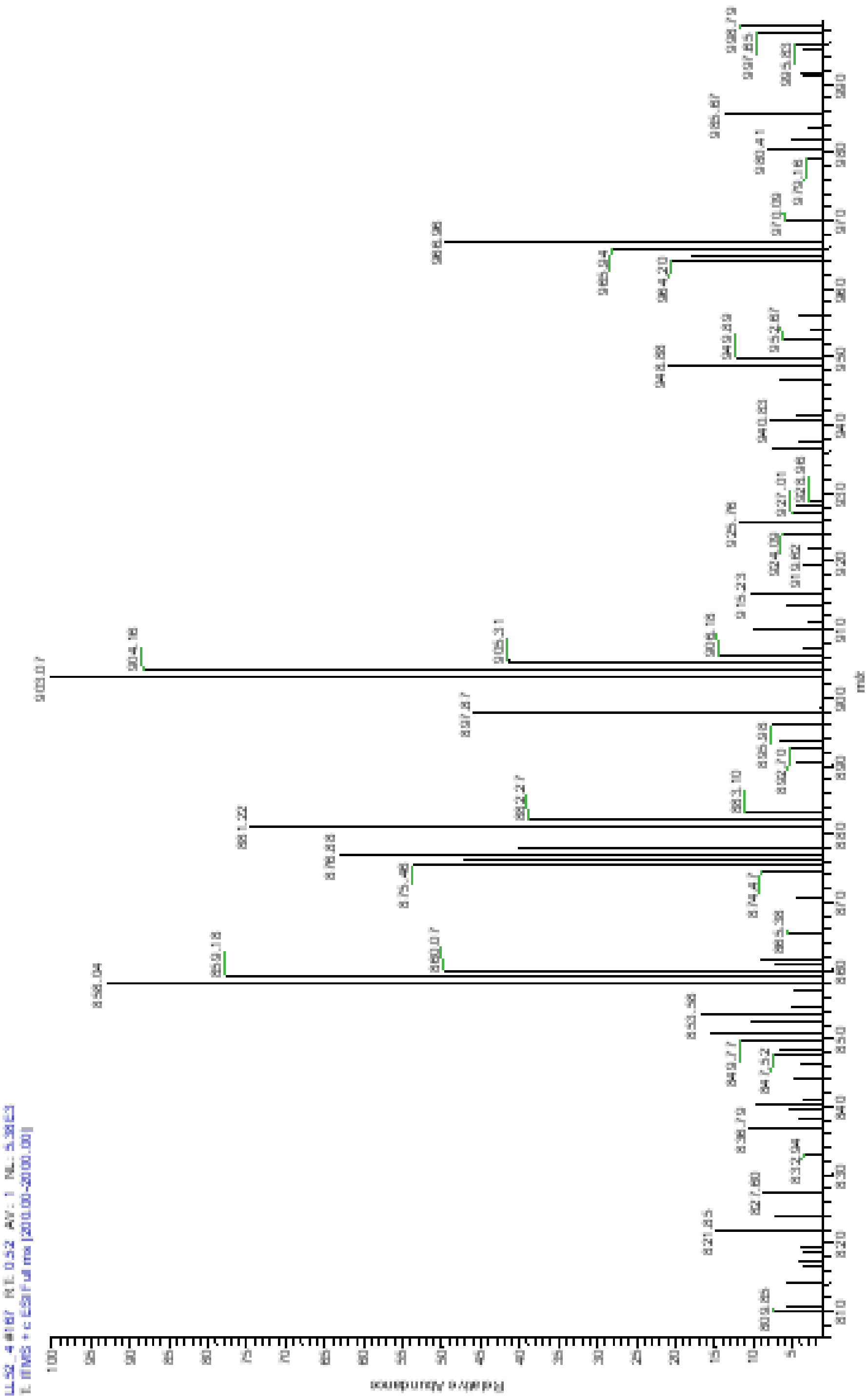

Ringraziamenti

Ringrazio in primo luogo il Prof. E. Menna per avermi dato la possibilità di svolgere il periodo di Tesi nel suo gruppo di ricerca. Ringrazio la Prof. S. Bonacchi e I. Fortunati per i preziosi aiuti forniti durante le analisi spettroscopiche. Ringrazio tutti i membri del "Lab 205" per aver reso così speciale questi momenti e averli resi forse i migliori di tutto il mio percorso universitario. Ringrazio infinitamente Luca, per gli innumerevoli spunti di riflessione forniti, per la pazienza infinita e per avermi accolto nel suo progetto da pari. Ringrazio Ilenia, la mia compagna, per avermi sempre appoggiato, nei momenti bui e in quelli gioiosi, per essere sempre stata al mio fianco, per aver sopportato le innumerevoli lamentele durante tutto il percorso di Tesi Magistrale. Ringrazio i miei genitori, per avermi affiancato e sostenuto sempre, e avermi permesso di intraprendere la mia strada.

Ultimo ma non meno importante, voglio ringraziare me stesso, per aver creduto in me, per aver dato tutto quello che potevo in questo percorso, e non aver mai mollato.